Study of a Passive Decay Heat Removal System and Tritium Mitigation for Fluoride-salt-cooled High-temperature Reactors

by

Sheng Zhang

A dissertation submitted in partial fulfillment
of the requirements for the degree of
Doctor of Philosophy
(Nuclear Engineering and Radiological Sciences)
in the University of Michigan
2020

Doctoral Committee:

Professor Xiaodong Sun, Chair
Professor Richard N. Christensen, University of Idaho
Professor Annalisa Manera
Professor Kevin Pipe
Dr. Kevin Robb, Oak Ridge National Laboratory

Sheng Zhang

shengzh@umich.edu

ORCID ID: 0000-0003-2304-0956

This dissertation is dedicated to my parents for their love and support.

Acknowledgements

This research was performed using funding received from the United States Department of Energy (DOE) Office of Nuclear Energy's Nuclear Energy University Program (NEUP).

Foremost, I would like to express my sincere gratitude to Professor Xiaodong Sun, my advisor, for his continuous guidance and support. He is a kind and knowledgeable person, who inspires me to overcome obstacles on my way to completing the graduate study.

In addition, I would like to thank other committee members, Professor Richard N. Christensen, Professor Annalisa Manera, Professor Kevin Pipe, and Dr. Kevin Robb for their encouragement and insightful comments and suggestions. Special thanks to Dr. David Holcomb, Dr. Graydon L. Yoder, Dr. Elvis E. Dominguez-Ontiveros, and Professor Farzad Rahnema for their advice and support for the project.

I would also be grateful for the help and support from my friends, Dr. Qiuping Lv, Dr. Minghui Chen, Dr. Hsun-Chia Lin, Dr. Shanbin Shi, Dr. Yang Liu, Dr. Adam Burak, Dr. Xiao Wu, Dr. Qingqing Liu, Dr. Peng Wang, Dr. Sunming Qin, Dr. Daniel Nunez, Dr. Keyong Cheng, Xiaoqin Zhang, Chengqi Wang, Jiaxin Mao, and Hanxing Sun.

The final appreciation is dedicated to my parents. Without their endless love, the work could not have been completed.

Table of Contents

List of Figures

List of Tables

Nomenclature

List of symbols

A_f: Cross-sectional flow area, m^2

A_{iw}, A_{ow}, A_{ish}, A_{oins}, A_{iiw}, A_{oiw}, A_{iow}, and A_{oow}: Inner and outer surface areas of the tube wall, inner surface area of the cooler shell, outer surface area of the thermal insulation, inner and outer surface areas of the inner tube wall, and inner and outer surface areas of the outer tube wall, respectively, m^2

$c_{p,fI}$, $c_{p,fII}$, $c_{p,t}$, $c_{p,sh}$, $c_{p,ins}$, $c_{p,if}$, $c_{p,af}$, and $c_{p,of}$: Specific heat capacity of Fluid I, Fluid II, tube, cooler shell, thermal insulation, inner fluid, annular fluid, and outer fluid, respectively, J/(kg-K)

$C_{T,bif}$, $C_{T,baf}$, $C_{T,bof}$, $C_{T,if-it}$, $C_{T,af-it}$, $C_{T,af-ot}$, and $C_{T,of-ot}$: Tritium molar concentration in the bulk inner fluid, bulk annular fluid, bulk outer fluid, interface between the inner fluid and inner tube, interface between the annular fluid and inner tube, interface between the annular fluid and outer tube, and interface between the outer fluid and outer tube, respectively, $\mathrm{mol/m}^3$

D_{AB}: Diffusivity of species A in species B, m^2/s

D_h, D_{iins} and D_{oins}: Hydraulic diameter, and inner and outer diameters of the thermal insulation, respectively, m

$E_{b\lambda}$: Spectral emissive power of a black body, $\mathrm{W/m}^3$

f: Darcy friction factor

f_r: Thermal radition effect factor

F_s: Safety factor

g: Acceleration due to earth's gravity, $\mathrm{m/s^2}$

Gr: Grashof number

Gz: Graetz number

h_c, h_r, $h_{it,all}$, h_{iiw}, h_{oiw}, h_{iow}, and h_{oow}: Convective and radiative heat transfer coefficients, overall heat transfer coefficient on the tube inner surface, convective heat transfer coefficient on the inner and outer surfaces of the inner tube wall, and convective heat transfer coefficient on the inner and outer surfaces of the outer tube wall, respectively, W/(m^2-K)

J_i and J_o: Tritium permeation rate through the inner and outer tubes, respectively, $\mathrm{mol/s}$

$\bar{k}_a$: Plank-mean absorption coefficient, $\mathrm{m^{-1}}$

$k_{H,T,if}$, $k_{H,T,af}$, and $k_{H,T,of}$: Henry's law constant for tritium in the inner, annular, and outer fluids, respectively, mol/(m^3-Pa)

$k_{l,\lambda,m}$ and $k_{l,\lambda,i}$: Number-density-average absorption coefficient of a mixture and absorption coefficient of constituent i, respectively, $\mathrm{m^{-1}}$

$k_{m,iiw}$, $k_{m,oiw}$, $k_{m,iow}$, and $k_{m,oow}$: Mass transfer coefficient on the inner and outer surfaces of the inner tube wall, and inner and outer surfaces of the outer tube wall, respectively, $\mathrm{m/s}$

k_{Pi} and k_{Po}: Permeability of the inner and outer tubes, respectively, mol/(m-s-Pa$^{0.5}$)

k_s, k_t, k_{ins}, k_{it} and k_{ot}: Thermal conductivity of salt, tube, thermal insulation, inner and outer tubes, respectively, W/(m-K)

$L_{laminar,hyd}$ and $L_{turbulent,hyd}$: Hydrodynamic entrance length of laminar and turbulent flows, respectively, m

$L_{laminar,T}$ and $L_{turbulent,T}$: Thermal entrance length of laminar and turbulent flows, respectively, m

m_{fI}, m_{fII}, m_t, m_{sh}, and m_{ins}: Weight of Fluid I, Fluid II, tube, cooler shell, and thermal insulation, respectively, kg

$\dot{m}_{fI}$, $\dot{m}_{fII}$, $\dot{m}_{if}$, $\dot{m}_{af}$, and $\dot{m}_{of}$: Mass flow rate of Fluid I, Fluid II, inner, annular, and outer fluids, respectively, kg/s

M_i: Molar mass of constituent i, g/mol

N_i: Number density of constituent i, $\mathrm{atom/m^3}$

N_q: Grid quantity

Nu: Nusselt number

Nu_t, Nu_c, and Nu_r: Nusselt number of the total, convective, and radiative heat transfer, respectively

$p_{T,if-it}$, $p_{T,it-if}$, $p_{T,af-it}$, $p_{T,it-af}$, $p_{T,af-ot}$, $p_{T,ot-af}$, $p_{T,of-ot}$, and $p_{T,ot-of}$: Tritium partial pressure on the inner-fluid-inner-tube interface close to the inner fluid and inner tube, tritium partial pressure on the annular-fluid-inner-tube interface close to the annular fluid and inner tube, tritium partial pressure on the annular-fluid-outer-tube interface close to the annular fluid and outer tube, and tritium partial pressure on the outer-fluid-outer-tube interface close to the outer fluid and outer tube, respectively, Pa

Δp_f: Frictional pressure drop, Pa

Pr_f and Pr_w: Prandtl number evaluated at the fluid and tube wall temperatures, respectively

q_c'' and q_r'': Convective and net radiative heat fluxes, respectively, $\mathrm{W/m^2}$

$\dot{Q}$ and $\dot{Q}_h$: Heat transfer rate and heating power, respectively, W

r : Radial coordinate, m

r_1, r_2, r_3, and r_4: Inner and outer radiuses of the inner tube, and inner and outer radiuses of the outer tube, respectively, m

R_g: Universal gas coefficient, 8.314 J/(mol-K)

Re: Reynolds number

Ri: Richardson number

s: Sign function

Sc: Schmidt number

Sh: Sherwood number

t: Time, s

T_{fI}, T_{fII}, T_t, T_{sh}, T_{ins}, T_{air}, T_a, T_{if}, T_{af}, T_{of}, T_{it}, T_{ot}, T_{iiw}, T_{oiw}, T_{iow}, and T_{oow}: Temperature of Fluid I, Fluid II, tube, cooler shell, thermal insulation, air, ambient, inner fluid, annular fluid, outer fluid, inner tube, outer tube, inner surface of the inner tube wall, outer surface of the inner tube wall, inner surface of the outer tube wall, and outer surface of the outer tube wall, respectively, K

$\bar{T}_{iw}$, $\bar{T}_f$, $\bar{T}_{in}$ and $\bar{T}_{out}$: Area-average temperature of the inner tube wall, arithmetic mean of the fluid bulk inlet and outlet temperatures, fluid bulk inlet temperature, and fluid bulk outlet temperature, respectively, K

u: Velocity, $\mathrm{m/s}$

V_i: Molar volume of the constituent i, $\mathrm{m^3/mol}$

V_t: Grid total volume, $\mathrm{m^3}$

X_{it-ot}: View factor from the inner tube to the outer tube

z and Δz: Axial coordinate and distance, m

Greek symbols

α_1, α_2, α_3, and α_s: Absorptivity of Media 1, 2, 3, and salt, respectively

β_{fI}: Thermal expansion coefficient of Fluid I, $\mathrm{K^{-1}}$

γ_{2-1} and γ_{3-2}: The grid refinement ratio between mesh options 1 and 2, and 2 and 3, respectively

ε_s, ε_t, and ε_{sh}: Emissivity of salt, tube, and cooler shell, respectively

ζ_1 and ζ_2: Grid size for options 1 and 2, respectively, m

λ: Wavelength, μm

μ_f and μ_w: Dynamic viscosity evaluated at the fluid and tube wall temperatures, respectively, kg/(m-s)

ρ_1, ρ_2, ρ_3, ρ_s, and ρ_t: Reflectivity of Media 1, 2, 3, salt, and tube, respectively

σ: Stefan-Boltzmann constant, $\sigma = 5.67 \times 10^{-8}$ W/(m^2-K^4)

τ_s: Transmissivity of the salt

ν_{fl}: Kinematic viscosity of Fluid I, m^2/s

χ_i: Mole fraction of constituent i

Acronyms

AHTR: Advanced High-Temperature Reactor

AWHX: Air-to-Water Heat eXchanger

CFD: Computational Fluid Dynamics

CSP: Concentrated Solar Power

CVD-SiC: Chemical Vapor Deposition Silicon Carbide

DHX: DRACS Heat eXchanger

DOE: Department of Energy

DP: Differential Pressure

DRACS: Direct Reactor Auxiliary Cooling System

DW-FTHX: Double-Wall Fluted-Tube Heat eXchanger

DWHX: Double-Wall Heat eXchanger

FHR: Fluoride-salt-cooled High-temperature Reactor

FLUSTFA: FLUoride Salt Test FAcility

GCI: Grid Convergence Index

HEMAT: HEat and MAss Transfer code

HTF: Heat Transfer Fluid

HX: Heat eXchanger

ID: Inner Diameter

IET: Integral Effect Test

IFOF: Inner Fluted tube with Outer Fluted tube

IFOP: Inner Fluted tube with Outer Plain tube

IPOF: Inner Plain tube with Outer Fluted tube

IPOP: Inner Plain tube with Outer Plain tube

I-PHX: Intermediate-to-Power cycle Heat eXchanger

LWR: Light Water Reactor

MHX: Maintenance Heat eXchanger

MSR: Molten Salt Reactor

NACCO: NAtural Circulation COde

NDHX: Natural Draft Heat eXchanger

NEUP: Nuclear Energy University Program

NRC: Nuclear Regulatory Commission

NSGA: Non-dominated Sorting Genetic Algorithms

OD: Outer Diameter

ORNL: Oak Ridge National Laboratory

PB-FHR: Pebble-Bed FHR

PIRT: Phenomena Identification and Ranking Table

P-IHX: Primary-to-Intermediate Heat eXchanger

SBO: Station Blackout

sCO_2: Supercritical CO_2

SmAHTR: Small modular Advanced High-Temperature Reactor

SS: Stainless Steel

SWHX: Single-Wall Heat eXchanger

SW-FTHX: Single-Wall Fluted-Tube Heat eXchanger

TES: Thermal Energy Storage

TGB: Tritium Getter Bed

TH: Thermal Hydraulics

TMSR-SF1: Thorium Molten Salt Reactor - Solid Fuel 1

TRISO: TRistructural ISOtropic

VFD: Variable Frequency Drive

Abstract

Molten Salt Reactors (MSRs) are a class of Generation IV nuclear reactors using molten salts as Heat Transfer Fluids (HTFs). MSRs have two major variants, namely, solid fuel reactor (salt-cooled reactor) and liquid fuel reactor (salt-fueled reactor). This study primarily focuses on the solid fuel MSRs, i.e., the Fluoride-salt-cooled High-temperature Reactors (FHRs).

FHRs adopt TRistructural-ISOtropic (TRISO) fuel particles, low-pressure liquid fluoride salts, and passive decay heat removal systems, such as the Direct Reactor Auxiliary Cooling System (DRACS). Although FHRs bring these benefits, there are a number of key technology gaps/issues that need to be addressed for FHR development. In this study, two key technology gaps/issues have been addressed for FHRs: (1) molten salt natural circulation in a passive decay heat removal system and (2) management/control of tritium, whose production rate in FHRs is expected to be significantly higher than that in Light Water Reactors (LWRs).

In this study, both the heat transfer and friction characteristics of molten salts in straight circular pipes were first numerically investigated by a Computational Fluid Dynamics (CFD) tool, STAR-CCM+. The CFD results were then validated by comparing with experimental data in the literature and correlation predictions. Our analysis showed that molten salts in the transitional and turbulent flow regimes acted as ordinary HTFs, for which conventional forced convective heat transfer correlations could be applied with ±20% uncertainties in general. As for molten salts in the laminar flow regime, however, both the correlation results and CFD predictions without considering the effects of buoyancy and radiative heat transfer in molten salts significantly

underestimated the salt Nusselt number, which could be as large as 40% and 30% lower, respectively. These significant discrepancies were attributed to the fact that the buoyancy effect and radiative heat transfer effect were generally not negligible for laminar flows of molten salts, which was demonstrated by good agreement (within ±14% uncertainties) between experimental data and CFD predictions considering those two effects.

The molten salt natural circulation in a single loop and multiple coupled loops, similar to the passive decay heat removal system DRACS, was then investigated by a one-dimensional (1D) NAtural Circulation COde, NACCO, developed in this research. The above finding, i.e., the non-negligible effects of buoyancy and radiative heat transfer in laminar flows of molten salts, was further confirmed by comparing the code results with two high-temperature natural circulation experiments using $NaNO_3$-KNO_3 and FLiBe as coolants, respectively. This validated 1D code NACCO was then applied to a FLUoride Salt Test FAcility, FLUSTFA, which was designed based on a scaling analysis and constructed in this research to experimentally investigate the DRACS performance under steady-state and various transient scenarios.

In addition, another technology gap/issue, tritium management, was studied for FHRs. Two strategies were proposed for tritium mitigation in FHRs, namely, Double-Wall Fluted-Tube Heat eXchanger (DW-FTHX) with a tritium carrier and Single-Wall FTHX (SW-FTHX) with a tritium barrier options. These two options were then evaluated by a 1D coupled HEat and MAss Transfer code, HEMAT, developed and benchmarked in this study. It was found that both the optimum designs of the two options, DW-FTHX with a tritium carrier (helium) and SW-FTHX with a tritium barrier (silicon carbide), could effectively reduce the total tritium leakage rate to several curies per day, the same order of magnitude in a typical LWR.

This research provides a comprehensive study of thermal-hydraulic characteristics of molten salts. The key findings identified in this research can help improve design and modeling of passive decay heat removal systems for FHRs/MSRs and accuracy of code predictions of FHR/MSR performance. In addition, the two strategies identified as effective ways for tritium mitigation can support advancing the development of FHRs, fusion reactors, and other reactors/fields where tritium management/control is needed.

Chapter 1 Introduction

1.1 Background

1.1.1 Fluoride-salt-cooled High-temperature Reactors

The Fluoride-salt-cooled High-temperature Reactors (FHRs) are promising Generation IV nuclear reactors due to their improved safety designs, near atmospheric working pressure, and high electric power conversion efficiency. An FHR layout is shown schematically in Figure 1-1, which consists of the primary loop, intermediate loop, Direct Reactor Auxiliary Cooling System (DRACS) loop, and power conversion loop (Varma et al., 2012). The heat generated in the reactor core is transferred through the Primary-to-Intermediate Heat eXchanger (P-IHX) from the primary salt to the intermediate salt and then through the Intermediate-to-Power cycle HX (I-PHX) from the intermediate salt to water/steam in a Rankine cycle or helium/supercritical CO_2 (sCO_2) in a Brayton cycle for power generation.

An example of the various FHR designs is the Advanced High-Temperature Reactor (AHTR) proposed by the Oak Ridge National Laboratory (ORNL) utilizing FLiBe (^7LiF-BeF_2) as the primary coolant (Holcomb et al., 2011). One of the key design features of the AHTR is the use of a passive decay heat removal system, namely, DRACS, with the ability to reject the heat to the environment following reactor shutdown. The DRACS consists of three coupled natural circulation/convection loops, relying completely on buoyancy as the driving force. Due to the density difference of the primary salt in the reactor core and the shell side of the DRACS Heat

eXchanger (DHX), a natural circulation flow of the primary salt develops in the reactor vessel and flows upward through the reactor core, while downward through the DHX shell side.

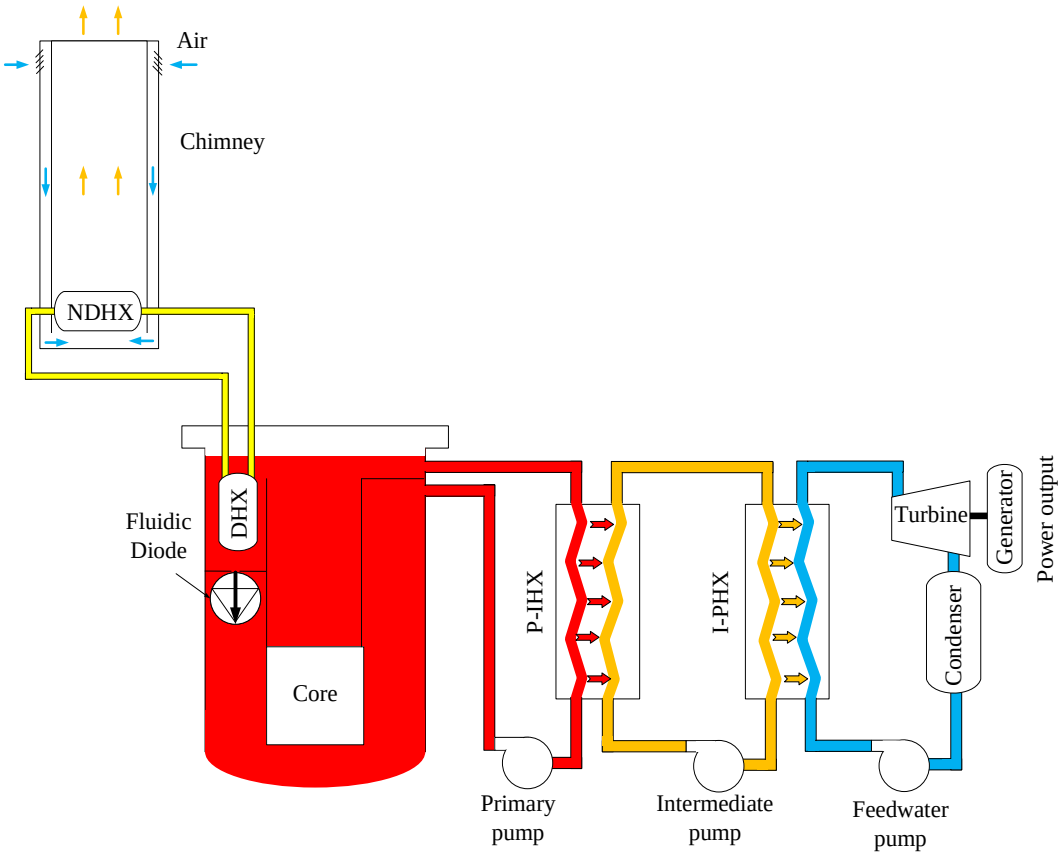

Figure 1-1 Schematic of an FHR

Similarly, a DRACS salt natural circulation flow develops due to the density difference of the DRACS salt on the tube sides of the DHX and Natural Draft Heat eXchanger (NDHX). Air flows on the NDHX shell side to remove heat by natural convection. Typically, a fluidic diode is employed beneath each DHX to provide a significantly larger flow resistance in the upward flow direction than that in the downward flow direction and prevent excessive heat losses to the DRACS during reactor normal operation. These natural circulation/convection loops are coupled through

the DHX, which is immersed in the primary coolant FLiBe in the reactor vessel, and the NDHX, which is located inside an air chimney. In the AHTR design, the decay heat is transferred through the DHX from the primary salt FLiBe to the DRACS salt KF-ZrF_4 and then through the NDHX from the DRACS salt KF-ZrF_4 to the ambient air in the air chimney.

There is no FHRs in operation currently, but related research activities have been significantly increased in recent years. In the U.S., a number of FHR designs have been proposed, such as the AHTR, a large FHR design of 3400 MWth, and Small modular AHTR (SmAHTR), a small modular FHR design of 125 MWth, proposed by ORNL (Varma et al., 2012; Greene et al., 2010), Pebble-Bed FHR (PB-FHR) proposed by a university consortium (Andreades et al., 2014), consisting of the Massachusetts Institute of Technology, University of California - Berkeley, and University of Wisconsin - Madison, and KP-FHR proposed by Kairos Power (2018). There are a number of FHR designs overseas as well, such as the Thorium Molten Salt Reactor - Solid Fuel 1 (TMSR-SF1) proposed by Shanghai Institute of Applied Physics in China (Dai and Liu, 2013; Liu et al., 2016).

Despite recent significant research and development activities on FHRs, a number of key technology gaps/issues exist for FHR neutronics, thermal hydraulics, and materials (Rahnema et al., 2019; Lin et al., 2019; Singh et al., 2019). A Thermal Hydraulics Phenomena Identification and Ranking Table (TH-PIRT) study was performed to identify the key technology gaps/issues related to thermal hydraulics of the AHTR (Lin et al., 2019). For the events of Station Blackout (SBO) and simultaneous inadvertent withdrawal of all control rods, key phenomena related to thermal hydraulics that need further investigation were identified, including thermophysical properties of the FLiBe salt, molten salt natural circulation in the passive decay heat removal system DRACS, HX performance, primary pump performance, upper/lower plenum mixing, etc.

In addition, tritium control is another key technology gap/issue for FHRs, which will be discussed next. These key technology gaps/issues need to be addressed in support of FHR development, licensing, and future deployment.

1.1.2 Tritium in FHRs

The FHRs become one class of the promising non-Light Water Reactors (non-LWRs), but tritium control is perceived as a critical issue for FHRs since tritium is radioactive and its production rate is significantly larger than that in LWRs. For example, the tritium production rate is estimated to be 3400 Ci/day for the AHTR, which is several orders of magnitude larger than that in a typical LWR (Briggs, 1971). If tritium mitigation is not considered in FHRs, the tritium leakage rate to the atmosphere will be significantly larger than 1.9 Ci/day, an average tritium leakage rate in LWRs in 2003 (U.S. NRC). It is therefore necessary to reduce the tritium leakage rate for FHR designs, especially large FHRs, such as the AHTR.

1.2 Research Objectives

This research aims to address two technology gaps/issues discussed earlier for FHR development, licensing, and future deployment, namely, (1) molten salt natural circulation in the passive decay heat removal system and (2) tritium control/mitigation for FHRs.

To complete the first research objective, it is necessary to initially investigate and understand the thermal-hydraulic characteristics of molten salts in simple geometry, such as a straight circular pipe, then a single natural circulation loop, followed by coupled natural circulation/convection loops, similar to the passive decay heat removal system DRACS.

A Computational Fluid Dynamics (CFD) tool, STAR-CCM+, is first used to investigate heat transfer and friction characteristics of molten salts in straight circular pipes. An in-house one-dimensional (1D) NAtural Circulation COde, NACCO, is subsequently developed to predict the thermal-hydraulic performance of natural circulation loops and benchmarked by comparing with experimental data in the literature. The 1D code NACCO is then applied for a high-temperature FLUoride Salt Test FAcility (FLUSTFA), which is designed based on a scaling analysis to verify the DRACS performance in the AHTR. As for tritium control and mitigation in FHRs, two strategies are proposed and evaluated by a 1D coupled HEat and MAss Transfer code, HEMAT, developed in this study.

A number of tasks that need to be completed to meet the two objectives discussed earlier are summarized as follows:

- Identification of accurate thermophysical properties of molten salts of interest through a comprehensive literature review
- Identification of heat transfer and friction characteristics of molten salts in straight circular pipes using CFD models that are validated by comparing with experimental data in the literature and correlation results
- Evaluation of the thermal-hydraulic performance of a single molten salt natural circulation loop through the 1D code NACCO, which is developed and benchmarked in this study
- Evaluation of the thermal-hydraulic performance of coupled molten salt natural circulation loops (FLUSTFA), which is designed and constructed to experimentally investigate DRACS performance in the AHTR

- Evaluation of the two strategies for tritium mitigation through the 1D code HEMAT, which is developed and benchmarked in this study

1.3 Dissertation Organization

A number of peer-reviewed papers (Zhang et al., 2017a; Zhang et al., 2017b; Zhang et al., 2018; Zhang et al., 2019a; Zhang et al., 2019b; Zhang et al., 2020a; Zhang and Sun, 2020b; and Zhang et al., 2020c) published from this research are presented in the dissertation, which consists of a total of six chapters.

Chapter 1 introduces the background of FHRs, including the key systems, current activities, benefits, and key technology gaps/issues, and then outlines the objectives for the current research.

Chapter 2 reviews the thermophysical properties of three fluoride salts, FLiBe, FLiNaK, and KF-ZrF_4, which are coolants for the AHTR and the test facility FLUSTFA that is constructed to study the DRACS performance in the AHTR. In addition, a CFD study for heat transfer and friction characteristics of molten salts in straight circular pipes is performed and benchmarked by comparing with experiments and correlations in the literature. Our analysis shows that both the buoyancy effect and radiative heat transfer effect are normally non-negligible for molten salts in laminar flow regime. The buoyancy effect could be evaluated by mixed convective heat transfer correlations, while the latter is evaluated by a radiative heat transfer model developed and benchmarked in Chapter 2.

Chapter 3 presents the development and benchmark study of a 1D code NACCO to predict the thermal-hydraulic performance of molten salts in natural circulation loops. The key findings identified in Chapter 2, non-negligible effects of buoyancy and radiative heat transfer for molten salts in laminar flow regime, are further validated through comparisons between the predictions

by the 1D code NACCO and two high-temperature natural circulation experiments using the nitrate salt $NaNO_3$-KNO_3 and fluoride salt FLiBe as the coolants, respectively. A benchmark study with a low-temperature natural circulation experiment using water as the working fluid is also included as a reference.

Chapter 4 presents the application of the 1D code NACCO to an Itegral Effect Test (IET) facility, FLUSTFA, which is designed based on a scaling analysis to verify the DRACS performance in the AHTR. A number of shakedown tests, overcooling, and overheating transients are predicted by the 1D code NACCO. These predictions help optimize the operation procedure of the test facility and understand the transient scenarios.

Chapter 5 presents two strategies for tritium mitigation and evaluation of these strategies by the 1D code HEMAT. To reduce tritium leakage rate in FHRs, two design options, a Double-Wall Fluted-Tube Heat eXchanger (DW-FTHX) with a tritium carrier and Single-Wall FTHX (SW-FTHX) with a tritium barrier, are proposed for HXs, which provide major pathways for tritium leakage due to the elevated working temperatures and large heat transfer surface areas. In addition, four tritium carriers, including helium, FLiBe, FLiNaK, and KF-ZrF_4, and two tritium barriers, tungsten and silicon carbide (SiC), are investigated. To reduce the tritium leakage rate in the AHTR to a similar level of that in LWRs, helium and SiC are finally selected for the DW-FTHX and SW-FTHX designs, respectively.

Chapter 6 summarizes the key findings and major contributions of this research. In addition, a number of additional tasks are suggested for future work.

Chapter 2 Heat Transfer and Friction Characteristics of Molten Salts in Circular Pipes

Molten salts, such as fluoride, nitrate, chloride, and carbonate salts, could be used as Heat Transfer Fluids (HTFs) and/or Thermal Energy Storage (TES) fluids. Specifically, fluoride salts, such as FLiBe (LiF-BeF_2, 66-34 mol%), FLiNaK (LiF-NaF-KF, 46.5-11.5-42 mol%), and KF-ZrF_4 (58-42 mol%) are promising reactor coolants for FHRs due to their good thermophysical and nuclear properties (Williams et al., 2006). Nitrate salts, such as KNO_3-$NaNO_2$-KNO_3 (53-40-7 wt%), chloride salts, such as $MgCl_2$-KCl (68-32 mol%), and carbonate salts, such as Li_2CO_3-Na_2CO_3-K_2CO_3 (32-33-35 wt%), are promising candidates for HTFs and TES media in Concentrating Solar Power (CSP) plants, considering their thermophysical properties, cost, material compatibility, stability, and flammability (Mehos et al., 2017).

It is necessary to investigate heat transfer and friction characteristics of molten salts due to their wide applications as heat transfer media. However, accurate thermophysical properties need to be known for molten salts prior to any thermal-hydraulic analysis. In this section, accurate thermophysical properties of FLiBe, FLiNaK, and KF-ZrF_4 (58-42 mol%) will be identified initially through a literature review, which will then be used to reprocess some of the experimental data in the literature. The heat transfer and friction characteristics of molten salts in straight circular pipes will be investigated later by STAR-CCM+, followed by a benchmark study with the experimental data in the literature.

2.1 Thermophysical Properties of Fluoride Salts

2.1.1 LiF-BeF_2 (66-34 mol%)

Density

Cantor (1973) experimentally investigated the FLiBe (LiF-BeF_2, 66-34 mol%) density at T = 514.5 - 820.3 °C. In addition, Grimes (1966) proposed a method to estimate the salt mixture density, $\rho_{mix} = \sum(\chi_i M_i)/\sum(\chi_i V_i)$, where $\rho_{mix}, \chi_i, M_i,$ and V_i are the mixture density, mole fraction of the constituent salt i, molar mass of the constituent i, and molar volume of the constituent i, respectively. The FLiBe density estimated by Grimes using the molar volumes of LiF and BeF_2 at 600 and 800 °C (Williams et al., 2006) deviated from Cantor's experimental data by ±1.5%, which demonstrated good accuracy of the Grimes's approach to estimate the salt mixture density. It is therefore recommended

$$\rho\ (\mathrm{kg/m^3}) = 2279.7 - 0.4884T(℃) \tag{2-1}$$

to be used for the FLiBe density at T = 514.5 to 820.3 °C with ±0.3% uncertainties.

Dynamic viscosity

Cantor et al. (1968) estimated the FLiBe dynamic viscosity with ±15% uncertainties, which covered the FLiBe dynamic viscosity values estimated by Abe et al. (1981). Romatoski and Hu (2017) suggested Cantor's correlation for the FLiBe dynamic viscosity since it was widely reported in the literature. Cantor's correlation, given as

$$\mu\ (\mathrm{kg/m\text{-}s}) = 1.16 \times 10^{-4} e^{3755/[T(℃)+273.15]} \tag{2-2}$$

is therefore adopted to estimate the FLiBe dynamic viscosity at T = 540 to 1300 °C with ±15% uncertainties.

Specific heat capacity

Cantor et al. (1968) estimated the FLiBe specific heat capacity as 2386.5 J/kg-K without specifying the applicable temperature range and associated uncertainties, while Rosenthal et al. (1969) estimated it as 2415.8 J/kg-K with ±1.4% uncertainties, which covered Cantor's prediction. It is therefore recommended

$$c_p \text{ (J/kg-K)} = 2415.8 \tag{2-3}$$

to be used for the FLiBe specific heat capacity at T = 500 to 720 ˚C with ±1.4% uncertainties.

Thermal conductivity

Cantor et al. (1968) estimated the FLiBe thermal conductivity as 1.0 W/m-K with ±10% uncertainties, while Rosenthal et al. (1968) estimated it as 1.0 W/m-K at $T = 500$ ℃ and 1.1 W/m-K at T = 600 - 900 ˚C. In addition, Rao (1942) proposed an approach to estimate the thermal conductivity of a salt mixture, k (W/m-K) $= 0.0119\, T^{1/2}(\text{K})\rho^{2/3}(\text{kg/m}^3)/[M(\text{g/mol})/n]^{7/6}$, where T, ρ, M, and n are the salt melting temperature, density, molar mass, and ion number, respectively. Utilizing the FLiBe melting temperature of 454 °C (Thoma, 1959; Speirs, 1952), the FLiBe thermal conductivity estimated by Rao is 25% lower than Cantor's and Rosenthal's data. It is therefore recommended

$$k \text{ (W/m-K)} = 1.1 \tag{2-4}$$

to be used for the FLiBe thermal conductivity at T = 600 to 900 ˚C with ±10% uncertainties. The relevant thermophysical properties of FLiBe are summarized in Table 2-1.

2.1.2 KF-ZrF_4 (58-42 mol%)

Density

Darienko et al. (1988) experimentally investigated the KF-ZrF_4 density for two different mole fractions, 60-40 mol% and 55-45 mol%. A linear interpolation method could be applied to estimate the KF-ZrF_4 (58-42 mol%) density using Darienko's experimental data. Another approach is to use Grimes's method discussed earlier for the density estimation of a salt mixture. The KF-ZrF_4 density was estimated as $\rho(\mathrm{kg/m^3}) = 3416 - 0.887T(℃)$ using Grimes's approach, which had an 8% deviation compared with the data interpolated in Darienko's experiments. Since Grimes accurately estimated the density of another similar salt, NaF-ZrF_4, with ±1.5% discrepancies compared with the experimental data (Powers et al., 1963), Grimes's prediction on the KF-ZrF_4 density is likely to be more accurate. Therefore, it is recommended

$$\rho\ (\mathrm{kg/m^3}) = 3416 - 0.887T(℃) \tag{2-5}$$

to be used for the KF-ZrF_4 density at T = 600 to 800 °C with about ±1.5% uncertainties.

Dynamic viscosity

Due to the limited literature related to the KF-ZrF_4 dynamic viscosity, the following equation

$$\mu\ (\mathrm{kg/m\text{-}s}) = 1.59 \times 10^{-5} e^{3179/[T(℃)+273.15]} \tag{2-6}$$

suggested by Williams et al. (2006) is used for the KF-ZrF_4 dynamic viscosity at T = 600 to 800 °C with ±20% uncertainties.

Specific heat capacity

Williams et al. (2006) estimated the KF-ZrF_4 specific heat capacity as 1050.9 J/kg-K with ±10% uncertainties, while Khokhlov et al. (Powers et al., 1963) predicted it as 1063.3 J/kg-K located in the uncertainty range of Williams's prediction. It is therefore recommended

$$c_p \text{ (J/kg-K)} = 1050.9 \tag{2-7}$$

to be used for the KF-ZrF_4 specific heat capacity at T = 500 to 700 °C with ±10% uncertainties.

Thermal conductivity

Khokhlov et al. (2009) proposed an approach to estimate the thermal conductivity of a salt mixture, $k\,(\text{W/m-K}) = -0.34 + 5 \times 10^{-4} T(\text{K}) + 32/M$. The thermal conductivities of FLiBe and FLiNaK estimated by Khokhlov et al. (2009) were 1.11 and 0.92 W/m-K at 700 °C, respectively, which had a 3% deviation from their respective experimental data. For other fluoride salts investigated by Khokhlov et al. (2009), the relative discrepancy of the thermal conductivity between the prediction and experimental data was within ±15%. It is therefore recommended

$$k\,(\text{W/m-K}) = -0.169 + 5 \times 10^{-4} T(°\text{C}) \tag{2-8}$$

to be used for the KF-ZrF_4 thermal conductivity at T = 600 to 800 °C with ±15% uncertainties derived by Khokhlov's approach. The thermophysical properties of KF-ZrF_4 are summarized in Table 2-1.

2.1.3 FLiNaK (LiF-NaF-KF, 46.5-11.5-42 mol%)

Density

Using the measured densities of the three fluoride constituent salts LiF, NaF, and KF at two temperatures of 600 and 800 °C (Grimes, 1966), the FLiNaK density can be estimated by the rule of additivity of molar volumes (Grimes, 1966). The uncertainty in estimating the salt mixture density was within 5% (William, et al., 2006).

In addition to the model prediction of the FLiNaK density, a number of experimental investigations were conducted on the FLiNaK density. Chrenkova et al. (2003) experimentally measured the FLiNaK density for T = 667 - 897 °C with ±0.4% uncertainties, which was later demonstrated by Cibulkova et al. (2006). Kubikova et al. (2013) and Cheng et al. (2013) measured the FLiNaK density for T = 483 - 609 °C without specifying the associated uncertainty and for T = 480 - 700 °C with ±0.25% uncertainties, respectively. Figure 2-1 shows a comparison of the FLiNaK density values. The maximum discrepancy in the FLiNaK density for a temperature range of 500 - 800 °C is 3.5%. This relatively good agreement demonstrates that the rule of additivity of molar volumes (Grimes, 1966) can predict accurately the FLiNaK density. It is recommended the Chrenkova's correlation given as

$$\rho\ (\mathrm{kg/m^3}) = 2408.9 - 0.624T(^{\circ}\mathrm{C}) \tag{2-9}$$

to be used for the FLiNaK density at T = 500 to 800 °C with ±1% uncertainties to cover both Grimes's and Cheng's results.

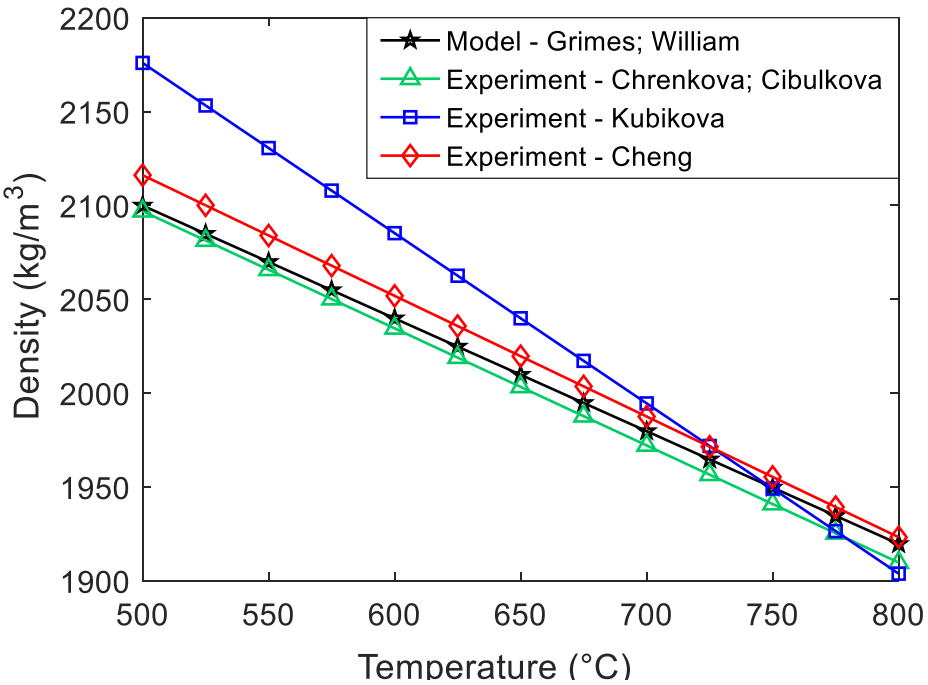

Figure 2-1 The FLiNaK density

Dynamic Viscosity

Powers et al. (1963) measured the FLiNaK dynamic viscosity for T = 500 - 800 °C with ±20% uncertainties. Chrenkova et al. (2003), Cibulkova et al. (2006) and Kubikova et al. (2012) also experimentally measured the dynamic viscosity of FLiNaK respectively for T = 500 - 700 °C with ±2% uncertainties, T = 660 - 890 °C with ±2.5% uncertainties, and T = 529 - 630 °C without specifying uncertainties using the torsion pendulum method. Merzlyakov et al. (2014) measured the FLiNaK kinematic viscosity for T = 454 - 871 °C without specifying uncertainties. In our current study, the kinematic viscosity of FLiNaK obtained by Merzlyakov et al. (2014) was converted to the dynamic viscosity using the FLiNaK density correlation recommended.

As shown in Figure 2-2, the FLiNaK dynamic viscosity estimated are within the ±20% uncertainty range of Powers' prediction. It is therefore recommended that Powers' correlation

$$\mu \text{ (kg/m-s)} = 4 \times 10^{-5} e^{4170/[T(^{\circ}\text{C})+273.15]} \tag{2-10}$$

to be used for the FLiNaK dynamic viscosity for T = 500 to 800 °C with ±20% uncertainties.

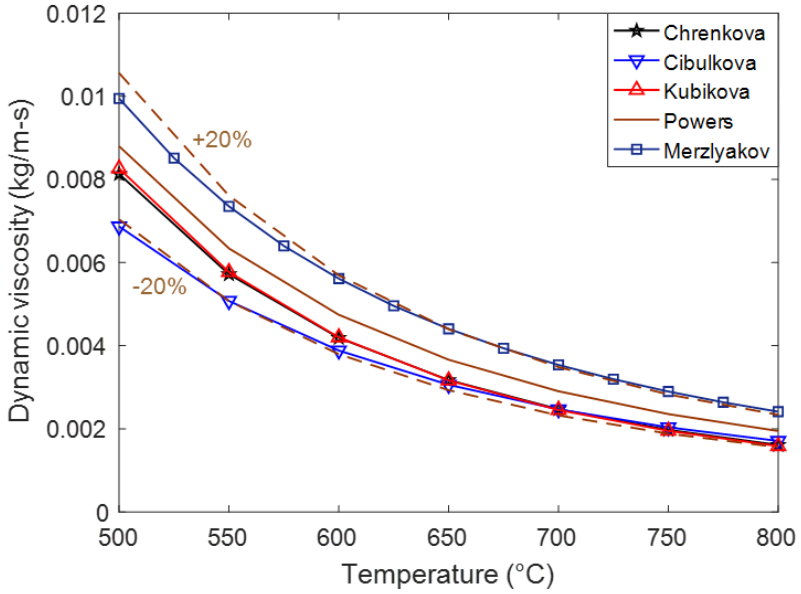

Figure 2-2 The FLiNaK dynamic viscosity

Specific Heat Capacity

The specific heat capacity of FLiNaK was given as 1904.8 J/kg-K for T = 477 - 557 °C with ±3% uncertainties by Janz and Tomkins (1981) and 1880 J/kg-K for T = 500 - 700 °C with ±4% uncertainties by An et al. (2015). These values generally agreed with Rogers's prediction (1982) as shown in Figure 2-3. It is therefore recommended

$$c_p \text{ (J/kg-K)} = 1880 \tag{2-11}$$

to be used for the FLiNaK specific heat capacity for T = 500 to 700 °C with ±5% uncertainties to cover both Rogers' and Janz's results.

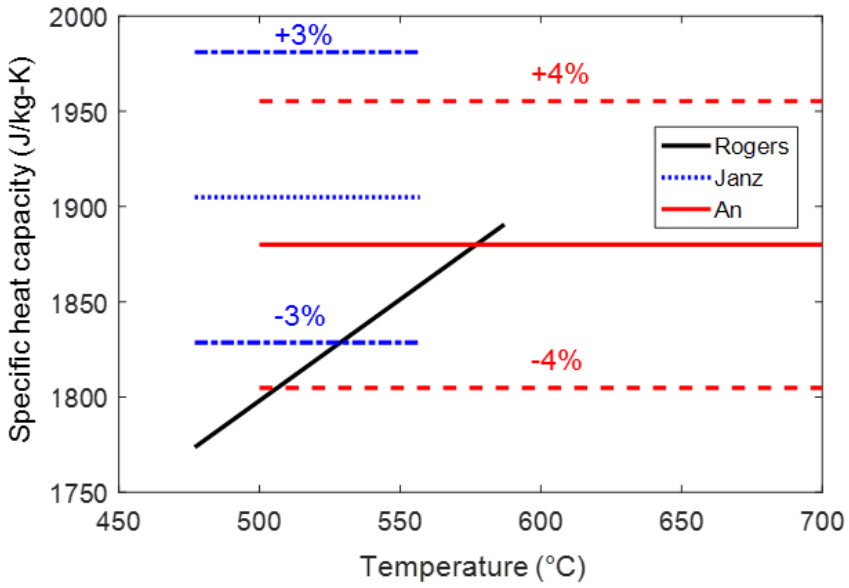

Figure 2-3 The FLiNaK specific heat capacity

Thermal Conductivity

Rosenthal et al. (1969) suggested a formula to estimate the thermal conductivity of the fluoride mixtures. Utilizing the FLiNaK melting temperature 454 °C (Bergman and Dergunov, 1941), the recommended Chrenkova correlation for the FLiNaK density, and ion number n = 2, the FLiNaK thermal conductivity could be estimated.

Janz and Tomkins (1981), Smirnov et al. (1987), and An et al. (2015) proposed polynomial correlations to estimate the FLiNaK thermal conductivity for T = 527 - 647 °C with ±25% uncertainties, T = 517 - 807 °C with ±4% uncertainties, and T = 500 - 700 °C with ±3.5% uncertainties, respectively. Cooper and Claiborne (1952) proposed values of 1.682, 1.508, and 1.45 W/m-K for the FLiNaK thermal conductivity for T = 690, 540, and 620 °C with uncertainties of ±13, ±8, and ±8%, respectively.

Figure 2-4 shows a comparison of the FLiNaK thermal conductivity. The maximum discrepancy could be as high as 250% for T = 500 °C and 400% for T = 800 °C. The significant

differences may result from the different approaches adopted to measure the FLiNaK thermal conductivity and impurities in the FLiNaK salt used in these experiments.

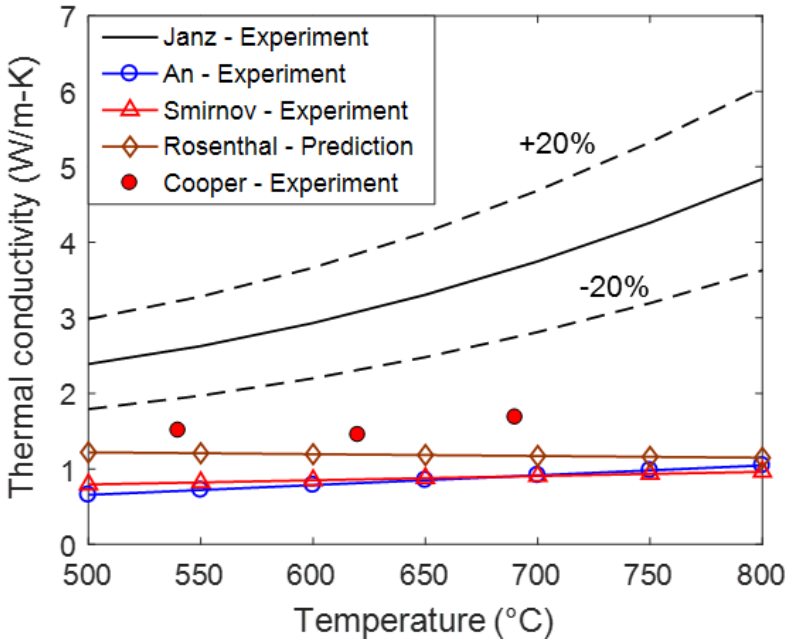

Figure 2-4 The FLiNaK thermal conductivity

Janz and Tomkins (1981) and Cooper and Claiborne (1952) used the parallel plate method to measure the FLiNaK thermal conductivity, which was calculated using the plate temperature difference and heat flux. The effects of the thermal radiation, natural convection, and axial conduction between the hot and cold plates resulted in larger values for the thermal conductivity. In addition, metal impurities, i.e., Fe, Al, Ni, Pb, Mn, and Mg, etc., presented in the FLiNaK salt led to an overestimated value for the FLiNaK thermal conductivity in the experiments.

An et al. (2015) used the laser flash technique developed by Parker et al. (1961) to measure the FLiNaK thermal conductivity. The thickness of the liquid FLiNaK salt in their container was 1.5 mm. Therefore, the convective heat transfer in the liquid FLiNaK was negligible in the

experiments. In addition, the FLiNaK salt used in their experiments was initially prepared under an H_2/HF environment to reduce the impurity level to be lower than 0.01 wt%. Therefore, it appears appropriate to assume that the prediction given by An, et al. for the FLiNaK thermal conductivity is more accurate.

Smirnov et al. (1987) used the coaxial platinum cylinder method to measure the FLiNaK thermal conductivity. In their experiments, the FLiNaK salt was purified to reduce its impurity level and therefore the corrosion effect. In addition, the radiative heat transfer was considered in their experiments (Smirnov et al., 1987). Therefore, Smirnov's correlation was suggested by Romatoski and Hu (2017) for the FLiNaK thermal conductivity. Since both Ann's and Smirnov's correlations seem to be more accurate than others, an arithmetic mean of their results, written as

$$k\,(\text{W/m-K}) = 0.005 + 0.00093T(\text{K}) \tag{2-12}$$

is recommended for the FLiNaK thermal conductivity for T = 500 to 800 °C with ±10% uncertainties. The thermophysical properties of FLiNaK are summarized in Table 2-1.

Table 2-1 Thermophysical properties of the liquid fluoride salts (95% confidence level)

Item	Property	Temperature Range (°C)	Uncertainty (%)	Reference
LiF-BeF_2 (66-34 mol%)	$\rho\ (\mathrm{kg/m^3}) = 2279.7 - 0.4884T(°C)$	515 to 820	±0.3	Cantor, 1973
	μ (kg/m-s) $= 1.16 \times 10^{-4} e^{3755/[T(°C)+273.15]}$	540 to 1300	±15	Cantor et al., 1968
	C_p (J/kg-K) $= 2415.8$	500 to 720	±1.4	Rosenthal et al., 1969
	k (W/m-K) $= 1.1$	600 to 900	±10	
KF-ZrF_4 (58-42 mol%)	$\rho\ (\mathrm{kg/m^3}) = 3416 - 0.887T(°C)$	600 to 800	±1.5	Grimes, 1966
	μ (kg/m-s) $= 1.59 \times 10^{-5} e^{3179/[T(°C)+273.15]}$	600 to 800	±20	Williams et al., 2006
	C_p(J/kg-K) $= 1050.9$	500 to 700	±10	
	k (W/m-K) $= -0.169 + 5 \times 10^{-4} T(°C)$	600 to 800	±15	Khokhlov et al., 2009
LiF-NaF-KF (46.5-11.5-42 mol%)	$\rho\ (\mathrm{kg/m^3}) = 2408.9 - 0.624\,T(°C)$	773 to 1073	±1	Chrenkova et al., 2003
	μ (kg/m-s) $= 4 \times 10^{-5} e^{4170/(T(°C)+273.15)}$	773 to 1073	±20	Powers et al., 1963
	C_p (J/kg-K) =1880	773 to 1073	±5	An et al., 2015
	k (W/m-K) $= 0.259 + 9.3 \times 10^{-4}\,T(°C)$	773 to 1073	±10	See note

Note: An arithmetic mean of An's (2015) and Smirnov's (1987) correlation results.

2.2 CFD Study for Molten Salts in Circular Pipes without the Effects of Buoyancy and Radiative Heat Transfer

As discussed earlier, it is necessary to investigate the thermal-hydraulic performance of molten salts, especially considering their relatively large Prandtl number as shown in Figure 2-5 with air and saturated water included as references. The Prandtl number of molten salts of interest are in the range of 2 to 32 at their respective potential working temperatures. The high Prandtl number may lead to additional/different heat transfer characteristics compared with those for the conventional fluids, such as water and air. It is therefore necessary to investigate heat transfer and friction characteristics of molten salts first in simple geometry, straight circular pipe, and validate the numerical results using the experimental data from molten salt experiments in the literature.

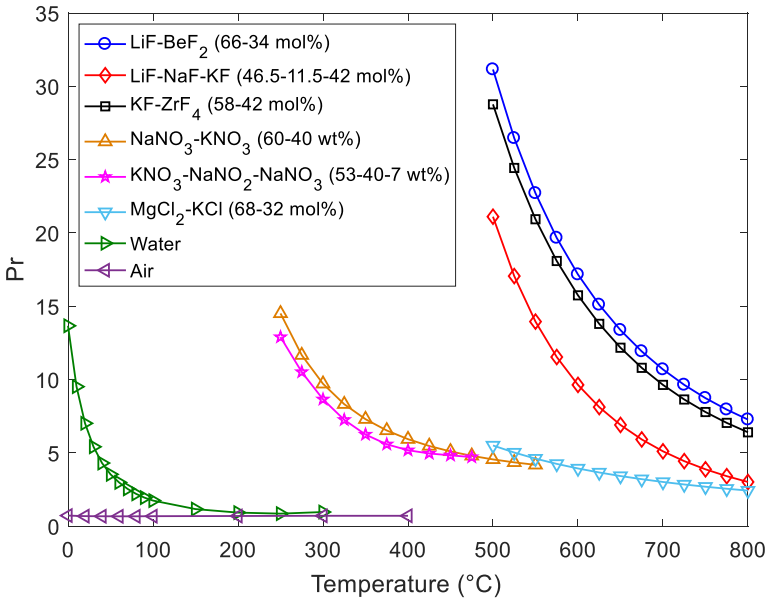

Figure 2-5 Prandtl numbers of various molten salts, air, and saturated water

In the literature, experimental studies on molten salts related to the salt thermal hydraulics started in 1950s. Grele and Gedeon (1954) investigated the heat transfer characteristics of FLiNaK in an electrically heated Inconel pipe at a temperature range of 540 to 730 °C. The heat transfer coefficient values estimated from the experimental data were at about 40% of the values given by the Dittus-Boelter correlation. Formation of a thermal resistance layer due to the intergranular corrosion to the Inconel pipe by the salt was proposed as the reason for the much lower heat transfer coefficients in the experiments. Hoffman and Lones (1955) experimentally studied the heat transfer of FLiNaK flowing in three pipes made of Nickel, Inconel, and Stainless Steel (SS) 316. The heat transfer coefficients estimated from the experimental data obtained from the Nickel and SS 316 pipes agreed well with the Dittus-Boelter correlation results, while the heat transfer coefficient from the Inconel pipe deviated significantly from the Dittus-Boelter correlation results. This much lower heat transfer coefficient obtained from the experiments was explained due to the existence of an interfacial thermal resistance in the FLiNaK-Inconel system. However, this

conclusion conflicted with Vriesema's finding (1979) where the experimental data obtained from a FLiNaK-Inconel system matched reasonably well the Dittus-Boelter correlation results, within ±20% uncertainties. The contradictory conclusions were resulted from different thermophysical property values used for FLiNaK in the data reduction process (Grele and Gedeon, 1954; Hoffman and Lones, 1955; Vriesema, 1979). Therefore, accurate thermophysical properties of FLiNaK will be identified and used to reprocess the salt experimental data.

In addition to the FLiNaK salt, other molten salts, including salts with dissolved nuclear fuels, i.e., fuel salts, were widely investigated as well. Hoffman and Cohen (1960) investigated the heat transfer performance of KNO_3-$NaNO_2$-$NaNO_3$ (53-40-7 wt%) in an Inconel pipe at 290 to 442 °C. In recent years, KNO_3-$NaNO_2$-$NaNO_3$ (53-40-7 mol%) was studied by Chen et al. (2016; 2017) and Qian et al. (2016; 2017). In addition, Wu et al. (2009) and Liu et al. (2009) studied the convective heat transfer of one same molten salt, $LiNO_3$, but proposed different convective heat transfer correlations. Fuel salts for Molten Salt Reactors (MSRs), such as LiF-BeF_2-ThF_4-UF_4 with different molar fractions, were studied by Silverman et al. (1976) and Cooke and Cox (1973). In addition, the friction factor of molten salts was experimentally investigated by Vriesema (1979), and Jeong and Bang (2010).

It is inconvenient to use various heat transfer coefficient and friction factor correlations for same molten salts and difficult to acquire local information of interest from the experiments, such as the salt temperature profiles. In addition, it is not cost-effective and perhaps unnecessary to perform extra experiments for other molten salts with similar ranges of the Prandtl number of the molten salts that have been widely investigated. The thermal-hydraulic characteristics of molten salts, such as the hydrodynamic and thermal entrance lengths, friction factor, and Nusselt number for molten salts in straight circular pipes are therefore numerically investigated.

2.2.1 Numerical Modeling

Numerical model

A three-dimensional (3D) CFD tool, STAR-CCM+ was used to investigate the thermal-hydraulic performance of molten salts, including the fluoride salt FLiNaK and fuel salt LiF-BeF_2-ThF_4-UF_4 (71.7-16-12-0.3 mol%) in straight circular pipes. The fluid domain of molten salt (FLiNaK and LiF-BeF_2-ThF_4-UF_4) and solid domain of a circular pipe made of SS 316 were constructed in STAR-CCM+.

The circular pipe has an inner diameter of 4 mm and pipe thickness of 1 mm as shown in Figure 2-6. The pipe length is 15 m when the flow in the pipe is laminar, while 1 m for turbulent flow cases. Several mesh models, such as polyhedral mesher, surface remesher, prism layer mesher, and extruder were enabled for meshing. Boundary conditions include a uniform velocity inlet at 500 °C, an atmospheric pressure outlet, and constant wall heat fluxes 4 and 100 kW/m^2 on the wall outer surface for laminar and turbulent flows, respectively. In addition, the realizable k-ε two-layer model is used for modeling of turbulent flows.

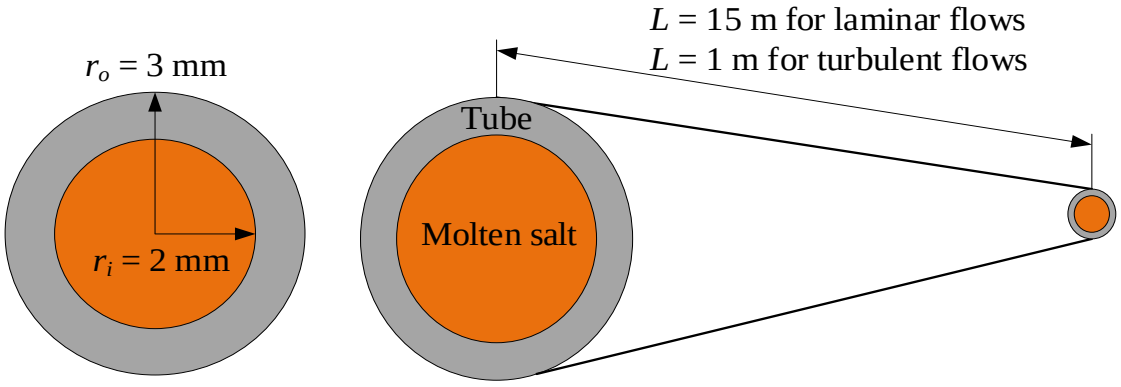

Figure 2-6 Dimensions of fluid and solid domains

Mesh independence study

A grid (mesh) independence study was first performed to investigate the spatial convergence of numerical results, which could be characterized by the Grid Convergence Index (GCI) (Schwer, 2008) as follows,

$$GCI_{2-1} = \frac{F_s}{\gamma_{2-1}^{\alpha}-1}\left|\frac{\psi_2-\psi_1}{\psi_1}\right| \tag{2-13}$$

where F_s, γ, α, and ψ are the safety factor, grid refinement ratio, order of convergence, and estimated variable, respectively. The safety factor F_s is empirically set to be 1.25. The grid refinement ratio for mesh options 1 and 2, γ_{2-1}, and order of convergence α (Schwer, 2008) are defined as

$$\gamma_{2-1} = \frac{\zeta_2}{\zeta_1} \tag{2-14}$$

$$\alpha = \frac{\left|\ln\left|\frac{\psi_3-\psi_2}{\psi_2-\psi_1}\right|+\ln\frac{\gamma_{2-1}^{\alpha}-s}{\gamma_{3-2}^{\alpha}-s}\right|}{\ln\gamma_{2-1}} \tag{2-15}$$

where, γ_{3-2} is the grid refinement ratio for mesh options 2 and 3, and s and ζ are respectively the sign function (Schwer, 2008) and grid size (Chen et al., 2019), which are defined as

$$s = \operatorname{sgn}\left(\frac{\psi_3-\psi_2}{\psi_2-\psi_1}\right) \tag{2-16}$$

$$\zeta = \left(\frac{V_t}{N_q}\right)^{1/3} \tag{2-17}$$

where V_t and N_q are the grid total volume and quantity, respectively.

A total of six sets of grid size were used for the mesh independence study for laminar (Re = 1,800) and turbulent (Re = 10,000) flows, and the results are summarized in Table 2-2. The GCI values of the Darcy friction factor f and temperature difference between the pipe inlet and outlet for laminar flows are significantly small, 0.15% and 0.08%, respectively. The simulation results using fine mesh option #1 are therefore considered to be mesh independent for laminar flows of the FLiNaK salt. In addition, the GCI values of the Darcy friction factor and temperature difference for turbulent flows are 0.62% and 0.48%, respectively. The y+ value ranges from about 0.40 to 1.62, while the majority of the salt domain ($L/D = 1$ to $L/D = 250$) has a y+ value lower than 1 for Re = 10,000 as shown in Figure 2-7. The simulation results using fine mesh option #4 are therefore considered to be mesh independent for turbulent flows of the FLiNaK salt. Both the two fine mesh options #1 and #4 are adopted in this study for the thermal and hydrodynamic analyses of molten salts in laminar and turbulent flow regimes, respectively.

Table 2-2 Results of the mesh independence study for the FLiNaK salt

Mesh option	Cell quantity (10^3)	Grid size (mm)	f	ΔT (°C)
Laminar flow (Re = 1,800)				
1 (Fine)	384.16	1.03	0.03338	12.27
2 (Medium)	160.78	1.38	0.03302	12.29
3 (Coarse)	73.93	1.80	0.03020	12.35
GCI (%)	N/A	N/A	0.15	0.08
Turbulent flow (Re = 10,000)				
4 (Fine)	139.74	0.59	0.03108	3.87
5 (Medium)	59.86	0.78	0.03101	3.90
6 (Coarse)	24.29	1.05	0.03090	4.01
GCI (%)	N/A	N/A	0.62	0.48

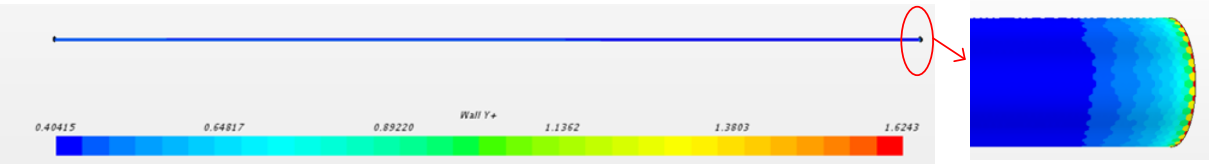

Figure 2-7 y+ value for the FLiNaK salt (fine mesh, Re = 10,000)

Data reduction

The Darcy friction factor used to estimate the frictional pressure loss is defined as

$$f = \frac{2\rho D_i A_f^2}{\Delta z \dot{m}^2} \Delta p_f \tag{2-18}$$

where D_i, A_f, $\dot{m}$, ρ, Δp_f, and Δz are the inner diameter, cross-sectional area of the pipe, mass flow rate, fluid density, frictional pressure drop, and axial distance, respectively.

The average heat transfer coefficient is defined as

$$\bar{h} = \frac{\dot{Q}}{A_{iw}(\bar{T}_{iw} - \bar{T}_f)} \tag{2-19}$$

where $\dot{Q}, A_{iw}, \bar{T}_{iw}$ *and* $\bar{T}_f$ are the heat transfer rate, heat transfer area of the pipe inner surface, area-averaged temperature of the pipe inner surface defined by Eq. (2-20), and arithmetic mean of the fluid bulk inlet and outlet temperatures defined by Eq. (2-21), respectively.

$$\bar{T}_{iw} = \frac{\int T_{iw} \mathrm{d}A}{A_{iw}} \tag{2-20}$$

$$\bar{T}_f = \frac{1}{2A_f}(\bar{T}_{in} + \bar{T}_{out}) \tag{2-21}$$

The fluid bulk inlet (or outlet) temperature is defined as

$$\bar{T}_{in} = \frac{\int \rho c_p u T_{in} \mathrm{d}A}{\int \rho c_p u \mathrm{d}A} \tag{2-22}$$

where u and c_p are the fluid velocity in the pipe axial direction and specific heat capacity, respectively.

2.2.2 Existing Molten Salt Experiments

Considering the possibility to extract the original experimental data for comparison with the CFD and correlation results, twelve salt heat transfer experiments and two hydrodynamic experiments were selected as summarized in Table 2-3. The working fluids used in these experiments include: FLiNaK (LiF-NaF-KF, 46.5-11.5-42 mol%), KNO_3-$NaNO_2$-$NaNO_3$ (53-40-7 wt% and 53-40-7 mol%), $LiNO_3$, $NaBF_4$-NaF (92-8 mol%), and LiF-BeF_2-ThF_4-UF_4 (71.7-16-12-0.3 mol% and 67.5-20-12-0.5 mol%). The salt temperature ranges from 200 to 830 °C.

Three experiments (Grele and Gedeon, 1954; Hoffman and Lones, 1955; Vriesema, 1979) investigated FLiNaK heat transfer performance in circular pipes made of different metals, such as Inconel X-750, Inconel 600, nickel, and SS 316. Although the FLiNaK salt of the same composition was investigated in these experiments, inconsistent thermophysical properties were used during the data reduction process in these experiments (Grele and Gedeon, 1954; Hoffman and Lones, 1955; Vriesema, 1979). The maximum discrepancies in the FLiNaK density, specific heat capacity, thermal conductivity, and dynamic viscosity used in the data reduction in these three experiments (Grele and Gedeon, 1954; Hoffman and Lones, 1955; Vriesema, 1979) were 7, 11, 246, and 45%, respectively. Significant discrepancies in the FLiNaK thermophysical properties used in these experiments, especially the one in the thermal conductivity, resulted in large differences in the Prandtl number, Reynolds number, and Nusselt number calculations. It is therefore necessary to use accurate thermophysical properties of FLiNaK discussed earlier and reprocess the experimental data.

Table 2-3 Information for the selected molten salt experiments

	Molten salt	Flow channel material	Dimension (length L and *ID*) (mm)	Heating /cooling	Salt temperature (°C)	Reference
Heat transfer	FLiNaK (LiF-NaF-KF, 46.5-11.5-42 mol%)	Inconel X-750	609.6 and 6.23	Heating	540-730	Grele and Gedeon (1954)
		Nickel	1182 and 2.98		530-745	Hoffman and Lones (1955)
		Inconel	1182 and 4.45			
		SS 316	1182 and 4.57			
		Inconel 600	2050 and 26	Cooling	575-675	Vriesema (1979)
	KNO_3-$NaNO_2$-$NaNO_3$ (53-40-7 wt%)	Inconel	241.3 and 4.57	Heating	290-442	Hoffman and Cohen (1960)
	KNO_3-$NaNO_2$-$NaNO_3$ (53-40-7 mol%)	Inconel 600	1200 and 20	Cooling	200-300	Chen et al. (2016; 2017)
	KNO_3-$NaNO_2$-$NaNO_3$ (53-40-7 mol%)	Stainless steel	350 and 10.45		200-300	Qian et al. (2016)
	KNO_3-$NaNO_2$-$NaNO_3$ (53-40-7 mol%)		Gas cooled HX: 350 and 10.45 Molten salt to salt HX: 500 and 10		258-298	Qian et al. (2017)
	$LiNO_3$		1000 and 20		272-441	Wu et al. (2009)
					294-441	Liu et al. (2009)
	$NaBF_4$-NaF (92-8 mol%)	Hastelloy N	3500 and 10.52	Heating	450-610	Silverman et al. (1976)
	LiF-BeF_2-ThF_4-UF_4 (71.7-16-12-0.3 mol%)		3500 and 10.52		550-765	
	LiF-BeF_2-ThF_4-UF_4 (67.5-20-12-0.5 mol%)		622.3 and 4.57		580-830	Cooke and Cox (1973)
Friction factor	FLiNaK (LiF-NaF-KF, 46.5-11.5-42 mol%)	Inconel 600	1200 and 41.25	Adiabatic	575-675	Vriesema (1979)
			650 and 1.4	Heating	595-620	Jeong and Bang (2010)

To have a general understanding of the level of changes in the experimental data after data reprocessing, the original values of the three characteristic non-dimensional numbers, Pr, Re, and Nu in Grele's experiment (1954) are compared with their modified values using the recommended thermophysical properties of the FLiNaK salt in the data reduction as shown in Figure 2-8. It is clear that these modified values of the characteristic numbers deviate significantly from their original values, especially for the Prandtl and Nusselt numbers. The discrepancies between the original and modified values of the Prandtl, Reynolds, and Nusselt numbers are 283 to 328%, 17 to 33%, and 331 to 431%, respectively. These large discrepancies are mainly due to the different thermal conductivity and dynamic viscosity values used for FLiNaK in the data reduction of Grele's experiment (1954) and this research. In addition, the recommended thermophysical properties of FLiNaK result in a significant change of the $Nu/Pr^{1/3}$ values as shown in Figure 2-9, leading to a different heat transfer correlation.

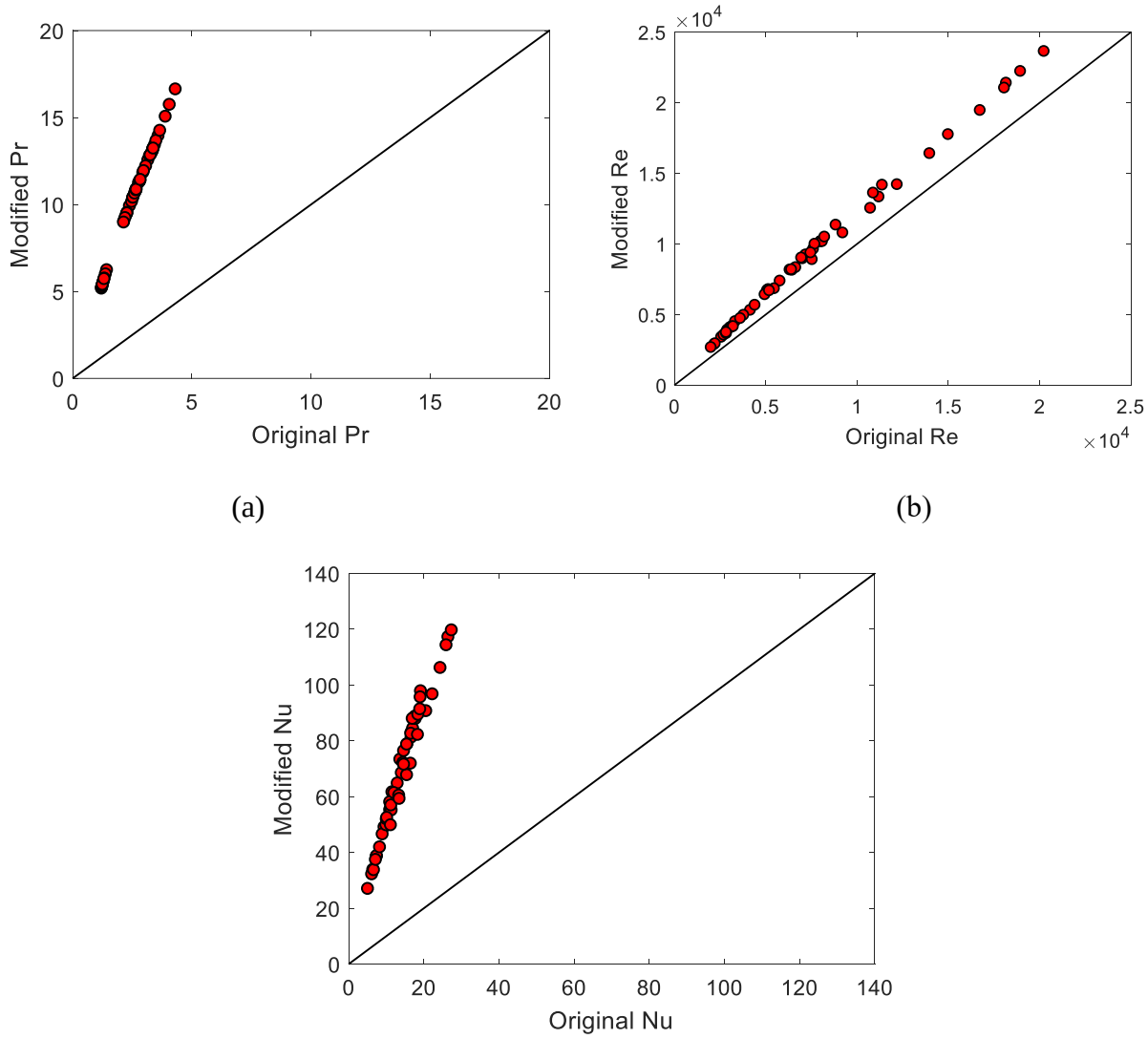

Figure 2-8 Comparison of (a) Pr, (b) Re, and (c) Nu using the FLiNaK thermophysical property values in Grele's experiment (1954) and recommended property values in this research

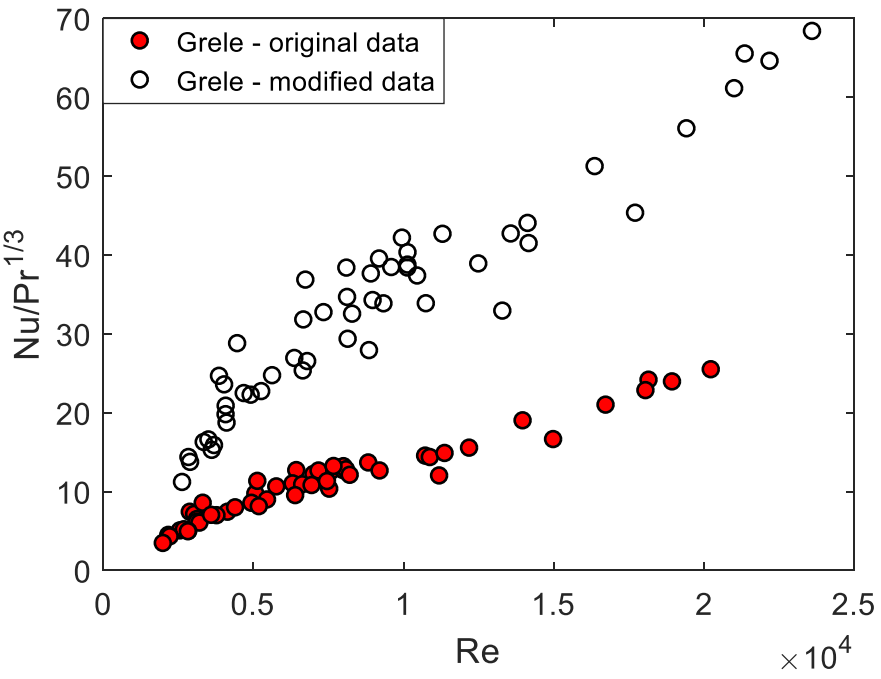

Figure 2-9 Comparison between the original heat transfer data in Grele's experiment (1954) and modified data using the recommended thermophysical property values of FLiNaK

2.2.3 Results and Discussion

It is necessary to compare the numerical results with the existing molten salt experimental data as well as the friction factor and forced convective heat transfer correlations summarized in Table 2-4 to identify their applicability for the molten salts of interest. In addition, the hydrodynamic and thermal entrance lengths of molten salts flowing in straight circular pipes are investigated.

Table 2-4 Forced convective heat transfer and friction factor correlations for internal flows

	Correlation	Reynolds number	Reference
Hydrodynamic entrance length	$L/D \approx 0.05\mathrm{Re}$	$\mathrm{Re} \leq 2{,}300$	Bergman et al. (2011)
	$10 \leq L/D \leq 60$	$\mathrm{Re} \geq 10^4$	
	$L/D = 4.4\mathrm{Re}^{1/6}$		Cimbala and Cengel (2005)
Thermal entrance length	$L/D \approx 0.05\mathrm{RePr}$	$\mathrm{Re} \leq 2{,}300$	Bergman et al. (2011)
	$L/D \approx 10$	$\mathrm{Re} \geq 10^4$	
Darcy friction factor (fully-developed flow)	$f = 64/\mathrm{Re}$	$\mathrm{Re} \leq 2{,}300$	
	$f = 0.0055\left[1 + \left(2 \times 10^4 \frac{\varepsilon}{D} + \frac{10^6}{\mathrm{Re}}\right)^{1/3}\right]$	$4{,}000 \leq \mathrm{Re} \leq 5 \times 10^8$	Moody (1944)
	$f = 0.316/\mathrm{Re}^{1/4}$	$\mathrm{Re} \leq 10^5$	Massey (2006)
	$f = (0.79\ln\mathrm{Re} - 1.64)^{-2}$	$3{,}000 \leq \mathrm{Re} \leq 5 \times 10^6$	Bergman et al. (2011)
Forced convective heat transfer	Dittus-Boelter correlation $\mathrm{Nu} = 0.023\mathrm{Re}^{0.8}\mathrm{Pr}^n$ $n = 0.4$ for heating and 0.3 for cooling	$\mathrm{Re} \geq 10^4$	
	Sieder-Tate correlation for turbulent flows: $\mathrm{Nu} = 0.027\mathrm{Re}^{0.8}\mathrm{Pr}^{1/3}\left(\mu_f/\mu_w\right)^{0.14}$	$\mathrm{Re} \geq 10^4$	
	Gnielinski correlation: $\mathrm{Nu} = 0.012(\mathrm{Re}^{0.87} - 280)\mathrm{Pr}^{0.4}\left[1 + (L/D)^{-2/3}\right]\left(Pr_f/Pr_w\right)^{0.11}$	$2300 \leq \mathrm{Re} \leq 10^6$	Kakac et al. (2014)
	Hausen correlation: $\mathrm{Nu} = 0.116\left(\mathrm{Re}^{2/3} - 125\right)\mathrm{Pr}^{1/3}\left(\mu_f/\mu_w\right)^{0.14}$	$3500 \leq \mathrm{Re} \leq 1.2 \times 10^4$	Hausen (1959)
	Sieder-Tate correlation for laminar flows $\mathrm{Nu} = 1.86\mathrm{Re}^{1/3}\mathrm{Pr}^{1/3}(L/D)^{-1/3}\left(\mu_f/\mu_w\right)^{0.14}$	$\mathrm{Re} \leq 2300$	Sieder and Tate (1936)

Hydrodynamic entrance length

Figure 2-10 shows the non-dimensional hydrodynamic entrance length L_{hyd}/D as a function of the Reynolds numbers in a range of 100 to 1,800, where L_{hyd} is the hydrodynamic entrance length. The CFD results show that the non-dimensional hydrodynamic entrance length is linearly dependent on the FLiNaK Reynolds number. The relative discrepancy between the modeling results and a widely used correlation for the hydrodynamic entrance length of laminar flows (Bergman et al., 2011)

$$L_{laminar,hyd}/D \approx 0.05\mathrm{Re} \tag{2-23}$$

is within 30% for Re = 100 - 1,800.

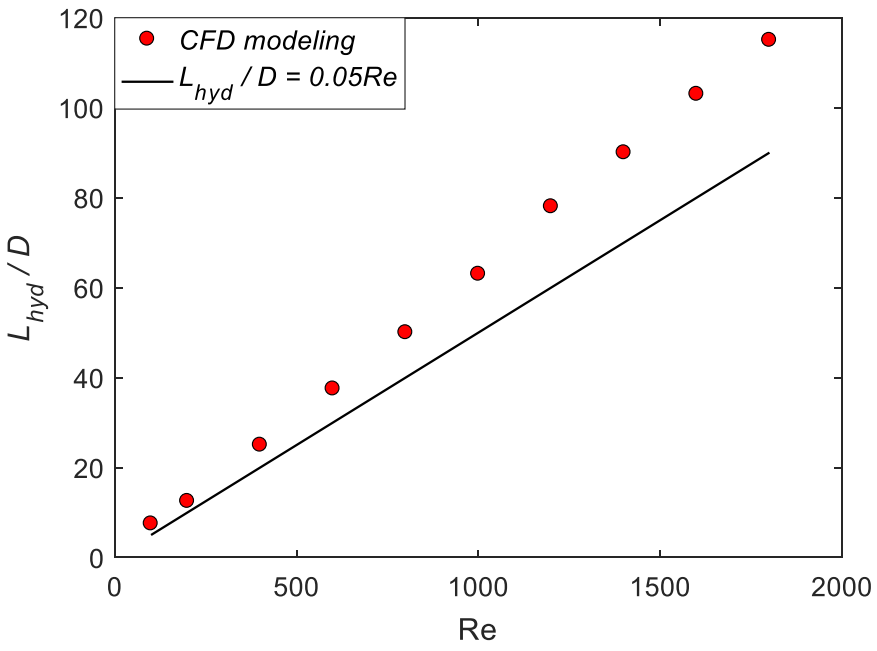

Figure 2-10 Hydrodynamic entrance length for FLiNaK in laminar flow regime

A similar simulation has also been performed for FLiNaK in the turbulent flow regime. Figure 2-11 shows the non-dimensional hydrodynamic entrance length L_{hyd}/D as a function of the Reynolds numbers in a range of 10,000 to 100,000. The modeling results agree well with a widely used correlation for the hydrodynamic entrance length of turbulent flows (Bergman et al., 2011)

$$10 \leq L_{turbulent,hyd}/D \leq 60 \tag{2-24}$$

However, the modeling results deviate from the correlation given by Cimbala and Cengel (2005) as

$$L_{turbulent,hyd}/D = 4.4\mathrm{Re}^{1/6} \tag{2-25}$$

by 35%.

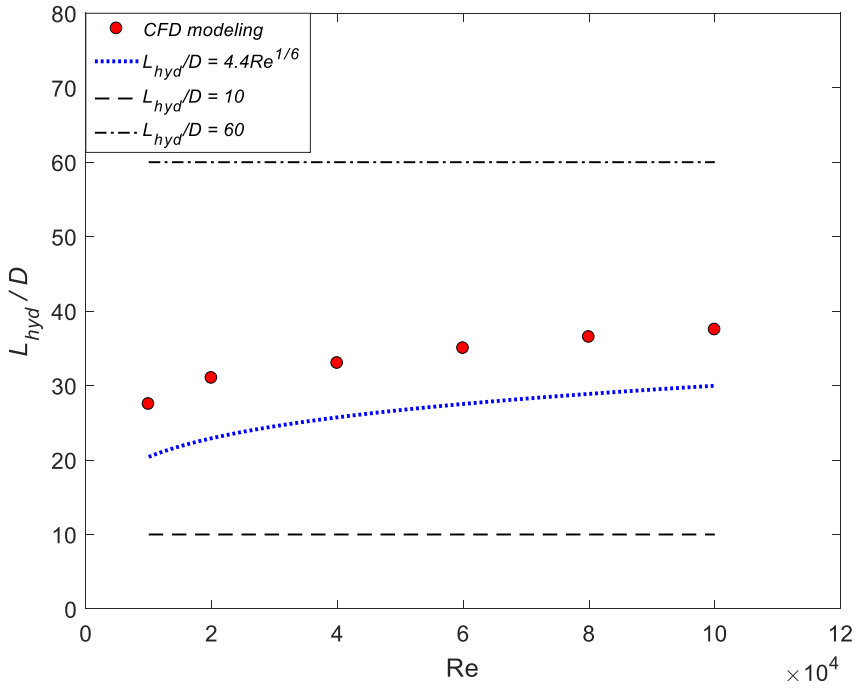

Figure 2-11 Hydrodynamic entrance length for FLiNaK in turbulent flow regime

Thermal entrance length

The thermal entrance length is identified to be 500D at Re = 400 and Pr = 22.8 for FLiNaK at 500 °C, which has a 9.6% discrepancy compared to the results estimated by Bergman et al. (2011):

$$L_{laminar,T}/D \approx 0.05\mathrm{RePr} \tag{2-26}$$

A similar simulation has been performed for FLiNaK in turbulent flow regime. The thermal entrance length for FLiNaK is identified to be 12.5D at Re = 10,000, which has a 20% discrepancy compared to the results given by Bergman et al. (2011):

$$L_{turbulent,T}/D \approx 10 \tag{2-27}$$

Friction characteristics

The Darcy friction factor in the developing and hydrodynamically fully-developed regions are numerically investigated for Re = 100 - 1,800 and 10,000 - 100,000. The friction factor decreases significantly along the flow direction in the developing flow region, while it remains nearly constant in the fully-developed flow region as shown in Figure 2-12(a) for laminar flows and Figure 2-12(b) for turbulent flows. The laminar flows as shown in Figure 2-12(a) are hydrodynamically fully developed at $z/D > 115$ or earlier. In addition, the turbulent flows as shown in Figure 2-12(b) are hydrodynamically fully developed at $z/D > 40$ or earlier. The CFD results of FLiNaK in the fully-developed flow region will be used to estimate heat transfer and friction characteristics of molten salts in straight circular pipes.

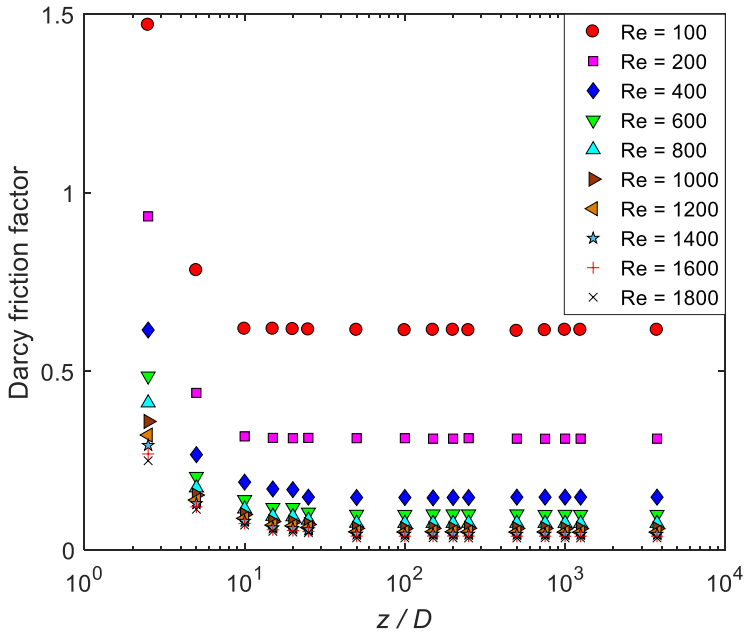

(a)

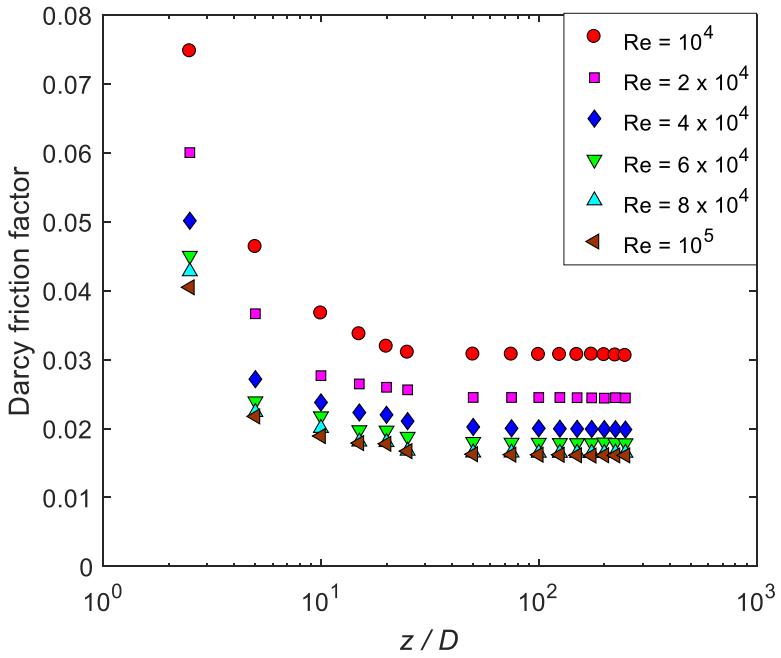

(b)

Figure 2-12 Local Darcy friction factor of FLiNaK in (a) laminar and (b) turbulent flow regimes

Figure 2-13 shows the Darcy friction factor of FLiNaK in laminar and turbulent flow regimes obtained by the CFD study for hydrodynamically and thermally fully-developed flows, widely used friction factor correlations, and isothermal experiments (Jeong and Bang, 2010; Vriesema, 1979). No additional data reprocessing is needed for the experimental data, such as for the Reynolds number and friction factor in the literature (Jeong and Bang, 2010) for laminar flows of FLiNaK due to the negligible differences between the thermophysical properties used in the literature during data reduction (Jeong and Bang, 2010) and recommended values in this research for FLiNaK (Table 2-1).

As shown in Figure 2-13(a), the CFD results agree well with both the experimental data and the correlation for fully-developed laminar flows (Bergman et al., 2011):

$$f = 64/\mathrm{Re} \tag{2-28}$$

The relative discrepancies between the CFD results and the experimental data, CFD and correlation Eq. (2-28) results are within 13.7% and 6.3%, respectively. It is therefore appropriate to use $f = 64/\mathrm{Re}$ for the friction factor estimation of FLiNaK in fully-developed laminar flow regime.

The numerical results of the friction factor for hydrodynamically fully-developed turbulent flows are compared with the FLiNaK experimental data as shown in Figure 2-13(b). Due to the large differences between the thermophysical properties used during data reduction in the literature (Vriesema, 1979) and recommended values in this research for FLiNaK (Table 2-1), the original experimental data from Vriesema (1979) have been reprocessed by adopting the recommended properties of FLiNaK.

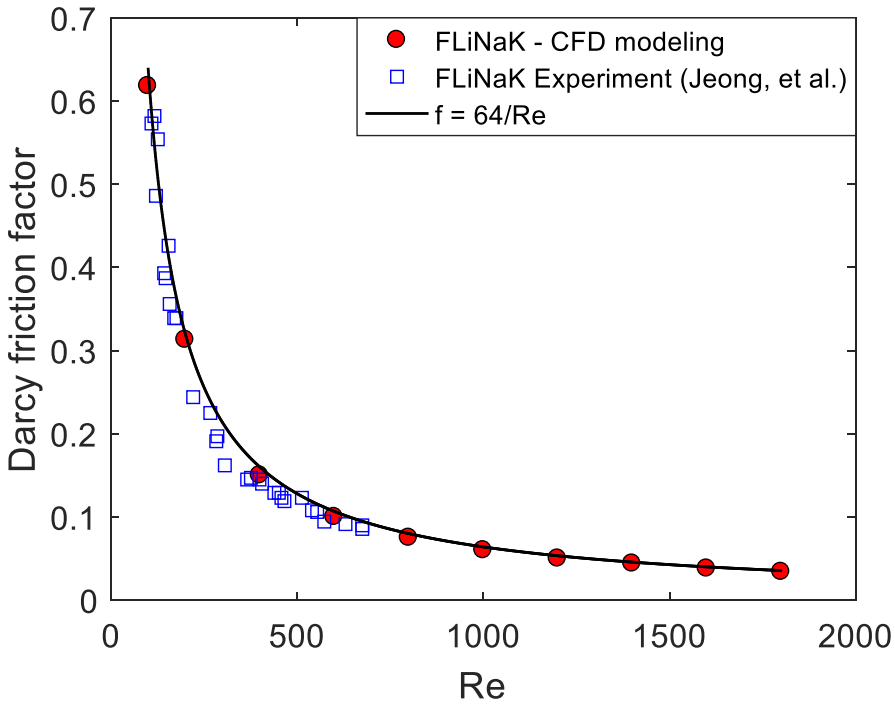

(a)

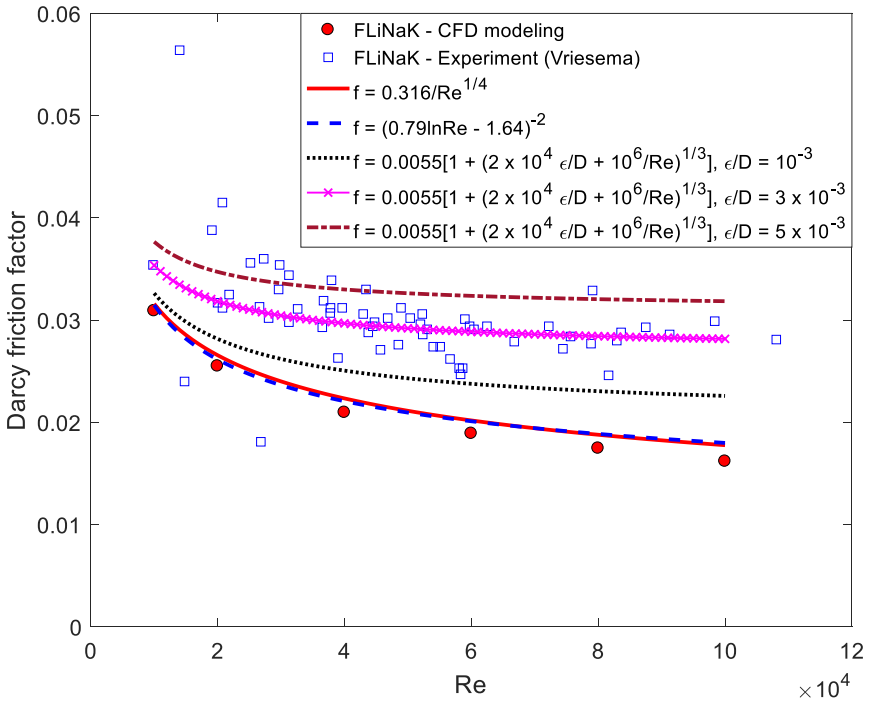

(b)

Figure 2-13 Darcy friction factor of FLiNaK in (a) laminar and (b) turbulent flow regimes

In addition, it needs to be noted that there is one typo in a figure in Vriesema (1979) when summarizing the experimental data in the literature: The pressure loss of FLiNaK in a straight-pipe test section was misplaced in the column for the pressure loss of FLiNaK in a Venturi pipe. The pressure drop over a Venturi pipe was used to calculate the FLiNaK velocity, which was then used to compute the FLiNaK Reynolds number. This typo is recognized because: (1) The pressure loss in the Venturi pipe should be several times larger than that in the straight-pipe test section based on the methodology adopted in the literature (Vriesema, 1979). However, the trend in Figure 3.3-7 of the literature (Vriesema, 1979) is the opposite; and (2) The computed friction factor after this correction (switch the pressure drop experimental data for the straight-pipe test section with those in the Venturi pipe) completely agrees with the friction factor plot Figure 3.3-9 in the literature (Vriesema, 1979).

The Darcy friction factor of FLiNaK for turbulent flows in smooth pipes obtained from our CFD simulations is compared with two following correlations (Bergman et al., 2011; Massey, 2006):

$$f = 0.316/\mathrm{Re}^{1/4} \tag{2-29}$$

$$f = (0.79\ln\mathrm{Re} - 1.64)^{-2} \tag{2-30}$$

The relative discrepancy between the CFD and correlation results is within 9.7% as shown in Figure 2-13(b). However, it is in general significantly lower than the experimental values. This large discrepancy may be due to the increased roughness of the pipe inner surface considering the corrosion effect of the FLiNaK salt to the test section wall at high temperatures. A static corrosion test of Inconel 617 in the FLiNaK salt environment at 850 °C for 500 hours suggested a relative roughness of $\varepsilon/D = 10^{-3}$ (Olson, 2009). Since the corrosion rate in a dynamic test is usually larger

than that in a static test considering the flow-accelerated corrosion, the pipe relative roughness resulting from salt corrosion in the experiments (Vriesema, 1979) is likely to be larger than 10^{-3}. In viewing this, we used three relative roughness, $\varepsilon/D = 10^{-3}$, 3×10^{-3}, and 5×10^{-3}, to estimate the friction factor of turbulent flows in a rough pipe using the following correlation (Moody, 1944):

$$f = 0.0055\left[1 + \left(2\times10^{4}\frac{\varepsilon}{D} + \frac{10^{6}}{\mathrm{Re}}\right)^{1/3}\right] \tag{2-31}$$

The FLiNaK friction factor based on Eq. (2-31) with $\varepsilon/D = 3\times10^{-3}$ agrees well (±23.6% uncertainties) with 95% of the experimental data. It is suggested to investigate the effect of salt corrosion on the pipe surface roughness as the future work.

Thermal characteristics for laminar flows

For high-Prandtl number fluids, such as molten salts, the thermal entrance length in a circular pipe can be significantly large for laminar flows. Taking D = 0.01 m, Re = 1,000, and Pr = 10 as an example, the thermal entrance length L can be as high as 5 m. It is therefore difficult to ensure that the flow is thermally developed prior to entering the test section in a limited laboratory space.

Utilizing the correlations discussed earlier to predict the entrance length, both the hydrodynamic and thermal entrance lengths could be obtained for the molten salt experiments as summarized in Table 2-5. The thermally developing flows were observed for all the three experiments (Chen et al., 2017; Silverman et al., 1976; Cooke and Cox, 1973) due to their much larger thermal entrance lengths compared with the test section lengths. In addition, the effect of the hydrodynamic entrance length was expected to be non-negligible, especially for the first two experiments (Chen et al., 2017; Silverman et al., 1976).

Table 2-5 Entrance length for the experiments (Chen et al., 2017; Silverman et al., 1976; Cooke and Cox, 1973)

Fluid	L_{hyd}/D	L_T/D	L_{test}/D	Reference
KNO_3-$NaNO_2$-$NaNO_3$ (53-40-7 mol%)	16.6 to 101.9	366.3 to 2853.9	60.0*	Chen et al., 2017
LiF-BeF_2-ThF_4-UF_4 (71.7-16-12-0.3 mol%)	77.7 to 108.4	994.6 to 1376.7	123.9**	Silverman et al., 1976
LiF-BeF_2-ThF_4-UF_4 (67.5-20-12-0.5 mol%)	20.3 to 42.0	310.6 to 558.6	136.1	Cooke and Cox, 1973

*: Excluding an additional entrance length of $L/D = 53$

**: Excluding an additional entrance length of $L/D = 40$

Since the Nusselt numbers presented in the literature (Chen et al., 2017; Silverman et al., 1976; Cooke and Cox, 1973) were obtained for developing flows in circular pipes, they should be larger than 4.36 as shown in Figure 2-14(a), a theoretical Nu value for fully-developed laminar flows in circular pipes under constant wall heat flux conditions. However, the CFD results for fully-developed laminar flows of FLiNaK and LiF-BeF_2-ThF_4-UF_4 agree well with the theoretical value within 6.9% difference. A forced convective heat transfer correlation, Sieder-Tate correlation, will be used to predict the Nusselt number considering the entrance effect for laminar flows.

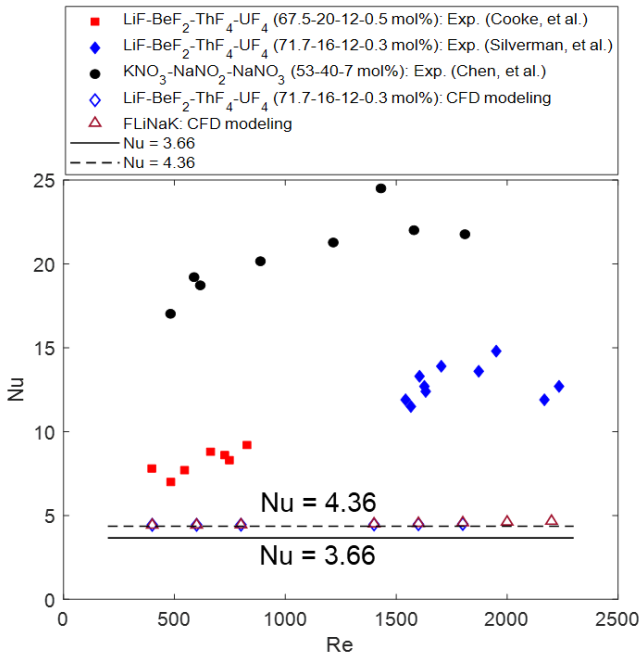

(a)

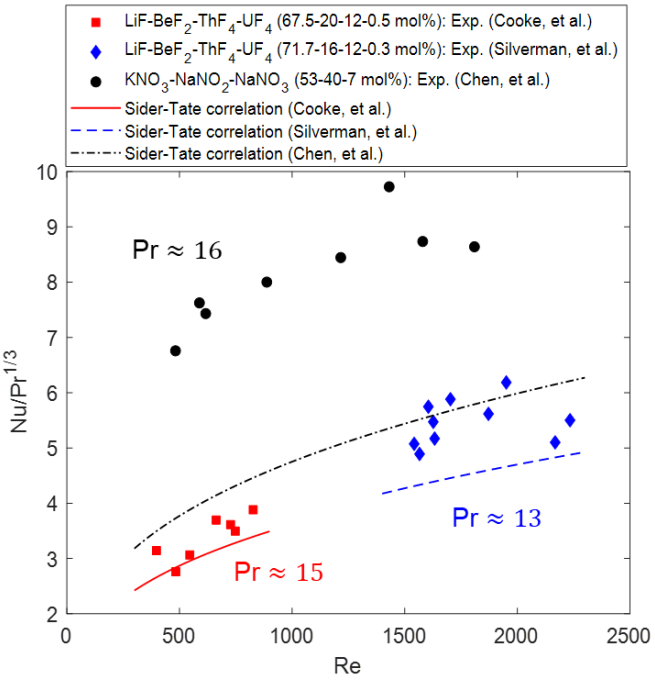

(b)

Figure 2-14 Nusselt numbers of KNO_3-$NaNO_2$-$NaNO_3$ and LiF-BeF_2-ThF_4-UF_4 in laminar flow regime compared with (a) Nu = 4.36 and 3.66, and (b) Sieder-Tate laminar flow correlation

The Sieder-Tate correlation (laminar flows) (1936)

$$\mathrm{Nu} = 1.86\mathrm{Re}^{1/3}\mathrm{Pr}^{1/3}(L/D)^{-1/3} \tag{2-32}$$

is compared with the experimental data in the literature (Chen et al., 2017; Silverman et al., 1976; Cooke and Cox, 1973) as shown in Figure 2-14(b). Compared to the theoretical values, Nu = 4.36 or 3.66 for fully-developed laminar flows in circular pipes under constant wall heat flux or wall temperature conditions, the Sieder-Tate correlation (laminar flows) results are closer to the experimental data by taking the entrance effect into consideration. The Sieder-Tate correlation results are 27% lower than the experimental data in the two fuel salt experiments (Silverman et al., 1976; Cooke and Cox, 1973) and 40% lower than the data in the nitrate salt experiment (Chen et al., 2017).

There are a number of potential reasons for these large discrepancies identified earlier, such as the underestimated entrance effect by the Sieder-Tate correlation for laminar flows in the experiments and/or incapability of the forced convective heat transfer correlation to completely represent the heat transfer phenomena existed in these molten salt experiments (Chen et al., 2017; Silverman et al., 1976; Cooke and Cox, 1973), such as the effects of buoyancy and radiative heat transfer. All these potential reasons will be justified in Section 2.3.

Thermal characteristics for transitional and turbulent flows

The Nusselt number computed based on the CFD simulations are compared with the experimental data in molten salt experiments and forced convective heat transfer correlations for transitional and turbulent flows, such as the Dittus-Boelter Eq. (2-33), Gnielinski Eq. (2-34), Sieder-Tate (turbulent) Eq. (2-35), and Hausen Eq. (2-36) correlations.

$$\mathrm{Nu} = 0.023\mathrm{Re}^{0.8}\mathrm{P}r^{n} \quad (n = 0.4 \text{ for heating and } 0.3 \text{ for cooling}) \tag{2-33}$$

$$\mathrm{Nu} = 0.012(\mathrm{Re}^{0.87} - 280)\mathrm{Pr}^{0.4}\left[1 + (L/D)^{-2/3}\right]\left(Pr_f/Pr_w\right)^{0.11} \tag{2-34}$$

$$\mathrm{Nu} = 0.027\mathrm{Re}^{0.8}\mathrm{Pr}^{1/3}\left(\mu_f/\mu_w\right)^{0.14} \tag{2-35}$$

$$\mathrm{Nu} = 0.116\left(\mathrm{Re}^{2/3} - 125\right)\mathrm{Pr}^{1/3}\left(\mu_f/\mu_w\right)^{0.14} \tag{2-36}$$

As shown in Figure 2-15, the CFD results of FLiNaK and LiF-BeF_2-ThF_4-UF_4 generally agree well with the experimental data. In addition, both the CFD results and about 90% of the total experimental data points fall within ±20% uncertainties of the Dittus-Boelter correlation. Therefore, the Dittus-Boelter correlation is generally good for modeling of molten salt heat transfer in turbulent flow regime.

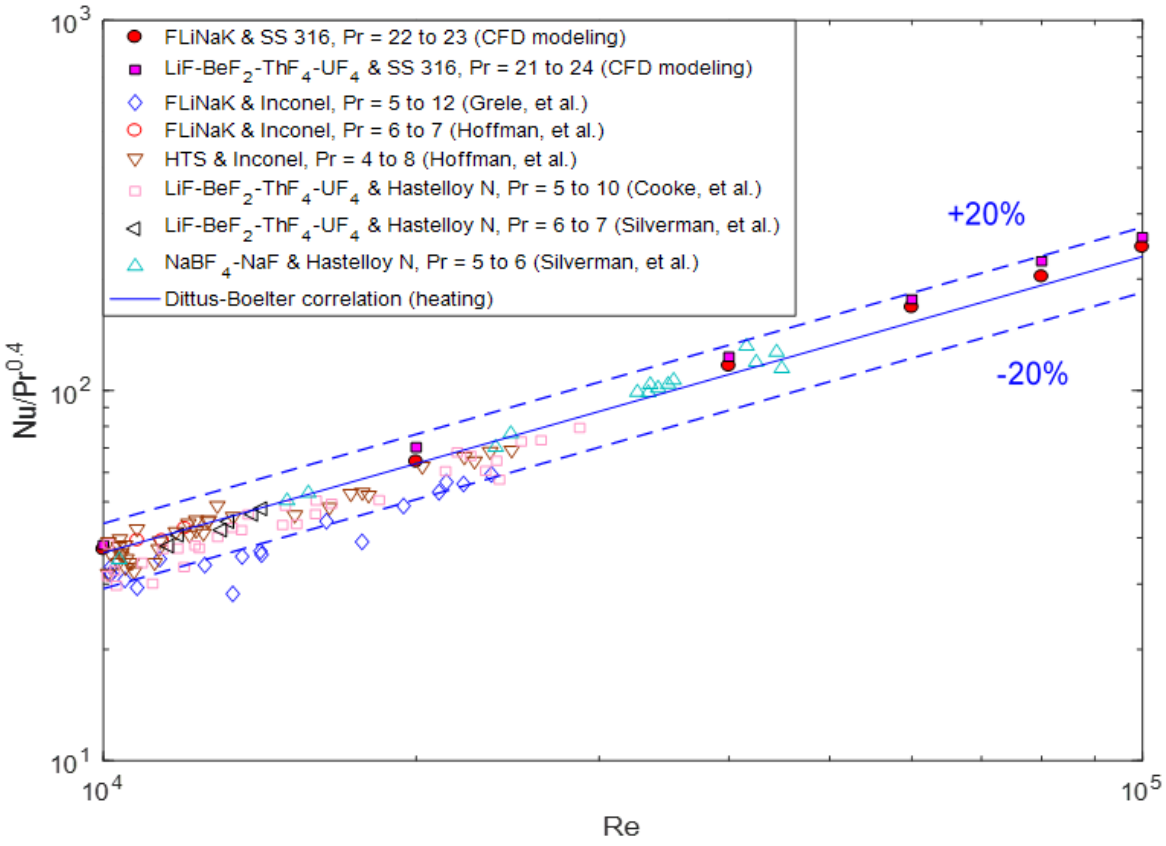

Figure 2-15 Comparison among the CFD results, experimental data, and Dittus-Boelter correlation for salt Nusselt number

Similarly, the CFD results of FLiNaK and LiF-BeF_2-ThF_4-UF_4 are within ±11.4% uncertainties of the Gnielinski correlation as shown in Figure 2-16. In addition, nearly 90% of the experimental data points fall within ±20% uncertainties of the Gnielinski correlation, while 5% of the experimental data points deviate from the Gnielinski correlation results significantly, by 40% and the remaining 5% data points deviate by 150%. Except for the experimental data from Hoffman and Lones (1955) who used nickel and SS 316 pipes in the experiments, the Gnielinski correlation in general predicts accurately the molten salt heat transfer behavior for 2,300 ≤ Re ≤ 50,000.

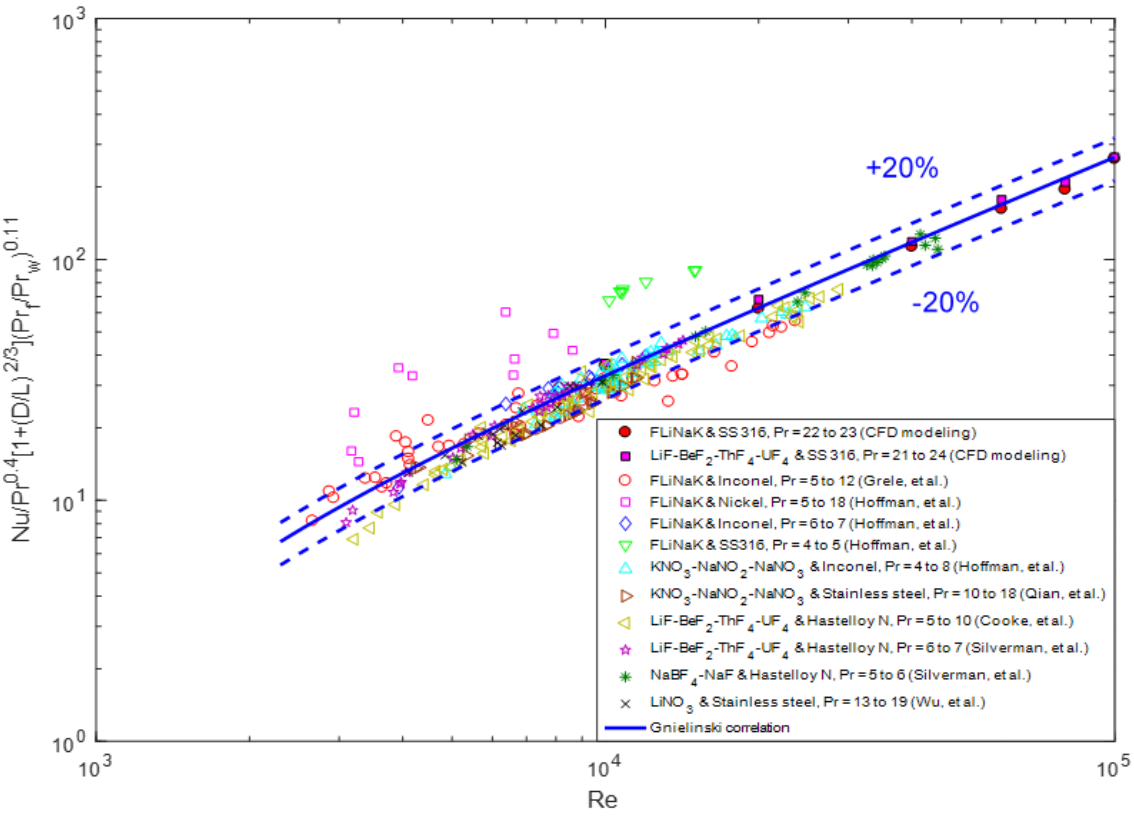

Figure 2-16 Comparison among the CFD results, experimental data, and Gnielinski correlation for salt Nusselt number

In Hoffman's experiments, nickel, Inconel, and SS 316 were used as the pipe materials. Since the Nusselt values derived from the FLiNaK-Inconel experimental data were much lower than those derived from their other two experiments, i.e., FLiNaK-nickel and FLiNaK-SS 316 experiments, Hoffman concluded that the significant deviation was due to the formation of a corrosion layer on the inner pipe surface during the FLiNaK-Inconel experiment. However, the explanation was disputed (Zhang et al., 2020a; Ambrosek et al., 2009; Yoder, 2014a) since Inconel and SS 316 should exhibit similar corrosion resistant to FLiNaK at similar temperatures.

Table 2-6 summarizes the nominal compositions of Inconel 600, Nickel 200, and SS 316. Chromium (Cr) contents in Inconel 600 and SS 316 are in very similar ranges. Chromium is more

likely to dissolve in FLiNaK, compared with Ni and Fe, due to the lowest free energy of formation for CrF_2 as summarized in Table 2-7 (Baes, 1974). Therefore, the salt corrosion effect on FLiNaK heat transfer experiments using Inconel 600 and SS 316 as the pipe materials should behave similarly if the initial purity level in FLiNaK is the same for the three tests and the rest of testing conditions are very similar, including the salt temperature, salt volume, and test duration. A number of publications (Rahnema, 2016; Zhang et al., 2017a; Feron, 2012) demonstrated that compared with Inconel 600, SS 316L/316H has a similar or even lower corrosion rate in FLiNaK salt environment. However, the experimental data from Hoffman's FLiNaK-SS 316 experiment are about 100% higher than those from their own FLiNaK-Inconel experiment. In addition, Nickel 200 is corrosion resistant to FLiNaK, but the experimental data using the nickel pipe show significantly higher values than those using Hastelloy N, another corrosion resistant alloy to FLiNaK. It is therefore hypothesized that there were most likely some abnormal conditions unaddressed in Hoffman's FLiNaK-SS 316 and FLiNaK-Nickel experiments. New heat transfer experiments for FLiNaK in SS 316 and nickel pipes are suggested.

Table 2-6 Nominal compositions of Inconel 600, nickel 200, and SS 316 (wt%) (Special Metals)

	Ni	Cr	Fe	Mo	Mn	Si	C
Inconel 600	> 72.0	14.0-17.0	6.0-10.0	--	< 1.0	< 0.5	< 0.15
Nickel 200	> 99.0	--	--	--	< 0.35	< 0.35	< 0.15
SS 316	10.0-14.0	16.0-18.0	Balance	2.0-3.0	< 2.0	< 0.75	< 0.08

Table 2-7 Free energy of formation for fluorides at 1000 K (Baes, 1974)

Compound	CrF_2	FeF_2	NiF_2	MoF_6
Free energy (kJ)	-314	-280	-230	-209

Since most of the heat transfer experimental data presented in the literature are in the form of $Nu/Pr^{1/3}$, the CFD results are written in the same functional form and compared with those experimental data and Sieder-Tate (turbulent) and Hausen correlations as shown in Figure 2-17. The experimental data using oil as the working fluid (Morris and Whitman, 1928) are included as well. The CFD results of FLiNaK and LiF-BeF_2-ThF_4-UF_4 agree well with the experimental data, except again for the data derived from Hoffman's experiments. In addition, both the CFD results and most of the experimental data are within ±20% uncertainties of the Sieder-Tate correlation (turbulent) for $10{,}000 \leq Re \leq 120{,}000$. In addition, Hausen correlation predicts the molten salt heat transfer coefficient with ±20% uncertainties for $5{,}000 \leq Re \leq 10{,}000$, while ±40% uncertainties for $2{,}300 \leq Re \leq 5{,}000$.

The much larger experimental values compared to the CFD results and Hausen correlation especially for Re = 2,300 to 3,000 is likely due to the entrance effect, buoyancy effect, and radiative heat transfer effect in molten salts. In addition, the comparison as shown in Figure 2-17 appears to suggest that these potential reasons discussed earlier could be neglected for flows of large salt Reynolds numbers, such as Re > 3,000 because of significantly increased convective heat transfer coefficient.

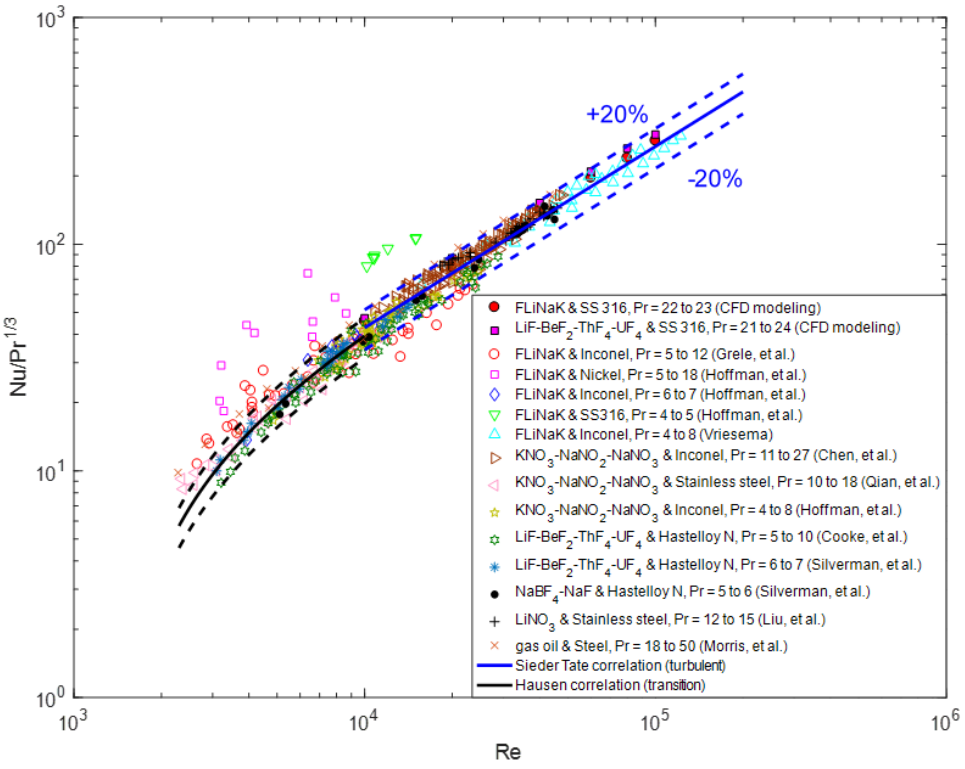

Figure 2-17 Comparison among the CFD results, experimental data, Sieder-Tate and Hausen correlations for salt Nusselt number

2.3 CFD Study for Molten Salts in Circular Pipes with the Effects of Buoyancy and Radiative Heat Transfer

As observed in Figure 2-14 in Section 2.2, the Nusselt number of molten salts in laminar flow region is significantly underestimated by the CFD predictions for fully-developed flows and Sieder-Tate correlation for developing laminar flows. Several potential reasons were proposed as discussed earlier, including (1) underestimation by the Sieder-Tate correlation and/or (2) incapability of the forced convective heat transfer correlation, Sieder-Tate correlation, to completely represent the heat transfer phenomena present in the molten salt experiments, such as the effects of buoyancy and radiative heat transfer. All these potential reasons will be investigated in this section through a CFD study.

STAR-CCM+ was used for modeling of the thermal-hydraulic performance of three different molten salts, namely, KNO_3-$NaNO_2$-$NaNO_3$ (53-40-7 mol%), LiF-BeF_2-ThF_4-UF_4 (71.7-16-12-0.3 mol%), and LiF-BeF_2-ThF_4-UF_4 (67.5-20.0-12-0.5 mol%) in their corresponding test sections as shown in Figure 2-18, the same configurations as those in the experiments (Chen et al., 2017; Silverman et al., 1976; Cooke and Cox, 1973). In addition, the thermophysical properties of these molten salts used in the numerical modeling are the same as those adopted in their respective experiments.

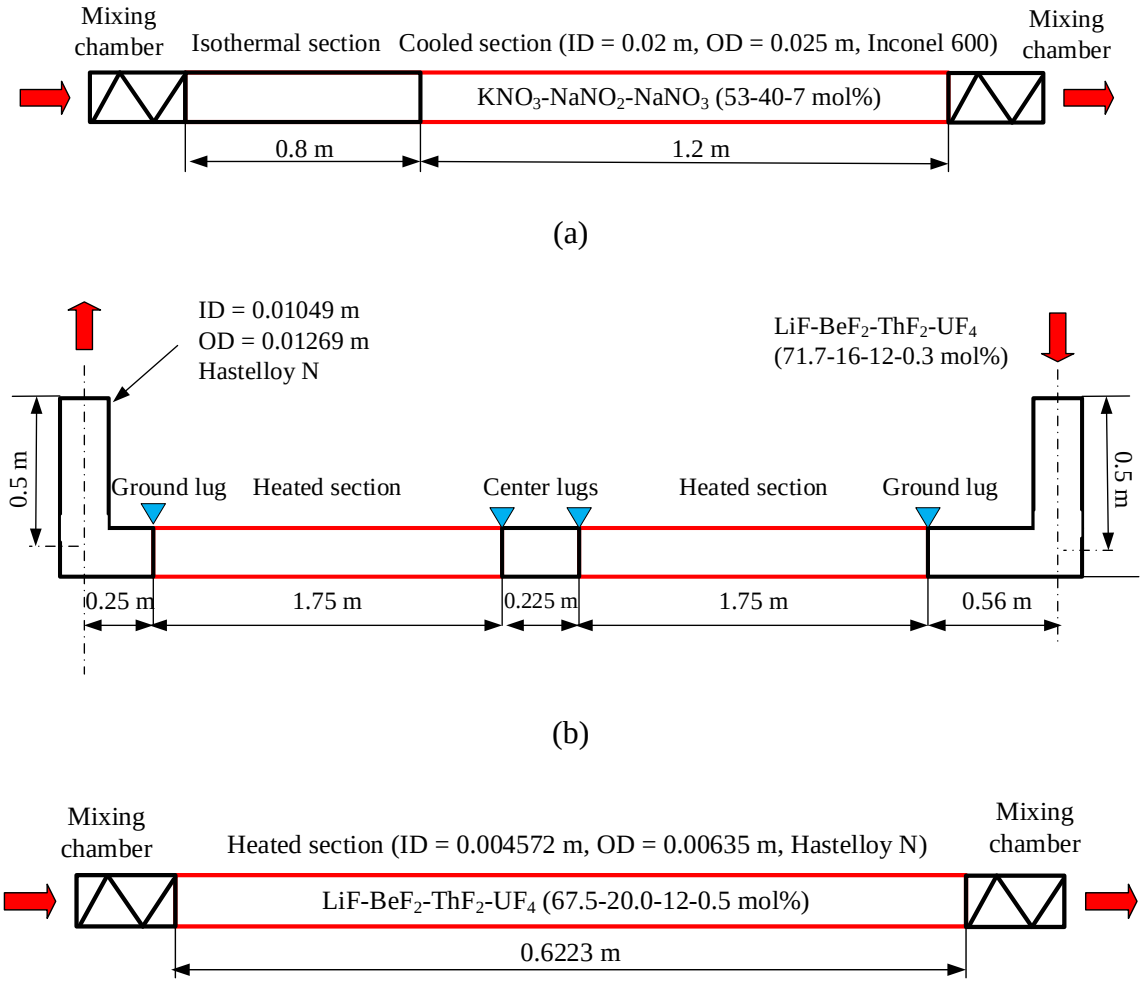

Figure 2-18 Geometry and dimensions of the test sections in the experiments by: (a) Chen et al. (2017); (b) Silverman et al. (1976); and (c) Cooke and Cox (1973)

2.3.1 Numerical Modeling

Several mesh models, such as polyhedral mesher, surface remesher, and prism layer mesher were enabled for meshing. The boundary conditions for the two fuel salt experiments (Silverman et al., 1976; Cooke and Cox, 1973) include a mass flow rate inlet at a certain temperature, an atmospheric pressure outlet, and a constant wall heat flux condition. Since the two fuel salt experiments (Silverman et al., 1976; Cooke and Cox, 1973) were recorded in detail, the inlet mass flow rate, inlet temperature, and surface-averaged wall heat flux used in the numerical modeling are exactly the same as those for each of the experimental data points in the experiments (Silverman, et al., 1976; Cooke and Cox, 1973). For the nitrate salt experiment (Chen et al., 2017), boundary conditions include a mass flow rate inlet at 250 °C (523 K), an atmospheric pressure outlet, and a constant wall temperature of 172 °C (445 K).

The mesh independence study has been performed for the experiments investigated. As an example, three sets of grid size were used for the fuel salt at Re = 405 in the experiments (Cooke and Cox, 1973), and the results are summarized in Table 2-8. The GCI value of the average heat transfer coefficient is significantly small, 0.11%. Therefore, the simulation results using fine mesh option #1 are considered to be mesh independent.

Table 2-8 Results of the mesh independence study for the fuel salt at Re = 405 (Cooke and Cox, 1973)

Mesh option	Cell quantity (10^3)	Grid size (mm)	$\bar{h}$ (W/m^2-K)
1 (Fine)	3439.14	0.14	1794.4
2 (Medium)	917.45	0.22	1786.5
3 (Coarse)	281.77	0.33	1773.1
GCI (%)	N/A	N/A	0.11

Three cases will be investigated by employing: (1) Forced convective heat transfer; (2) Mixed convective heat transfer to include the buoyancy effect; and (3) Combined mixed convective and radiative heat transfer in molten salts.

2.3.2 CFD Study for Forced Convective Heat Transfer

Figure 2-19 shows the CFD predictions for the three experiments (Chen et al., 2017; Silverman et al., 1976; Cooke and Cox, 1973) without considering the effects of buoyancy and radiative heat transfer in the salts. The relative discrepancies between the CFD predictions and experimental data are within 29.8%, 22.8%, and 12.0% for the three experiments, Chen et al. (2017), Silverman et al. (1976), and Cooke and Cox (1973), respectively. It is observed that the CFD predictions are generally larger than the Sieder-Tate correlation results and closer to the experimental data as shown in Figure 2-14 and Figure 2-19. Therefore, the Sieder-Tate correlation is likely to underestimate the entrance effect on the thermal performance of laminar flows of molten salts.

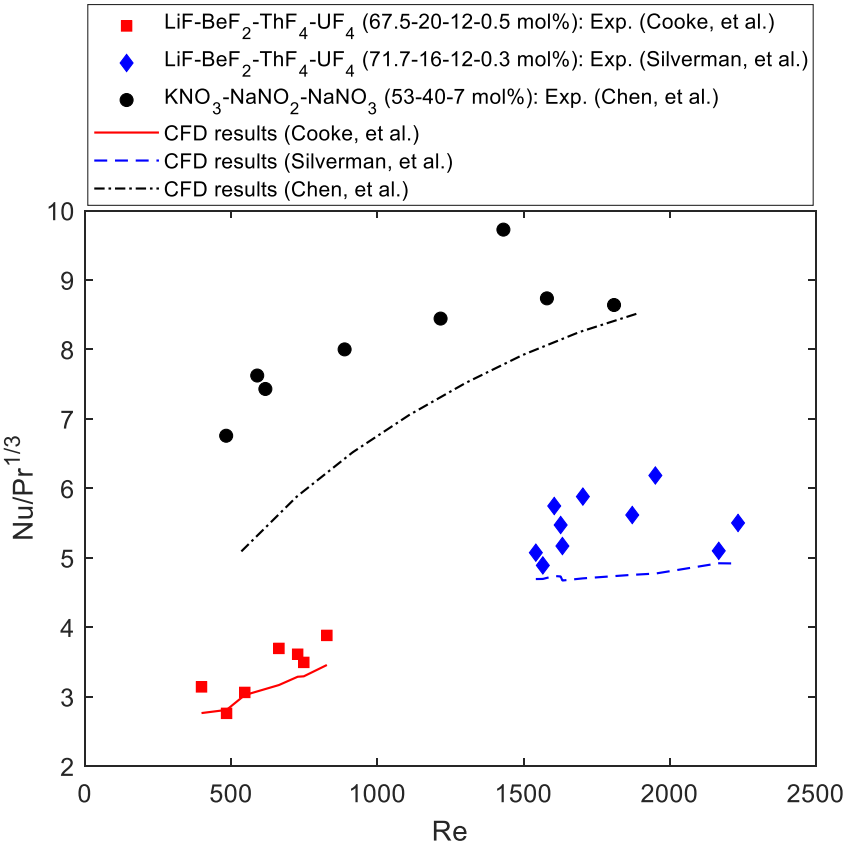

Figure 2-19 CFD results for forced convective heat transfer of KNO_3-$NaNO_2$-$NaNO_3$ and LiF-BeF_2-ThF_4-UF_4 in laminar flow regime

In addition, the generally lower CFD predictions compared with the experimental data as shown in Figure 2-19 suggest the existence of additional heat transfer enhancement mechanisms in the experiments, which should be considered in the CFD study. The effects of buoyancy due to the temperature difference between the wall and bulk salt and radiative heat transfer in semi-transparent fluids, molten salts, are likely to be reasons for the heat transfer enhancement, which will be investigated next using a CFD tool, STAR-CCM+.

2.3.3 CFD Study for Mixed Convective Heat Transfer (Buoyancy Effect)

Figure 2-20 shows the CFD predictions for the three experiments (Chen et al., 2017; Silverman et al., 1976; Cooke and Cox, 1973) considering the buoyancy effect in the salts. The relative discrepancies between the CFD predictions and experimental data are within 18.5%, 15.5%, and 9.2% for the three experiments, Chen et al. (2017), Silverman et al. (1976), and Cooke and Cox (1973), respectively. By comparing the experimental data in Figure 2-19 and the conrresponding data in Figure 2-20, it is also identified that the buoyancy effect enhances the heat transfer up to 16.3%, 8.9%, and 9.1% for the three experiments, Chen et al. (2017), Silverman et al. (1976), and Cooke and Cox (1973), respectively. Therefore, the buoyancy effect is non-negligible for laminar flows of molten salts in these experiments in order to have accurate predictions.

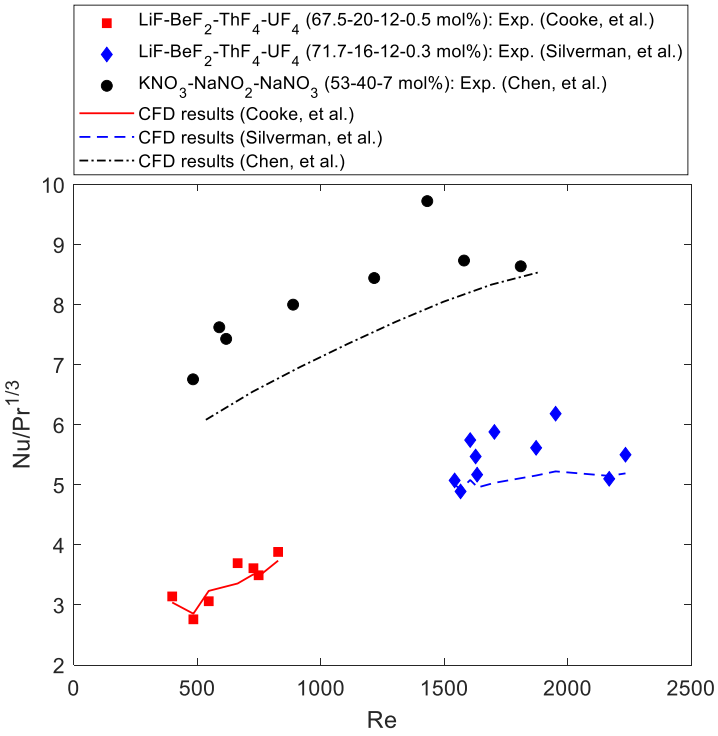

Figure 2-20 CFD results for mixed convective heat transfer of KNO_3-$NaNO_2$-$NaNO_3$ and LiF-BeF_2-ThF_4-UF_4 in laminar flow regime

In addition, the CFD predictions of $Nu/Pr^{1/3}$ are still generally lower than the experimental data for the two experiments, Chen et al. (2017) and Silverman et al. (1976). The radiative heat transfer in molten salts will then be considered in the CFD study.

2.3.4 CFD Study for Combined Mixed Convective and Radiative Heat Transfer

The DOM model in STAR-CCM+ is enabled to consider the radiative heat transfer in molten salts. A number of thermal radiation related parameters need to be known to set up the DOM model, in which one key parameter is the absorption coefficient of molten salts.

Absorption coefficient

Currently, the absorption coefficients of the fuel salt LiF-BeF_2-ThF_4-UF_4 and nitrate salt KNO_3-$NaNO_2$-$NaNO_3$ are not available. Therefore, the number-density-averaged absorption coefficient of a mixture, widely used in the literature (Chaleff et al., 2016; Zhang and Sun, 2020b) and written as

$$k_{l,\lambda,m} = \frac{\sum(N_i k_{l,\lambda,i})}{\sum N_i} \tag{2-37}$$

is adopted to estimate the absorption coefficient of LiF-BeF_2-ThF_4-UF_4 (67.5-20-12-0.5 mol%), LiF-BeF_2-ThF_4-UF_4 (71.7-16-12-0.3 mol%), and KNO_3-$NaNO_2$-$NaNO_3$ (53-40-7 mol%). *N* is for the number density and the subscripts *m* and *i* are for the mixture and *i*th constituent. The absorption coefficient for LiF, BeF_2, ThF_4, UF_4, KNO_3, $NaNO_2$, and $NaNO_3$ need to be known.

The absorption coefficients of LiF, BeF_2, ThF_4, and UF_4 have been investigated in the literature (Toth and Gilpatrick, 1972; Li, 1979; Baldwin and Mackenzie, 1979; Mouchart et al., 1985; Chaleff et al., 2018) and plotted in Figure 2-21. For Region I, $\lambda = 0.10 - 0.12$ μm as shown

in Figure 2-21, the absorption coefficient of LiF is significantly larger than others if it is extrapolated. For Region II, $\lambda = 0.12 - 2.46$ μm, the absorption coefficients of UF_4 and ThF_4 are significantly larger than the absorption coefficients of LiF and BeF_2 if they are extrapolated. For Region III, $\lambda = 2.46 - 5.11$ μm, the absorption coefficient of ThF_4 after extrapolation is significantly larger than others. For Region IV, $\lambda = 5.11 - 7.84$ μm, both BeF_2 after extrapolation and ThF_4 have dominating absorption coefficients. For Region V, $\lambda = 7.84 - 15.88$ μm, both LiF and BeF_2 have larger absorption coefficients than others. For Region VI, $\lambda = 15.88 - 100$ μm, LiF has the largest absorption coefficient.

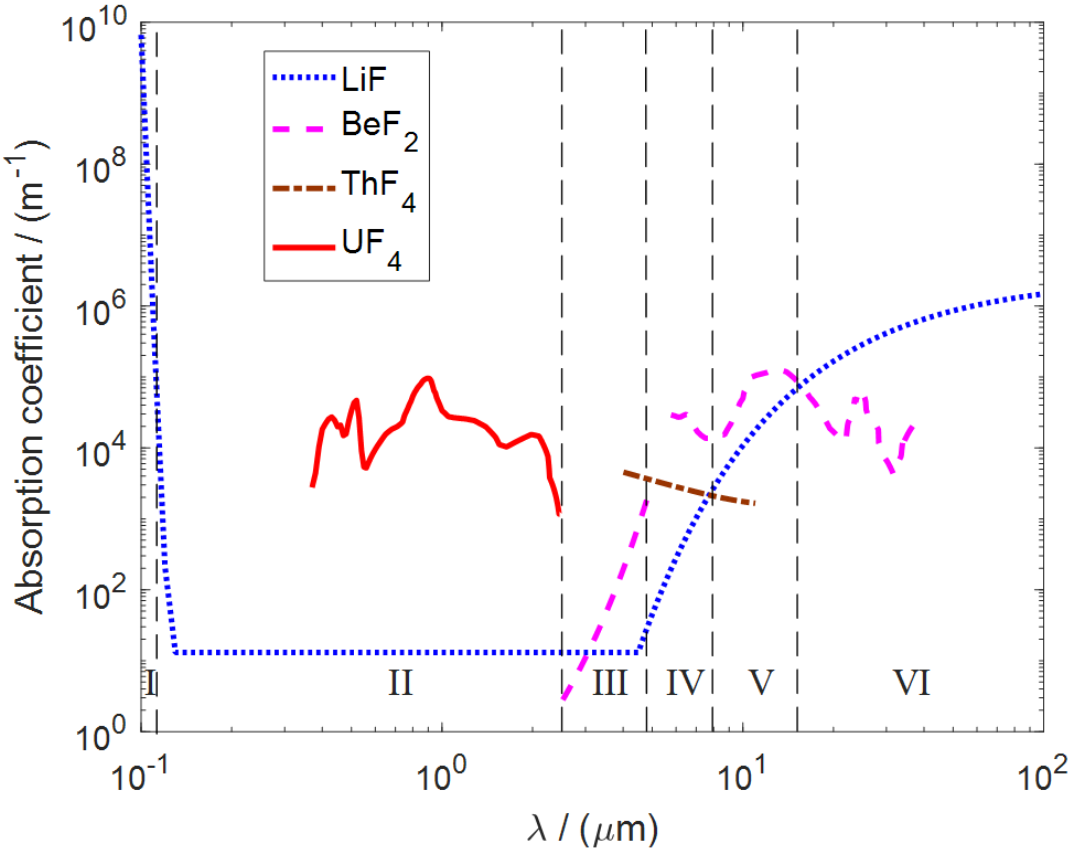

Figure 2-21 Absorption coefficients of LiF, BeF_2, ThF_4, and UF_4 (Toth and Gilpatrick, 1972; Li, 1979; Baldwin and Mackenzie, 1979; Mouchart et al., 1985; Chaleff et al., 2018)

Figure 2-22 shows the absorption coefficient of LiF-BeF_2-ThF_4-UF_4 considering: (1) The extrapolated absorption coefficient of BeF_2 for $\lambda = 0.10 - 2.51$ μm and $4.94 - 5.76$ μm, while an averaged absorption coefficient of 3.77×10^4 m^{-1} for $\lambda = 37.80 - 100.00$ μm; (2) The extrapolated absorption coefficient of ThF_4 for $\lambda = 0.10 - 4.00$ μm and $11.00 - 100.00$ μm; and (3) An averaged absorption coefficient of 2.13×10^4 m^{-1} for UF_4 for $\lambda = 0.10 - 0.36$ μm and $2.46 - 100.00$ μm. The spectral absorption coefficients of LiF-BeF_2-ThF_4-UF_4 (71.7-16.0-12.0-0.3 mol%) and LiF-BeF_2-ThF_4-UF_4 (67.5-20.0-12.0-0.5 mol%) are overlapped as shown in Figure 2-22 due to the close molar fraction of each constitute in the two fuel salts. One spectral absorption coefficient is therefore used for these two fuel salts as a convenience.

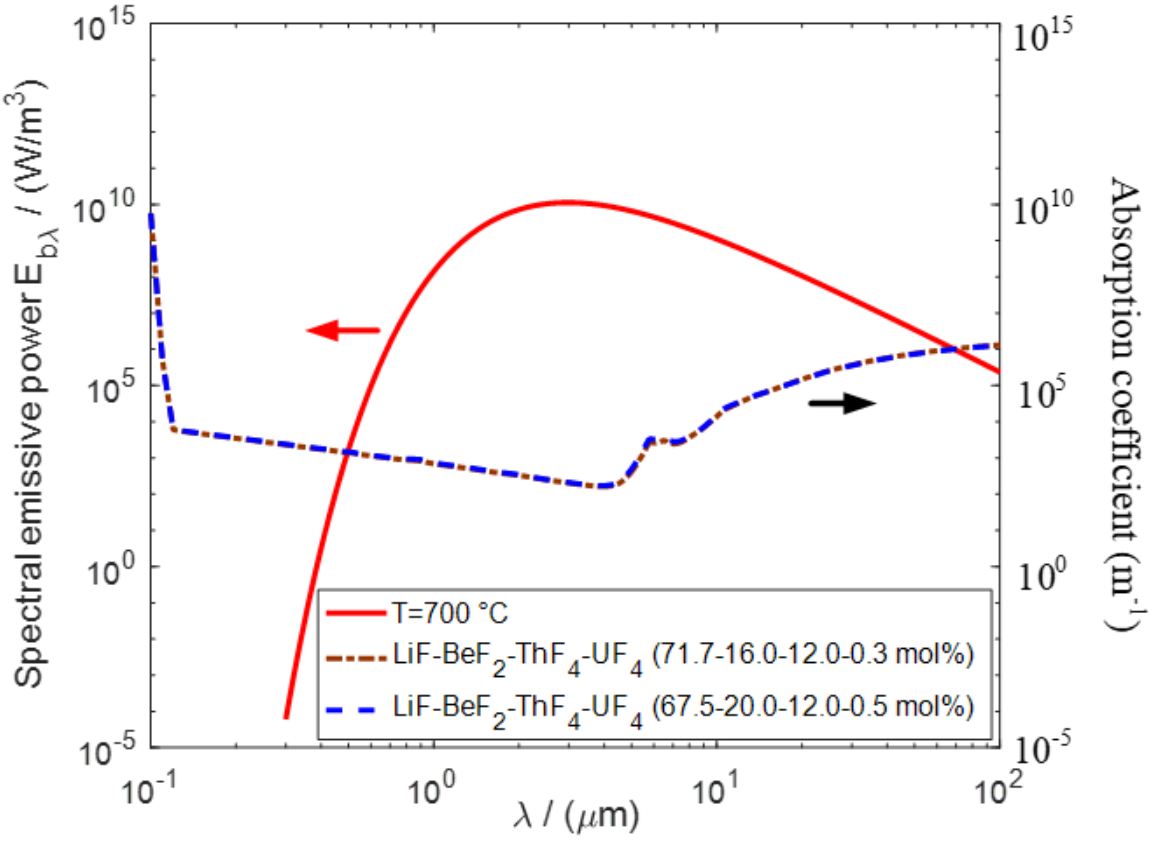

Figure 2-22 Absorption coefficient of LiF-BeF_2-ThF_4-UF_4

Independence study for the number of bands for the absorption coefficient

The absorption coefficient in the DOM model needs to be discrete values. Therefore, the continuous curve for the absorption coefficient of LiF-BeF_2-ThF_4-UF_4 as shown in Figure 2-22 should be converted to a discrete value for each band. The Planck-mean absorption coefficient, widely used in the literature (Derdeyn et al., 2018; Coyle et al., 2019) and defined as

$$\bar{k}_a = \frac{\int_{\lambda_{min}}^{\lambda_{max}} k_{a\lambda} E_{b\lambda} \mathrm{d}\lambda}{\int_{\lambda_{min}}^{\lambda_{max}} E_{b\lambda} \mathrm{d}\lambda} \tag{2-38}$$

is used to calculate the equivalent gray absorption coefficient for each band, where $E_{b\lambda}$ is the spectral emissive power of a black body. In addition, $\lambda_{min} = 0.1$ μm and $\lambda_{max} = 100$ μm are adopted in this study, which includes 99.98% of the total blackbody emissive power at 700 °C.

The larger number of bands for the absorption coefficient leads to more accurate results. However, it significantly increases the computational time as well. It is therefore necessary to perform an independence study for the number of bands considering both the accuracy and computational time.

Three cases are investigated: 1 band, 3 bands, and 5 bands. The wavelength range for each band (λ_1 for lower limit and λ_2 for upper limit) is identified by equally distributing the total blackbody emissive power as summarized in Table 2-9. The Planck-mean absorption coefficient of the fuel salt in each band at 700 °C is plotted in Figure 2-23. The shape of 5-band Planck-mean absorption coefficient better captures the continuous curve for the absorption coefficient of the fuel salt compared with others.

Table 2-9 Planck-mean absorption coefficient of LiF-BeF_2-ThF_4-UF_4 (71.7-16.0-12.0-0.3 mol%) at 700 °C

Number of bands	Fraction of $\int_0^\infty E_{b\lambda} d\lambda$ (%)	λ_1 (μm)	λ_2 (μm)	$\bar{k}_a$ (m^{-1})
1	99.98	0.10	100	10165.98
3	33.34	0.10	3.36	262.16
	33.30	3.36	5.42	272.22
	33.36	5.42	100	29844.34
5	19.99	0.10	2.75	303.22
	19.97	2.75	3.68	191.89
	20.08	3.68	4.88	191.87
	20.05	4.88	7.07	1836.45
	19.91	7.07	100	48299.91

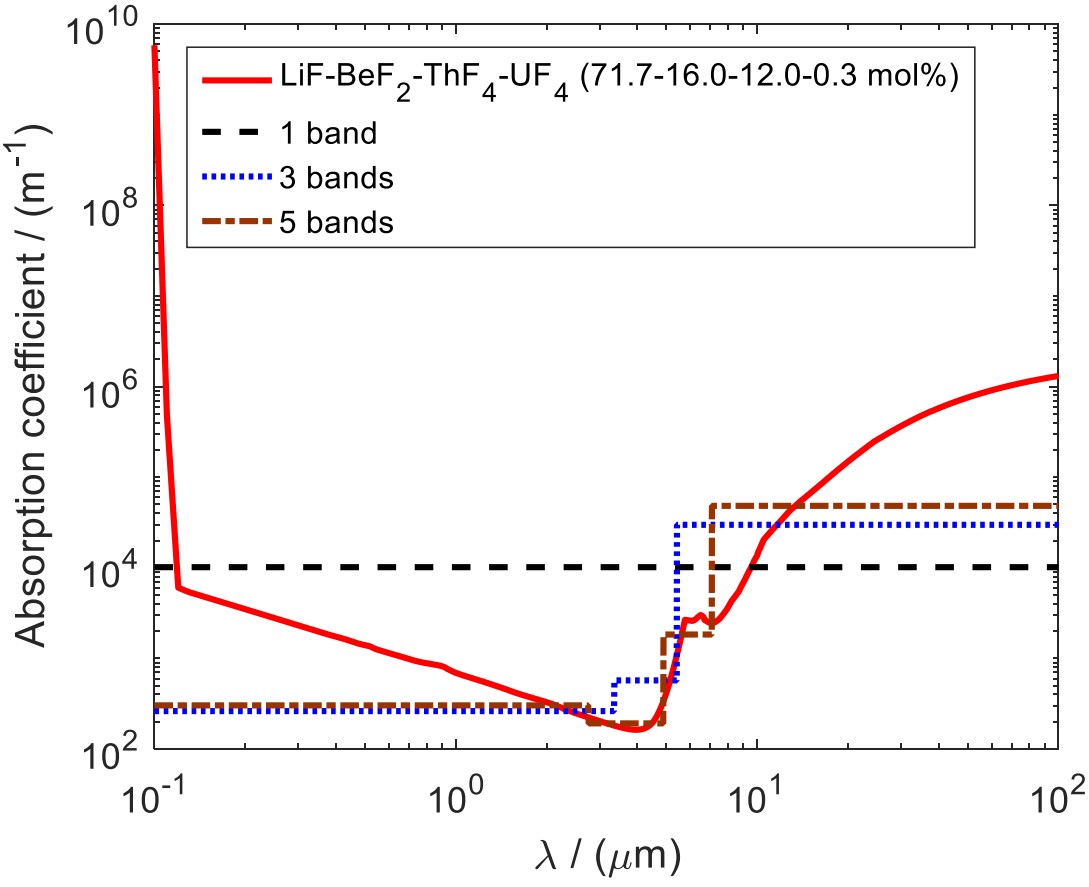

Figure 2-23 Planck-mean absorption coefficient of LiF-BeF_2-ThF_4-UF_4 (71.7-16.0-12.0-0.3 mol%)

Figure 2-24 shows the independence study for the number of bands. As the increase of the number of bands, the Nusselt number decreases continuously until reaching a plateau. The maximum discrepancies between the 1-band and 5-band results, and 3-band and 5-band results are 1.1% and 0.2%, respectively. Considering the much lower computational cost and appropriate accuracy for the 1-band condition, it is therefore selected for the following analysis of the radiative heat transfer in molten salts.

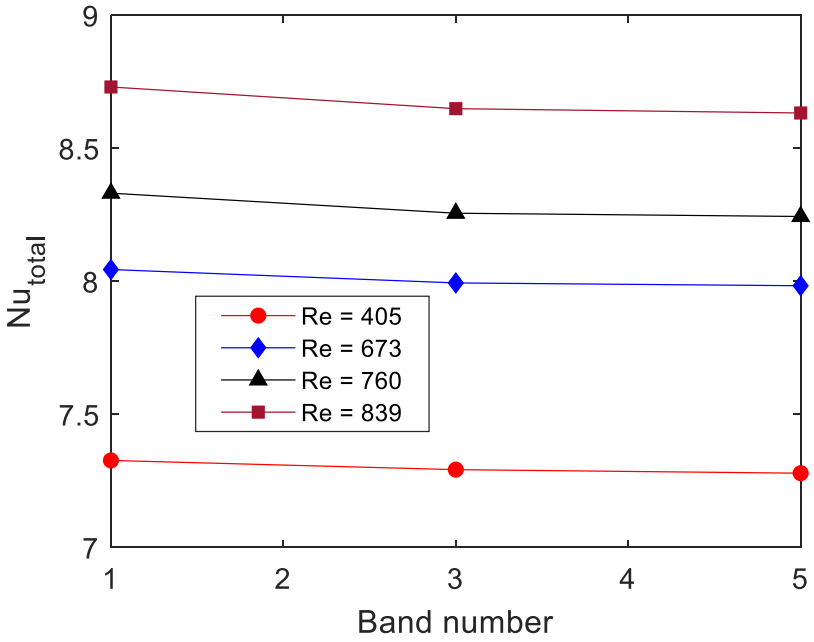

Figure 2-24 Independence study for the number of bands for LiF-BeF_2-ThF_4-UF_4 (71.7-16.0-12.0-0.3 mol%)

Comparison with experiments

Figure 2-25 shows the CFD predictions for the three experiments (Chen et al., 2017; Silverman et al., 1976; Cooke and Cox, 1973) considering both the effects of buoyancy and radiative heat transfer in the salts. The relative discrepancies between the CFD predictions and

experimental data are within 13.6%, 10.3%, and 11.7% for the three experiments, Chen et al. (2017), Silverman et al. (1976), and Cooke and Cox (1973), respectively. By comparing the experimental data in Figure 2-20 and the corresponding data in Figure 2-25, it is identified that the radiative heat transfer represents up to 5.6%, 9.1%, and 5.9% of the total heat transfer for the three experiments, Chen et al. (2017), Silverman et al. (1976), and Cooke and Cox (1973), respectively. Therefore, the radiative heat transfer is non-negligible for laminar flows of molten salts in these experiments in order to have accurate predictions. Next, we need to know under what conditions it is necessary to consider the radiative heat transfer in molten salts.

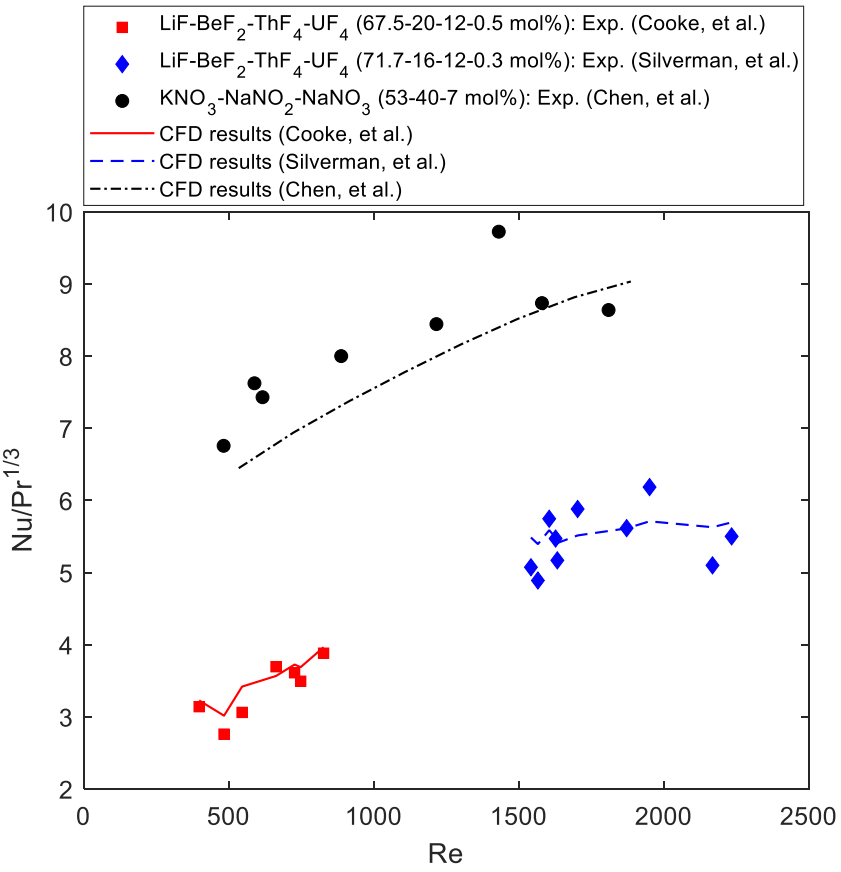

Figure 2-25 CFD results for mixed convective and radiative heat transfer of KNO_3-$NaNO_2$-$NaNO_3$ and LiF-BeF_2-ThF_4-UF_4 in laminar flow regime

2.4 Radiative Heat Transfer Model

A radiative heat transfer model will be developed in this section to identify conditions where the radiative heat transfer is non-negligible, which will then be incorporated in a 1D code NACCO to predict the thermal-hydraulic performance of molten salts in natural circulation loops.

2.4.1 Model Development

To estimate the thermal radiation effect on the total heat transfer rate for a fluid flowing inside a pipe or channel, a thermal radiation effect factor f_r, defined as

$$f_r = \frac{\mathrm{Nu}_r}{\mathrm{Nu}_r + \mathrm{Nu}_c} \tag{2-39}$$

is adopted in this study. The salt Nusselt number due to the convective and radiative heat transfer are defined respectively as:

$$\mathrm{Nu}_c = \frac{h_c D_i}{k_s} = \frac{q_c'' D_i}{k_s (T_f - T_w)} \tag{2-40}$$

$$\mathrm{Nu}_r = \frac{h_r D_i}{k_s} = \frac{q_r'' D_i}{k_s (T_f - T_w)} \tag{2-41}$$

where h_c, h_r, q_c'', q_r'', T_f, T_w, D_i, and k_s are the convective and radiative heat transfer coefficients, convective and net radiative heat fluxes, bulk fluid and wall temperatures, pipe inner diameter (ID), and salt thermal conductivity, respectively. Utilizing Eqs. (2-40) and (2-41), the thermal radiation effect factor can be written as

$$f_r = \frac{q_r''}{q_r'' + q_c''} \tag{2-42}$$

in a form of the convective and net radiative heat fluxes.

If the convective and net radiative heat fluxes, q_c'' and q_r'' between the fluid and the channel or pipe wall are known, f_r could be estimated. A radiative heat transfer model will be developed to estimate the net radiative heat flux q_r''. In addition, the conventional convective heat transfer

correlations will be used to estimate the convective heat flux q_c''. Prior to developing the radiative heat transfer model, some thermal radiation related parameters will be briefly introduced.

Parameters related to the thermal radiation

Thermal radiation related variables include the emissivity ε_r, absorptivity α_r, reflectivity ρ_r, and transmissivity τ_r, as defined in Eqs. (2-43) to (2-46), respectively. E is the irradiation (power per unit area) by a medium, while E_b is the irradiation by a blackbody at the same temperature. Since the radiative heat flux (E_{total}) from Medium 1 to Medium 2 shown in Figure 2-26 is either absorbed (E_α) by, reflected (E_ρ) by, or permeates (E_τ) through Medium 2, the sum of the absorptivity, reflectivity, and transmissivity should be unity (See Eq. (2-47)).

$$\varepsilon_r = \frac{E}{E_b} \tag{2-43}$$

$$\alpha_r = \frac{E_\alpha}{E_{total}} \tag{2-44}$$

$$\rho_r = \frac{E_\rho}{E_{total}} \tag{2-45}$$

$$\tau_r = \frac{E_\tau}{E_{total}} \tag{2-46}$$

$$\alpha_r + \rho_r + \tau_r = 1 \tag{2-47}$$

For a simplified analysis, it is assumed that the emissivity, absorptivity, reflectivity, and transmissivity depend on the wavelength λ, temperature T, and material species $M_{s,i}$:

$$\psi_r = \psi_r(\lambda, T, M_{s,i}) \tag{2-48}$$

where ψ_r can be ε_r, α_r, ρ_r, or τ_r.

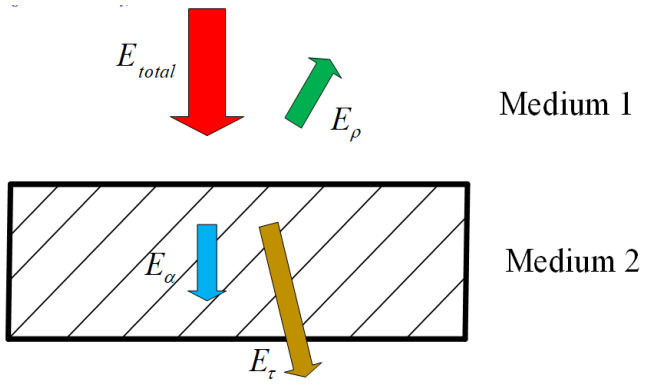

Figure 2-26 Schematic of the thermal radiation with two media

Figure 2-27 shows a schematic of the energy transfer process from photons emitted from a planar Medium 1 to the planar wall surface of Medium 2 assuming no scattering in Medium 1. It is also assumed that Media 2 and 3 are sufficiently thick and therefore no spectral transmission is considered, i.e., $\tau_{r2} = \tau_{r3} = 0$. The emitted photons from Media 1 to 2 undergo the following steps:

(1) Medium 1 emits photons with a radiative heat flux of E_1 (corresponding to a wavelength λ_1) to Medium 2;

(2) A fraction of the initial photons are absorbed by Medium 2 and the deposited energy per unit area in Medium 2 is $\alpha_2 E_1$;

(3) The remaining photons are reflected by Medium 2 with a radiative heat flux of $\rho_2 E_1$;

(4) These photons are partially absorbed by Medium 1 with a deposited energy per unit area in Medium 1 of $\alpha_1 \rho_2 E_1$;

(5) Some photons are reflected by Medium 1 with a radiative heat flux of $\rho_1 \rho_2 E_1$. Similar to the initial photons in Step (1), these photons can be further absorbed and reflected by Medium 2 and undergo Steps (2) to (8);

(6) Other photons further permeate through Medium 1 with a radiative heat flux of $\tau_1 \rho_2 E_1$;

(7) The permeated photons are partially absorbed by Medium 3 with a deposited energy per unit area of $\alpha_3\tau_1\rho_2E_1$;

(8) The rest of these permeated photons are reflected by Medium 3 with a radiative heat flux of $\tau_1\rho_2\rho_3E_1$. Similar to photons in Step (3), these photons can permeate, be absorbed and reflected by Medium 1, and undergo Steps (4) to (8);

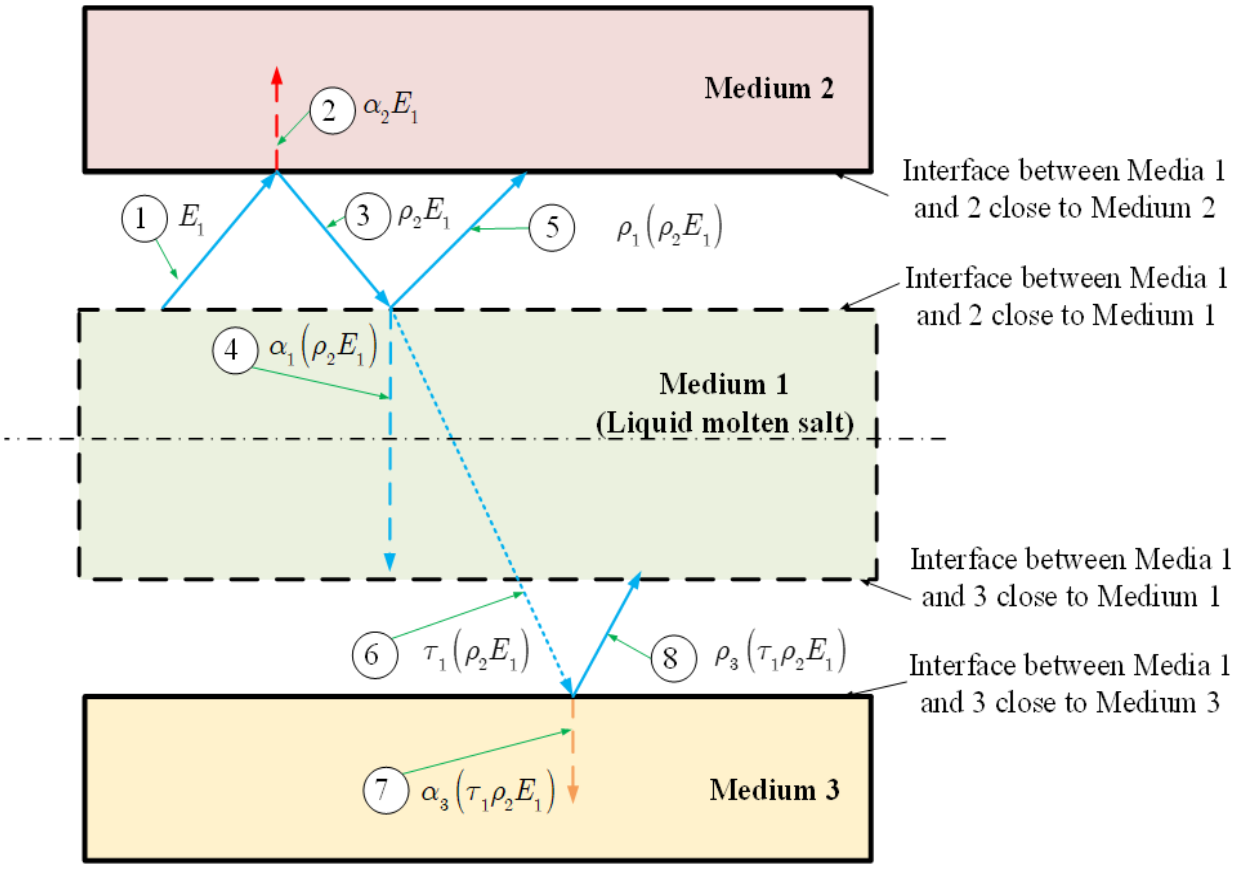

Figure 2-27 Schematic of the energy transfer process from photons emitted from a planar Medium 1 to a planar Medium 2 ($0 < \alpha_1, \rho_1, \tau_1 < 1$)

The emitted photons from Media 1 to 3 undergo the similar steps in Figure 2-27. Since photons could permeate through, and be absorbed and reflected by Medium 1, the net radiative heat flux among Media 1, 2, and 3 becomes complicated. However, molten salts exhibit nearly zero reflectivity or transmissivity in certain wavelength intervals (Li, 1979), which makes the development of a simplified radiative heat transfer model become feasible. Therefore, two cases, namely (1) zero reflectivity and (2) zero transmissivity of Medium 1, will be discussed to compute the net radiative heat flux from Media 1 to 2 and 3.

Zero reflectivity of Medium 1 ($\rho_1 = 0$)

Figure 2-28 shows the radiative heat transfer process among the planar Media 1, 2, and 3 if the reflectivity of Medium 1 is zero. Photons emitted by Medium 1 with a radiative heat flux of E_1 as shown in Figure 2-28(a) are absorbed and reflected by Medium 2. The reflected photons are partially absorbed by Medium 1 while the remaining photons permeate through Medium 1. Then a fraction of the permeated photons are absorbed by Medium 3 while the rest is reflected back to Medium 1. Some of these photons are absorbed by Medium 1 while others further permeate through Media 1 to 2, which complete one cycle. Photons emitted by Medium 2 with a radiative heat flux of E_2 as shown in Figure 2-28(b) are partially absorbed by Medium 1 while the rest permeate through Medium 1. A fraction of these permeated photons are absorbed by Medium 3 while the rest is reflected. Then some of these reflected photons are absorbed by Medium 1 while the others further permeate through Medium 1 and reach Medium 2 to complete one cycle.

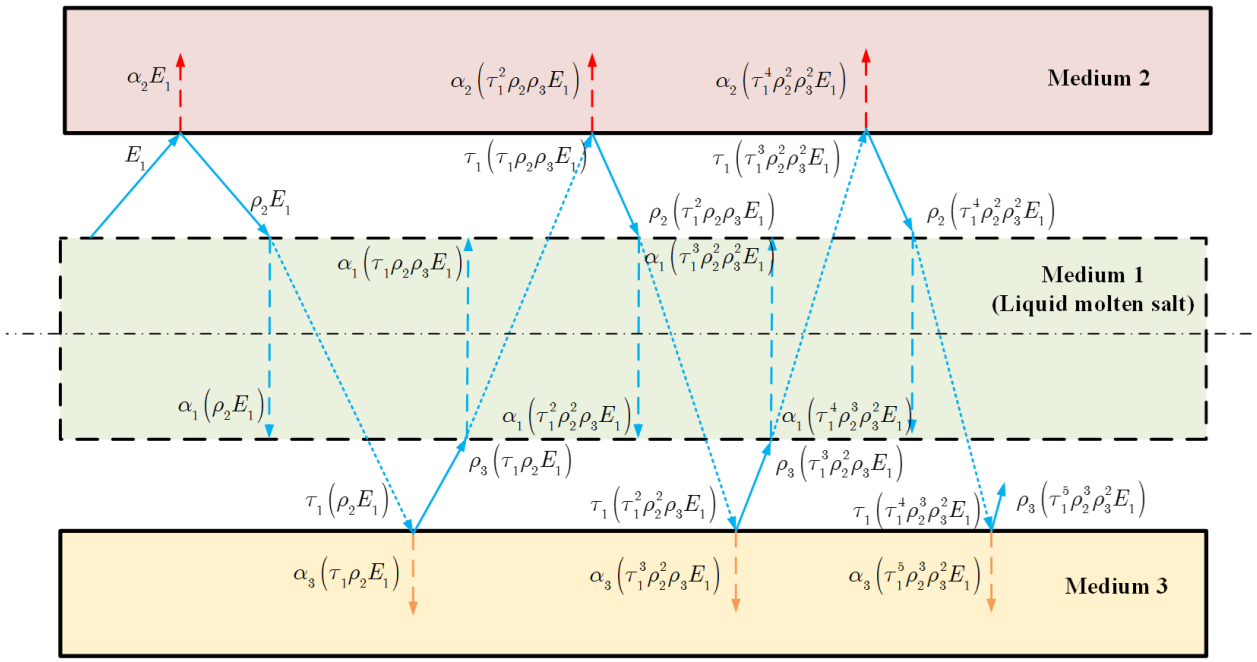

(a)

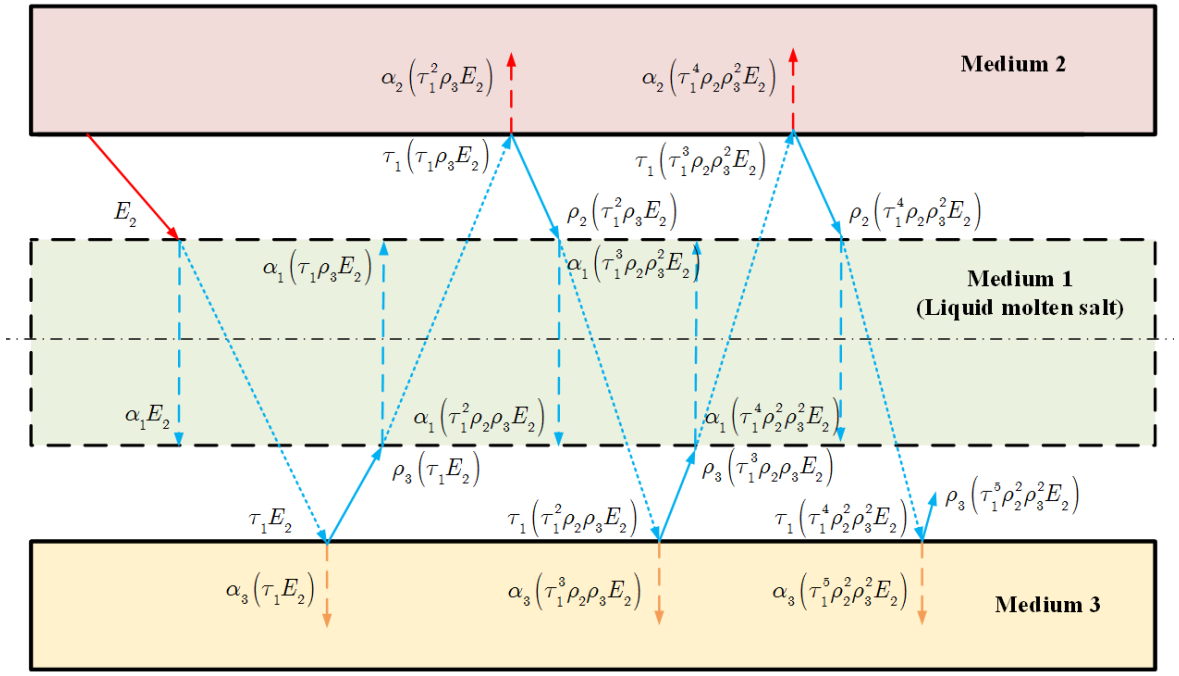

(b)

Figure 2-28 Schematic of the energy transfer process: (a) Photons emitted from Media 1 to 2 and (b) Photons emitted from Media 2 to 1 ($\rho_1 = 0$)

The net radiative heat flux from Media 1 to 2 and 3 can be given by

$$E_{1-2\&3}(\rho_1 = 0) = 2E_1 - \alpha_1 \frac{(1+\tau_1\rho_3)(\rho_2 E_1 + E_2) + (1+\tau_1\rho_2)(\rho_3 E_1 + E_3)}{1-\tau_1^2\rho_2\rho_3} \tag{2-49}$$

A detailed derivation of Eq. (2-49) is summarized in the Appendix. Although Eq. (2-49) is derived to estimate the net radiative heat flux for a system of three infinite planar media, it could be modified for a two-medium system, i.e., a molten salt flowing in a tube/pipe. By treating Media 2 and 3 as one medium, the net radiative heat flux from the molten salt to the outside tube/pipe can be estimated by

$$E_{s-t}(\rho_s = 0) = \varepsilon_s E_{bs} - \alpha_s \frac{\rho_t \varepsilon_s E_{bs} + \varepsilon_t E_{bt}}{1-\tau_s\rho_t} \tag{2-50}$$

where $E_2 = E_3 = E_t$ and $\rho_2 = \rho_3 = \rho_t$ are assumed. This equation is in a wavelength-independent form for the net radiative heat flux. Since the radiation related parameters depend on the wavelength, it is necessary to estimate the net radiative heat flux per a certain wavelength (also called the spectral emissive power), which can be written as

$$E_{s-t,\lambda}(\rho_{\lambda,s} = 0) = \varepsilon_{\lambda,s} E_{b\lambda,s} - \alpha_{\lambda,s} \frac{\rho_{\lambda,t}\varepsilon_{\lambda,s} E_{b\lambda,s} + \varepsilon_{\lambda,t} E_{b\lambda,t}}{1-\tau_{\lambda,s}\rho_{\lambda,t}} \tag{2-51}$$

The overall net radiative heat flux from the molten salt to the tube/pipe is an integral of the spectral emissive power over the entire range of the associated wavelengths as

$$E_{s-t,all}(\rho_{\lambda,s} = 0) = \int_0^\infty E_{s-t,\lambda}(\rho_{\lambda,s} = 0)\, \mathrm{d}\lambda \tag{2-52}$$

Zero transmissivity of Medium 1 ($\tau_1 = 0$)

Figure 2-29 shows the radiative heat transfer process among planar Media 1, 2, and 3 if the transmissivity of Medium 1 is set to be zero. The photons emitted by Medium 1 with a radiative

heat flux of E_1 as shown in Figure 2-29(a) are absorbed and reflected by Medium 2. The reflected photons are partially absorbed by Medium 1 while the remaining photons are reflected to Medium 2 to complete one cycle. The photons emitted by Medium 2 with a radiative heat flux of E_2 as shown in Figure 2-29(b) are partially absorbed while the rest is reflected by Medium 1. A fraction of these reflected photons are absorbed by Medium 2 while the rest is reflected back to Medium 1 to complete one cycle.

The net radiative heat flux from Media 1 to 2 and 3 is given by

$$E_{1-2\&3}(\tau_1 = 0) = 2E_1 - \alpha_1 \left[\frac{\rho_2 E_1 + E_2}{1-\rho_1\rho_2} + \frac{\rho_3 E_1 + E_3}{1-\rho_1\rho_3}\right] \tag{2-53}$$

A detailed derivation of Eq. (2-53) is summarized in the Appendix. By treating Media 2 and 3 as one medium, the net radiative heat flux from the molten salt to the outside tube/pipe can be estimated by

$$E_{s-t}(\tau_s = 0) = \varepsilon_s E_{bs} - \alpha_s \frac{\rho_t \varepsilon_s E_{bs} + \varepsilon_t E_{bt}}{1-\rho_s\rho_t} \tag{2-54}$$

where $E_2 = E_3 = E_t$ and $\rho_2 = \rho_3 = \rho_t$ are assumed. The corresponding spectral emissive power is therefore written as

$$E_{s-t,\lambda}(\tau_{\lambda,s} = 0) = \varepsilon_{\lambda,s} E_{b\lambda,s} - \alpha_{\lambda,s} \frac{\rho_{\lambda,t} \varepsilon_{\lambda,s} E_{b\lambda,s} + \varepsilon_{\lambda,t} E_{b\lambda,t}}{1-\rho_{\lambda,s}\rho_{\lambda,t}} \tag{2-55}$$

The overall net radiative heat flux from the molten salt to the tube/pipe is an integral of the spectral emissive power over the entire range of the associated wavelengths as:

$$E_{s-t,all}(\tau_{\lambda,s} = 0) = \int_0^\infty E_{s-t,\lambda}(\tau_{\lambda,s} = 0)\, \mathrm{d}\lambda \tag{2-56}$$

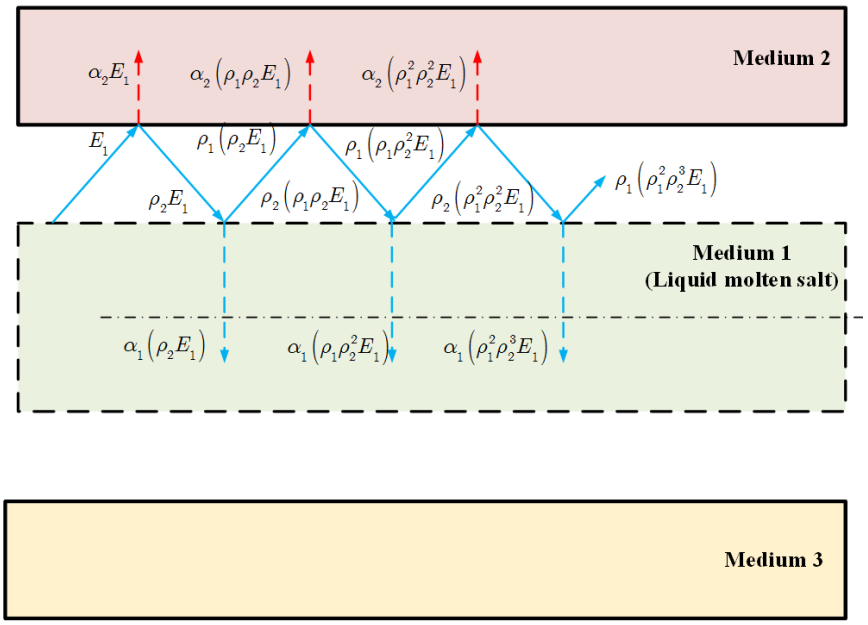

(a)

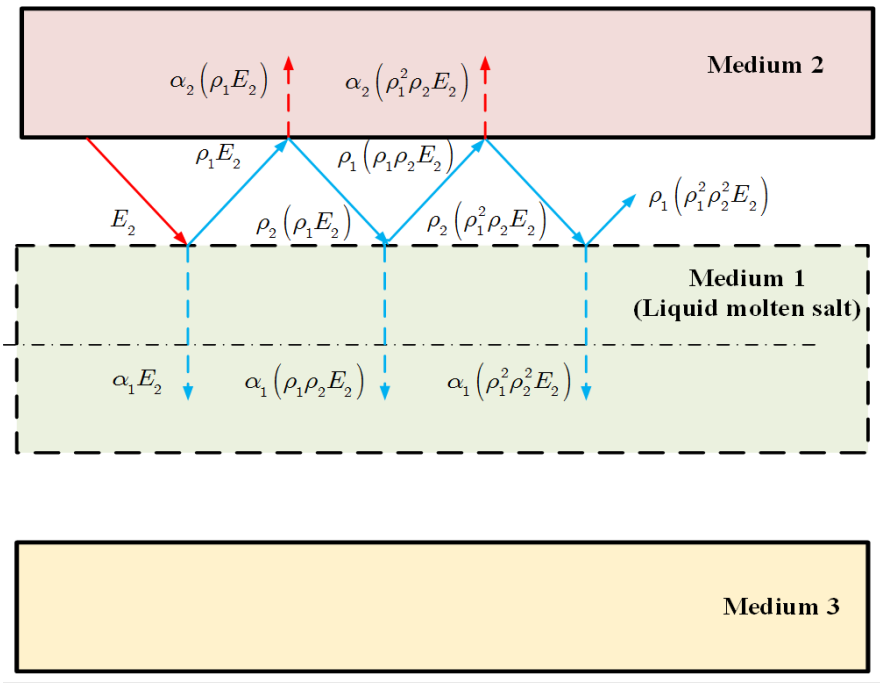

(b)

Figure 2-29 Schematic of the energy transfer process: (a) Photons emitted from Media1 to 2 and (b) Photons emitted from Media 2 to 1 ($\tau_1 = 0$)

Net radiative heat flux

The net radiative heat flux from the molten salt to the outside tube/pipe can be estimated by Eq. (2-52) if $\rho_{\lambda,s} = 0$ or Eq. (2-56) if $\tau_{\lambda,s} = 0$. By applying:

(1) Kirchhoff's law, $\varepsilon_{\lambda,s} = \alpha_{\lambda,s}$ and $\varepsilon_{\lambda,t} = \alpha_{\lambda,t}$;

(2) Beer's law (neglecting scattering), $\tau_{\lambda,s} = e^{-k_{l,\lambda}L}$, where $k_{l,\lambda}$ and L are the absorption coefficient at a certain wavelength and the path length, respectively. L can be estimated by the mean beam length L_m for an arbitrary geometry;

(3) $\alpha_{\lambda,s} + \rho_{\lambda,s} + \tau_{\lambda,s} = 1$;

(4) $\alpha_{\lambda,t} + \rho_{\lambda,t} = 1$

for Eq. (2-52), the net radiative heat flux from the molten salt to the outside pipe can be written, if $\rho_{\lambda,s} = 0$, as:

$$E_{s-t,all}(\rho_{\lambda,s}=0) = \int_0^\infty \varepsilon_{\lambda,t}(1-e^{-k_{l,\lambda}L_m})\frac{E_{b\lambda,s}-E_{b\lambda,t}}{1-(1-\varepsilon_{\lambda,t})e^{-k_{l,\lambda}L_m}}\,\mathrm{d}\lambda \tag{2-57}$$

Similarly, applying these conditions, except Beer's law, to Eq. (2-56), the net radiative heat flux from the molten salt to the outside pipe can be written, if $\tau_{\lambda,s} = 0$, as:

$$E_{s-t,all}(\tau_{\lambda,s}=0) = \int_0^\infty \varepsilon_{\lambda,t}(1-\rho_{\lambda,s})\frac{E_{b\lambda,s}-E_{b\lambda,t}}{1-\rho_{\lambda,s}(1-\varepsilon_{\lambda,t})}\,\mathrm{d}\lambda \tag{2-58}$$

A number of variables, i.e., L_m, $k_{l,\lambda}$, $\rho_{\lambda,s}$, $\varepsilon_{\lambda,t}$, $E_{b\lambda,s}$, and $E_{b\lambda,t}$, need to be known, which have been discussed in detail in the literature (Zhang and Sun, 2020b). Utilizing Eq. (2-41), the salt Nusselt number due to the radiative heat transfer for zero reflectivity and transmissivity cases can be respectively written as:

$$\mathrm{Nu}_r\left(\rho_{\lambda,s}=0\right)=\frac{D_i\int_0^\infty \varepsilon_{\lambda,t}\left(1-e^{-0.9k_{l,\lambda}D_i}\right)\frac{E_{b\lambda,s}-E_{b\lambda,t}}{1-\left(1-\varepsilon_{\lambda,t}\right)e^{-0.9k_{l,\lambda}D_i}}\mathrm{d}\lambda}{k_s\left(T_f-T_w\right)} \tag{2-59}$$

$$\mathrm{Nu}_r\left(\tau_{\lambda,s}=0\right)=\frac{D_i\int_0^\infty \varepsilon_{\lambda,t}\left(1-\rho_{\lambda,s}\right)\frac{E_{b\lambda,s}-E_{b\lambda,t}}{1-\rho_{\lambda,s}\left(1-\varepsilon_{\lambda,t}\right)}\mathrm{d}\lambda}{k_s\left(T_f-T_w\right)} \tag{2-60}$$

2.4.2 Model Benchmark

The best way to validate the radiative heat transfer model is to compare it with the associated experiments, where the radiative heat transfer dominates. However, such experiments are currently unavailable. Therefore, the radiative heat transfer model developed in this study is benchmarked by comparing with the CFD results. Since the CFD study for the mixed convective heat transfer and combined mixed convective and radiative heat transfer have been performed, the following equation

$$\mathrm{Nu}_r=\mathrm{Nu}_t-\mathrm{Nu}_c \tag{2-61}$$

is then used to obtain the Nusselt number Nu_r due to the radiative heat transfer from the CFD results, where Nu_c and Nu_t are the Nusselt numbers due to the mixed convective heat transfer and combined mixed convective and radiative heat transfer, respectively.

Figure 2-30 shows the code benchmark study by comparing the CFD predictions with the in-house radiative heat transfer model results. It is observed that the discrepancy is within 15%. It is mainly due to the fact that the radiative heat transfer is a three-dimensional effect. In the current study, the in-house radiative heat transfer model will be incorporated in the 1D code NACCO to predict the thermal-hydraulic performance of molten salts in natural circulation loops in Chapter 3.

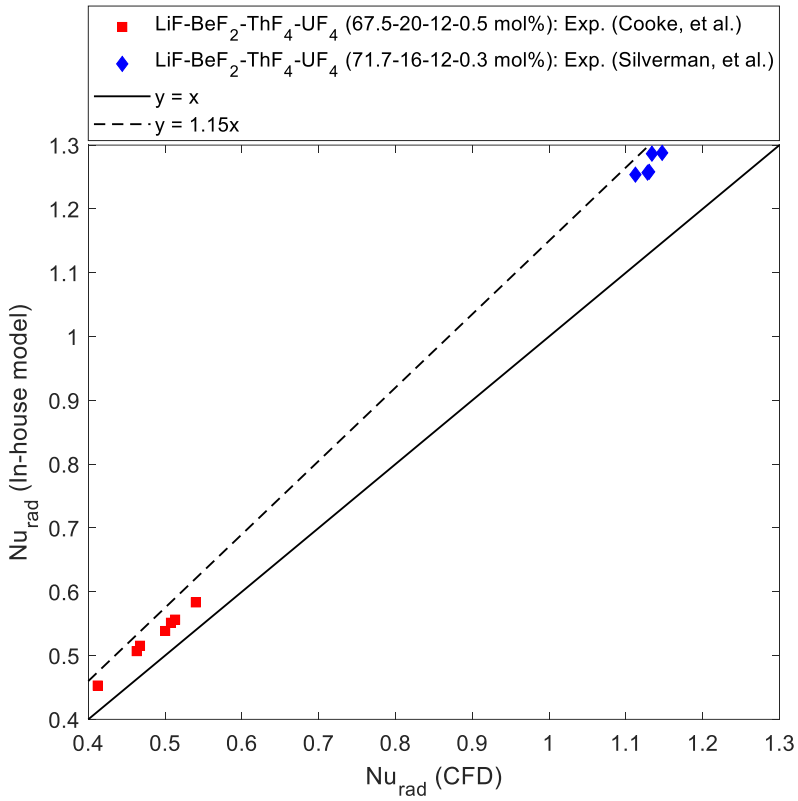

Figure 2-30 Validation of the radiative heat transfer model

2.4.3 Sensitivity Study

The effects of various variables, including the pipe ID (5 to 50 mm), salt temperature (500 to 1000 ˚C), salt and wall temperature difference (5 to 100 ˚C), and salt absorption coefficient (1 to 100 m^{-1}), will be investigated for fully-developed flows of FLiNaK.

Effect of the pipe ID under different Reynolds numbers for fully-developed flows

Figure 2-31 shows the heat transfer coefficient of FLiNaK under different salt Reynolds numbers. The radiative heat transfer coefficient estimated by the developed radiative heat transfer model is 28.5 W/(m^2-K) under the conditions investigated (D_i = 50 mm, $\Delta T = T_{salt} - T_w$ = 10 ˚C, T_{salt} = 700 ˚C). In addition, the convective heat transfer coefficient is kept at 66.7 W/(m^2-K) for Re

< 2,300 under fully-developed flow and constant wall temperature conditions (Nu = 3.66), while it increases to 1309.3 W/(m^2-K) for Re = 10,000.

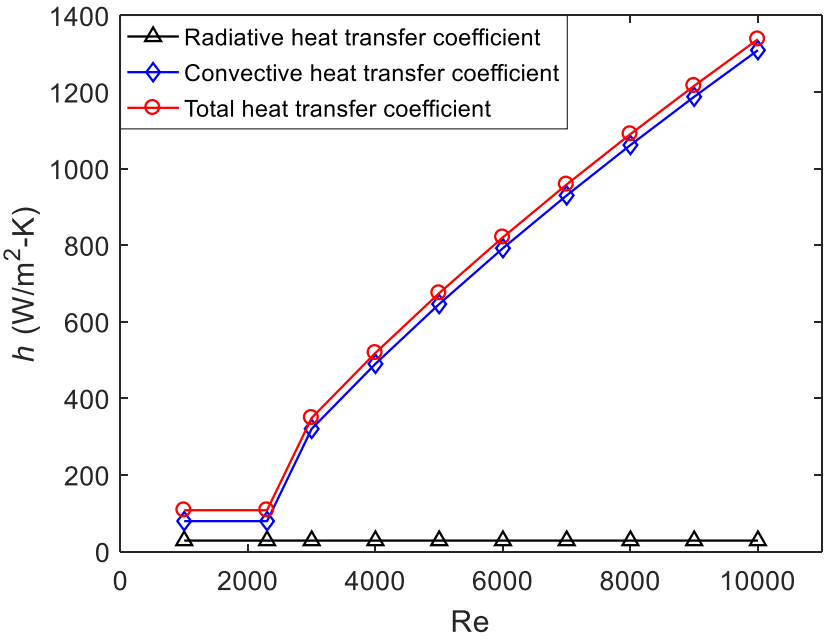

Figure 2-31 Relationship between the heat transfer coefficient and salt Reynolds number (D_i = 50 mm, $\Delta T = T_{salt} - T_w$ = 10 ˚C, T_{salt} = 700 ˚C)

Figure 2-32 shows the effects of the pipe ID on the thermal radiation effect factor. The thermal radiation effect factor keeps constant for Re ≤ 2,300 at ΔT = 10 ˚C and T_{salt} = 700 ˚C, but it significantly decreases for Re > 2,300. This is because the radiative heat transfer coefficient keeps constant for Re = 1,000 – 10,000 under the conditions investigated (ΔT = 10 ˚C and T_{salt} = 700 ˚C), while the convective heat transfer coefficient is initially a constant for Re ≤ 2,300 but it increases significantly for Re > 2,300. The radiative heat transfer is therefore more important for laminar flows than transitional flows under the conditions investigated. Compared with laminar and transitional flows, the thermal radiation effect factor for turbulent flows is smaller due to the

larger convective heat transfer coefficient. As an example, the radiative heat transfer rate represents 29.9% of the total heat transfer rate for a laminar flow in a 50-mm ID pipe under the specified conditions in Figure 2-32. However, it significantly decreases to 2.1% for Re = 10,000.

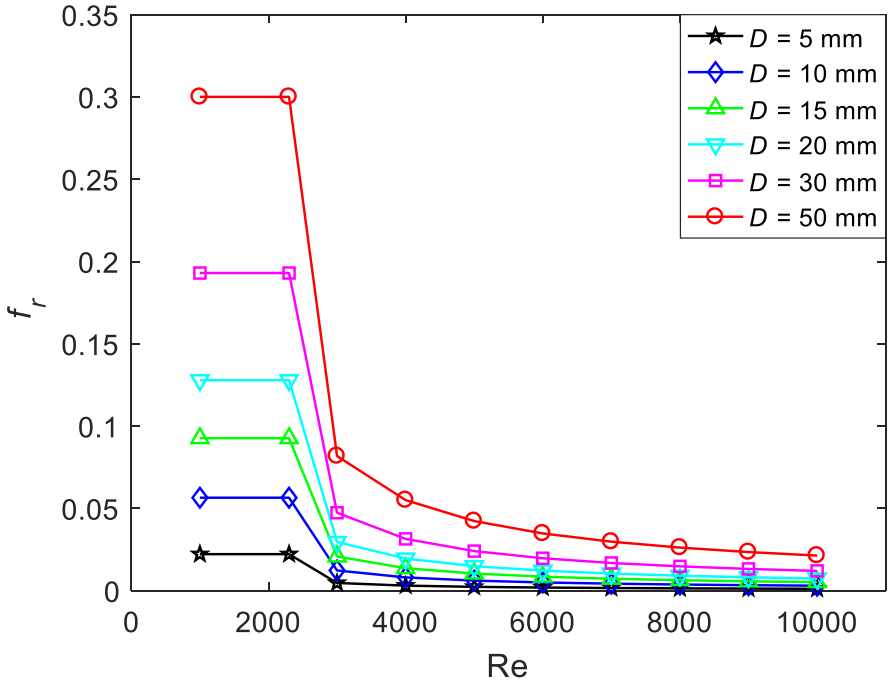

Figure 2-32 Relationship between the thermal radiation effect factor, salt Reynolds number, and pipe ID ($\Delta T = T_{salt} - T_w = 10\ ^\circ\text{C}$, $T_{salt} = 700\ ^\circ\text{C}$)

In addition to the salt Reynolds number, the pipe size has an important effect on the radiative heat transfer as well. The thermal radiation effect factor is 2.2% for laminar flows in a 5-mm ID pipe, which is significantly small compared to 29.9% in a 50-mm ID pipe. This is because the distance for the light travelling through the molten salt is longer in larger ID pipes, where the salt absorbs more radiant heat per unit time.

Effects of the pipe ID and salt temperature for fully-developed laminar flows

Figure 2-33 shows the effects of the pipe ID and salt temperature on the thermal radiation effect factor. For a certain pipe ID, i.e., 50 mm, the thermal radiation effect factor is 21.3% at T_{salt} = 500 ˚C, while 42.2% at T_{salt} = 1000 ˚C. For a certain salt temperature, i.e., 1000 ˚C, the thermal radiation effect factor increases from 3.4% at D_i = 5 mm to 42.2% at D_i = 50 mm. As the increase of the pipe ID from 5 to 50 mm at T_{salt} = 1000 ˚C, the radiative heat transfer coefficient increases from 31.0 to 63.7 W/(m^2-K) as shown in Figure 2-34. Therefore, the radiative heat transfer is more important for flows in larger ID pipes under the conditions investigated.

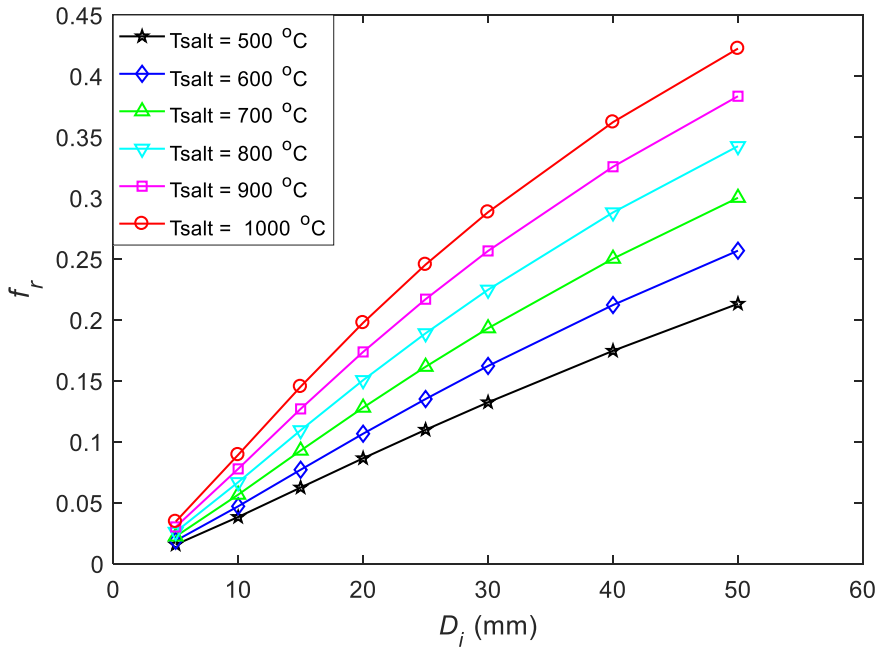

Figure 2-33 Relationship between the thermal radiation effect factor, pipe ID, and salt temperature (ΔT = 10 ˚C, laminar flow Nu = 3.66)

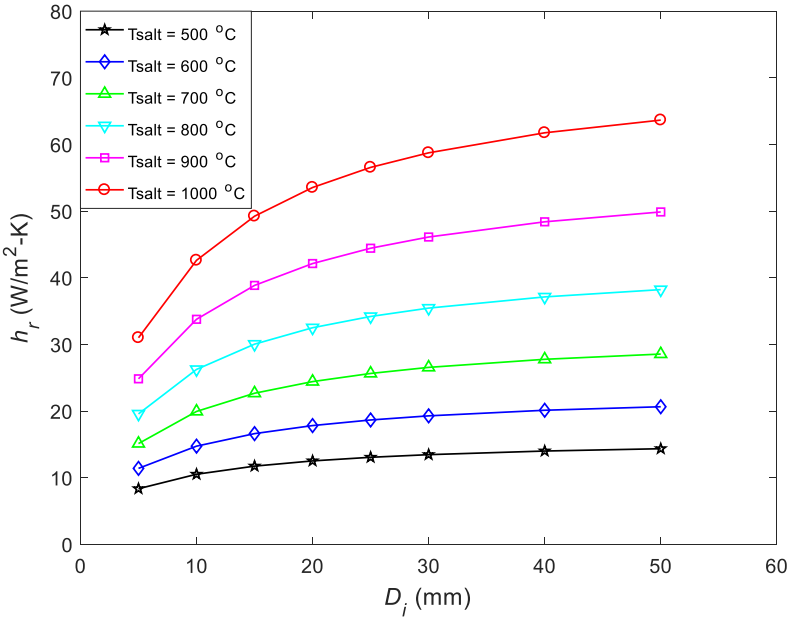

Figure 2-34 Relationship between the radiative heat transfer coefficient, pipe ID, and salt temperature (ΔT = 10 °C, laminar flow Nu = 3.66)

Effects of the salt and wall temperature difference, and salt temperature for fully-developed laminar flows

Figure 2-35 shows the effects of the salt and wall temperature difference, and salt temperature on the thermal radiation effect factor. For a certain salt and wall temperature difference, i.e., ΔT = 5 °C, the thermal radiation effect factor increases from 3.9% at T_{salt} = 500 °C to 9.0% at T_{salt} = 1000 °C. For a certain salt temperature, i.e., 1000 °C, the thermal radiation effect factor decreases from 9.0% to 8.1% as the salt and wall temperature difference is increased from 5 to 100 °C. This is mainly due to the decrease of the radiative heat transfer coefficient as shown in Figure 2-36. For example, the radiative heat transfer coefficient decreases from 42.9 to 38.6 W/(m^2-K) at T_{salt} = 1000 °C when the salt and wall temperature difference is increased from 5 to 100 °C. Therefore, the salt and wall temperature difference has a relatively small effect on the radiative heat transfer under the conditions investigated.

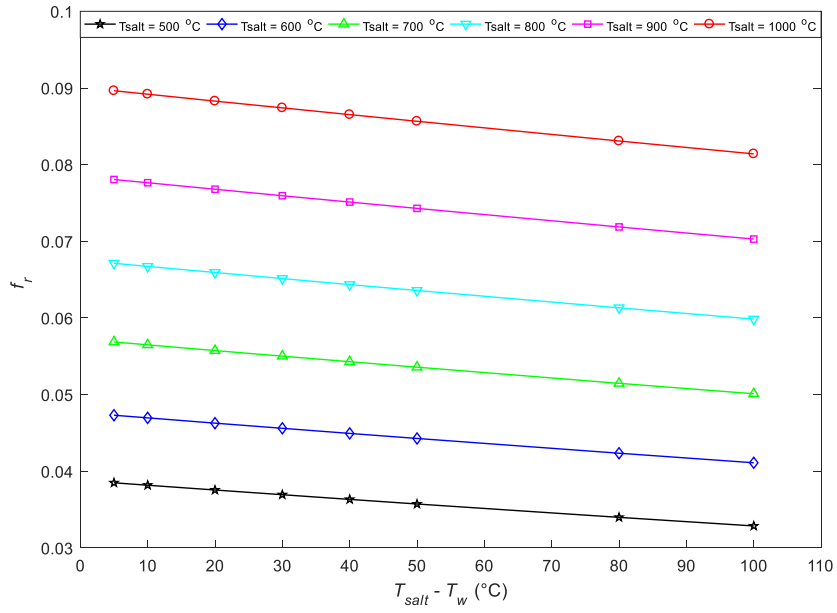

Figure 2-35 Relationship between the thermal radiation effect factor, salt and wall temperature difference, and salt temperature (D_i = 10 mm, laminar flow Nu = 3.66)

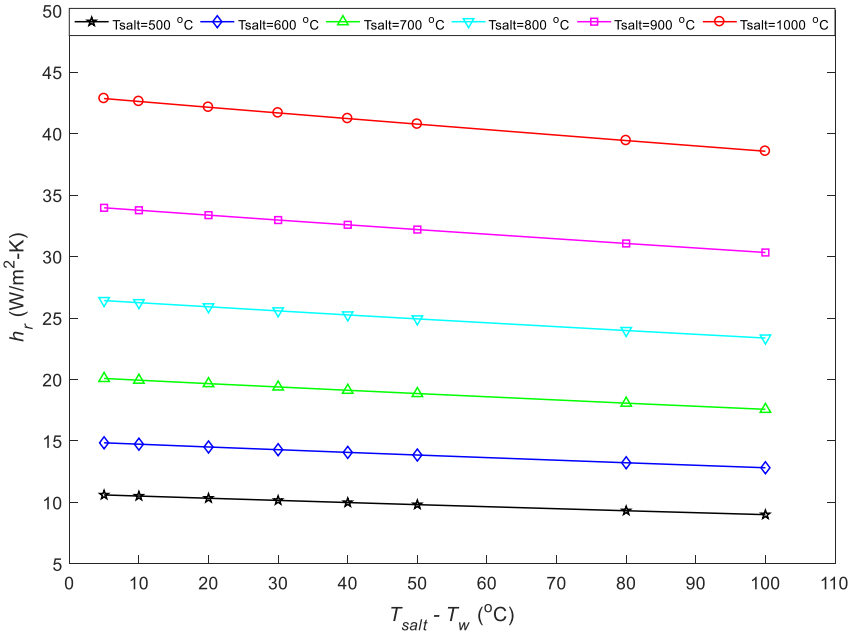

Figure 2-36 Relationship between the radiative heat transfer coefficient, salt and wall temperature difference, and salt temperature (D_i = 10 mm, laminar flow Nu = 3.66)

Effect of the salt absorption coefficient in the IR region

Figure 2-37 shows the effect of the salt absorption coefficient on the thermal radiation effect factor. As the increase of the salt impurity level, the salt absorption coefficient increases due to the addition of the impurities. The thermal radiation effect factor significantly increases from 1.2 to 12.6% at T_{salt} = 1000 °C when the salt absorption coefficient is increased from 1 to 100 m^{-1}. Therefore, the salt absorption coefficient has a relatively large effect on the radiative heat transfer under the conditions investigated.

It should be noted that the impurity level in the salts increases as the increase of the corrosion products, such as CrF_2 (Chaleff et al., 2016). Therefore, the radiative heat transfer or thermal radiation effect factor becomes larger for a salt loop with increased corrosion. In other words, even if it is acceptable to initially neglect the radiative heat transfer in the salts, it may need to be considered due to severe corrosion after a certain period of operation.

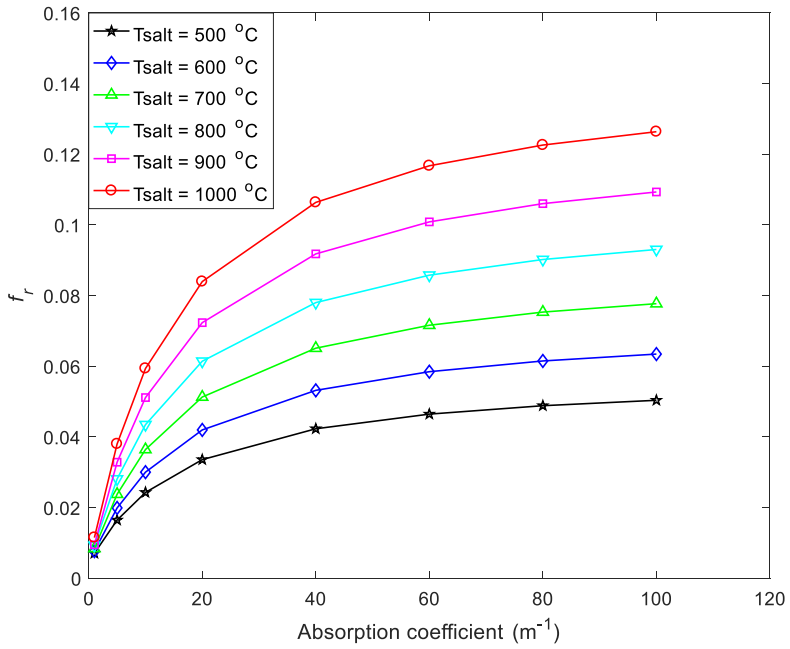

Figure 2-37 Relationship between the thermal radiation effect factor, salt absorption coefficient, and salt temperature (D_i = 10 mm, ΔT = 10 °C, laminar flow Nu = 3.66)

2.5 Summary

This section numerically investigated heat transfer and friction characteristics of molten salts in straight circular pipes using a CFD tool, STAR-CCM+. The numerical results were validated by comparing with (1) modified experimental data using more accurate and consistent thermophysical properties of molten salts and (2) widely used correlations for forced convective heat transfer and friction factor. It has been identified that the effects of buoyancy and radiative heat transfer are generally non-negligible for laminar flows of molten salts.

In addition, a radiative heat transfer model was developed to quantitatively evaluate the effect of the radiative heat transfer for different conditions of (1) pipe size (circular pipe ID from 5 to 50 mm), (2) salt temperature (500 to 1000 $^{\circ}$C), (3) salt and wall temperature difference (5 to 100 $^{\circ}$C), and (4) salt absorption coefficient (1 to 100 m^{-1}).

Several concluding remarks are summarized as follows:

(1) Both the hydrodynamic and thermal entrance lengths for laminar and turbulent flows of molten salts could be preliminarily estimated by Eqs. (2-23) to (2-27). The discrepancy between the correlation results and CFD predictions ranged from 9.6% to 35%;

(2) The friction factor of molten salts in the fully-developed laminar flow regime could be appropriately estimated by a CFD analysis and conventional correlation, Eq. (2-28). The maximum discrepancies by comparing the CFD and correlation results with the majority of the experimental data were ±6.3% and ±18.8%, respectively. However, the friction factor values for fully-developed turbulent flows of molten salts estimated by STAR-CCM+ and correlations, Eqs. (2-29) and (2-30), were in general much lower (< 38%) than the experimental data. The large discrepancy most likely resulted from the increased roughness of the pipe inner surface, which was due to corrosion of the pipe material in the salt

environment at elevated temperatures; If a relative roughness $\varepsilon/D = 3\times10^{-3}$ is adopted in Eq. (2-31) to consider the increased surface roughness due to corrosion, the discrepancy between the correlation results and the experimental data will decrease to 23.6%;

(3) For molten salt heat transfer in laminar and turbulent flow regimes, the Nusselt number estimated by STAR-CCM+ was within ±20% uncertainties of convective heat transfer correlations, including the Dittus-Boelter, Gnielinski, and Sieder-Tate correlations.

(4) The Dittus-Boelter correlation predicted the molten salt heat transfer coefficient with ±20% uncertainties for $10{,}000 \leq Re \leq 50{,}000$ and $4 \leq Pr \leq 12$;

(5) The Gnielinski correlation predicted the molten salt heat transfer coefficient with ±20% uncertainties for $2{,}300 \leq Re \leq 50{,}000$ and $4 \leq Pr \leq 19$;

(6) The Sieder-Tate correlation for turbulent flows predicted the molten salt heat transfer coefficient with ±20% uncertainties for $10{,}000 \leq Re \leq 120{,}000$ and $4 \leq Pr \leq 27$, while the Sieder-Tate correlation for laminar flows underestimated the fuel salt heat transfer coefficient by 27% and 40% for the nitrate salt heat transfer coefficient for $400 \leq Re \leq 2{,}300$ and $5 \leq Pr \leq 16$. Two potential reasons were proposed as the entrance effect underestimated by the Sieder-Tate (laminar) correlation and incapability of the Sieder-Tate (laminar) correlation to include the effects of buoyancy and radiative heat transfer in the salts. These two reasons were later justified by a CFD study considering the entrance effect, buoyancy effect, and radiative heat transfer effect;

(7) The Hausen correlation predicted the molten salt heat transfer coefficient with ±20% uncertainties for $5{,}000 \leq Re \leq 50{,}000$ and $4 \leq Pr \leq 27$, while ±40% uncertainties for $2{,}300 \leq Re \leq 5{,}000$ and $4 \leq Pr \leq 27$;

(8) The radiative heat transfer was identified to be more important for laminar flows than transitional and turbulent flows under the conditions investigated. As an example, the radiative heat transfer rate for the FLiNaK salt in a pipe (D_i = 50 mm, T_{salt} = 700 °C, and ΔT = 10 °C) represented 29.9% of the total heat transfer rate for fully-developed laminar flows while it became less than 8.2% for transitional and turbulent flows;

(9) The radiative heat transfer was identified to be more important for larger ID pipes under the conditions investigated. As an example, the radiative heat transfer rate represented 2.2% of the total heat transfer rate for fully-developed salt flow in a 5-mm ID pipe while 29.9% for flow in a 50-mm ID pipe (Re ≤ 2,300, T_{salt} = 700 °C, and ΔT = 10 °C);

(10) The salt temperature, as compared with the temperature difference between the salt and wall, was identified to have a larger effect on the radiative heat transfer for the conditions investigated. The radiative heat transfer rate increased from 3.9% to 9.0% of the total heat transfer rate as the salt temperature increased from 500 °C to 1000 °C for fully-developed laminar flows (Re ≤ 2,300, D_i = 10 mm, and ΔT = 10 °C). However, a much smaller change was observed for the radiative heat transfer rate as the temperature difference between the salt and wall varied from 5 °C to 100 °C (Re ≤ 2,300, D_i = 10 mm, and T_{salt} = 1000 °C);

(11) The salt absorption coefficient was identified to have a relatively large effect on the radiative heat transfer for laminar flows. The radiative heat transfer rate increased significantly from 1.2% to 12.6% of the total heat transfer rate as the salt absorption coefficient increased from 1 m^{-1} to 100 m^{-1} for fully-developed laminar flows (Re ≤ 2,300, D_i =10 mm, T_{salt} = 1000 °C, and ΔT = 10 °C).

Chapter 3 Natural Circulation of Molten Salts in a Single Loop

The heat transfer and friction characteristics of molten salts in straight circular pipes are numerically investigated in Chapter 2. It has been identified that the effects of buoyancy and radiative heat transfer are non-negligible especially for laminar flows of molten salts. In this chapter, both the buoyancy effect and radiative heat transfer effect will be investigated for molten salts in a single natural circulation loop.

3.1 Development of the 1D Code NACCO for a Single Natural Circulation Loop

A 1D code NACCO will be developed in this section to predict the thermal-hydraulic performance of a single molten salt natural circulation loop, which consists of a horizontal heating section at the bottom, a horizontal cooling section at the top, and two vertical sections connecting the heating and cooling sections. Figure 3-1 shows a schematic of the single natural circulation loop. The heating section includes the working fluid (Fluid I), piping, heater, and thermal insulation, while the cooling section consists of Fluid I, piping, Fluid II, and thermal insulation. Fluid I is assumed to be a semi-transparent fluid, while Fluid II is a totally transparent fluid to thermal radiation. In addition, the bottom surface heater is assumed to have a negligible volume. The heat loss rate from the thermal insulation to the ambient air due to both natural convection and thermal radiation is considered in the 1D code NACCO. In addition, the radiative heat transfer in Fluid I in heating and cooling sections is considered as well.

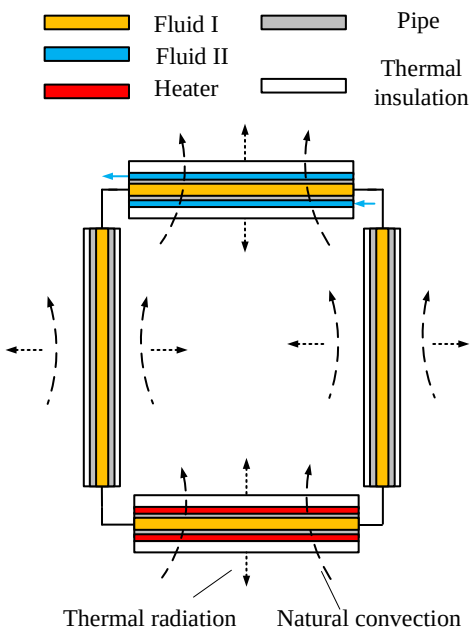

Figure 3-1 Schematic of a single natural circulation loop

The energy balance equation for Fluid I in the loop is written as

$$c_{p,fI} m_{fI} \frac{\mathrm{d}T_{fI}}{\mathrm{d}t} = h_{it,all} A_{iw} \left(T_t - \frac{T_{fI,in} + T_{fI,out}}{2} \right) + c_{p,fI} \dot{m}_{fI} \left(T_{fI,in} - T_{fI,out} \right) \tag{3-1}$$

where $c_{p,fI}, m_{fI}, \dot{m}_{fI}, h_{it,all}, A_{iw}, T_t, T_{fI}, T_{fI,in}, T_{fI,out}$ and t are the specific heat of Fluid I, weight of Fluid I, mass flow rate of Fluid I, overall heat transfer coefficient on the tube/pipe inner surface, heat transfer area of the tube/pipe inner surface, temperature of the tube/pipe surface, temperature of Fluid I, inlet and outlet temperatures of Fluid I, and time, respectively.

The overall heat transfer coefficient on the tube/pipe inner surface is evaluated by

$$h_{it,all} = \frac{(\mathrm{Nu}_c + \mathrm{Nu}_r) k_{fI}}{D_{it}} \tag{3-2}$$

where k_{fI}, and D_{it} are the thermal conductivity of Fluid I and tube/pipe inner diameter, respectively. The convective Nusselt number Nu_c can be estimated by the correlations identified

to be appropriate for molten salt applications (Zhang et al., 2020a), while the radiative Nusselt number Nu_r is estimated by the radiative heat transfer model developed earlier. If Fluid I is a medium transparent to thermal radiation, the Nusselt number Nu_r is then set to be zero.

The energy balance equation for Fluid II in the cooling section is written as

$$c_{p,fII} m_{fII} \frac{\mathrm{d}T_{fII}}{\mathrm{d}t} = h_{ot} A_{ow} \left(T_t - \frac{T_{fII,in} + T_{fII,out}}{2} \right) + h_{ish} A_{ish} \left(T_{sh} - \frac{T_{fII,in} + T_{fII,out}}{2} \right) + c_{p,fII} \dot{m}_{fII} \left(T_{fII,in} - T_{fII,out} \right) \quad (3\text{-}3)$$

where $c_{p,fII}, m_{fII}, \dot{m}_{fII}, h_{ot}, h_{ish}, A_{ow}, A_{ish}, T_{sh}, T_{fII}, T_{fII,in}$, and $T_{fII,out}$ are the specific heat of Fluid II, weight of Fluid II, mass flow rate of Fluid II, convective heat transfer coefficients on the outer surface of the inner tube and inner surface of the outer tube (shell), heat transfer areas of the outer surface of the inner tube and inner surface of the shell, shell surface temperature, Fluid II bulk temperature, and inlet and outlet temperatures of Fluid II, respectively.

It is assumed that the conductive thermal resistance of the metal tube/pipe in the loop is negligible. The energy balance equation for the tube/pipe in the loop except the cooling section is written as

$$c_{p,t} m_t \frac{\mathrm{d}T_t}{\mathrm{d}t} = \dot{Q}_h - \frac{2\pi k_{ins} L_{ins} (T_{iins} - T_{oins})}{\ln(D_{oins}/D_{iins})} - h_{it,all} A_{iw} \left(T_t - \frac{T_{fI,in} + T_{fI,out}}{2} \right) \quad (3\text{-}4)$$

where $c_{p,t}, m_t, k_{ins}, L_{ins}, D_{iins}, D_{oins}, \dot{Q}_h, T_{iins}$, and T_{oins} are the specific heat of the tube, tube weight, thermal conductivity of the thermal insulation, axial length of the thermal insulation, inner and outer diameters of the thermal insulation, heating power, and temperatures on the inner and outer surfaces of the thermal insulation, respectively. The heating power $\dot{Q}_h$ in Eq. (3-4) is set to be the heater power for heating section, while $\dot{Q}_h = 0$ for hot and cold legs.

The energy balance equation for the tube/pipe in the cooling section is written as

$$c_{p,t}m_t\frac{\mathrm{d}T_t}{\mathrm{d}t} = h_{it,all}A_{iw}\left(\frac{T_{fI,in}+T_{fI,out}}{2} - T_t\right) - h_{ot}A_{ow}\left(T_t - \frac{T_{fII,in}+T_{fII,out}}{2}\right) - \frac{\sigma A_{ow}\left(T_t^4 - T_{sh}^4\right)}{\frac{1}{\varepsilon_t}+\frac{A_{ow}}{A_{ish}}\left(\frac{1}{\varepsilon_{sh}}-1\right)} \quad (3\text{-}5)$$

where σ, ε_t, and ε_{sh} are the Stefan-Boltzmann constant, tube emissivity, and shell emissivity, respectively.

The energy balance equation for the shell in the cooling section is written as

$$c_{p,sh}m_{sh}\frac{\mathrm{d}T_{sh}}{\mathrm{d}t} = \frac{\sigma A_{ow}\left(T_t^4 - T_{sh}^4\right)}{\frac{1}{\varepsilon_t}+\frac{A_{ow}}{A_{ish}}\left(\frac{1}{\varepsilon_{sh}}-1\right)} - h_{ish}A_{ish}\left(T_{sh} - \frac{T_{fII,in}+T_{fII,out}}{2}\right) - \frac{2\pi k_{ins}L_{ins}\left(T_{iins}-T_{oins}\right)}{\ln\left(D_{oins}/D_{iins}\right)} \quad (3\text{-}6)$$

where $c_{p,sh}$ and m_{sh} are the specific heat and weight of the cooler shell, respectively.

The energy balance equation for the thermal insulation is written as

$$c_{p,ins}m_{ins}\frac{\mathrm{d}T_{ins}}{\mathrm{d}t} = \frac{2\pi k_{ins}L_{ins}\left(T_{iins}-T_{oins}\right)}{\ln\left(D_{oins}/D_{iins}\right)} - h_{oins,all}A_{oins}\left(T_{oins} - T_{air}\right) - \varepsilon_{ins}\sigma A_{oins}\left(T_{oins}^4 - T_a^4\right) \quad (3\text{-}7)$$

where $c_{p,ins}, m_{ins}, h_{oins,all}$, $A_{oins}, \varepsilon_{ins}$, T_{air} and T_a are the specific heat, weight, overall heat transfer coefficient on the outer surface, outer surface area of the thermal insulation, emissivity of the thermal insulation, air temperature, and ambient temperature, respectively.

The integral momentum balance equation for Fluid I in the entire loop is written as

$$\frac{\mathrm{d}\dot{m}_{fI}}{\mathrm{d}t}\sum\frac{L_i}{A_i} = g\rho_{fI}\beta_{fI}\Delta TH - \frac{\dot{m}_{fI}^2}{2\rho}\sum\frac{1}{A_i^2\left(\frac{f_iL_i}{D_h}+K_i\right)} \quad (3\text{-}8)$$

where g, ρ_{fI}, β_{fI}, $\Delta T, H,$ and D_h are the specific gravity, density of Fluid I, thermal expansion coefficient of Fluid I, temperature difference of Fluid I in the heating and cooling sections, vertical

distance between the thermal centerlines of the heating and cooling sections, and hydraulic diameter, respectively. $L_i, A_i,\ f_i,$ and K_i are the length, flow area, friction factor, and form loss factor of section i, respectively.

Benchmark study of the developed 1D code will be discussed in the following sections by comparing the code results with three natural circulation experiments using (1) water (Hallinan and Viskanta, 1986); (2) nitrate salt $NaNO_3$-KNO_3 60-40 wt% (Kudariyawar et al., 2016; Srivastava et al., 2016); and (3) fluoride salt LiF-BeF_2 66-34 mol% (Britsch et al., 2019) as the working fluids, respectively.

3.2 Code Benchmark with a Natural Circulation Experiment Using Water

3.2.1 Overview of the Loop

Hallinan and Viskanta (1986) investigated natural circulation of water in a single loop as shown in Figure 3-2(a) with the corresponding model used for code benchmark as shown in Figure 3-2(b). The rectangular loop consisted of a vertical section for tube bundle #1, another vertical section for tube bundle #2, and two horizontal sections. The hot water in tube bundle #1 which consisted of 21 tubes served as a heat source for the loop, while the cold water in tube bundle #2 which consisted of 7 tubes served as a heat sink for the loop. The circulating water flowed outside these two tube bundles, but within the containment pipes as shown in Figure 3-2(b). A parallel-flow arrangement was observed for the circulating water and hot water, while a counter-current-flow arrangement for the circulating water and cold water. The effects of buoyancy and radiative heat transfer were negligible in the experiments (Hallinan and Viskanta, 1986) since (1) the temperature difference between the wall and bulk fluid was small; (2) the working temperature

was low; and (3) water can be treated as an opaque medium to thermal radiation. Therefore, the forced convective heat transfer correlations will be applied to water in the loop.

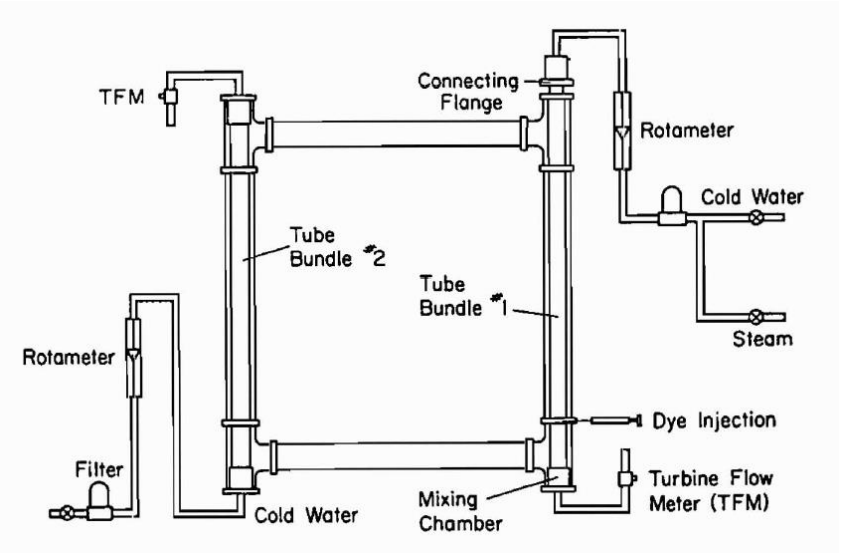

(a)

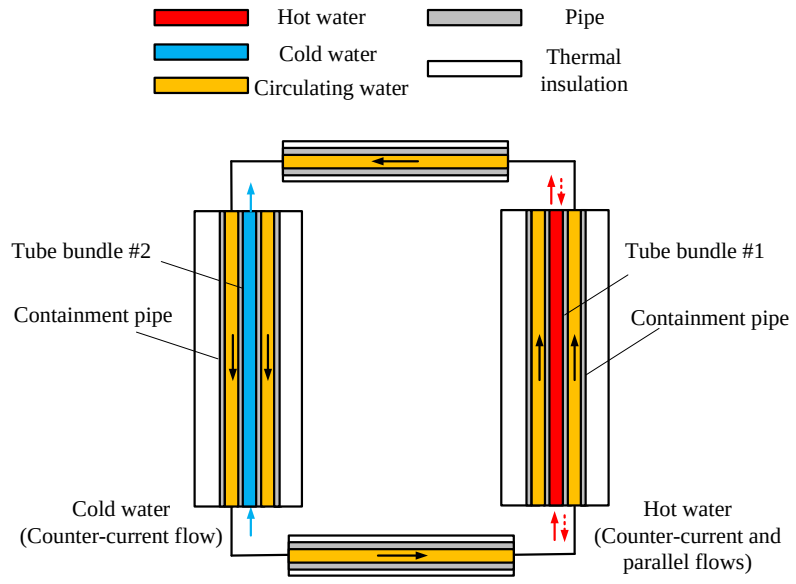

(b)

Figure 3-2 Schematic of (a) the experimental setup for a natural circulation loop using water as the working fluid (Hallinan and Viskanta 1986) and (b) the corresponding model used for code benchmark

3.2.2 Heat Transfer Process

The following heat transfer processes as shown schematically in Figure 3-3 are evaluated in the 1D code NACCO for the natural circulation loop using water as the working fluid:

(1) Heating section: Convective heat transfer from the hot water to the tube bundle wall (Bundle #1), conductive heat transfer across the tube bundle, convective heat transfer from the tube bundle wall to the circulating water, convective heat transfer from the circulating water to the containment pipe, conductive heat transfer across the containment pipe and thermal insulation, and finally convective heat transfer from the thermal insulation to the ambient air;

(2) Cooling section: One process is the convective heat transfer from the circulating fluid to the tube bundle wall (Bundle #2), conductive heat transfer cross the tube bundle, and convective heat transfer from the tube bundle wall to the cold water. Another process is the convective heat transfer from the circulating fluid to the containment pipe, conductive heat transfer cross the containment pipe and thermal radiation, and finally convective heat transfer from the thermal insulation to the ambient air;

(3) Hot/Cold legs: Convective heat transfer from the circulating water to the piping wall, conductive heat transfer across the piping wall and thermal insulation, and finally convective heat transfer from the thermal insulation to the ambient air.

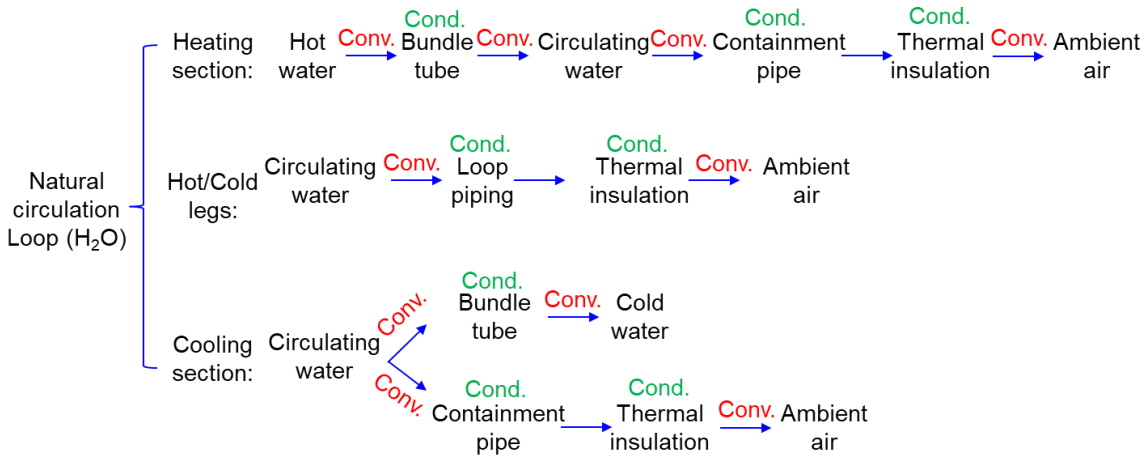

Figure 3-3 Heat transfer processes for the natural circulation loop using water as the working fluid

3.2.3 Correlations for Heat Transfer and Friction Factor

The Gnielinski correlation (Kakac et al., 2014) is used to estimate the forced convective heat transfer of the hot and cold water on the tube side of the two tube bundles for transitional and turbulent flows if applicable, while the Sieder-Tate correlation (Sieder and Tate, 1936) is used for laminar flows of the circulating water in horizontal pipes. It should be noted that the Sieder-Tate correlation considers the effects of (1) the developing flow region where the heat transfer is enhanced and (2) variance of the thermophysical properties due to the large temperature difference between the wall and bulk fluid.

In addition, the following correlation (Hallinan and Viskanta, 1985)

$$\mathrm{Nu}_c = 0.051\mathrm{Re}^{0.8}\mathrm{Pr}^{0.43} \tag{3-9}$$

is used to estimate the thermal performance of the circulating water on the shell side of Bundle #1 (Rectangular arrangement) for parallel flows, while another correlation (Gruszcynski and Viskanta, 1983)

$$\mathrm{Nu}_c = 0.067\mathrm{Re}^{0.8}\mathrm{Pr}^{0.43} \tag{3-10}$$

is used for the circulating water on the shell side of Bundle #2 (Triangular arrangement) for counter-current flows.

The heat loss is calculated by the following two correlations

$$\mathrm{Nu}_c = \left\{0.825 + \frac{0.387\mathrm{Ra}^{1/6}}{\left[1+(0.492/\mathrm{Pr})^{9/16}\right]^{8/27}}\right\}^2 \tag{3-11}$$

$$\mathrm{Nu}_c = \left\{0.6 + \frac{0.387\mathrm{Ra}^{1/6}}{\left[1+(0.559/\mathrm{Pr})^{9/16}\right]^{8/27}}\right\}^2 \tag{3-12}$$

for natural convection from vertical plates/cylinders (small curvature effect) and horizontal cylinders to the ambient, respectively.

In addition to the heat transfer correlations, the friction factor correlations for the loop (Hallinan and Viskanta, 1986) need to be known as well. The Darcy friction factor correlations

$$f = 172/\mathrm{Re} \tag{3-13}$$

$$f = 124.8/\mathrm{Re} \tag{3-14}$$

proposed by Hallinan and Viskanta (1985) respectively for the horizontal pipes and vertical tube bundles in the same natural circulation loop (Hallinan and Viskanta, 1986), are used in this study, while different correlations were adopted by Lv et al. (2015a) and Lin (2020) in their numerical studies to estimate the flow resistance for the same loop (Hallinan and Viskanta, 1986).

3.2.4 Results and Discussions

One startup transient in the experiments (Hallinan and Viskanta, 1986) for parallel flows in Bundle #1 is used for validation of the 1D code NACCO. It is assumed that the working fluids in the loop including the two tube bundles are initially stagnant with a temperatures of 19 °C, the initial inlet temperature for the circulating water in Bundle #1 measured by Hallinan and Viskanta (1986). The NACCO results in this study, SAM and RELAP5 code results performed by Lin (2020), and experimental data (Hallinan and Viskanta, 1986) are compared as shown in Figure 3-4 and Figure 3-5.

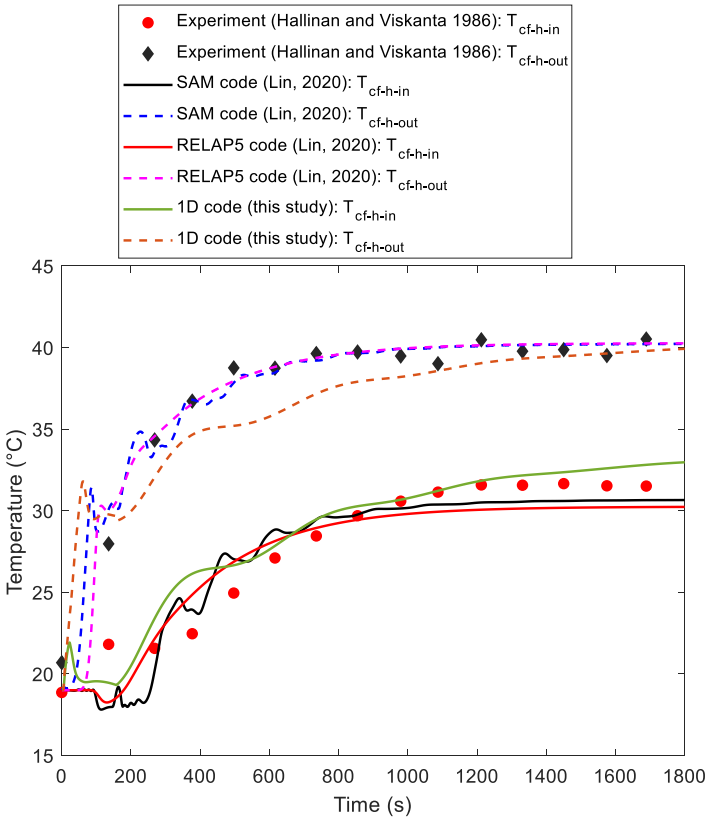

Figure 3-4 Comparison of the circulating water temperature estimated by the 1D code NACCO (this study), SAM and RELAP5 codes (Lin, 2020), and experimental data (Hallinan and Viskanta, 1986) for parallel flows in Bundle #1

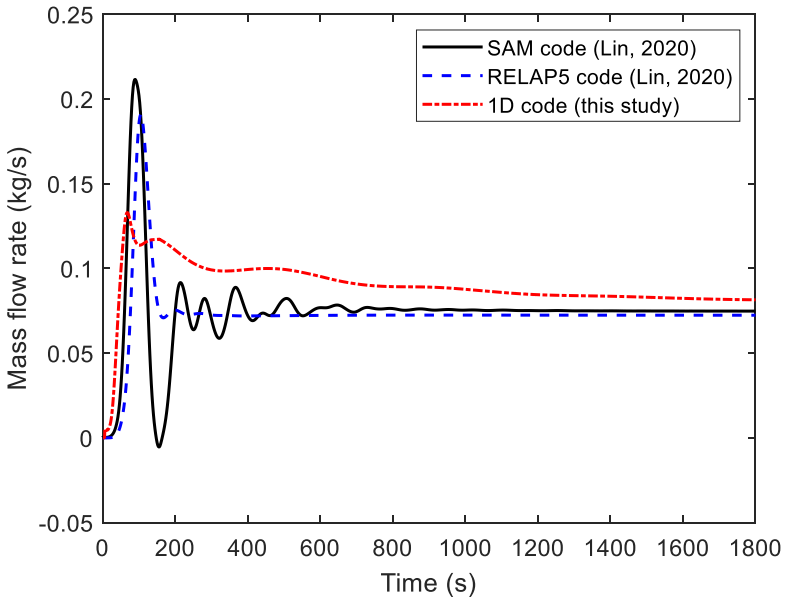

Figure 3-5 Comparison of the loop mass flow rate estimated by the 1D code NACCO (this study), SAM and RELAP5 codes (Lin, 2020) for parallel flows in Bundle 1

The 1D code NACCO developed in this study and two other codes used by Lin (2020) capture key trends of inlet and outlet temperatures of the circulating water for parallel flows in Bundle #1 as shown in Figure 3-4. The maximum discrepancies for the circulating fluid temperature between the 1D code NACCO predictions and experimental data are 10.6% and 6.3% under transient and steady-state conditions, respectively. In addition, the maximum differences for the mass flow rate between the 1D code NACCO predictions and the RELAP5 predictions are 31.6% and 13.9% under transient and steady-state conditions, respectively. Since the predictions by the 1D code NACCO for the circulating water temperature and mass flow rate generally agree with the experimental data and other code predictions, the heat transfer and friction characteristics of water in a single natural circulation loop could be properly modeled by the 1D code NACCO developed in this study.

3.3 Code Benchmark with a Natural Circulation Experiment Using $NaNO_3$-KNO_3

3.3.1 Overview of the Loop

Kudariyawar et al. (2016) and Srivastava et al. (2016) experimentally investigated molten salt natural circulation in a rectangular loop as shown in Figure 3-6(a) using a nitrate salt, $NaNO_3$-KNO_3 (60-40 wt%), as the working fluid and the corresponding model used for code benchmark study as shown in Figure 3-6(b). The rectangular loop consisted of a vertical heating section, a horizontal cooling section, and several vertical/horizontal pipe sections. The nitrate salt, $NaNO_3$-KNO_3 was heated by electrical heaters in the heating section, while it was cooled by air in the cooling section. Three steady-state experiments at different power levels, 1.7, 1.8, and 2.0 kW, are selected for code benchmark.

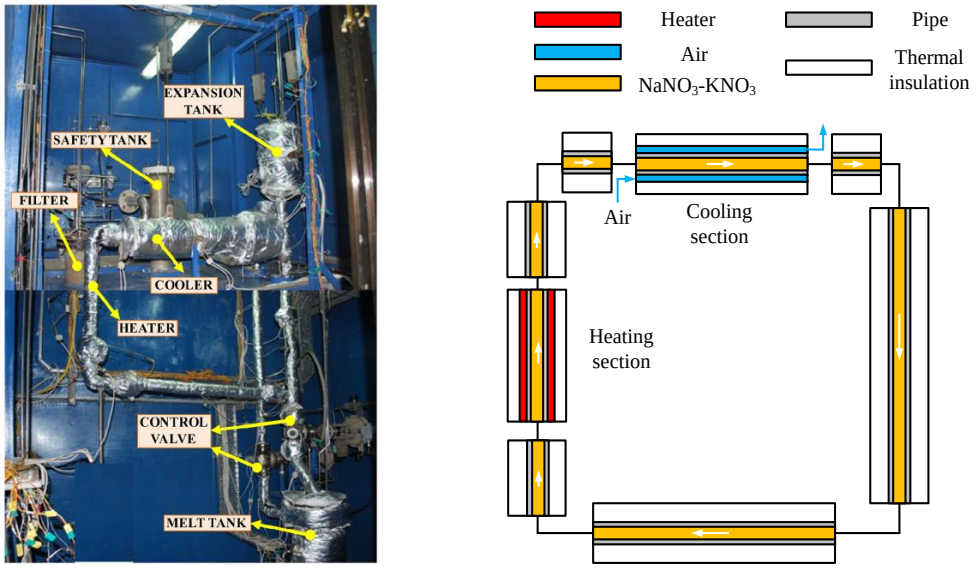

(a) (b)

Figure 3-6 Schematic of (a) the experimental setup for a natural circulation loop using $NaNO_3$-KNO_3 (60-40 wt%) as the working fluid (Srivastava et al., 2016) and (b) the corresponding model used for code benchmark

3.3.2 Heat Transfer Process

The nitrate salt temperature in the cooler estimated by Kudariyawar et al. (2016) through a 3D CFD study suggested a much larger value than its melting temperature 220 °C for $NaNO_3$-KNO_3 (60-40 wt%). In addition, the tube wall temperature in the cooling section predicted by the 1D code NACCO was at least 30 °C higher than the melting temperature of $NaNO_3$-KNO_3 (60-40 wt%). Therefore, the nitrate salt $NaNO_3$-KNO_3 (60-40 wt%) should be in the liquid phase in the entire loop during the experiments (Kudariyawar et al., 2016).

In addition, it is necessary to identify whether the buoyancy effect in the loop needs to be considered. The Richardson number, defined as

$$\mathrm{Ri} = \frac{\mathrm{Gr}}{\mathrm{Re}^2} \tag{3-15}$$

is normally used to identify the dominating effect between the natural and forced convections. Typically, the natural convective heat transfer dominates the total heat transfer if Ri > 10, while the forced convective heat transfer dominates if Ri < 0.1. Both the natural and forced (mixed) convective heat transfer should be considered if 0.1 < Ri < 10.

The Grashof number is defined as

$$\mathrm{Gr} = \frac{\beta_{fI} g D_{it}^3 (T_t - T_{bfI})}{\nu_{fI}^2} \tag{3-16}$$

where β_{fI}, ν_{fI}, and T_{bfI} are the thermal expansion coefficient, kinematic viscosity, and bulk temperature of the fluid, respectively. The Richardson number estimated for different power levels investigated ranges from 2.6 to 4.7 for the heating section, 3.0 to 4.6 for the cooling section, while less than 0.1 for other sections of the loop. Therefore, the mixed convection should be considered for both the heating and cooling sections, while the forced convection is considered for others.

The following processes as schematically shown in Figure 3-7 are evaluated by the 1D code NACCO for the natural circulation loop using nitrate salt $NaNO_3$-KNO_3 (60-40 wt%) as the working fluid:

(1) Heating section: One way is the conductive heat transfer across the piping, convective and radiative heat transfer from the piping to the nitrate salt. Another way is the conductive heat transfer across the thermal insulation, and finally convective and radiative heat transfer from the thermal insulation to the ambient air;

(2) Cooling section: Convective and radiative heat transfer from the nitrate salt to the inner tube of the cooler, convective heat transfer from the inner tube and shell of the cooler to the air in the annulus if the cooler shell temperature is higher than the air temperature, radiative heat transfer from the inner tube to the shell, conductive heat transfer across the shell and thermal insulation, and finally convective and radiative heat transfer from the thermal insulation to the ambient air;

(3) Hot/Cold legs: Convective heat transfer from the nitrate salt to the piping, conductive heat transfer across the piping and thermal insulation, and finally convective and radiative heat transfer from the thermal insulation to the ambient air.

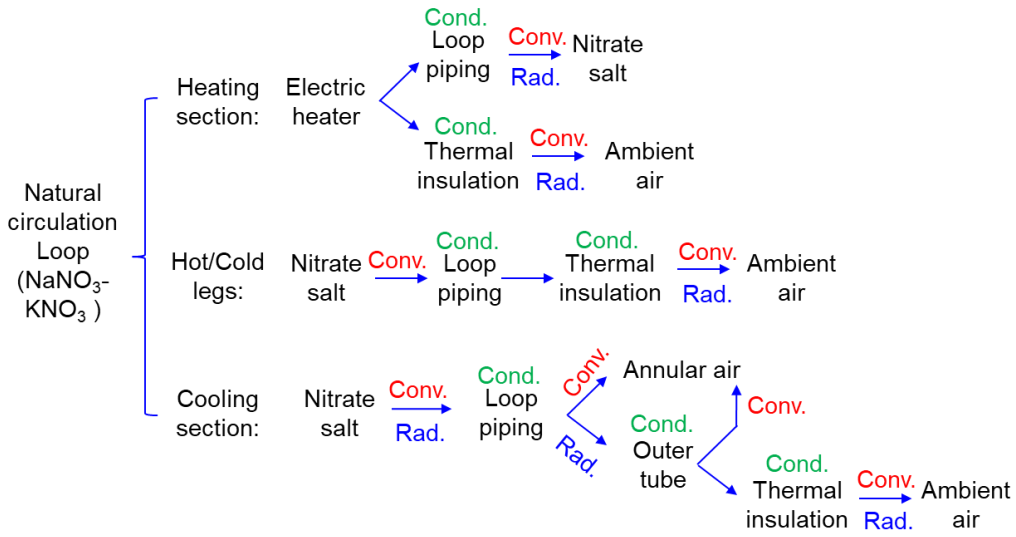

Figure 3-7 Heat transfer processes for the natural circulation loop using $NaNO_3$-KNO_3 (60-40 wt%) as the working fluid

3.3.3 Correlations for Heat Transfer and Friction Factor

The mixed convective heat transfer correlation (Martinelli and Boelter, 1942),

$$\mathrm{Nu}_m = 1.75\sqrt[3]{\mathrm{Gz} + 0.0722\left(\mathrm{GrPr}\frac{D_h}{L}\right)^{0.75}} \tag{3-17}$$

is used for the nitrate salt in the vertical heating section, while another mixed convective heat transfer correlation (Depew and August, 1971)

$$\mathrm{Nu}_m = 1.75\left(\frac{\mu_{bfl}}{\mu_t}\right)^{0.14}\sqrt[3]{\mathrm{Gz} + 0.12\left(\mathrm{GzGr}^{1/3}\mathrm{Pr}^{0.36}\frac{D_h}{L}\right)^{0.88}} \tag{3-18}$$

is used for the nitrate salt in the horizontal cooling section, where Gz is the Graetz number, defined as

$$\mathrm{Gz} = \frac{\pi}{4}\mathrm{RePr}\frac{D_h}{L} = \frac{c_{p,fl}\dot{m}_{fl}}{k_{fl}L} \tag{3-19}$$

The Sieder-Tate correlation is used for forced convective heat transfer of $NaNO_3$-KNO_3 (60-40 wt%) in the hot and cold legs. The following heat transfer correlation

$$\mathrm{Nu}_c' = \left[12\frac{D_h}{L} + 0.86\left(\frac{D_{ot}}{D_{is}}\right)^{-0.16}\right]\mathrm{Nu}_c \tag{3-20}$$

is used for air in the annulus of the cooling section considering the cross-flow effect in both inlet and outlet regions of a double-pipe HX (Aicher and Kim, 1998), where Nu_c is estimated by

$$\mathrm{Nu}_c = \frac{(f/8)(\mathrm{Re}-1000)\mathrm{Pr}}{1+12.7\sqrt{f/8}(\mathrm{Pr}^{2/3}-1)}\left[1+\left(\frac{D_h}{L}\right)^{2/3}\right] \tag{3-21}$$

and the friction factor in Eq. (3-21) is calculated by the following equation,

$$f = [1.82\log_{10}(\mathrm{Re}) - 1.64]^{-2} \tag{3-22}$$

The surface-to-surface radiative heat transfer in the top tube-in-tube cooler is also considered as

$$\dot{\mathrm{Q}}_{it-ot} = \frac{A_{oit}\sigma\left(T_{oit}^4 - T_{iot}^4\right)}{\frac{1}{\varepsilon_{oit}} - 1 + \frac{1}{X_{it-ot}} + \frac{A_{oit}}{A_{iot}}\left(\frac{1}{\varepsilon_{iot}} - 1\right)} \tag{3-23}$$

where A_{oit}, A_{iot}, ε_{oit}, ε_{iot}, X_{it-ot}, and σ are the outer surface of the inner tube, inner surface of the outer tube (shell), emissivity of the outer surface of the inner tube, emissivity of the inner surface of the outer tube, view factor from the inner tube to the outer tube, and Stefan-Boltzmann coefficient, respectively.

The Darcy friction factor correlation

$$f = 22.26/\mathrm{Re}^{0.6744} \tag{3-24}$$

proposed by Vijayan and Austregesilo (1994) for a rectangular natural circulation loop is adopted for the nitrate salt loop (Kudariyawar et al., 2016; Srivastava et al., 2016).

3.3.4 Independence Study for the Mesh Size

The nitrate salt temperature varies significantly in the heating and cooling sections. It is therefore necessary to perform an independence study for the mesh size used to divide the heating and cooling sections in the 1D code NACCO.

Four different mesh sizes in the axial direction will be used for the independence study, namely, 100, 50, 20, and 10 mm. The initial conditions include a heating power of 2.0 kW, salt temperature of 300 °C, air inlet temperature of 20 °C, and salt mass flow rate of 1.0 g/s. As shown in Figure 3-8, both the salt inlet and outlet temperatures in the heating section increase significantly until reaching a plateau after a certain period. This is because the heating power is larger than the heat loss rate initially, leading to an increase of the salt temperature until reaching an equivalence between the heating power and heat loss rate.

The salt temperature under steady-state conditions or in the plateau is of interest and therefore adopted as shown in Figure 3-9. As the decrease of the mesh size or increase of the mesh quantity, the salt inlet and outlet temperatures decrease significantly at a faster rate initially, while they decrease at a slower rate afterwards. The mesh size of 20 mm is suggested considering the computational time and accuracy for the salt inlet and outlet temperatures.

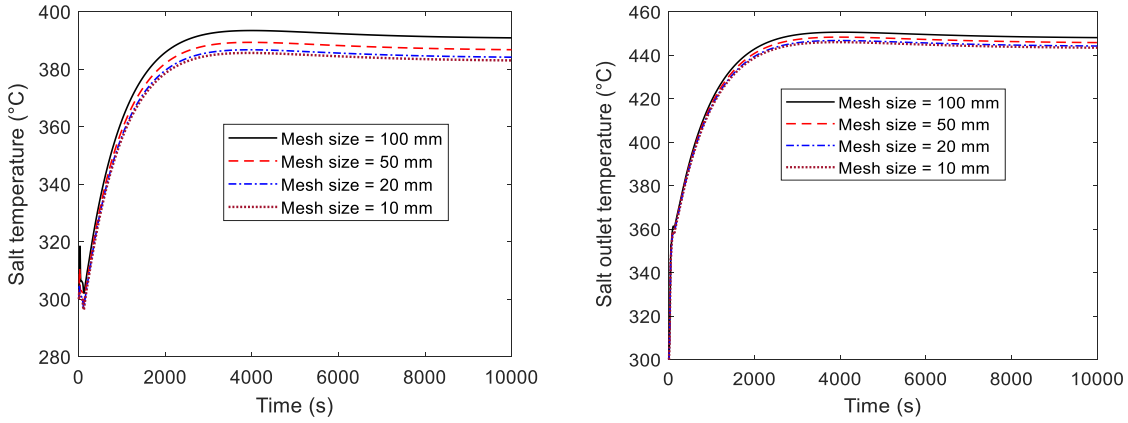

(a) (b)

Figure 3-8 Nitrate salt temperature under transient conditions at the (a) inlet and (b) outlet of the heating section predicted by the 1D code NACCO

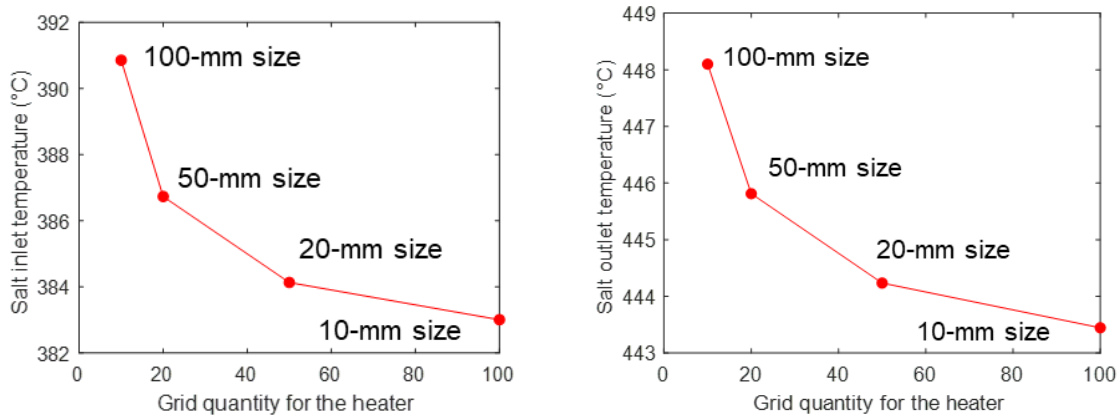

(a) (b)

Figure 3-9 Nitrate salt temperature under steady-state conditions at the (a) inlet and (b) outlet of the heating section predicted by the 1D code NACCO

Similar analysis is performed for the salt velocity. The salt velocity increases significantly initially until reaching a plateau after a certain period as shown in Figure 3-10. This is because the initial velocity is too small to support the large heat transfer rate specified. The salt velocity under

steady-state conditions is of interest and therefore adopted as shown in Figure 3-11. As the decrease of the mesh size or increase of the mesh quantity, the salt velocity increases at a faster rate initially, while a slower rate afterwards. The mesh size of 20 mm is finally suggested for the 1D code NACCO developed to model and simulate the nitrate salt loop considering the computational time and accuracy for the salt temperature and velocity.

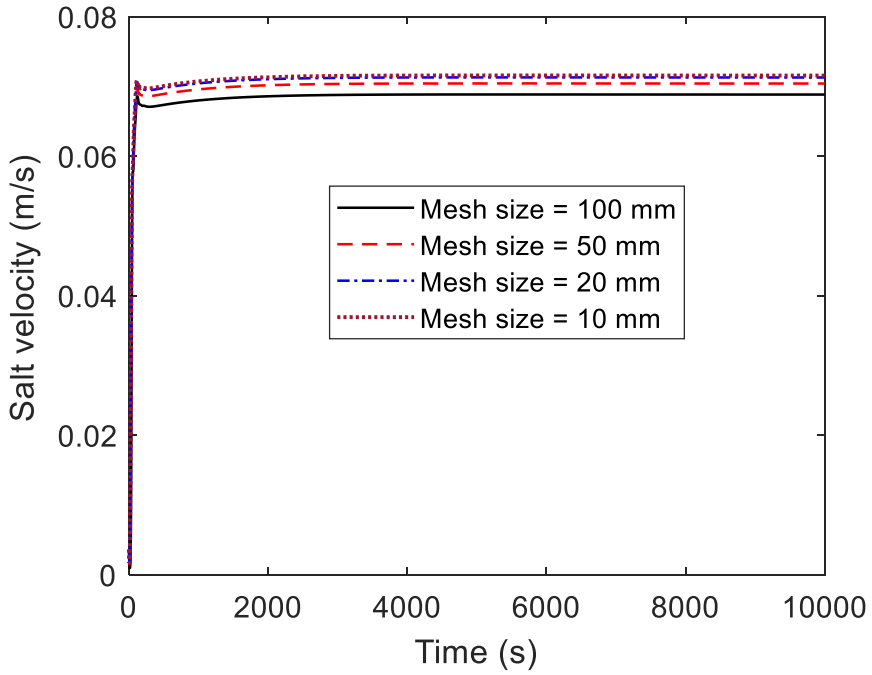

Figure 3-10 Nitrate salt velocity under transient conditions at the inlet of the heating section predicted by the 1D code NACCO

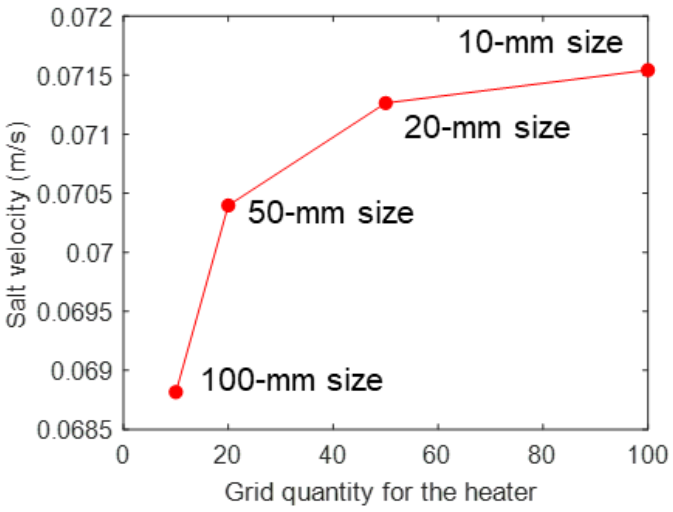

Figure 3-11 Nitrate salt velocity under steady-state conditions at the inlet of the heating section predicted by the 1D code NACCO

3.3.5 Results and Discussions

Three cases have been investigated by the 1D code NACCO: (1) Case I, forced convective heat transfer; (2) Case II, mixed convective heat transfer; and (3) Case III, combined mixed and radiative heat transfer. As shown in Figure 3-12, the discrepancy for the salt inlet temperature is 10.0 °C between Cases I and III and 3.7 °C between Cases II and III. Similarly, the discrepancy for the salt outlet temperature is 9.1 °C between Cases I and III and 3.6 °C between Cases II and III. These discrepancies for the salt temperature result from different heat transfer correlations applied to Cases I, II, and III.

The Nusselt numbers calculated for the nitrate salt in the heating section are respectively 8.0, 13.9, and 15.6 for Cases I, II, and III, while they are 6.0, 7.7, and 8.9 for Cases I, II, and III in the cooling section, respectively. Therefore, the buoyancy effect enhances the total heat transfer by 37.8% and 19.1% for the nitrate salt in the heating and cooling sections, respectively. In addition, the radiative heat transfer enhances the total heat transfer by 10.9% and 13.5% for the

nitrate salt in the heating and cooling sections, respectively. Therefore, both the effects of buoyancy and radiative heat transfer should be considered in the 1D code NACCO for modeling and simulation of the nitrate salt natural circulation experiments (Kudariyawar et al., 2016).

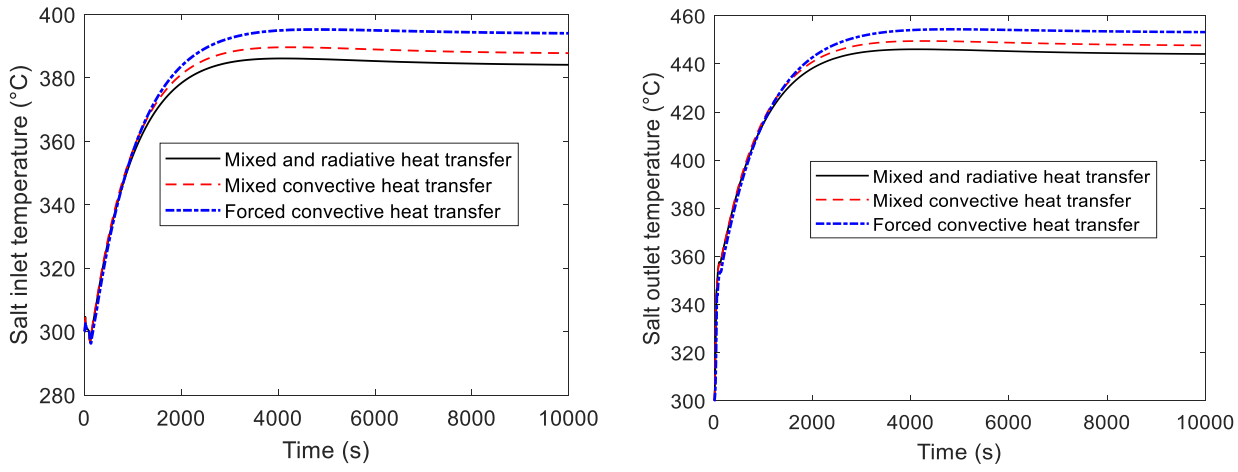

(a) (b)

Figure 3-12 Nitrate salt temperature under transient conditions at the (a) inlet and (b) outlet of the heating section predicted by the 1D code NACCO for Cases I, II, and III

Figure 3-13 shows comparison of the nitrate salt temperature between the experiments (Kudariyawar et al., 2016) and 1D code NACCO predictions considering the effects of buoyancy and radiative heat transfer for three different power levels: 1.7, 1.8, and 2.0 kW. The nitrate salt temperature profile along the loop, from the heater inlet to heater outlet, cooler inlet, and cooler outlet, predicted by the 1D code NACCO is agreeable with the experimental data. In addition, the relative salt temperature difference between the 1D code NACCO predictions and experimental data ranges from 1.4% to 3.8%.

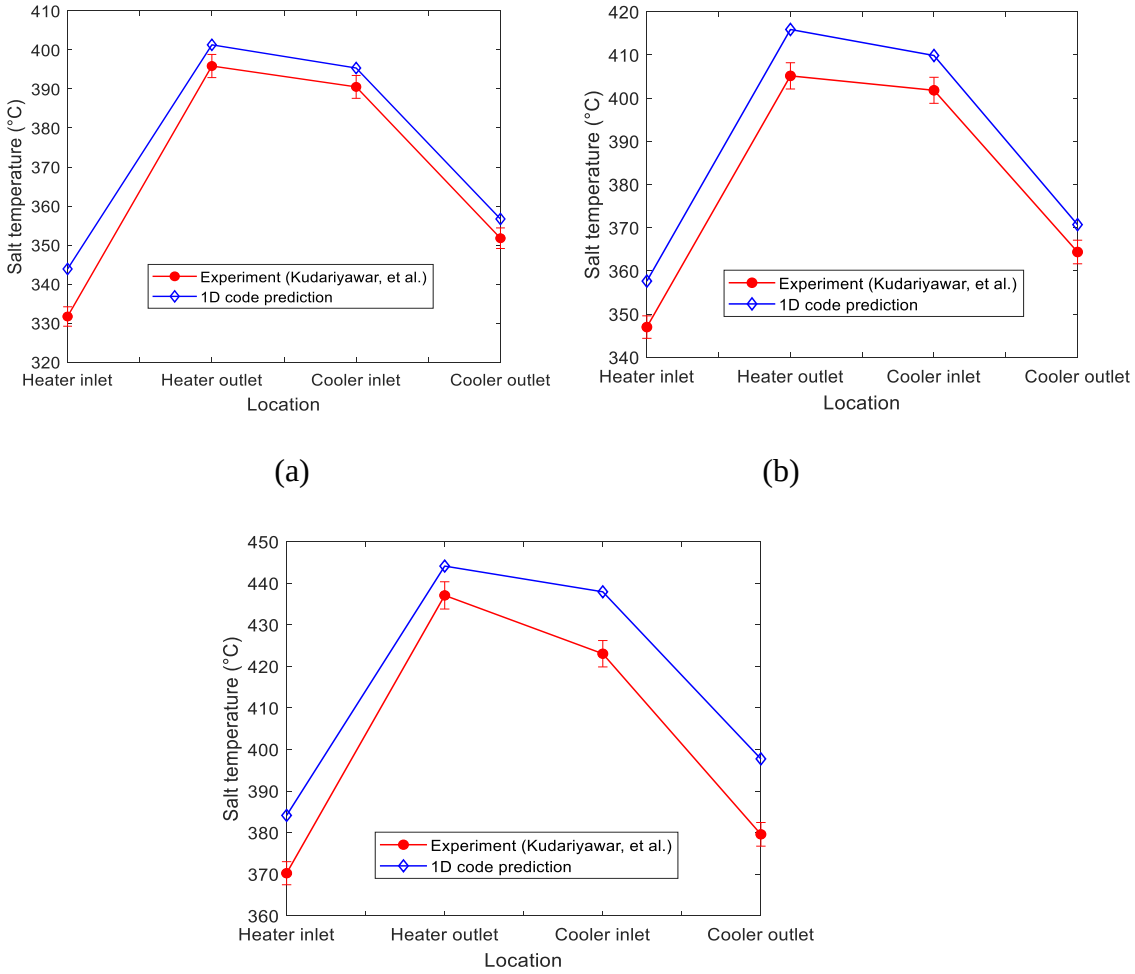

Figure 3-13 Comparison of the nitrate salt temperature between the experiments (Kudariyawar et al., 2016) and 1D code NACCO predictions considering the effects of buoyancy and radiative heat transfer for (a) 1.7 kW; (b) 1.8 kW; and (c) 2.0 kW

Another observation is that the nitrate salt temperature predicted is 4.9 °C to 18.2 °C higher than the experimental data. One potential reason is that the heat transfer correlation used for air in the cooler may underestimate the heat loss rate. The heat transfer correlation used has an uncertainty of ±20%, leading to ±12.7 °C to ±14.1 °C temperature change for the power level of 2.0 kW. It is therefore suggested to perform new experiments or additional CFD studies for the

specific tube-in-tube cooler adopted in the experiments (Kudariyawar et al., 2016). Since the information for the cooler geometry is incomplete in the literature (Kudariyawar et al., 2016), such a CFD study to develop an accurate heat transfer correlation for the cooler becomes difficult.

The 1D code NACCO predictions are in line with the nitrate salt temperature in terms of the overall trend and relative temperature difference. Although the absolute temperature difference could be as high as about 18 °C, it seems to be acceptable considering the nitrate salt temperature up to 450 °C. In addition, the higher predictions for the salt temperature suggest that the 1D code NACCO is conservative for the design of natural circulation loops, such as the passive decay heat removal system.

3.4 Code Benchmark with a Natural Circulation Experiment Using FLiBe

3.4.1 Overview of the Loop

Oak Ridge National Laboratory (ORNL) built a number of natural circulation loops as shown in Figure 3-14(a) to study the corrosion behavior of different alkali-metal fluorides. After about half a century, the University of Wisconsin (UW) built a similar loop as shown in Figure 3-14(b) using FLiBe as the working fluid for material testing and thermal-hydraulic experiments. The “diamond-shape” single-phase natural circulation loop consisted of two heating sections at the bottom and left sides and two cooling sections at the top and right sides of the loop, while the right-side cooling section was disabled during the heat transfer experiments (Britsch et al., 2019).

The fluoride salt, FLiBe, was heated by four sets of radiant-mode heaters, half of which were located on each of the two heating sections as shown in Figure 3-15. There was about 0.5” gap between the heaters and piping, where the surface-to-surface radiative heat transfer dominated.

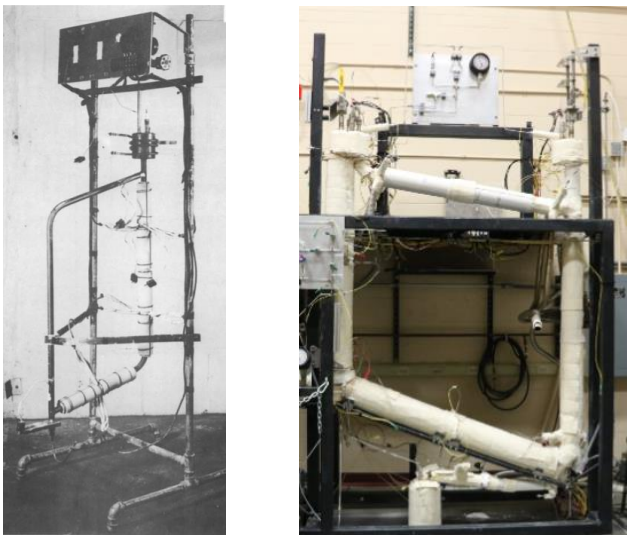

(a) (b)

Figure 3-14 Natural circulation loops for fluoride salts at (a) ORNL (Adamson et al., 1953) and (b) UW (Britsch et al., 2019)

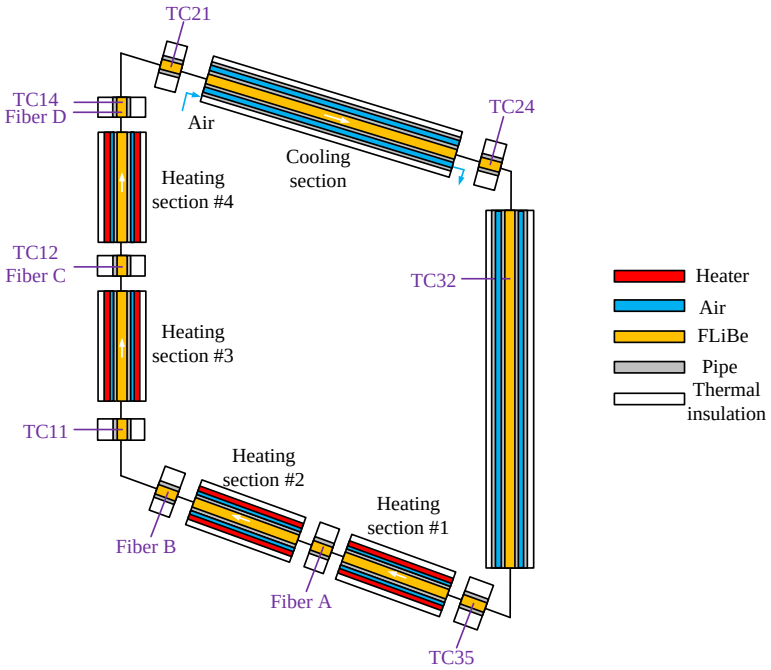

Figure 3-15 Schematic of modules used in the 1D code NACCO for modeling of the natural circulation loop using FLiBe ($LiF\text{-}BeF_2$ 66-34 mol%) as the working fluid (Britsch et al., 2019)

3.4.2 Heat Transfer Process

The Richardson number estimated ranges from 0.7 to 3.3, 0.6 to 2.4, and 0.3 to 4.5 for the bottom and left heating sections, and top cooling section respectively. Therefore, the mixed convection should be considered for FLiBe in these heating and cooling sections. In addition, the forced convection is applied to FLiBe in other sections due to their much smaller Richardson numbers.

The following processes as schematically shown in Figure 3-16 are evaluated by the 1D code NACCO for the natural circulation loop using FLiBe as the working fluid:

(1) Heating section: One way is the radiative and conductive heat transfer from the radiant-mode heaters across the gap filled with air to the piping, conductive heat transfer across the piping, radiative and convective heat transfer from the piping to the FLiBe salt. Another way is the conductive heat transfer across the thermal insulation, and finally convective and radiative heat transfer from the thermal insulation to the ambient air;

(2) Top cooling section: Convective and radiative heat transfer from the FLiBe salt to the inner tube of the top cooler, conductive heat transfer across the inner tube, convective heat transfer from the inner tube and shell of the top cooler to the air in the annulus if the cooler shell temperature is higher than the air temperature, radiative heat transfer from the inner tube to the shell, conductive heat transfer cross the shell and thermal insulation, and finally convective and radiative heat transfer from the thermal insulation to the ambient air;

(3) Right cooling section (closed): Convective heat transfer from the FLiBe salt to the inner tube of the right cooler, conductive heat transfer across the inner tube, radiative and conductive heat transfer across the gap filled with air in the annulus, conductive heat

transfer cross the shell of the right cooler and thermal insulation, and finally convective and radiative heat transfer from the thermal insulation to the ambient air;

(4) Other piping: Convective heat transfer from the FLiBe salt to the piping, conductive heat transfer across the piping and thermal insulation, and finally convective and radiative heat transfer from the thermal insulation to the ambient air.

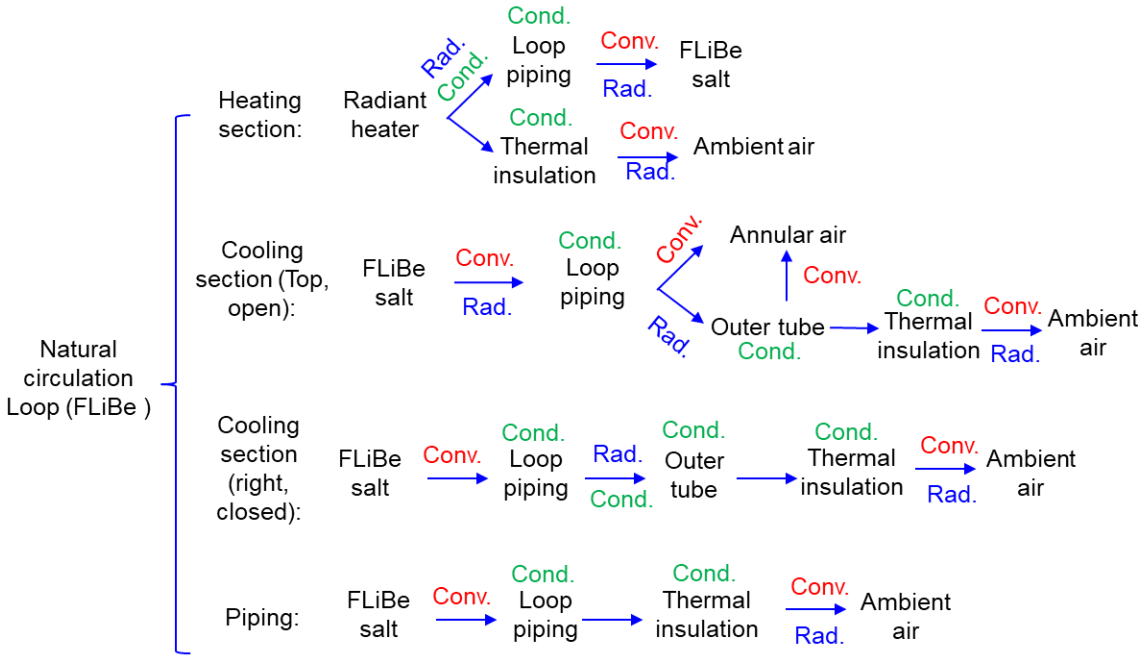

Figure 3-16 Heat transfer processes for the natural circulation loop using FLiBe as the working fluid

3.4.3 Correlations for Heat Transfer and Friction Factor

Eq. (3-17) is used to calculate the mixed convective heat transfer of the FLiBe salt in the vertical heating section, while Eq. (3-18) is applied to the bottom heating and top cooling sections. In addition, the Sieder-Tate correlation is applied to the FLiBe salt in other sections.

In addition to the heat transfer correlations, another key input is the friction factor correlation for FLiBe in the natural circulation loop. Lin (2020) used $f = 64/\mathrm{Re}$ (Bergman et al., 2011) for the FLiBe salt natural circulation in the loop (Britsch et al., 2019). It was verified numerically to be an appropriate correlation for the friction factor of molten salts in fully-developed laminar flow regime in circular tubes (Zhang et al., 2020a). However, the simulation results for the salt mass flow rate (Lin, 2020) were much higher than the experimental data (Britsch et al., 2019). This is because the correlation used in the simulation (Lin, 2020) underestimates the friction factor of molten salts considering (1) secondary flows (Vijayan and Austregesilo, 1994) and (2) developing flows (Zhang et al., 2020a) in confined natural circulation loops. The same correlation, Eq. (3-24), originally used for the nitrate salt natural circulation (Kudariyawar et al., 2016) in Section 3.3, is adopted for the FLiBe salt natural circulation loop (Britsch et al., 2019).

3.4.4 Independence Study for the Mesh Size

The FLiBe salt temperature changed significantly flowing through the heating and cooling sections in the experiments (Britsch et al., 2019). Therefore, it is necessary to perform an independence study for the mesh size.

Four different mesh sizes (along the axial direction of the flow loop) are used in the 1D code NACCO, namely, 100, 50, 20, and 10 mm. The initial conditions include a heating power of 1298 W per heater, salt temperature of 600 °C, air inlet temperature of 20 °C, and salt mass flow rate of 10^{-3} g/s. As shown in Figure 3-17, both the inlet and outlet temperatures of the FLiBe salt in the heating section (TC35 and TC14) increase significantly until reaching a plateau. This is because the heating power specified is larger than the initial heat loss rate, leading to an increase of the salt temperature until a balance between the heating power and heat loss rate.

The salt temperature under steady-state conditions is of interest and therefore adopted as a figure of merit for comparison as shown in Figure 3-18. As the decrease of the mesh size or increase of the mesh quantity, the salt inlet and outlet temperatures increase until reaching a plateau. The mesh size of 20 mm is suggested considering the computational time and accuracy for the FLiBe salt temperature.

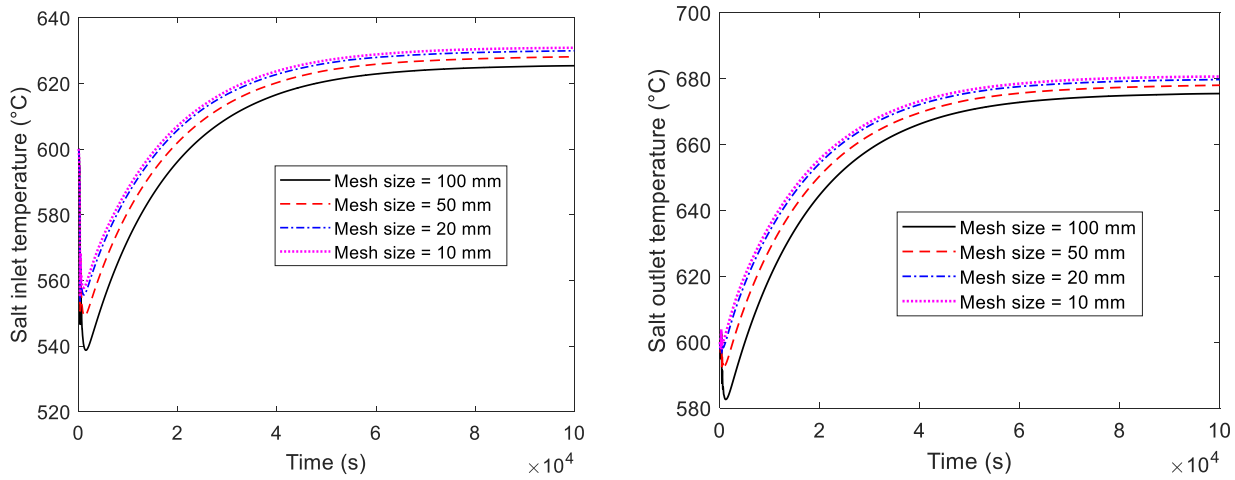

Figure 3-17 FLiBe salt temperature under transient conditions at the (a) inlet and (b) outlet of the heating section predicted by the 1D code NACCO

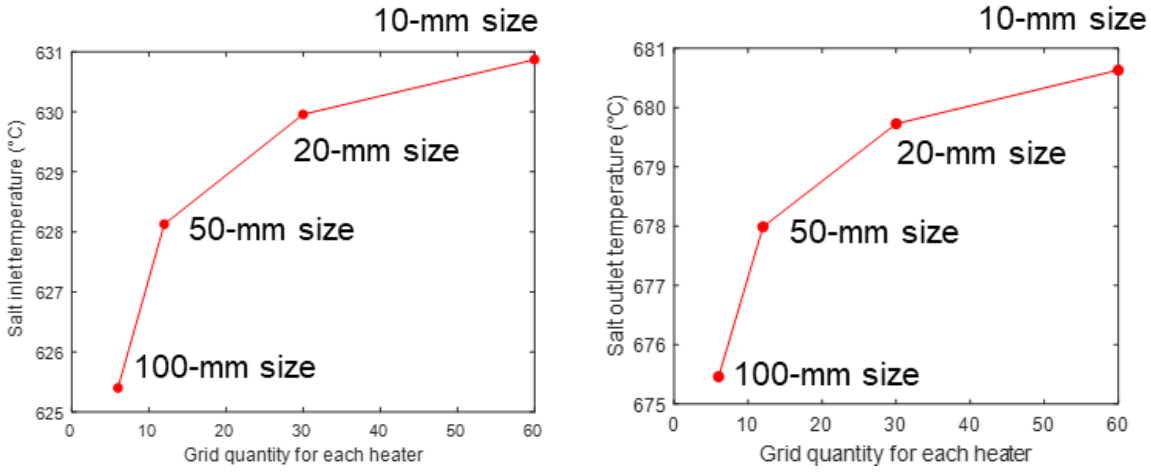

Figure 3-18 FLiBe salt temperature under steady-state conditions at the (a) inlet and (b) outlet of the heating section predicted by the 1D code NACCO

Similar analysis is performed for the FLiBe salt velocity as shown in Figure 3-19. The FLiBe salt velocity increases significantly until reaching a plateau. This is because the initial velocity is too small to support the large heat transfer rate specified. The salt velocity under steady-state conditions for different mesh sizes is plotted in Figure 3-20. As the mesh size decreases from 100 to 10 mm or the mesh quantity increases from 6 to 60 grids for one heater, the salt velocity increases at a faster rate initially, then a slower rate afterwards. The mesh size of 20 mm is finally suggested for the 1D code NACCO developed to model and simulate the FLiBe salt natural circulation loop considering the computational time and accuracy for the salt temperature and velocity.

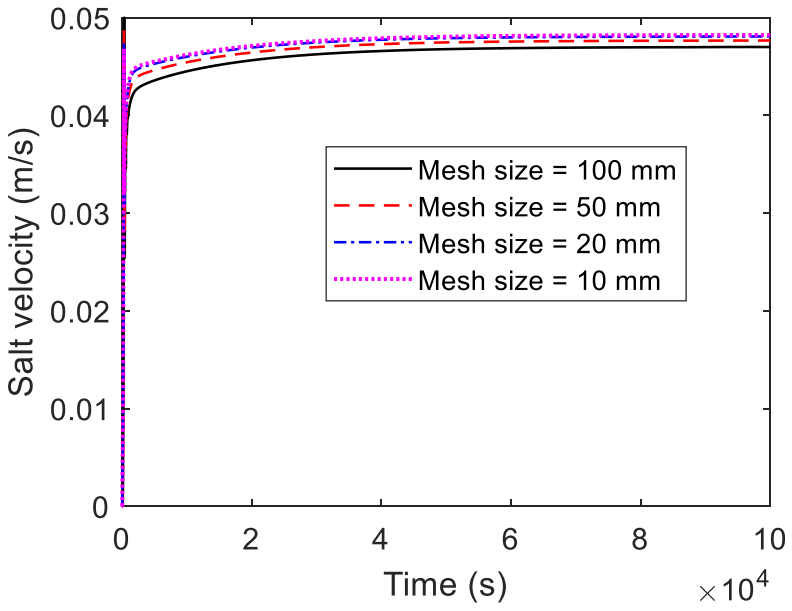

Figure 3-19 FLiBe salt velocity under transient conditions at the inlet of the heating section predicted by the 1D code NACCO

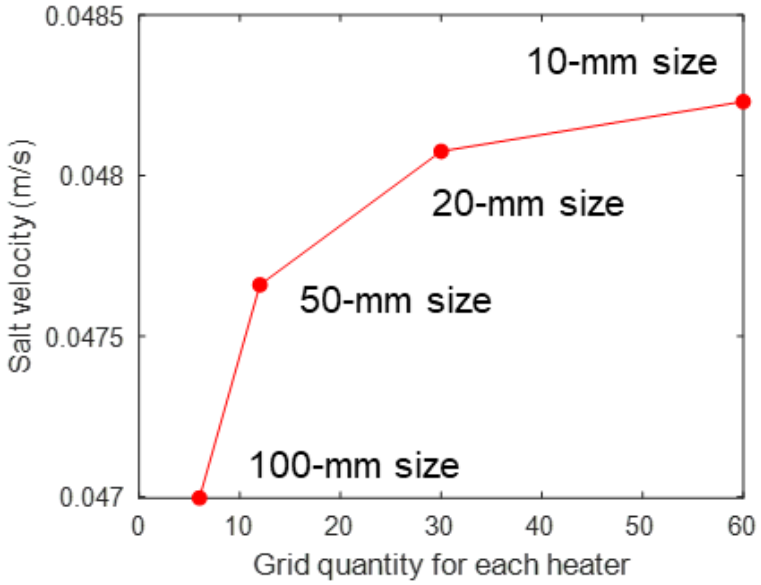

Figure 3-20 FLiBe salt velocity under transient conditions at the inlet of the heating section predicted by the 1D code NACCO

3.4.5 Results and Discussions

Three cases have been investigated: (1) Case I, forced convective heat transfer; (2) Case II, mixed convective heat transfer; and (3) Case III, combined mixed and radiative heat transfer. As shown in Figure 3-21, the discrepancy for the FLiBe salt inlet temperature is 10.3 °C between Case I and Case III and 8.0 °C between Case II and Case III. Similarly, the discrepancy for the salt outlet temperature is 9.7 °C between Case I and Case III and 7.7 °C between Case II and Case III. These discrepancies for the salt temperature result from different heat transfer correlations applied to Cases I, II, and III.

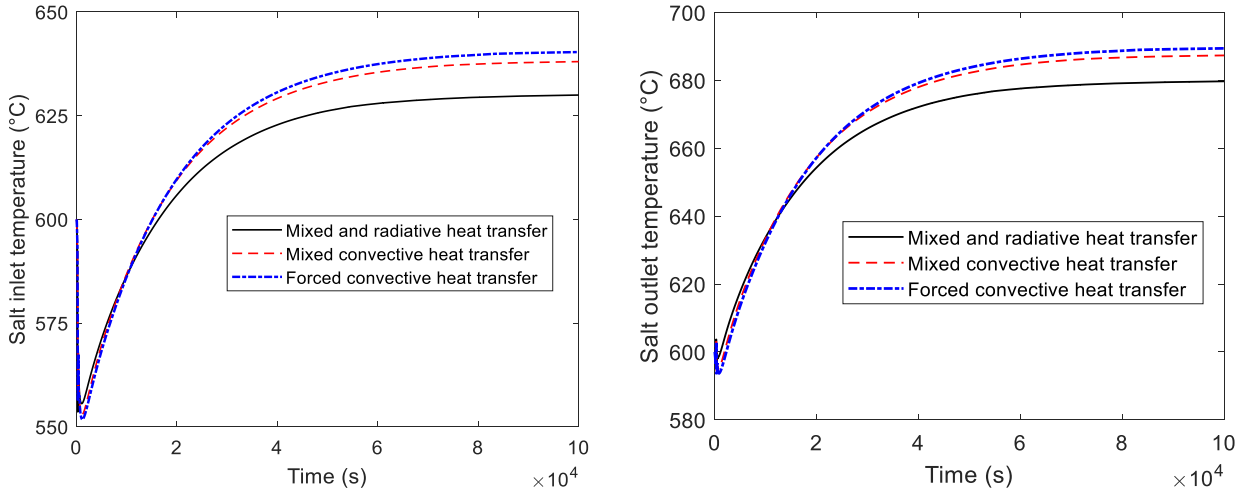

Figure 3-21 FLiBe salt temperature under transient conditions at the (a) inlet and (b) outlet of the heating section predicted by the 1D code NACCO with/without the effects of buoyancy and/or radiative heat transfer

The Nusselt numbers calculated for the FLiBe salt in the heating section are respectively 9.5, 11.0, and 13.3 for Cases I, II, and III, while they are 6.4, 7.1, and 9.8 for Cases I, II, and III for the FLiBe salt in the cooling section, respectively. Therefore, the buoyancy effect enhances the total heat transfer by 11.3% and 7.1% for the FLiBe salt in the heating and cooling sections, respectively. In addition, the radiative heat transfer enhances the total heat transfer by 17.3% and 27.6% for the FLiBe salt in the heating and cooling sections, respectively. Therefore, both the effects of buoyancy and radiative heat transfer should be considered in the 1D code NACCO for modeling and simulation of the FLiBe salt natural circulation experiments ((Britsch et al., 2019).

There were total ten tests obtained from Campaign #4 and Campaign #5 in the experiments (Britsch et al., 2019). Two potential issues existed in these ten tests: Corrosion and salt freezing. Considering the air, especially oxygen and moisture, might enter the loop and lead to severe corrosion after the maintenance between Campaigns #4 and #5, it is more meaningful to

benchmark the 1D code NACCO with the Campaign #4 results compared with the Campaign #5 results. In addition, the working fluid FLiBe may be partially frozen in the top cooling section for a number of tests in Campaign #4 (Britsch et al., 2019). Therefore, it is necessary to identify no-freezing test in Campaign #4 initially.

A preliminary screening approach to identify no-freezing test(s) in Campaign #4 is adopted by examining the FLiBe salt temperature difference and velocity as shown Figure 3-22. Since the buoyancy provides the driving force, the FLiBe salt velocity should increase as the increase of the salt temperature difference in the heating section. However, an opposite trend is observed for each of the three groups as shown in Figure 3-22: (1) Tests #1 to #3, where the air-cooling rates are the same as summarized in Table 3-1; (2) Tests #3 and #4, where the heating powers are the same; and (3) Tests #5 to #7, where the heating powers are the same.

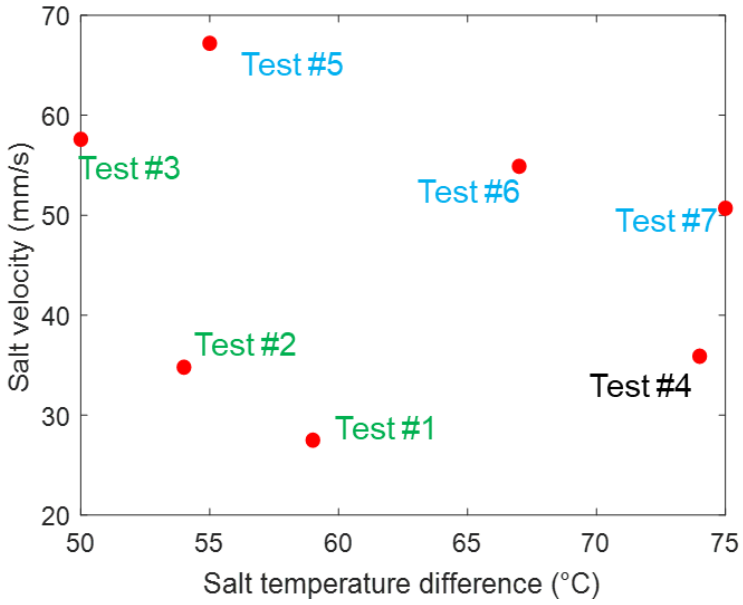

Figure 3-22 Relationship between the FLiBe salt temperature difference and velocity

Table 3-1 Operation conditions for Tests #1 to #7 in Campaign #4 in the experiments (Britsch et al., 2019)

	Heating power (W)	Air velocity (m/s)	T_{Salt} at the cooler outlet (°C)
Test #1	952	2.23	490.4
Test #2	1125	2.19	553.1
Test #3	1298	2.19	**620.9**
Test #4	1298	6.49	502.1
Test #5	1471	2.16	**672.7**
Test #6	1471	6.49	562.3
Test #7	1471	9.19	510.2

The low heating power or high cooling rate in the tests may lead to salt freezing in the cooler, which increases the flow resistance and inhibits the heat transfer to the cooler due to the small thermal conductivity of the FLiBe salt. The increased friction and reduced temperature difference finally lead to this "abnormal" trend: The FLiBe salt velocity decreases as the increase of the FLiBe salt temperature difference in the heating section. Tests #3 and #5 are least likely to have the salt freezing issue compared with other tests since the FLiBe salt outlet temperatures at the cooling section are over 600 °C, much higher than the FLiBe salt melting temperature.

A CFD study is performed for the top cooler for Test #3. The tube-in-tube cooler has an inner diameter of 19.4 mm for the FLiBe salt and inner/outer diameter of 25.4/60.0 mm for the cooling air in the annulus as shown in Figure 3-23. Several mesh models, such as polyhedral mesher, surface remesher, and prism layer mesher were enabled for meshing. In addition, the realizable k-ε two-layer model is used for modeling of turbulent flows of air in the cooler.

Boundary conditions for CFD modeling of Test #3 consists of a uniform velocity inlet (0.0576 m/s) at a bulk temperature of 667.6 °C for the inner tube-side salt (FLiBe), a mass flow

inlet (5.99 g/s) at a bulk temperature of 25.1 °C for the annular-side air, an atmospheric pressure outlet for each fluid (FLiBe and air), and a constant wall heat flux of -10 W/m^2 on the surface of the outer tube to simulate the parasitic heat loss rate. It should be noted that the actual inlet velocity profile of the FLiBe salt in the experiments (Britsch et al., 2019) was not uniform due to the expansion tank installed at the upstream of the cooler as shown in Figure 3-14(b). Since the salt level in the expansion tank and cover-gas pressure (pressure boundary) are not presented in the literature (Britsch et al., 2019), it is difficult to determine the actual inlet velocity profile of the FLiBe salt in the cooler. A uniform velocity profile of the FLiBe salt at the cooler inlet is therefore used instead.

A mesh independence study has been performed and a fine mesh option (5.2 million meshes) as shown in Figure 3-24 is finally selected for the top tube-in-tube cooler. The *y*+ value for the air domain is less than 1.14 for the fine mesh option as shown in Figure 3-25.

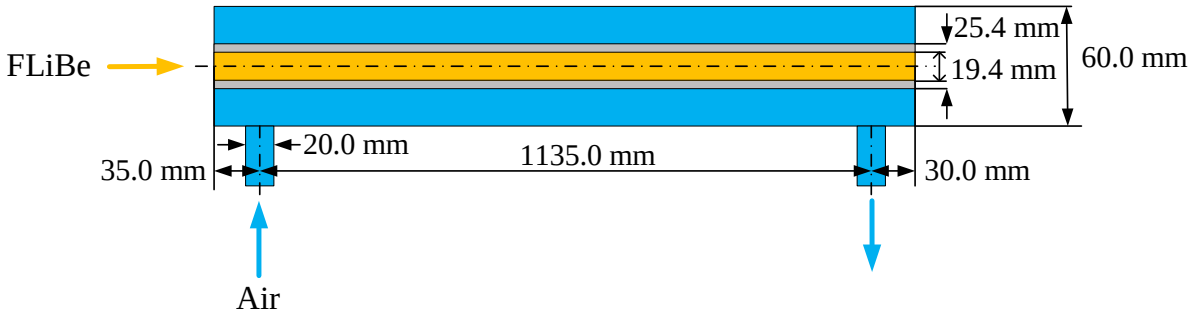

Figure 3-23 Dimensions of the cooler used in the FLiBe natural circulation experiments (Britsch et al., 2019)

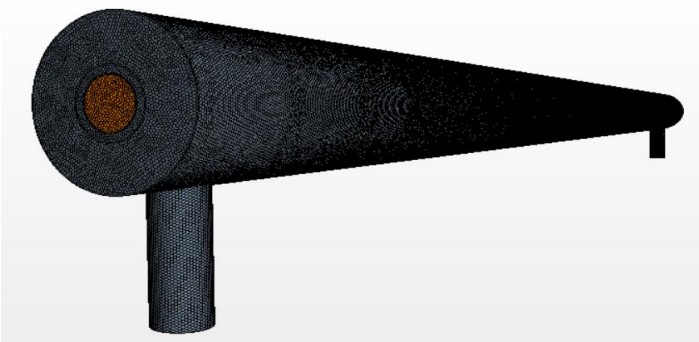

Figure 3-24 Mesh for the cooler used in the FLiBe natural circulation experiments (Britsch et al., 2019)

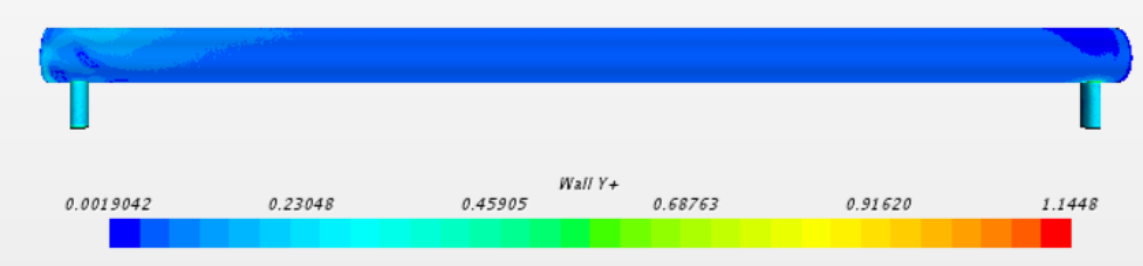

Figure 3-25 *y*+ value for the air domain

The temperature contour of the cooler is shown in Figure 3-26. It is identified that the minimum temperature for the FLiBe salt is 590.5 °C, much higher than 459 °C, the FLiBe salt melting temperature. Therefore, there should be no salt freezing in Test #3 based on the CFD analysis. In addition, it is believed that no salt freezing occurred in Test #5 either due to the larger heating power in Test #5 than that in Test #3 for the same air-cooling rate. Tests #3 and #5 are therefore selected for the benchmark study of the 1D code NACCO.

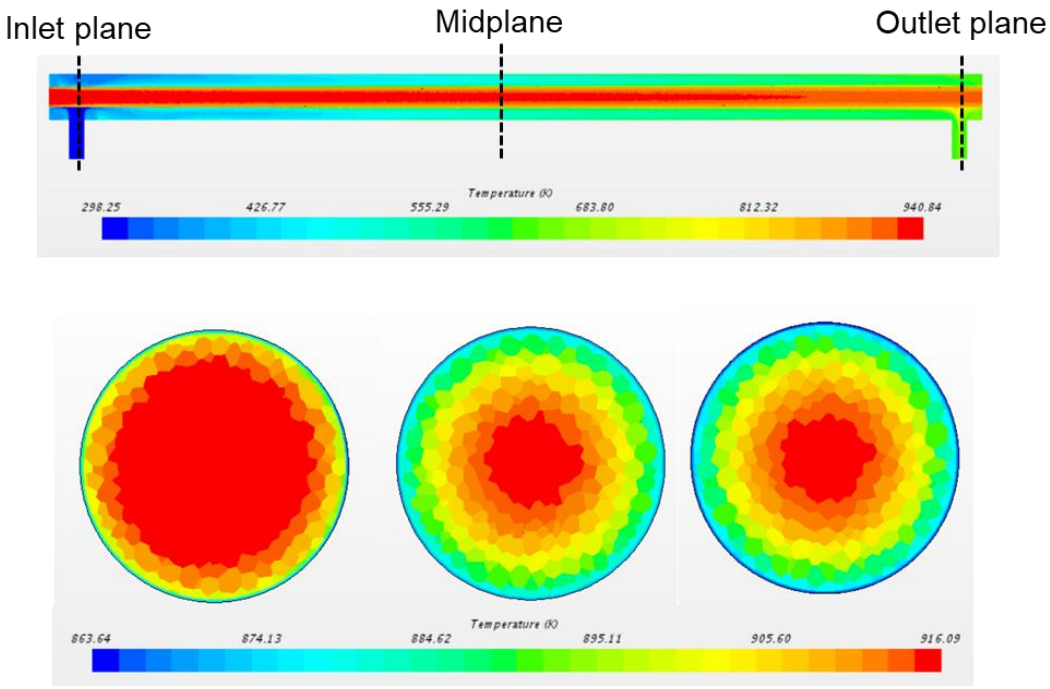

Figure 3-26 Temperature contour of the cooler for Test #3 in the FLiBe natural circulation experiments (Britsch et al., 2019)

Figure 3-27 shows a comparison of the FLiBe salt temperature for Test #3 between the experiments (Britsch et al., 2019) and 1D code NACCO predictions considering the effects of buoyancy and radiative heat transfer. The FLiBe salt temperature profile along the loop predicted by the 1D code NACCO is generally agreeable with the experimental data. In addition, the relative salt temperature difference between the 1D code NACCO predictions and experimental data ranges from 1.7% to 3.7%.

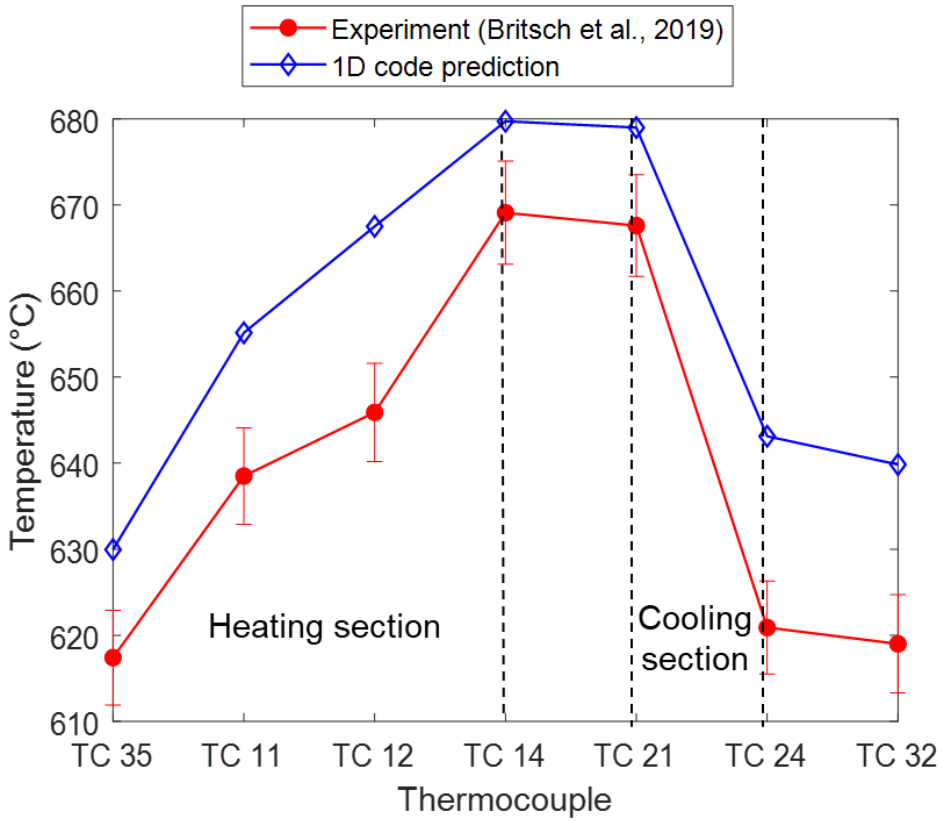

Figure 3-27 Comparison of the FLiBe salt temperature between the experiments (Britsch et al., 2019) and 1D code NACCO predictions considering the effects of buoyancy and radiative heat transfer for Test #3

Another observation is that the FLiBe salt temperature predicted is 11.5 °C to 23.1 °C higher than the experimental data. One potential reason is that the heat transfer correlation used for air in the top cooler may underestimate the heat removal rate. The heat transfer correlation used has an uncertainty of ±20%, leading to ±13.0 °C to ±13.9 °C temperature change for the FLiBe salt in Test #3.

Another potential reason is the large difference between the mass-flow-averaged temperature (bulk temperature) and centerline temperature for the FLiBe salt. All the thermocouples measured the FLiBe salt centerline temperature as shown in Figure 3-27. The bulk

temperature in the experiments (Britsch et al., 2019) is however a better choice for benchmark study. These two reasons will be justified next.

To justify the first potential reason, underestimation of the heat removal rate by the top cooler, a CFD study is performed for the top cooler for Test #3, which has been discussed earlier. It is identified that the Nusselt number calculated in the CFD study is about 14% larger than the correlation results, leading to a 9.3 °C to 9.9 °C decrease of the FLiBe salt temperature if it is used in the 1D code NACCO rather than the original value adopted as shown in Figure 3-28. The new Nusselt number generally lead to a smaller discrepancy between the predictions and experimental data.

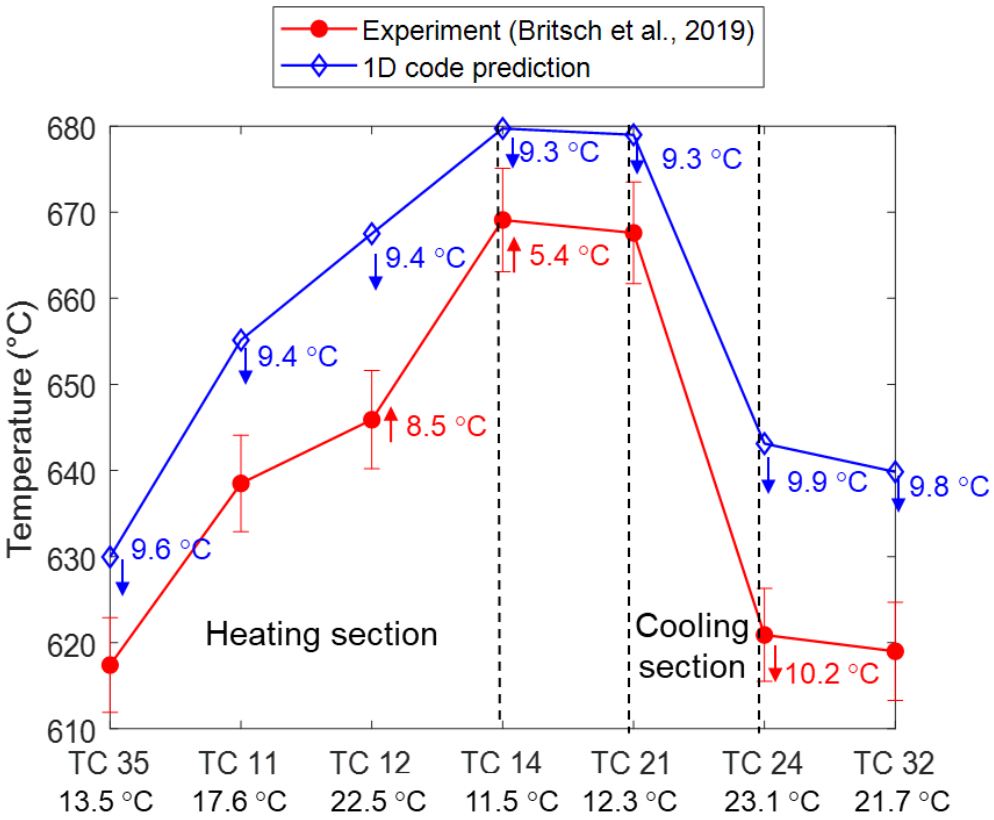

Figure 3-28 Variation of the FLiBe salt temperature considering accurate Nusselt number obtained in the CFD study for the top cooler and bulk temperature in the experiments (Britsch et al., 2019) for Test #3

The bulk temperature, defined as Eq. (2-22), is calculated to justify the second potential reason. Figure 3-29 shows the radial temperature profiles of the FLiBe salt at different axial locations in Test #3: Locations of TC12 and TC24. Assuming a fully-developed velocity profile and utilizing the radial temperature profile measured in the experiments (Britsch et al., 2019) as plotted in Figure 3-29(a), the FLiBe salt bulk temperature at the location of TC 12 becomes 654.4 °C, 8.5 °C larger than its centerline temperature measured by the thermocouple.

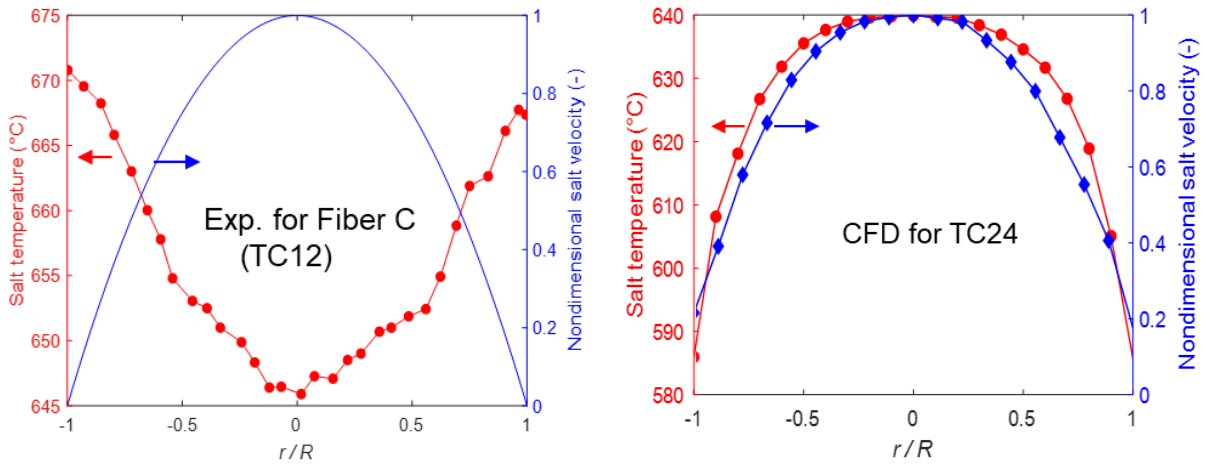

(a) (b)

Figure 3-29 Radial temperature profiles of the FLiBe salt at different axial locations in Test #3: Locations of (a) TC12 and (b) TC24

Similarly, the FLiBe salt bulk temperatures at the location of TC 24, the outlet of the heating section, becomes 674.5 °C, 5.4 °C larger than its centerline temperature measure by the thermocouple. This is because the FLiBe salt temperature close to the wall in the heating section is much higher than its centerline temperature. Utilizing the FLiBe salt bulk temperature rather than the centerline temperature for the code benchmark study, the discrepancy between the predictions and experimental data becomes smaller for the FLiBe salt in heating section.

Similar analysis could be applied to calculate the bulk temperature of the FLiBe salt at the location of TC 12 as shown in Figure 3-29(b), the outlet of the top cooler. Another way is to directly use a built-in function in STAR-CCM+ for the bulk temperature. The bulk temperature for the FLiBe salt at the location of TC 12 is 10.2 °C smaller than its centerline temperature as shown in Figure 3-28. This is because the FLiBe salt temperature close to the cooler wall is much lower than its centerline temperature. Utilizing the FLiBe salt bulk temperature rather than the centerline temperature for the benchmark study, the discrepancy between the predictions and experimental data remains nearly the same value, 23°C, for the FLiBe salt in the cooling section.

Figure 3-30 shows comparison of the FLiBe salt temperature between the experiments (Britsch et al., 2019) and 1D code NACCO predictions considering the effects of buoyancy and radiative heat transfer for Test #5. The FLiBe salt temperature profile along the loop predicted by the 1D code NACCO is agreeable with the experimental data. In addition, the relative salt temperature difference between the 1D code NACCO predictions and experimental data ranges from 3.2% to 5.3%.

Another observation is that the FLiBe salt temperature predicted is 23.4 °C to 35.4 °C higher than the experimental data, which may result from the underestimation of the heat removal rate by the top cooler and/or large difference between the bulk temperature and centerline temperature as discussed earlier for Test #3. A CFD study has been performed for the top cooler for Test #5, where the Nusselt number calculated through the CFD study is about 27% larger than the correlation results, leading to 20.9 °C to 22.2 °C decrease of the FLiBe salt temperature as shown in Figure 3-30.

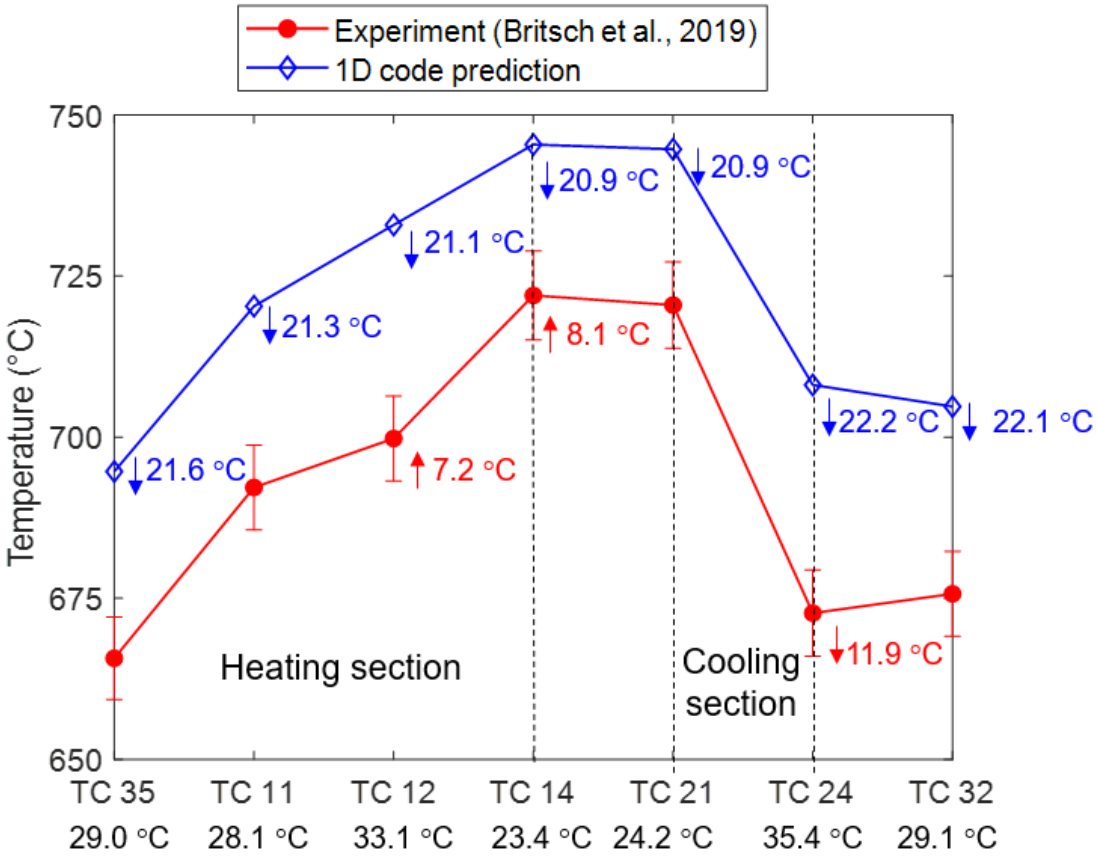

Figure 3-30 Variation of the FLiBe salt temperature considering accurate Nusselt number obtained in the CFD study for the top cooler and bulk temperature in the experiments (Britsch et al., 2019) for Test #5

As for the bulk temperature, it is 707.0 °C for the FLiBe salt at the location of TC12 and 730.1 °C at TC14, 7.2 °C and 8.1 °C larger than their centerline temperatures as shown in Figure 3-30, respectively. Similarly, the FLiBe salt bulk temperatures at the location of TC 24, the outlet of the heating section, is 11.9 °C smaller than its centerline temperature as shown in Figure 3-30. Utilizing the new Nusselt number obtained through a CFD analysis for the top cooler and FLiBe salt bulk temperature for the benchmark study, the discrepancy between the 1D code NACCO predictions and experimental data significantly decreases for Test #5.

The 1D code NACCO predictions are generally in line with the FLiBe salt temperature in the experiments (Britsch et al., 2019) in terms of the overall trend and relative temperature difference. Although the absolute salt temperature difference could be as high as about 35 °C, it seems to be acceptable considering the FLiBe salt temperature up to 750 °C and the significantly reduced temperature difference if an accurate heat transfer correlation is applied to the heat sink. The higher predictions for the FLiBe salt temperature suggest that the 1D code NACCO is conservative for the design of natural circulation loops, such as the passive decay heat removal system.

In addition, although it is better to use the bulk temperature for code benchmark, it is usually unavailable since both the radial temperature and velocity profiles are needed. The benchmark study for Tests #3 and #5 also suggests that the difference between the centerline temperature and bulk temperature ranges from 5 to 10 °C for the FLiBe salt centerline temperature up to 750 °C.

3.5 Summary

An in-house 1D code NACCO was developed considering the effects of buoyancy and radiative heat transfer in molten salts. It was then benchmarked with three natural circulation experiments using water, nitrate salt $NaNO_3$-KNO_3 (60-40 wt%), and fluoride salt FLiBe as the working fluids, respectively.

Several concluding remarks are summarized as follows:

(1) The effects of buoyancy and radiative heat transfer are negligible for low-temperature experiments utilizing water as the working fluid, but they need to be evaluated for high-temperature experiments utilizing molten salts as coolants to have accurate predictons.

Usually, they are non-negligible for molten salts in natural circulation loops, where the salts are in the laminar flow regime;

(2) The 1D code NACCO considering both the effects of buoyancy and radiative heat transfer in molten salts captures the overall trend of the axial temperature profile. In addition, if the salt centerline temperature in the experiment is used as a reference, the 1D code overestimates the salt temperature by < 18 °C for the nitrate salt centerline temperature up to 450 °C and < 35 °C for the FLiBe salt centerline temperature up to 750 °C.

(3) An accurate heat transfer correlation for the main heat sink, such as the tube-in-tube cooler in the experiment, is strongly suggested since it affects the code predictions for the salt temperatures significantly;

(4) The salt bulk temperature is more meaningful for the code benchmark study compared with its centerline temperature. However, it is usually unavailable since both the radial temperature and velocity profiles are not necessarily be known in the high-temperature salt experiments. Through an analysis for the FLiBe salt natural circulation experiments (Britsch et al., 2019), the difference between the salt centerline temperature and bulk temperature ranges from 5 to 10 °C for the salt centerline temperature up to 750 °C.

Chapter 4 Thermal-Hydraulic Performance of Molten Salts in FLUSTFA

A prototypic DRACS design is initially proposed for a 3400-MWth solid-fuel MSR, AHTR. A scaling analysis is then performed to develop key non-dimensional characteristic numbers for the design of an IET facility, FLUSTFA. The 1D code NACCO will be finally used to predict the thermal-hydraulic performance of the FLiNaK salt in the IET facility FLUSTFA, including predictions for the shakedown test, overcooling, and overheating transients.

4.1 Design of the Prototypic DRACS

A typical DRACS includes a DHX, a NDHX, an air chimney, and associated piping. The prototypic DRACS design, as shown in Figure 4-1, is developed for the AHTR. It is designed to remove 8.5 MW, 0.25% of the full reactor power 3,400 MWth per one DRACS (Varma et al., 2012). ^{7}LiF-BeF_2 (66-34 mol%) works as the primary salt, while KF-ZrF_4 (58-42 mol%) works as the intermediate and DRACS salts.

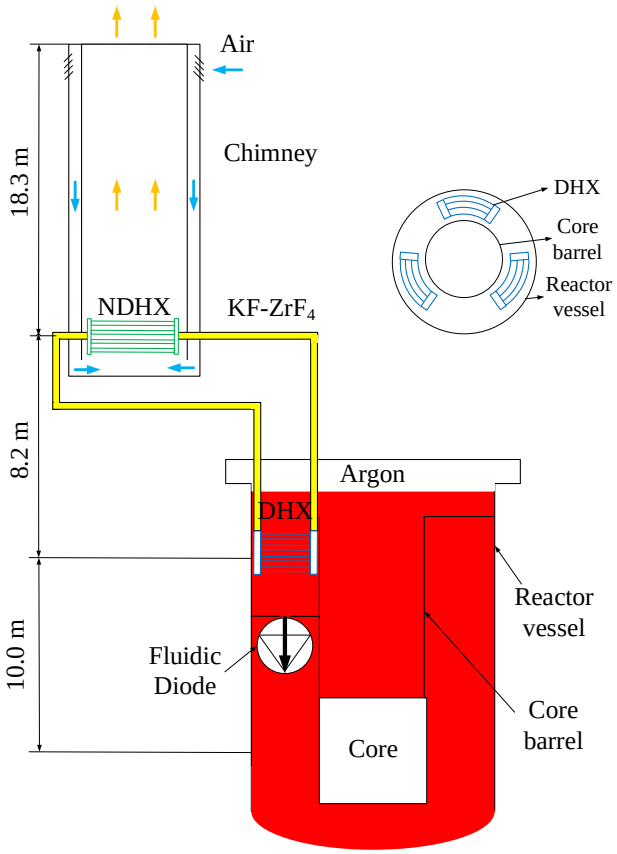

Figure 4-1 A prototypic DRACS design for the AHTR

Figure 4-2 shows a flowchart for the DRACS design, which is a coupled process for the DHX, NDHX, and air chimney designs. Input variables, such as the shell- and tube-side mass flow rates, thermal loads, and coolant inlet temperatures, should be initially specified for the DHX, NDHX, and air chimney designs. The thermal loads for the coolants FLiBe, KF-ZrF_4, and air, are set to be the same under steady-state conditions. The $H_{DHX\text{-}NDHX}$ and $H_{NDHX\text{-}chimney}$, which respectively represent the vertical distances between the DHX and NDHX, and the NDHX and air inlet location on the chimney, could be determined by equating the buoyancy with the flow resistance. $H_{core\text{-}DHX}$, the vertical distance between the core and DHX, is used to estimate the DHX shell-side FLiBe mass flow rate. A large $H_{core\text{-}DHX}$ is beneficial for the decay heat removal since it increases the DHX shell-side heat transfer coefficient by increasing the distance between the cold

and hot fluids (primary and DRACS salts) and therefore the salt mass flow rate. A maximum achievable value for $H_{core\text{-}DHX}$ is about 10 m for AHTR, which is then adopted in the current DRACS design.

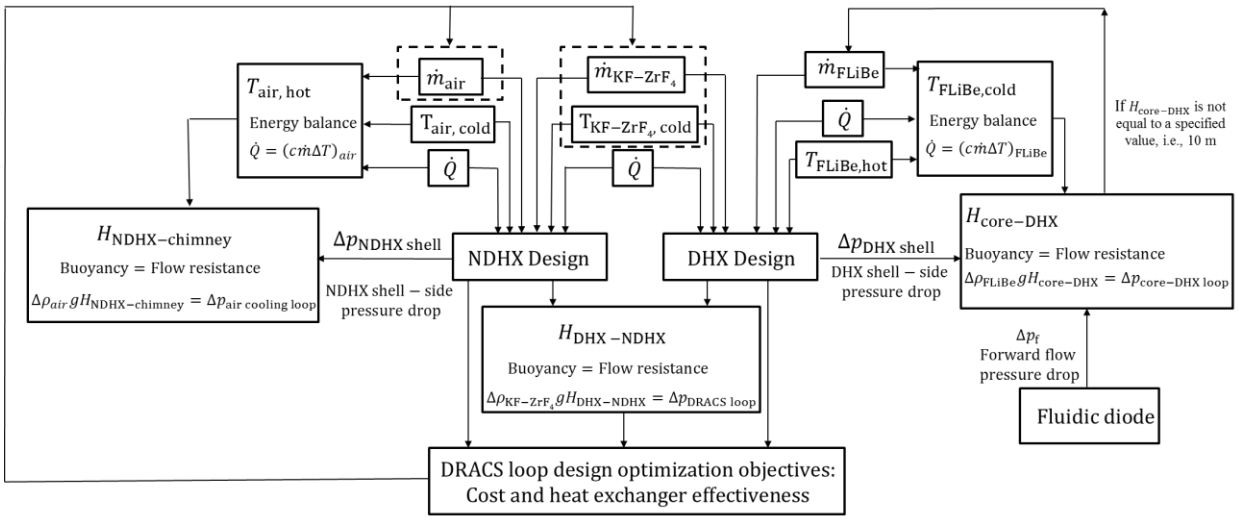

Figure 4-2 Flowchart for the DRACS design

The heat load for each DRACS loop is 8.5 MW and the inlet temperature of the DHX shell-side salt is set to be 700 °C. The NDHX tube length is a design variable, while the DHX tube length is fixed due to the limited physical space in the AHTR downcomer. Considering the available angular space in the downcomer for the DHXs, the average length of a DHX tube is set to be 3 m. The inlet temperature of the DHX tube-side salt is another design variable, which should be significantly higher than the salt melting temperature 390 °C (Rao, 1942) to maintain a certain safety margin. The TRACE simulation results presented in the literature (Wang et al., 2015) are used as references to set ranges for other variables, i.e., DHX tube-side salt and NDHX shell-side air mass flow rates.

Figure 4-3 shows the DRACS design optimization using the Non-dominated Sorting in Genetic Algorithms (NSGA) approach, which is normally used for multi-objective optimization problems (Srinivas and Deb, 1994). The arithmetic average HX effectiveness and the total cost are the two objectives adopted for the DRACS design optimization. The design points are scattered after one NSGA generation as shown in Figure 4-3(a). However, they are located on the pareto front, where optimum designs are located, after 50 NSGA generations as shown in Figure 4-3(b). Since the total DRACS construction cost and average HX effectiveness are two competitive optimization objectives, it is therefore impossible to achieve a maximum average HX effectiveness and a minimum cost simultaneously. The least squares in regression analysis is applied to identify one optimum design for the DRACS. Key design parameters for the optimum prototypic DRACS are summarized in Table 4-1. The prototypic DRACS design for the AHTR was presented in the literature (Zhang et al., 2019a).

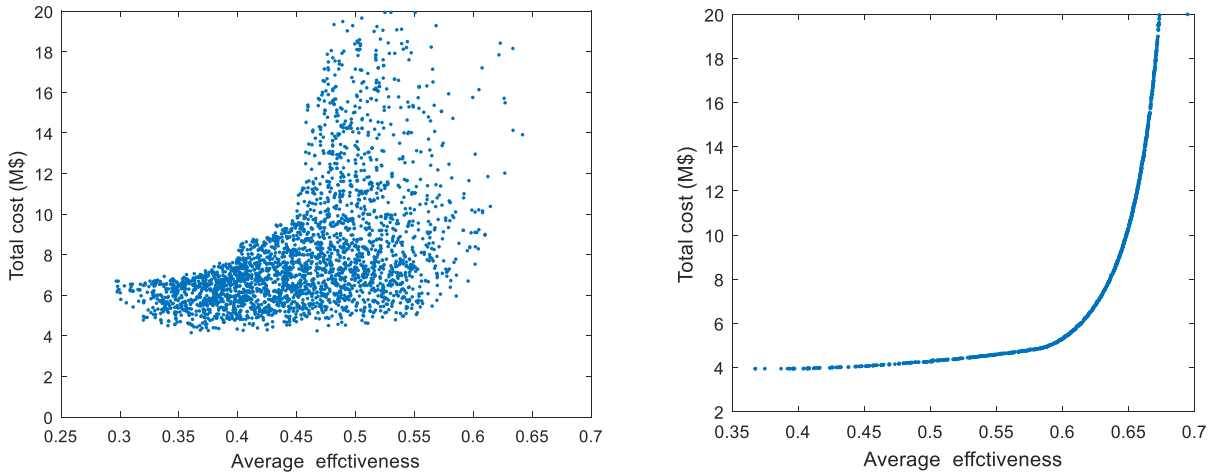

(a) (b)

Figure 4-3 DRACS design optimization after (a) one generation and (b) fifty generations

Table 4-1 Key design parameters for the AHTR DRACS

Flute tube size (mm)	D_{bi} = 10.67, D_{eo} = 16.64, T_w = 0.508, p = 8.23, N_s = 4, L = 3000
DHX/NDHX tube quantity	2100/2625
DHX and NDHX number of rows/columns	140/15 and 25/105
Pitch to diameter ratio	1.5
DHX and NDHX tube/shell-side fluids	KF-ZrF_4/FLiBe and KF-ZrF_4/Air
DHX and NDHX tube/shell-side mass flow rates (kg/s)	102.3/68.9 and 102.3/24.1
DHX and NDHX tube-side inlet/outlet temperatures (°C)	546/625 and 625/546
DHX and NDHX shell-side inlet/outlet temperatures (°C)	700/649 and 20/365
Heat removal capacity (MW)	8.5
DHX-NDHX vertical height difference (m)	8.15
DRACS loop piping diameter (m)	0.3
DRACS loop piping length (m)	56.3
Core-DHX vertical height difference (m)	10
NDHX-chimney vertical height difference (m)	18.3
Chimney inner / outer shell diameters (m)	3.7/4.7

4.2 Scaling Analysis

A scaling analysis is needed to design an IET facility, which can appropriately mimic the molten salt natural circulation in the prototypic DRACS proposed earlier for the AHTR. The scaling analysis includes several steps: (1) Develop governing equations for the DRACS; (2) Obtain non-dimensional characteristic numbers by non-dimensionalizing these governing equations; and (3) Establish similarity laws based on these non-dimensional characteristic numbers.

4.2.1 Governing Equations

Governing equations for a single-phase natural circulation loop can be written as (Ishii, 1984)

Continuity equation:

$$u_i = \frac{a_o}{a_i} u_r \tag{4-1}$$

Integral momentum equation:

$$\frac{\mathrm{d}u_r}{\mathrm{d}t}\left(\sum_i \frac{a_o}{a_i} l_i\right) = \beta g \rho \Delta T l_h - \frac{\rho u_r^2}{2}\left[\sum_i \left(\frac{f_i l_i}{d_i} + K_i\right)\left(\frac{a_o}{a_i}\right)^2\right] \tag{4-2}$$

Fluid energy equation for i^{th} section:

$$\rho c_p \left(\frac{\partial T}{\partial t} + u \frac{\partial T}{\partial z}\right) = \frac{4h}{d_h}(T_s - T) \tag{4-3}$$

Solid energy equation for i^{th} section:

$$\rho_s c_{ps} \frac{\partial T_s}{\partial t} + k_s \nabla^2 T_s - \dot{q}_s = 0 \tag{4-4}$$

The boundary condition between the fluid and solid for i^{th} section:

$$-k_s \frac{\partial T_s}{\partial y} = h(T_s - T) \tag{4-5}$$

where a, l, d, u, β, ρ, t, g, T, ΔT, f, K, c_p, z, y, h, k, and $\dot{q}$ are the flow area, axial length, hydraulic diameter, velocity, thermal expansion coefficient, density, time, gravitational acceleration, temperature, temperature difference, friction factor, form loss factor, specific heat capacity, axial coordinate, transverse coordinate, heat transfer coefficient, thermal conductivity, and volumetric heat generation, respectively. The subscripts i, 0, r, h, and s are the i^{th} section, initial value, representative variable, hot fluid section, and solid, respectively.

4.2.2 Non-dimensional Characteristic Numbers

Eqs. (4-1) to (4-5) can be non-dimensionalized by dimensionless parameters summarized in Table 4-2.

Table 4-2 Reference values and dimensionless parameters

Items	Reference values	Dimensionless parameters
Velocity	u_0: Fluid velocity at the inlet of the fluidic diode	$U_i = u_i/u_0\,, U_r = u_r/u_0$
Length	l_0: Vertical distance between thermal centers of the heat source and heat sink in a loop	$L_i = l_i/l_0\,, L_h = l_h/l_0$ $Z = z/l_0$
	δ_0: Conduction depth	$\nabla^{*2} = \delta^2/\nabla^2\,, Y = y/d$
Area	a_0: Cross-sectional area of the fluidic diode inlet	$A_i = a_i/a_0$
Time	l_0 / u_0	$\tau = tu_0/l_0$
Temperature	ΔT_0: Temperature difference across the heat source in a loop	$\theta = \Delta T/\Delta T_0$

The dimensionless governing equations are written as

Non-dimensional continuity equation:

$$U_i A_i = U_r \tag{4-6}$$

Non-dimensional integral momentum equation:

$$\frac{\mathrm{d}U_r}{\mathrm{d}\tau}\left(\sum_i \frac{L_i}{A_i}\right) = \mathrm{Ri}(\theta_h - \theta_c)L_h - \frac{U_r^2}{2}\left(\sum_i \frac{\mathrm{F}_i}{A_i^2}\right) \tag{4-7}$$

Non-dimensional fluid energy equation for i^{th} section:

$$\frac{\partial \theta_i}{\partial \tau} + \frac{U_r}{A_i}\frac{\partial \theta_i}{\partial Z} = \mathrm{St}_i(\theta_{si} - \theta_i) \tag{4-8}$$

Non-dimensional solid energy equation for i^{th} section:

$$\frac{\partial \theta_{si}}{\partial \tau} - \mathrm{T}^{*}\nabla_i^{*2}\theta_{si} - \mathrm{Q}_{si} = 0 \tag{4-9}$$

Non-dimensional boundary condition between the fluid and solid for i^{th} section:

$$\frac{\partial \theta_{si}}{\partial \mathrm{Y}_i} = \mathrm{Bi}_i(\theta_i - \theta_{si}) \tag{4-10}$$

The non-dimensional characteristic numbers in Eqs. (4-6) to (4-10) are defined as

Richardson number (ratio of the buoyancy and inertia force):

$$\mathrm{Ri} \equiv \frac{\beta g \Delta T_0 l_0}{u_0^2} \tag{4-11}$$

Friction number (ratio of the friction and inertia force):

$$\mathrm{F}_i \equiv \left(\frac{fl}{d} + K\right)_i \tag{4-12}$$

Modified Stanton number (ratio of the wall convection and axial convection):

$$\mathrm{St}_i \equiv \left(\frac{4hl_0}{\rho c_p u_0 d}\right)_i \tag{4-13}$$

Time ratio number (ratio of the transport time and conduction time):

$$\mathrm{T}_i^{*} \equiv \left(\frac{\alpha_s}{\delta^2}\frac{l_0}{u_0}\right)_i \tag{4-14}$$

Heat source number (ratio of the heat source and axial energy change):

$$\mathrm{Q}_{si} \equiv \left(\frac{\dot{q}_s l_0}{\rho_s c_{ps} u_0 \Delta T_0}\right)_i \tag{4-15}$$

Biot number (ratio of the wall convection and conduction):

$$\mathrm{Bi}_i \equiv \left(\frac{h\delta}{k_s}\right)_i \tag{4-16}$$

4.2.3 Similarity Laws

Similarity laws are established using the non-dimensional characteristic numbers developed earlier. For a non-dimensional characteristic number ψ, the similarity law is defined as

$$\psi_R \equiv \frac{\psi_m}{\psi_p} = \frac{\psi \text{ for model}}{\psi \text{ for prototype}} = 1 \tag{4-17}$$

Similarly, the similarity laws for the physical non-dimensional numbers are defined as

$$\mathrm{Ri}_R \equiv \left(\frac{\beta g \Delta T_0 l_0}{u_0^2}\right)_R = 1 \tag{4-18}$$

$$(\textstyle\sum_i \mathrm{F}_i/A_i^2)_R \equiv \left[\sum_i \left(\frac{fl}{d} + K\right)_i / (a_i/a_0)^2\right]_R = 1 \tag{4-19}$$

$$\mathrm{St}_{iR} \equiv \left(\frac{4hl_0}{\rho c_p u_0 d}\right)_{iR} = 1 \tag{4-20}$$

$$\mathrm{T}^*_{iR} \equiv \left(\frac{\alpha_s}{\delta^2}\frac{l_0}{u_0}\right)_{iR} = 1 \tag{4-21}$$

$$\mathrm{Q}_{siR} \equiv \left(\frac{\dot{q}_s l_0}{\rho_s c_{ps} u_0 \Delta T_0}\right)_{iR} = 1 \tag{4-22}$$

$$\mathrm{Bi}_{iR} \equiv \left(\frac{h\delta}{k_s}\right)_{iR} = 1 \tag{4-23}$$

In addition, the similarity laws for the geometrical non-dimensional numbers are defined as

$$A_{iR} = (a_i/a_0)_R = 1 \tag{4-24}$$

$$(\sum_i L_i/A_i)_R = 1 \tag{4-25}$$

4.2.4 Scaling Methodology

The scaling methodology starting from the reactor core scaling (Lv et al., 2015b) is adopted for the AHTR DRACS scaling analysis. Utilizing the energy balance equation under steady-state conditions

$$\dot{Q} = \rho c_p u_0 a_0 \Delta T_0 \tag{4-26}$$

and similarity law (4-18), the reference scales of the temperature difference and velocity can be obtained respectively as follows,

$$(\Delta T_0)_R = \left(\frac{\dot{Q}}{\rho c_p u_0 a_0}\right)_R \tag{4-27}$$

$$(u_0)_R = \left(\frac{\beta l_0 \dot{Q}}{\rho c_p a_0}\right)_R^{1/3} \tag{4-28}$$

Utilizing similarity laws (4-21) and (4-23), the time reference scale is given by

$$(\tau_0)_R = \left(\frac{l_0}{u_0}\right)_R = \left(\frac{k_s \rho_s c_{ps}}{h^2}\right)_R \tag{4-29}$$

There are five unknown variables, namely, $\left(\dot{Q}\right)_R, (u_0)_R, (l_0)_R, (a_0)_R,$ and $(\Delta T_0)_R$ in Eqs. (4-27) to (4-29). Therefore, two variables need to be specified for scaling analysis of molten salt

natural circulation in the reactor vessel (called "pool loop"). In this research, the power and length scales are specified for the pool loop.

For molten salt natural circulation in the DRACS loop, the similarity laws (4-27) and (4-28) hold as well. In addition, the convection time scales for the pool and DRACS loops are the same if the DHX tube thickness is much smaller than its inner diameter. If assuming (1) the decay heat is 100% removed by the DRACS and (2) negligible heat loss for the fluidic diode and piping, the power scale $(\dot{Q})_R$ for the DRACS loop should be the same as that for the pool loop. Therefore, only one variable needs to be specified for scaling analysis of the DRACS loop. In this research, the length scale is specified for the DRACS loop.

4.2.5 Scaling Results

Considering the lab power capacity and lab space constraint, the power and length scales are specified as 1/1250 and 1/10, respectively. Key scaling results for the IET facility FLUSTFA are summarized in Table 4-3.

Table 4-3 Key scaling results for the test facility

	Core	DHX shell side	DHX tube side	NDHX tube side
Q_{siR}	1.67	N/A	N/A	N/A
T_{iR}	0.10	0.46	0.80	0.69
B_{iR}	3.63	0.46	0.56	0.70
St_{iR}	0.14	0.34	0.45	0.53
Ri_R	2.44		5.56	
$\left(\sum_i F_i/A_i^2\right)_R$	1.95		3.64	
$\left(\sum_i L_i/A_i\right)_R$	15.52		0.72	

4.3 Design of the IET Facility FLUSTFA

FLUSTFA is comprised of a reservoir tank for salt storage and melting, a primary molten salt loop, a secondary molten salt loop, a closed air loop, and a chilled water loop as shown in Figure 4-4 and Figure 4-5. This salt facility uses FLiNaK (LiF-NaF-KF: 46.5-11.5-42 mol%) as the working fluids for both the primary and secondary salt loops, and operates up to 700 °C and near the atmospheric pressure.

The reservoir tank is wrapped with three band heaters to provide total 9 kW for salt melting. The primary molten salt loop consists of a simulated core where nineteen cartridge heaters are installed to provide a main heating power of 38 kW, shell side of a salt-to-salt HX (DHX) which exchanges heat between the primary and secondary fluids, primary molten salt pump for forced circulation of the primary coolant, high-temperature valves which adopt a dual-gasket system to avoid leakage, and stainless steel 316H piping. The secondary molten salt loop consists of the tube side of the DHX, tube side of a salt-to-air HX (NDHX), secondary molten salt pump for forced circulation of the secondary coolant, high-temperature valves, and stainless steel 316 piping. Twenty tape heaters installed on the primary and secondary molten salt loops provide total 8 kW for trace heating. The air loop consists of the shell side of the NDHX, shell side of an Air-to-Water HX (AWHX), air circulator, and stainless steel 304 piping. The chilled water loop includes the tube side of the AWHX which serves as the ultimate heat sink for the FLUSTFA, associated piping, etc.

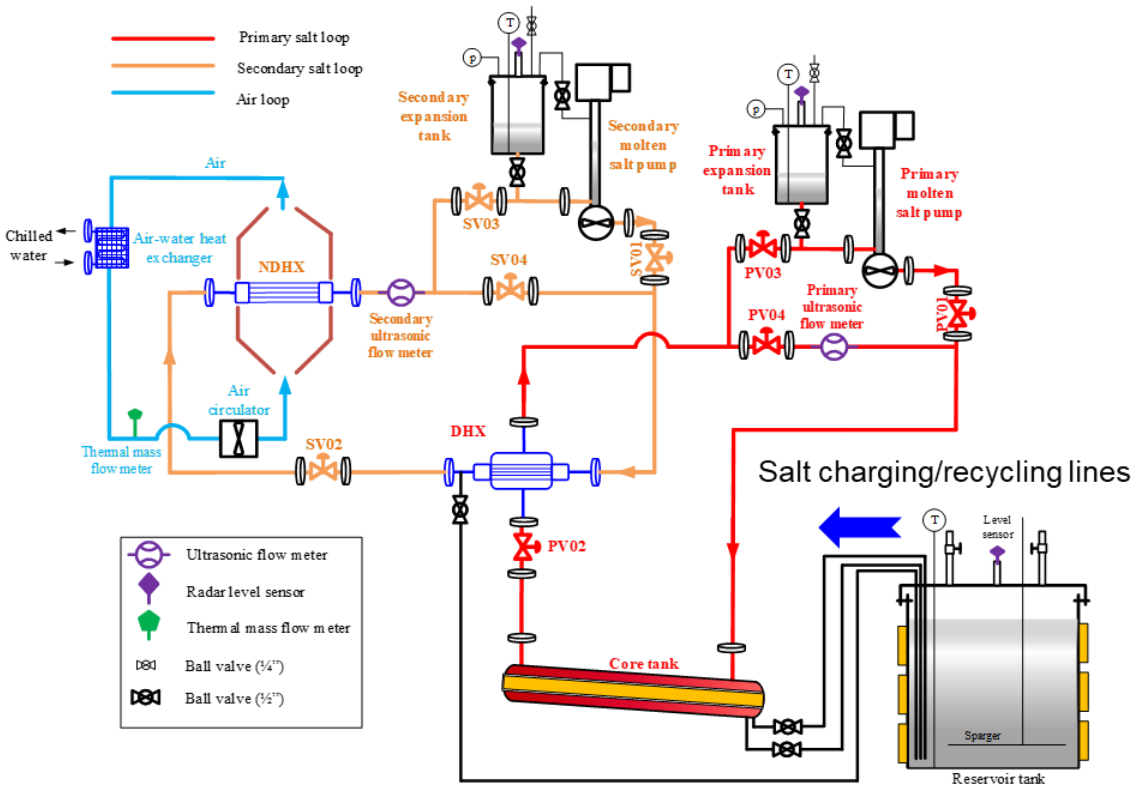

Figure 4-4 Schematic of the IET facility FLUSTFA

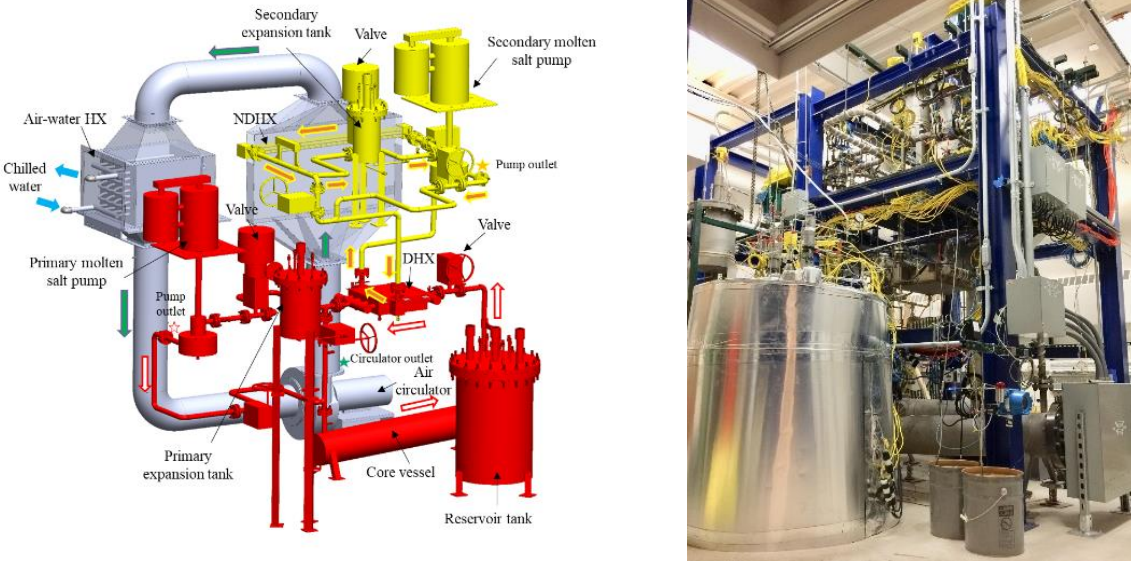

(a) (b)

Figure 4-5 (a) A 3D SOLIDWORKS model and (b) an image of the IET facility FLUSTFA

4.3.1 Simulated Core

It is necessary to know the thermophysical properties of the fuel assembly for the core scaling. Figure 4-6 shows the fuel assembly and fuel plate in the AHTR reactor core. There is a total of 252 fuel assemblies and each of them consists of 18 fuel plates. Each fuel plate has two fuel strip regions, one central matrix region, two exterior sleeves, and two spacer ridges. The fuel stripe and central matrix are considered in the core scaling.

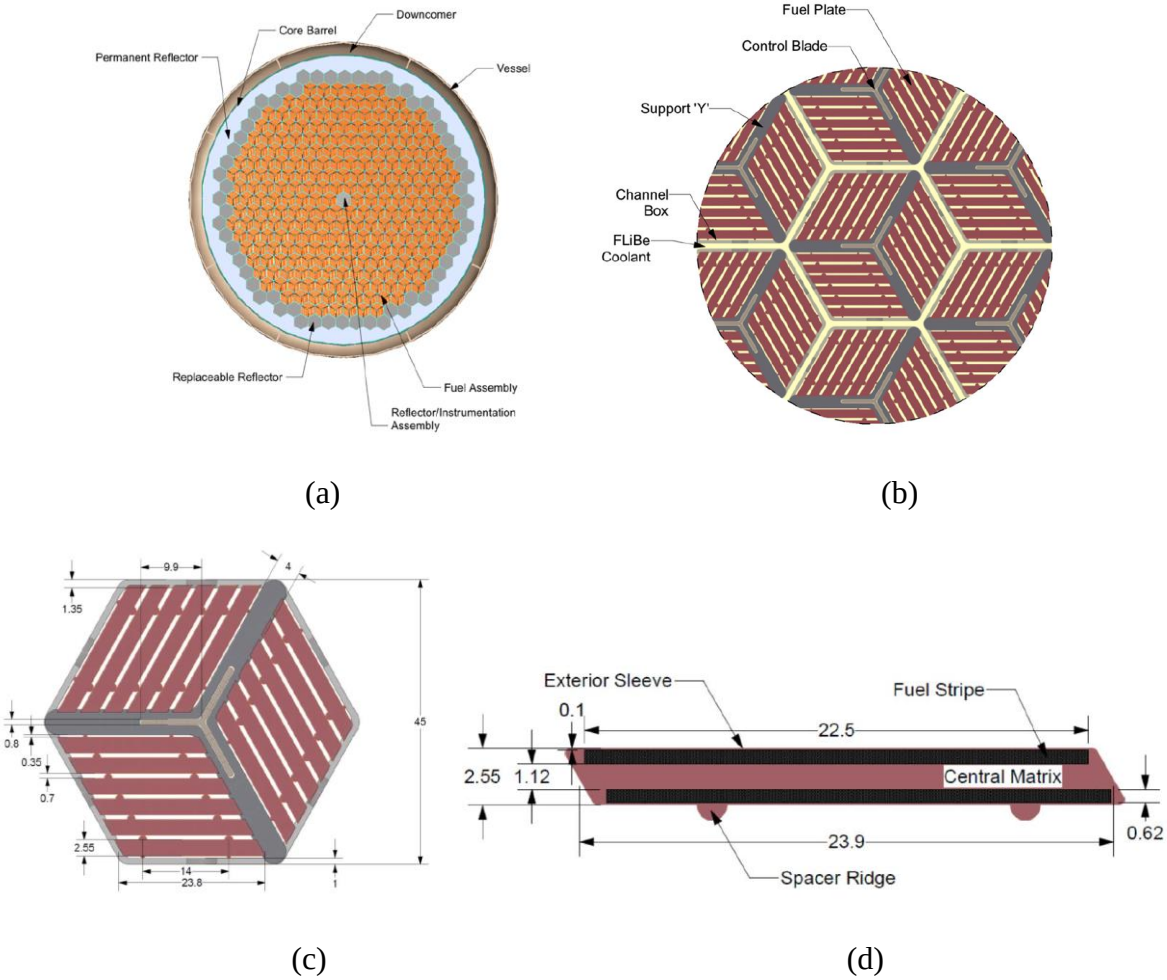

Figure 4-6 Cross-sectional view of (a) reactor vessel, (b) a group of fuel assemblies, (3) fuel assembly with dimensions, and (4) a fuel plate (unit: cm)

The effective density of a fuel plate is calculated based on the volume-averaged density of the fuel stripe and central matrix, which is defined as

$$\rho_{fp} = \frac{V_{fs}\rho_{fs}+V_{cm}\rho_{cm}}{V_{fp}} \tag{4-30}$$

where the subscripts *fp*, *fs*, and *cm* are the fuel plate, fuel stripe, and central matrix, respectively.

The effective specific heat capacity of a fuel plate is calculated based on the mass-averaged specific heat capacity of the fuel stripe and central matrix, which is defined as

$$c_{p,fp} = \frac{c_{p,fs}V_{fs}\rho_{fs}+c_{p,cm}V_{cm}\rho_{cm}}{V_{fp}\rho_{fp}} \tag{4-31}$$

The effective thermal conductivity of a fuel plate is calculated based on the thermal-resistance-averaged thermal conductivity of the fuel stripe and central matrix, which is defined as

$$k_{fp} = \frac{L_{fp}}{\left(\frac{L_{fs}}{k_{fs}A_{ht,fs}}+\frac{L_{es}}{k_{es}A_{ht,es}}\right)A_{ht,fp}} \tag{4-32}$$

where the subscripts *ht* and *es* are the heat transfer and exterior sleeve, respectively.

Utilizing the thermophysical properties of the fuel stripe and central matrix (Yoder et al., 2014b) summarized in Table 4-4 and Eqs. (4-30) to (4-32), the effective thermophysical properties of a fuel plate can be estimated and summarized in Table 4-4.

Table 4-4 Thermophysical properties of the fuel stripe, central matrix, and AHTR fuel plate

Items	Density (kg/m^3)	Specific heat (J/kg-K)	Thermal conductivity (W/m-K)
Fuel stripe	2250	708	24.0
Central matrix	3187	1191	43.8
Fuel plate	2758	1011	24.2

Next, we need to estimate the heat transfer coefficient of the primary salt flowing in the reactor core. The heat transfer correlation (Cohen and Rohsenow, 1984)

$$\mathrm{Nu} = \frac{1}{\sqrt{\frac{48}{\mathrm{Ra}} + \frac{2.51}{\mathrm{Ra}^{0.4}}}} \tag{4-33}$$

used for a natural circulation flow between two vertical plates is adopted to estimate the FLiBe salt heat transfer through the AHTR reactor core. The Rayleigh number is defined as

$$\mathrm{Ra} = \frac{\rho^2 g \beta c_p b^5 q''}{\mu L k^2} \tag{4-34}$$

where b and q" are the plate spacing and heat flux, respectively. It is estimated that the heat transfer coefficients for the FLiBe salt in the interior and wall channels in a fuel assembly are respectively 99.0 and 40.0 W/m^2-K under the steady-state mass flow rate of the FLiBe salt in the reactor core (three DRACS in operation). The effective heat transfer coefficient based on the heat transfer area is estimated to be 89.2 W/m^2-K.

Since this study is focused on the system-level thermal-hydraulic phenomenon, the simulated core is treated as a black box. Considering a relatively low friction factor, commercial availability, and cost, a simulated core vessel with straight cartridge heaters installed in a triangular arrangement is selected. Incoloy 800 is used as the sheath material with a thickness of 2.54 mm considering the good high-temperature resistant properties and relatively low corrosion rate at elevated temperatures (Olson et al., 2011). In addition, the heater sheath is filled with MgO. The thermophysical properties of MgO and Incoloy 800 sheath are summarized in Table 4-5. The effective thermophysical properties estimated by Eqs. (4-30) to (4-32) are calculated for the cartridge heater and summarized in Table 4-5.

Table 4-5 Thermophysical properties of MgO, Incoloy 800, and cartridge heater

Items	Density (kg/m^3)	Specific heat (J/kg-K)	Thermal conductivity at 800 °C (W/m-K)
MgO	3580	955	45.0
Incoloy 800	7950	460	24.7
Cartridge heater	5153	680	24.8

The dimension, pitch ratio, and quantity for cartridge heaters depend on the flow conditions, available lab power supply, lab space constraint, and some engineering concerns, such as the minimum space needed for the compression fittings to seal these cartridge heaters. Finally, a nineteen-heater core as shown in Figure 4-7 and Figure 4-8 is adopted as the simulated core.

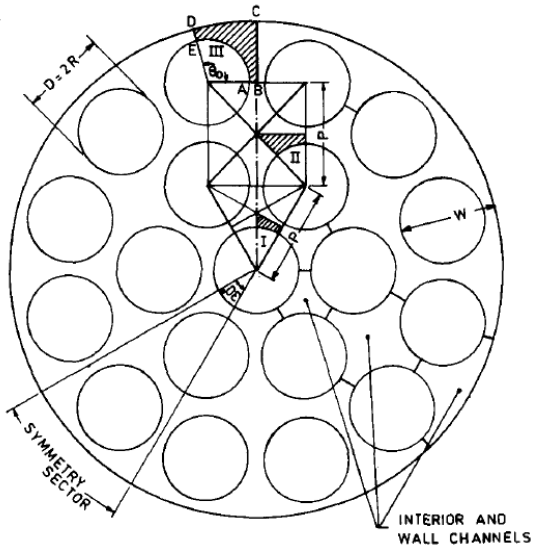

Figure 4-7 Cartridge heater arrangement (Mohanty and Sahoo, 1986)

Figure 4-8 Triangular arrangement of the nineteen cartridge heaters

The design specification for the simulated core includes: (1) Nineteen cartridge heaters; (2) Pitch ratio = 2; (3) 25.4 mm Outer Diameter (OD) for each heater; (4) 1.3-m heated section; (5) 2 kW heating power for each heater; (6) 208 V, single phase; and (7) a SS 316H vessel of NPS 10", Sch40. The average heat transfer coefficient for the FLiBe salt flowing in the simulated core is estimated to be 141.2 W/m^2-K using the extrapolated experimental values (Mohanty and Sahoo, 1986). The maximum temperature of the heater sheath is identified to be 794.2 $^{\circ}$C by STAR-CCM+, lower than the allowable temperature 815.6 $^{\circ}$C suggested by the vendor.

4.3.2 HXs

KF-ZrF_4 has been proposed as the DRACS salt in the AHTR (Varma et al., 2012), while FLiNaK is adopted as the working fluid in the IET facility FLUSTFA. To cover the KF-ZrF_4 salt Prandtl number range in the AHTR, the FLiNaK salt temperature on the NDHX tube side needs to span approximately from 535 to 565 $^{\circ}$C as shown in Figure 4-9(a). To achieve a safety margin from freezing, the FLiNaK salt working temperature should be higher than its melting temperature 454 °C (Bergman and Dergunov, 1941) by a certain level. Therefore, the lower limit of the FLiNaK

salt working temperature is set to be 550 ˚C, which provides an about 100 ˚C margin above its melting temperature. The NDHX tube length is set to be 1.32 m to achieve a relatively large temperature difference (15 °C) on the NDHX tube side as shown in Figure 4-9(b).

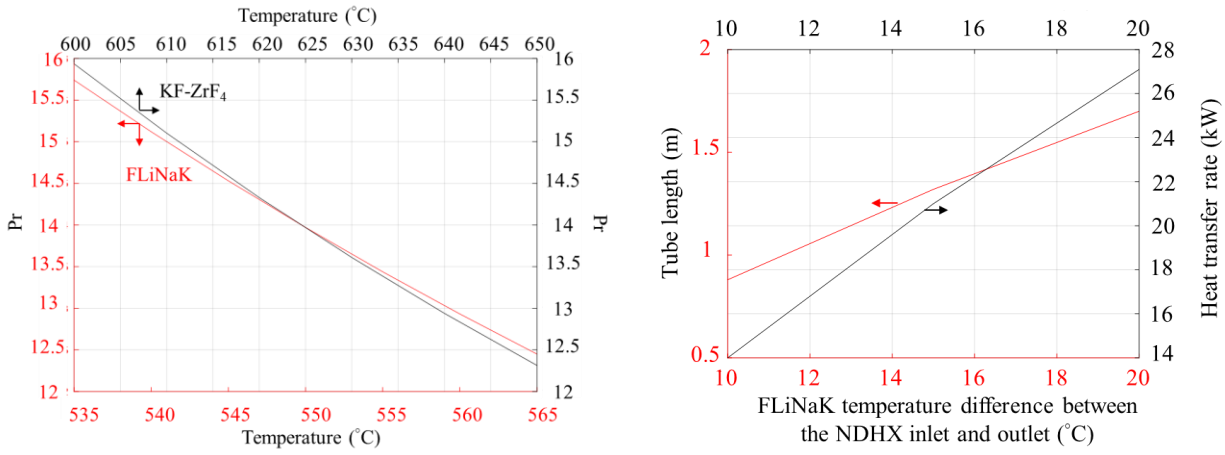

Figure 4-9 (a) Prandtl numbers of $KF\text{-}ZrF_4$ and FLiNaK and (b) identification of the NDHX tube length

FLiBe has been proposed as the primary coolant in the AHTR (Varma et al., 2012), while FLiNaK is the working fluid in the IET facility FLUSTFA. To cover the FLiBe salt Prandtl number range in the AHTR, the FLiNaK salt working temperature on the DHX shell side needs to span from 545 to 585 ˚C as shown in Figure 4-10(a). However, the FLiNaK salt temperature on the DHX shell-side should be much higher than the FLiNaK salt temperature on the DHX tube-side to achieve a relatively large salt temperature difference on the DHX shell-side and a reasonable DHX tube length as shown in Figure 4-10(b). The FLiNaK salt temperature on the DHX shell side inlet and the DHX tube length are therefore set to be 700 °C and 0.45 m, respectively.

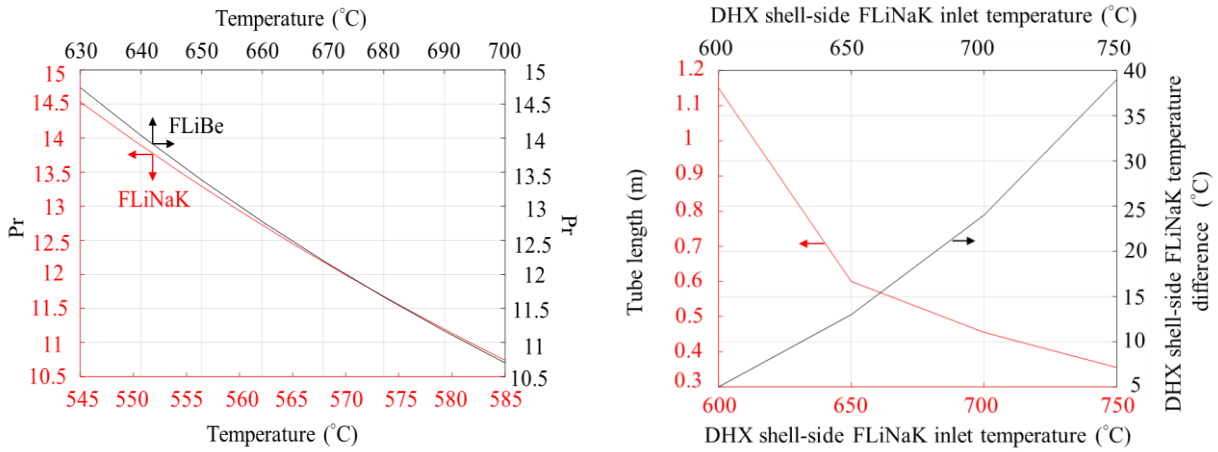

(a) (b)

Figure 4-10 (a) Prandtl number of FLiBe and FLiNaK and (b) identification of the DHX tube length

Figure 4-11 shows photos of the two lab-scale HXs, DHX and NDHX, and their dimensions are summarized in Table 4-6. The lab-scale HX designs was presented in detail in the literature (Zhang et al., 2019b).

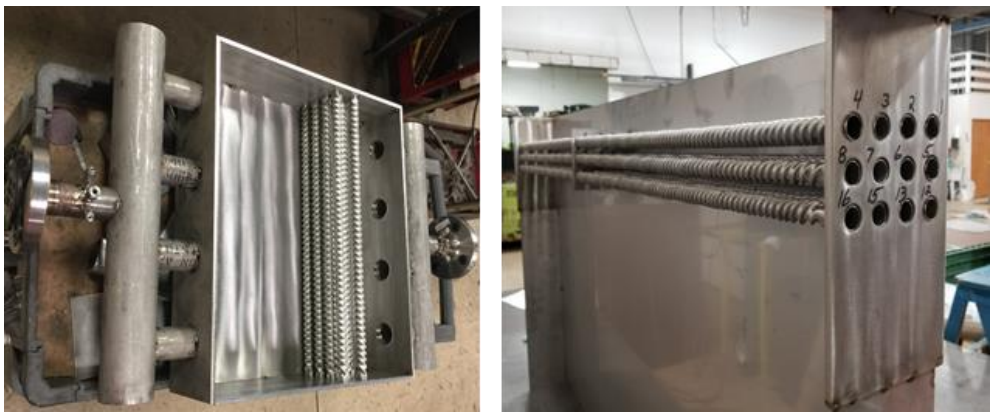

(a) (b)

Figure 4-11 Photos of the lab-scale (a) DHX and (b) NDHX

Table 4-6 Key design parameters for lab-scale HXs

Items	DHX	NDHX
Tube material	SS 316	
Flute tube size (mm)	D_{bi} = 10.67, D_{eo} = 16.64, T_w = 0.508, p = 8.23, N_s = 4, L = 3000	
Tube configuration	Staggered	Inline
Tube in each row	4/3/4	4/4/4
Pitch to envelope diameter ratio	1.5	
Tube length (m)	0.45	1.32
Tube/shell-side fluids	FLiNaK/FLiNaK	FLiNaK/Air

4.3.3 Fluidic Diode, Piping, and Air Chimney

The fluidic diode, piping, and air chimney need to be scaled. One key scaling requirement for these components is to maintain the scaling law Eq. (4-19), which is related to the friction factor number in both the prototype and test facility. No fluidic diode is adopted in the test facility to make the non-dimensional number $(\sum_i \mathrm{F}_i/A_i^2)_R$ close to 1. Although this simplification makes the test facility lose the capacity to model reverse flows, it keeps the capacity to model forward flows, which is essential for long-term cooling. Another major difference compared with the prototypic DRACS design is that the forced circulation is adopted for the NDHX shell-side air. This is mainly due to the lab constraint, which is located in the basement. This change however brings one advantage that it is convenient to keep a constant air inlet temperature for the NDHX in the experiments.

4.3.4 Molten Salt Pump

Most molten salt facilities used vertical cantilever shaft pumps (Sabharwall et al., 2010), which made an extra tank a necessity for each pump. Considering the lab space constraint and cost, a vertical cantilever dry pit pump, an in-line pump as shown in Figure 4-12, was used for each of

the two molten salt loops in the IET facility FLUSTFA to supply 7.9 m (26') FLiNaK head under 1.9×10^{-3} m^3/s (30 GPM). The wetted parts of the molten salt pumps are made of SS 316H.

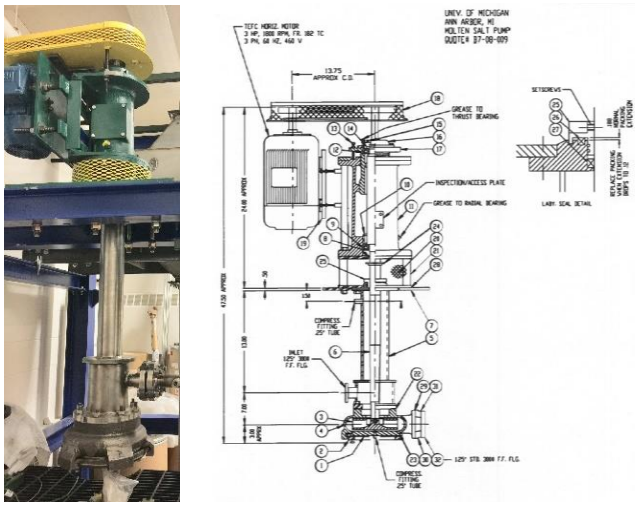

Figure 4-12 Vertical cantilever dry pit pump

One concern for the molten salt pump is the temperature control for the pump shaft seal. Since the graphite intensively reacts with oxygen at elevated temperatures, the pump shaft seal made of graphite is suggested to be used at temperatures lower than 455 ˚C, which is much lower than the salt working temperature in the IET facility FLUSTFA (550 – 700 °C). If the pump shaft seal fails, pump may not work property due to the severe corrosion of the pump shaft in the environment of the salt vapor, oxygen and moisture. Therefore, it is necessary to ensure the pump shaft seal temperature to be lower than its allowable working temperature. A long pump column is one option to avoid the pump shaft seal working at elevated temperatures.

ANSYS Fluent is used to identify the length needed for the pump column. The numerical study suggests that a 381-mm height column for the primary pump is sufficient to reduce the pump shaft seal temperature to 394.9 ˚C and a 254-mm height column for the secondary pump is

sufficient to reduce the pump shaft seal temperature to 401.9 °C. Therefore, the distance between the salt level and the mounting plate should be at least 381 mm and 254 mm respectively for the primary and secondary molten salt pumps to avoid the pump shaft seal temperature exceeding its temperature limit. To avoid the pump impeller exposure and cover gas entrainment, the minimum salt level recommended is 127 mm away from the centerline of the pump suction flange. Further considering the lab height constraint, the pump column height is finally identified to be 635 mm and 432 mm for the primary and secondary molten salt pumps, respectively.

4.3.5 Other Key Components

High-temperature valves

The IET facility FLUSTFA requires a total of eight valves to be installed for HX testing and investigation of the molten salt natural circulation. To reduce the possibility of leakage and ensure the valves working properly at elevated temperatures, a dual-gasket system is used. The primary gasket serves as the first set of the seal, which is a spiral-wound construction with a SS 316 winding and a flexible graphite filler, while the secondary gasket serves as the second set of the seal, which is made of Flexitallic Thermiculite 715 material.

Vessels/Tanks and Flange Gasket

Stainless steel 316H has been selected as the material for the reservoir tank, two expansion tanks, and core vessel considering the ASME Section VIII code requirement, relatively low cost, and good corrosion resistance with FLiNaK at elevated temperatures (Zhang et al., 2017a).

Considering the required FLiNaK inventory in the primary and secondary molten salt loops (5.15 ft^3), the dimensions for the reservoir tank are NPS 24”, height 40”, and volume 9.82 ft^3. To

accommodate the variation of the molten salt volume during transient tests, a primary expansion tank and a secondary expansion tank have been installed in the primary and secondary molten salt loops, respectively. The dimensions for the primary and secondary expansion tanks are NPS 12", height 20", volume 1.3 ft^3, and NPS 8, height 18", volume 0.5 ft^3, respectively.

The core vessel serves as a container for nineteen cartridge heaters, which provide the main heating power for the IET facility FLUSTFA. Considering the size and quantity for cartridge heaters, and the lab space constraint, the dimensions for the core vessel are NPS 10", length 68", and volume 3.1 ft^3. Figure 4-13 shows photos of the key components, including high-temperature valves, AWHX, air circulator, and tanks/vessels. In addition, the flange gasket used in the IET facility FLUSTFA is a spiral-wound gasket, which consists of an outer metal ring made of SS 316, an inner metal ring made of SS 316, and Flexitallic Thermiculite 835 filler.

Figure 4-13 Photos of the high-temperature valves, air-water HX, air circulator, and tanks/vessels

4.3.6 Instrumentation

A number of parameters, such as the heater power, flow rate, temperature, salt level, pressure/differential pressure, gas hazards are recorded and/or detected by instrumentation.

Power Measurement

There are three types of heaters installed in the IET facility FLUSTFA: (1) Nineteen cartridge heaters in the simulated core vessel to provide a total of 38 kW main heating power; (2) Three band heaters (total 9 kW) to be wrapped around the reservoir tank for salt melting; and (3) Twenty tape heaters (total 8 kW) to be wrapped on piping and vessels/tanks for trace heating. To control and monitor these heaters, electrical components, such as temperature controller, SCR, fuse, watt transducer, etc., are needed. For convenient control, cartridge heaters are divided into two groups: Group I with ten heaters and Group II with nine heaters. Similarly, band heaters are combined as one group and twenty tape heaters are divided into two groups evenly.

Figure 4-14 and Figure 4-15 show the wiring diagrams for the cartridge heaters, band and tape heaters, respectively. The power for cartridge heaters could be adjusted and recorded by an ASPYRE power controller. The power for band heaters is adjusted by a watt transducer, Watlow DC20-20S0-0000. The power for tape heaters is adjusted by a watt transducer, Watlow DC31-20S0-000, and recorded by three current transmitters. Temperature controller is operated in the PID mode to prevent overheating of these heaters. All I&C components are enclosed in the control panels as shown in Figure 4-16.

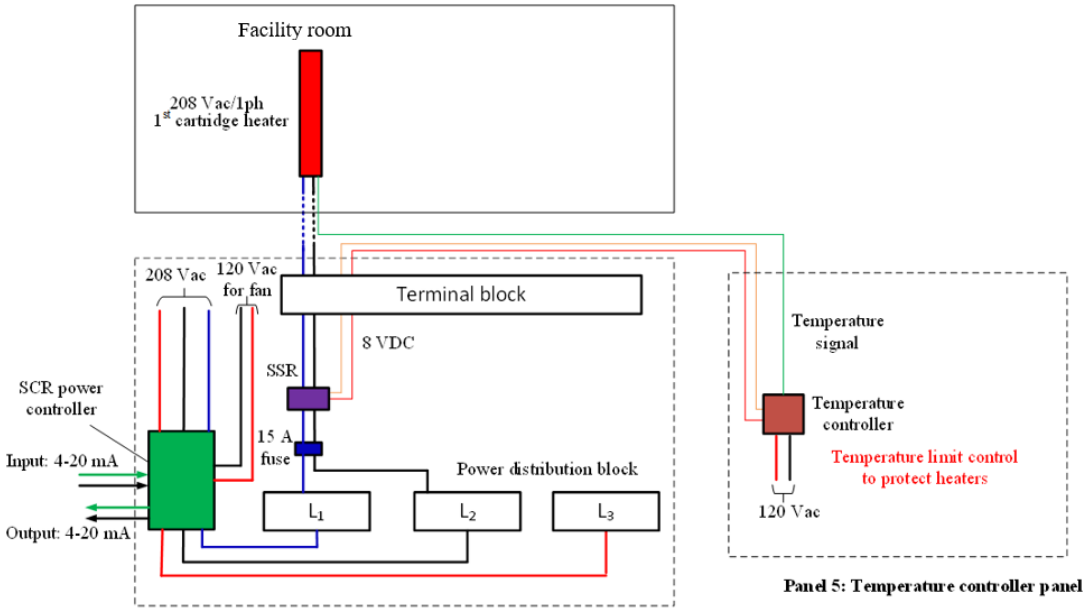

Figure 4-14 Wiring diagram for cartridge heaters in Panels #1 and #2

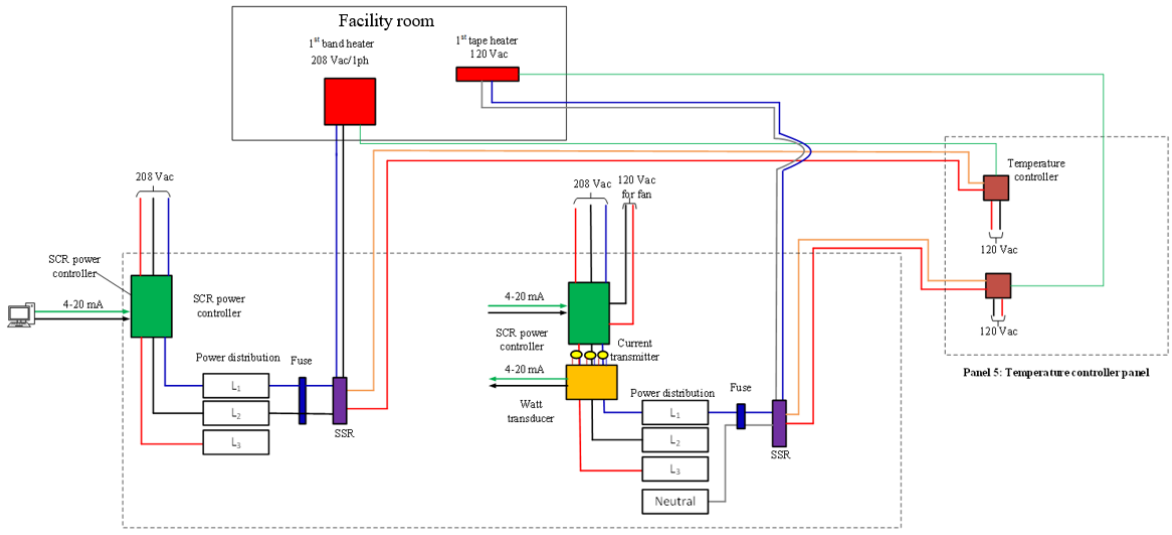

Figure 4-15 Wiring diagram for band heaters and tape heaters in Panels #3 and #4

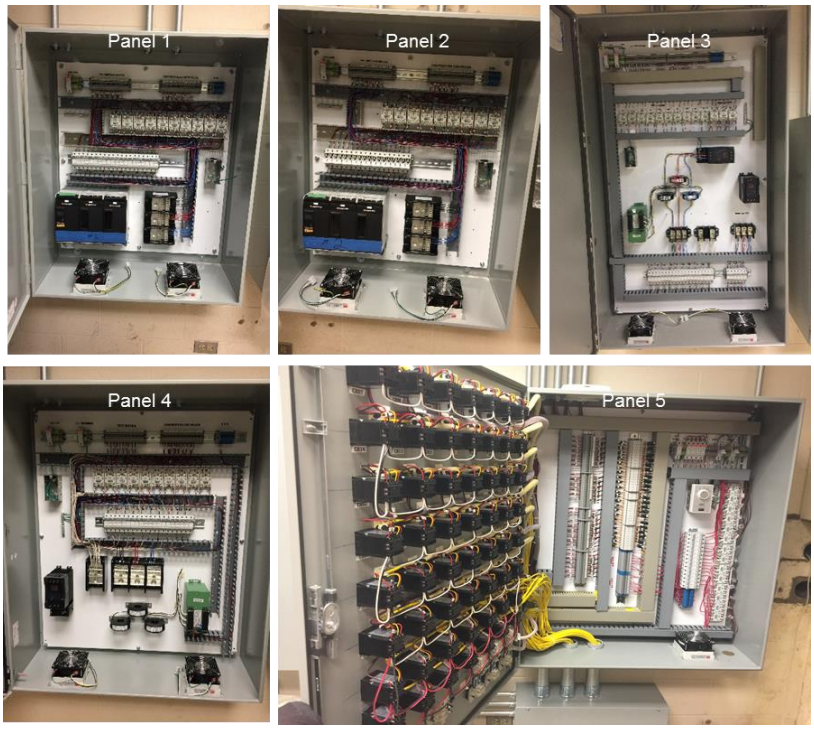

Figure 4-16 Photos of Panels #1 to #5

Flow Rate Measurement

The FLiNaK flow rate in the IET facility FLUSTFA can be automatically controlled by the molten salt pump on each loop using a Variable Frequency Drive (VFD) purchased from Automationdirect Inc., with a model number of GS3-23P0. The salt flow rate on each loop is measured by an ultrasonic flow meter, which has a 4-20 mA output recorded by LABVIEW. The specification for the ultrasonic flow meter is summarized in Table 4-7 and its photo is shown in Figure 4-17.

The air flow rate in the air loop can be automatically controlled by the air circulator using a VFD purchased from Automationdirect Inc., with a model number of GS3-2015. The air circulator has a capacity to provide a static gauge pressure of 15-inch water head for air at a flow rate of 2500 cfm (cubic feet per minute). The air flow rate is measured by a thermal mass flow

meter, Model 9840MPNH-INT-SS133-DC24-MW050-10”-Air purchased from Eldridge Products Inc., which has a 4-20 mA output recorded by LABVIEW. The specification for the thermal mass flow meter is summarized in Table 4-7 and its photo is shown in Figure 4-17.

The chilled water flow rate is currently manually controlled and measured by a rotameter, F-2000 purchased from Blue-White Industries Ltd., which has a 4-20 mA output recorded by LABVIEW. The specification for the rotameter is summarized in Table 4-7 and its photo is shown in Figure 4-17.

Salt Level Measurement

The salt level in the reservoir tank, primary and secondary expansion tanks needs to be measured. Due to the high working temperature conditions, a radar level sensor purchased from SW Controls Inc., with a model number of VEGAPULS 64 is used. The specification for the radar level sensor is summarized in Table 4-7 and its photo is shown in Figure 4-17.

Gas Flow Control

The flow rate of the cover gas nitrogen needs to be controlled for salt charging to the loop and salt recycling from the loop. A flow controller purchased from Teledyne Hastings Instruments, Inc is used for the cover gas nitrogen. The specification for the gas flow controller is summarized in Table 4-7 and its photo is shown in Figure 4-17.

Gas Sensor

HF and H_2 are generated during the salt melting process. Since HF is irritating and corrosive and H_2 is flammable, both of them need to be measured. In addition, it is beneficial to

measure the H_2O and O_2 concentrations in the off-gas line. The specifications for these gas/moisture sensors are summarized in Table 4-7 and their photos are shown in Figure 4-17.

Temperature Measurement

The salt temperature is measured by high accuracy K-type thermocouples with uncertainties of ±1.1 °C or ±0.4%, while the wall temperatures of tanks/vessels and HXs are measured by standard K-type thermocouples with uncertainties of ±2.2 °C or ±0.75%. The temperatures of air and chilled water are measured by high accuracy T-type thermocouples with uncertainties of ±0.5 °C or ±0.4%. The specifications for these thermocouples are summarized in Table 4-7.

Pressure and Differential Pressure Measurement

The cover gas nitrogen pressures in the reservoir tank, primary and secondary expansion tanks are measured by high accuracy pressure transducers. In addition, the Differential Pressure (DP) across the NDHX shell side is measured by a DP transducer.

Table 4-7 Instrumentation for flow rate measurements and gas/moisture detection in the IET facility FLUSTFA

Items	Measuring parameter	Range	Accuracy
Ultrasonic flow meter	Salt velocity	0.01 - 25 m/s	± (1.6% of reading + 0.01) m/s
Thermal mass flow meter	Air flow rate	0 - 2500 cfm	± (2% of reading + 1% of full scale) cfm
Rotameter	Chilled water flow rate	3 - 30 gpm	± 1% of full scale
Radar level sensor	Salt level	0 - 30 m	± 2 mm
Gas flow controller	Control gas flow rate	0 - 5 L/min	± 1% of full scale
HF sensor	HF concentration in the air	0 - 20 ppm	± 0.1 ppm
H_2 sensor	H_2 concentration in the off-gas line	1% warning 2% alarming	--
O_2 sensor	O_2 concentration in the off-gas line	0 - 1%, 0 - 25% 0 – 10 ppm, 0 – 100 ppm, 0 - 1000 ppm	± 1% of full scale
H_2O sensor	H_2O concentration in the off-gas line	0.1 - 100 ppm	± 0.1 ppm
Thermocouple	Salt temperature (K type)	-270 -1260 °C	±1.1 °C or ±0.4%
	Wall surface temperature (K type)	-270 -1260 °C	±2.2 °C or ±0.75%
	Insulation/air/chilled water temperature (T type)	-270 -370 °C	±0.5 °C or ±0.4%.

Figure 4-17 Photos of instrumentation used in the IET facility FLUSTFA

4.3.7 Gas/Salt Flow Control System

A gas/salt flow control system as shown in Figure 4-18 is used to fulfill the following three functions: (1) Vacuum and charge the cover gas nitrogen to the reservoir tank, primary and secondary molten salt loops; (2) Charge the FLiNaK salt from the reservoir tank to the primary and secondary molten salt loops; (3) Recycle the FLiNaK salt from the primary and secondary molten salt loops to the reservoir tank for storage.

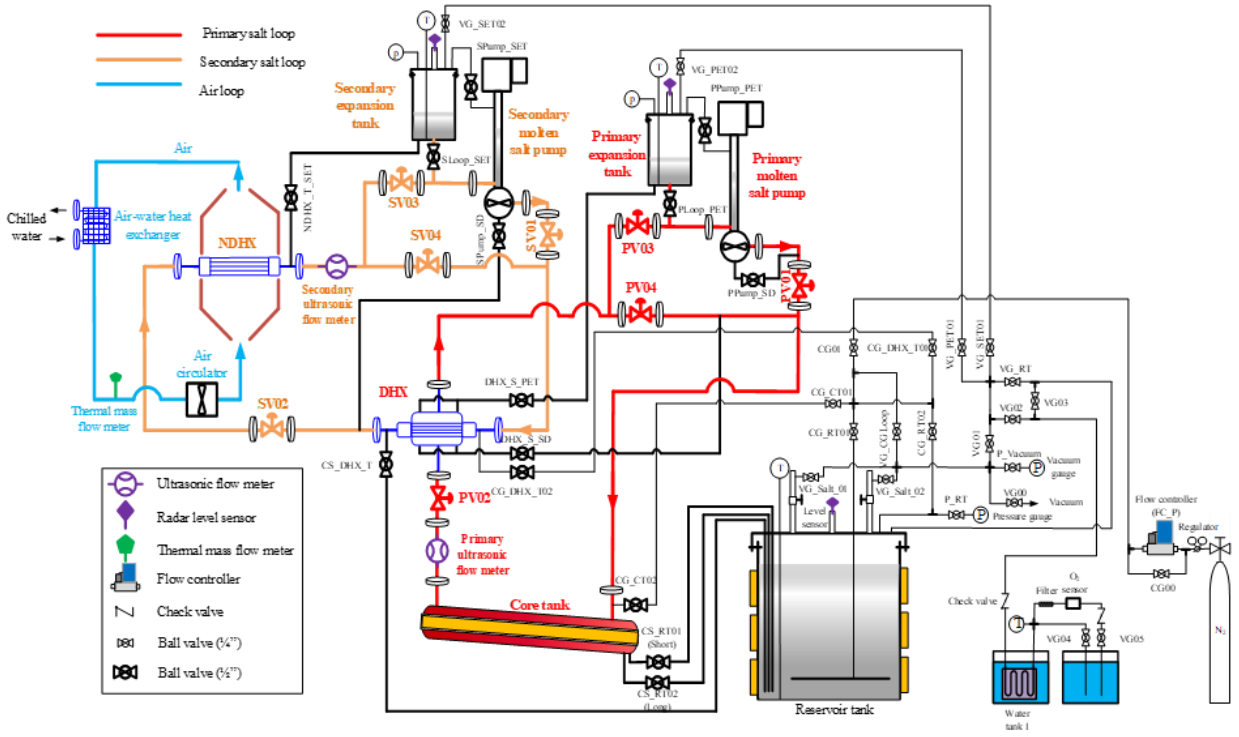

Figure 4-18 Gas/Salt flow control system

4.4 Operation

The IET facility FLUSTFA is capable of operating in both natural and forced circulation modes for the primary and secondary molten salt loops. Therefore, there are four operation cases: (1) forced circulation for the primary loop and natural circulation for the secondary loop; (2)

natural circulation for both the primary and secondary loops; (3) forced circulation for both the primary and secondary loops; and (4) natural circulation for the primary loop and forced circulation for the secondary loop. The second case, natural circulation for both the primary and secondary loops as schematically shown in Figure 4-19 will be investigated in this study.

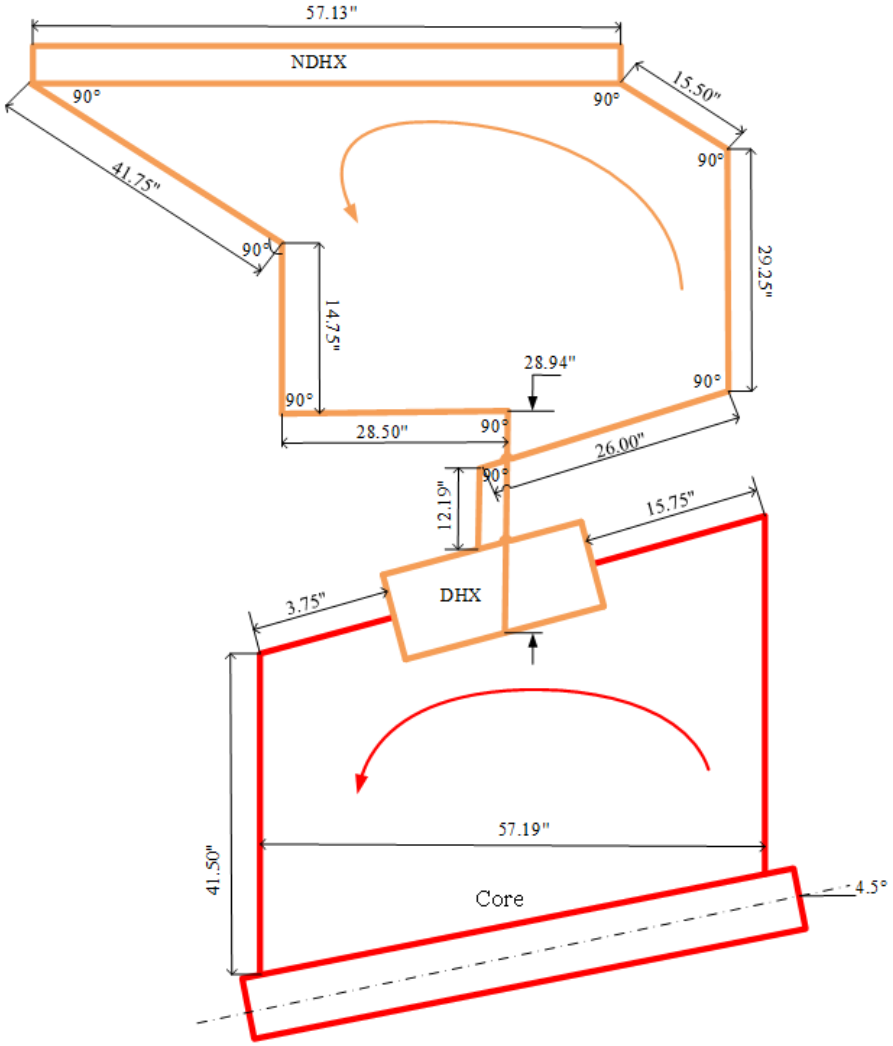

Figure 4-19 Dimensions of the IET facility FLUSTFA in natural circulation mode

4.5 Correlations for Heat Transfer and Friction Factor

4.5.1 Heat Transfer for Flows in the Simulated Core

The simulated core as shown in Figure 4-7 has three different sub-channels, namely, the interior sub-channels of the triangular array (Region I) and square array (Region II), and the wall sub-channels (Region III). The quantities for Regions I, II, and III in the simulated core are 72, 48, and 24, respectively. In addition, the corresponding angles for Regions I, II, and III are 30°, 45°, and 105°, respectively.

The FLiNaK salt is in laminar flow regime in the simulated core for natural circulation experiments. Therefore, the following three equations,

$$\mathrm{Nu}_{c,i,tri} = 15.36 \tag{4-35}$$

$$\mathrm{Nu}_{c,i,sq} = 15.09 \tag{4-36}$$

$$\mathrm{Nu}_{c,w} = 6.704 \tag{4-37}$$

are used to calculate the heat transfer coefficient of laminar flows in Regions I and II (Sahoo and Mohanty, 1987), and Region III (Mohanty and Sahoo, 1986) under uniform heat flux boundary conditions, respectively.

The average Nusselt number for laminar flows in the simulated core, which is defined as

$$\overline{\mathrm{Nu}}_c = \frac{\mathrm{Nu}_{c,i,tri}A_{i,tri}+\mathrm{Nu}_{c,i,sq}A_{i,sq}+\mathrm{Nu}_{c,w}A_w}{A_{i,tri}+A_{i,sq}+A_w} \tag{4-38}$$

is adopted in this study based on the heated surface area $A_{i,tri}$, $A_{i,sq}$, and A_w for Regions I, II, and III, respectively. The heated-surface-area-averaged Nusselt number for laminar flows in the simulated core is therefore calculated as

$$\overline{\mathrm{Nu}_c} = 12.09 \tag{4-39}$$

It should be noted that Eq. (4-39) is applicable for fully-developed forced convective heat transfer of laminar flows in the simulated core. Considering the buoyancy, radiative heat transfer, and entrance effect, the total heat transfer of the FLiNaK salt in the simulated core should be larger than that calculated by Eq. (4-39). These effects will be evaluated once the experimental data is available. Currently, however, the forced convective heat transfer correlation, Eq. (4-39), which was originally used in the design process for the simulated core under steady-state natural circulation conditions, is adopted in the 1D code NACCO for modeling of the thermal-hydraulic performance of FLiNaK in the IET facility FLUSTFA.

4.5.2 Heat Transfer for Flows in the FTHXs

The spirally fluted tubes have been widely used for the design of HXs due to their superior heat transfer performance. However, most of previous studies (Srinivasan, 1993; Chen et al., 2001) focused on the effect of a few geometric parameters, such as the flute pitch and depth, on heat transfer performance of low-Prandtl-number fluids, such as air or water. The correlations developed in their studies may not be applicable or accurate for high-Prandtl-number fluids, such as molten salts. A numerical analysis using STAR-CCM+ is therefore carried out to develop heat transfer correlations for laminar flows of molten salts in spirally fluted tubes for $p/D_c =$ 0.44 to 3.51, $e/D_c = 0.10$ to 0.40, $\theta/90 = 0.20$ to 0.81, and $L_{tr}/D_c = 0.71$ to 2.16, where p, D_c, e, θ, and L_{tr} are respectively the flute pitch, characteristic length, flute depth, flute helix angle, and trough length as shown in Figure 4-20.

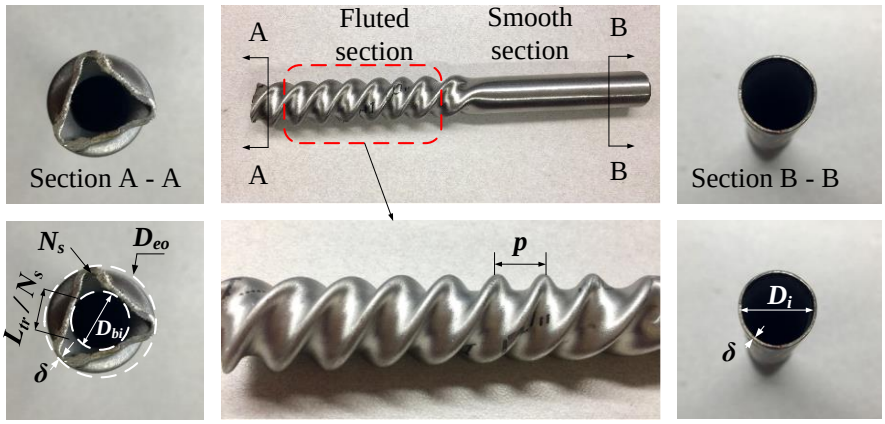

Figure 4-20 A three-start spirally fluted tube

The non-dimensional geometric parameters are defined and then used to correlate data for spirally fluted tubes. The geometric parameters, such as the flute pitch, flute depth, and trough length, are nondimensionlized by the characteristic length, written respectively as

$$p^* = \frac{p}{D_c} \tag{4-40}$$

$$e^* = \frac{e}{D_c} \tag{4-41}$$

$$L_{tr}^* = \frac{L_{tr}}{D_c} \tag{4-42}$$

The flute helix angle is nondimensionlized as

$$\theta^* = \frac{\theta}{90} \tag{4-43}$$

Two heat transfer correlations are proposed for spirally fluted tubes as follows,

$$\mathrm{Nu} = G_1(\mathrm{Re}, \mathrm{Pr}, p^*, e^*) \tag{4-44}$$

$$\mathrm{Nu} = G_2(\mathrm{Re}, \mathrm{Pr}, p^*, e^*, \theta^*, L_{tr}^*) \tag{4-45}$$

Since a power of 1/3 has been widely used for Prandtl number, it is adopted in this study as well to correlate heat transfer data as follows,

$$\mathrm{Nu} = m_0 \mathrm{Re}^{m_1} \mathrm{Pr}^{1/3} \left(\frac{p}{D_c}\right)^{m_2} \left(\frac{e}{D_c}\right)^{m_3} \tag{4-46}$$

$$\mathrm{Nu} = n_0 \mathrm{Re}^{n_1} \mathrm{Pr}^{1/3} \left(\frac{p}{D_c}\right)^{n_2} \left(\frac{e}{D_c}\right)^{n_3} \left(\frac{\theta}{90}\right)^{n_4} \left(\frac{L_{tr}}{D_c}\right)^{n_5} \tag{4-47}$$

where $m_0, m_1, m_2, m_3, n_0, n_1, n_2, n_3, n_4,$ and n_5 are unknowns which need to be determined. Through a multiple linear regression approach for 171 data points for the FLiNaK salt in nineteen different fluted tubes and 42 data points for water in six different fluted tubes, the heat transfer correlations are developed as follosws,

$$\mathrm{Nu} = 0.05623 \mathrm{Re}^{0.7587} \mathrm{Pr}^{1/3} \left(\frac{p}{D_c}\right)^{-0.0274} \left(\frac{e}{D_c}\right)^{-0.1544} \tag{4-48}$$

$$\mathrm{Nu} = 0.06082 \mathrm{Re}^{0.7606} \mathrm{Pr}^{1/3} \left(\frac{p}{D_c}\right)^{-0.0402} \left(\frac{e}{D_c}\right)^{-0.1649} \left(\frac{\theta}{90}\right)^{-0.0922} \left(\frac{L_{tr}}{D_c}\right)^{-0.3588} \tag{4-49}$$

The coefficient of determination R^2 is 0.9316 for Eq. (4-48) and 0.9526 for Eq. (4-49). In addition, the relative residual is plotted in Figure 4-21. It is identified that Eqs. (4-48) and (4-49) respectively predict 69.0% and 81.8% of the total 213 data points within ± 20% uncertainties of the true values, while 85.9% and 91.5% of the total data points within ± 25% uncertainties, respectively. Eq. (4-49) is therefore suggested to predict the Nusselt number for spirally fluted tubes under the following conditions: Re = 105 to 1,600, Pr = 5 to 23, p^* = 0.44 to 3.51, e^* = 0.10 to 0.40, θ^* = 0.20 to 0.81, and L_{tr}^* = 0.71 to 2.16.

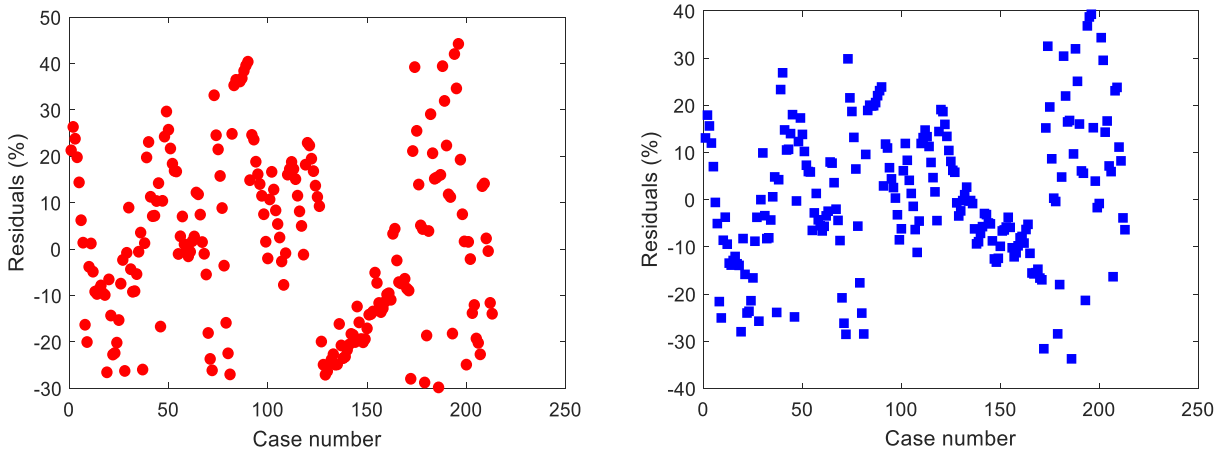

(a) (b)

Figure 4-21 Relative residuals of Nusselt number predicted by different correlations for spirally fluted tubes

In addition, the following correlation,

$$\mathrm{Nu} = 20.388\mathrm{Re}^{0.36}\mathrm{Pr}^{0.303}Ns^{-0.617}\left(\frac{p}{D_c}\right)^{-0.68e/D_c}\left(\frac{e}{D_c}\right)^{0.703} \tag{4-50}$$

proposed by Garimella et al. (1990) for the confined cross flows in spirally fluted tube bundles is applied to the shell-side flows in the spirally fluted tube HX, DHX and NDHX. The Sieder-Tate correlation is applied to laminar flows in piping.

4.5.3 Friction Factor

In addition to the heat transfer correlations, the friction factor correlation is another key input for the 1D code NACCO to predict the FLUSTFA performance. Both the primary and secondary natural circulation loops of the IET facility FLUSTFA are divided into four subsections individually. The primary natural circulation loop consists of (1) the simulated core; (2) hot leg

from the core outlet to the DHX shell-side inlet; (3) DHX shell side; and (4) cold leg from the DHX shell-side outlet to the core inlet, while the secondary natural circulation loop consists of (1) DHX tube side; (2) hot leg from the DHX tube-side outlet to the NDHX tube-side inlet; (3) NDHX tube side; and (4) cold leg from the NDHX tube-side outlet to the DHX tube-side inlet.

The pressure loss coefficient, ξ, defined as

$$\xi = fL/D + K = \frac{\Delta p}{\rho u^2/2} \tag{4-51}$$

was measured for each of the subsections in the primary and secondary natural circulation loops as shown in Figure 4-22 and Figure 4-23. The corresponding Darcy friction factor correlations are proposed as follows,

$$\xi_{core} = \frac{61.273}{\mathrm{Re}^{0.441}} \tag{4-52}$$

$$\xi_{core-DHX} = \frac{15.037}{\mathrm{Re}^{0.218}} \tag{4-53}$$

$$\xi_{DHX\ shell} = \frac{485.62}{\mathrm{Re}^{0.651}} \tag{4-54}$$

$$\xi_{DHX-core} = \frac{538.25}{\mathrm{Re}^{0.636}} \tag{4-55}$$

$$\xi_{DHX\ tube} = \frac{4099.7}{\mathrm{Re}^{0.788}} \tag{4-56}$$

$$\xi_{DHX-NDHX} = \frac{1321.1}{\mathrm{Re}^{0.698}} \tag{4-57}$$

$$\xi_{NDHX\ tube} = \frac{4749.9}{\mathrm{Re}^{0.731}} \tag{4-58}$$

$$\xi_{NDHX-DHX} = \frac{13.422}{\mathrm{Re}^{0.14}} \tag{4-59}$$

where the Reynolds numbers for all these components are calculated based on the inner diameter of the loop piping.

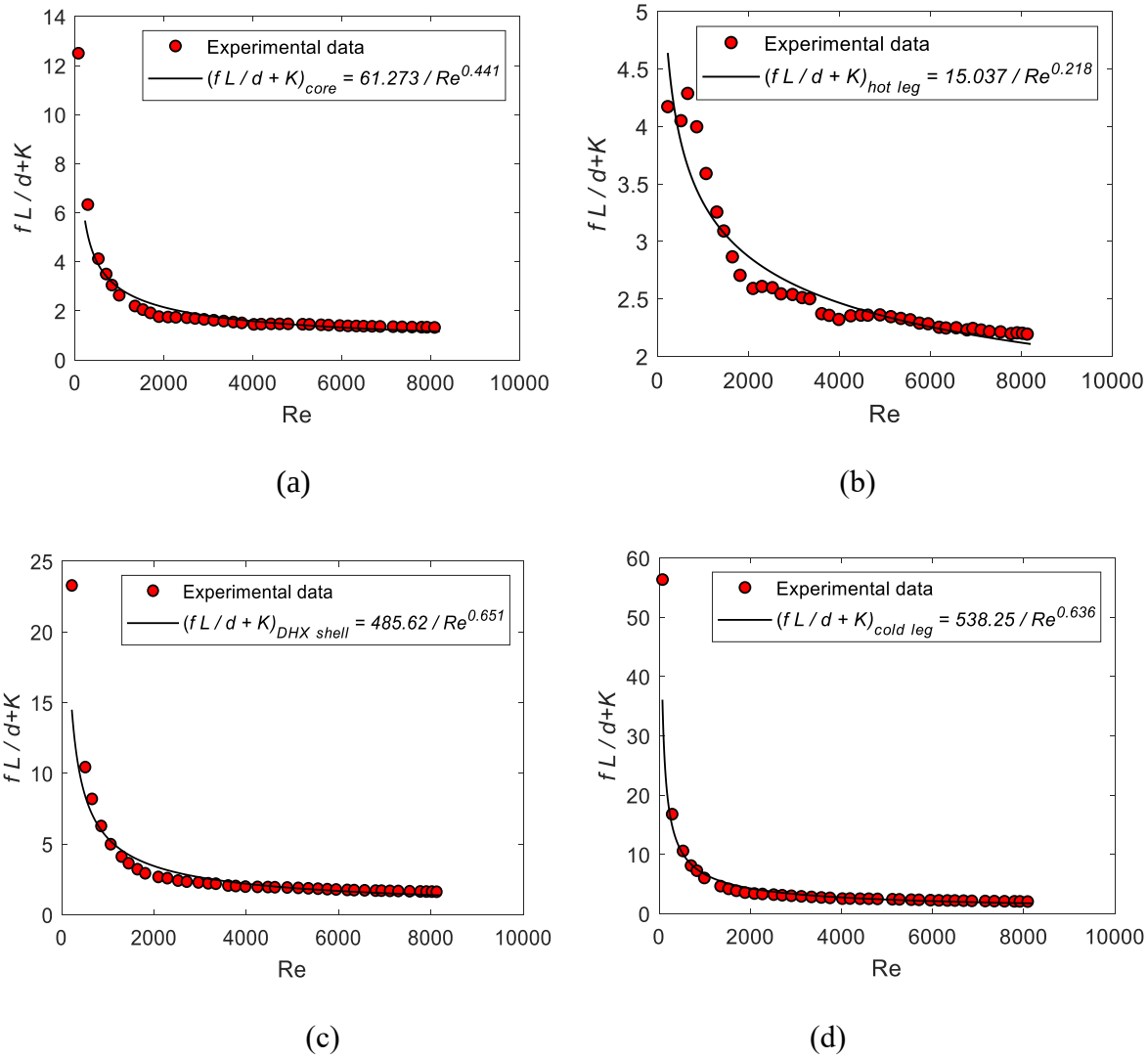

Figure 4-22 Pressure loss coefficient for the primary natural circulation loop, including (a) the simulated core; (b) hot leg from the core outlet to the DHX shell-side inlet; (c) DHX shell side; and (d) cold leg from the DHX shell-side outlet to the core inlet

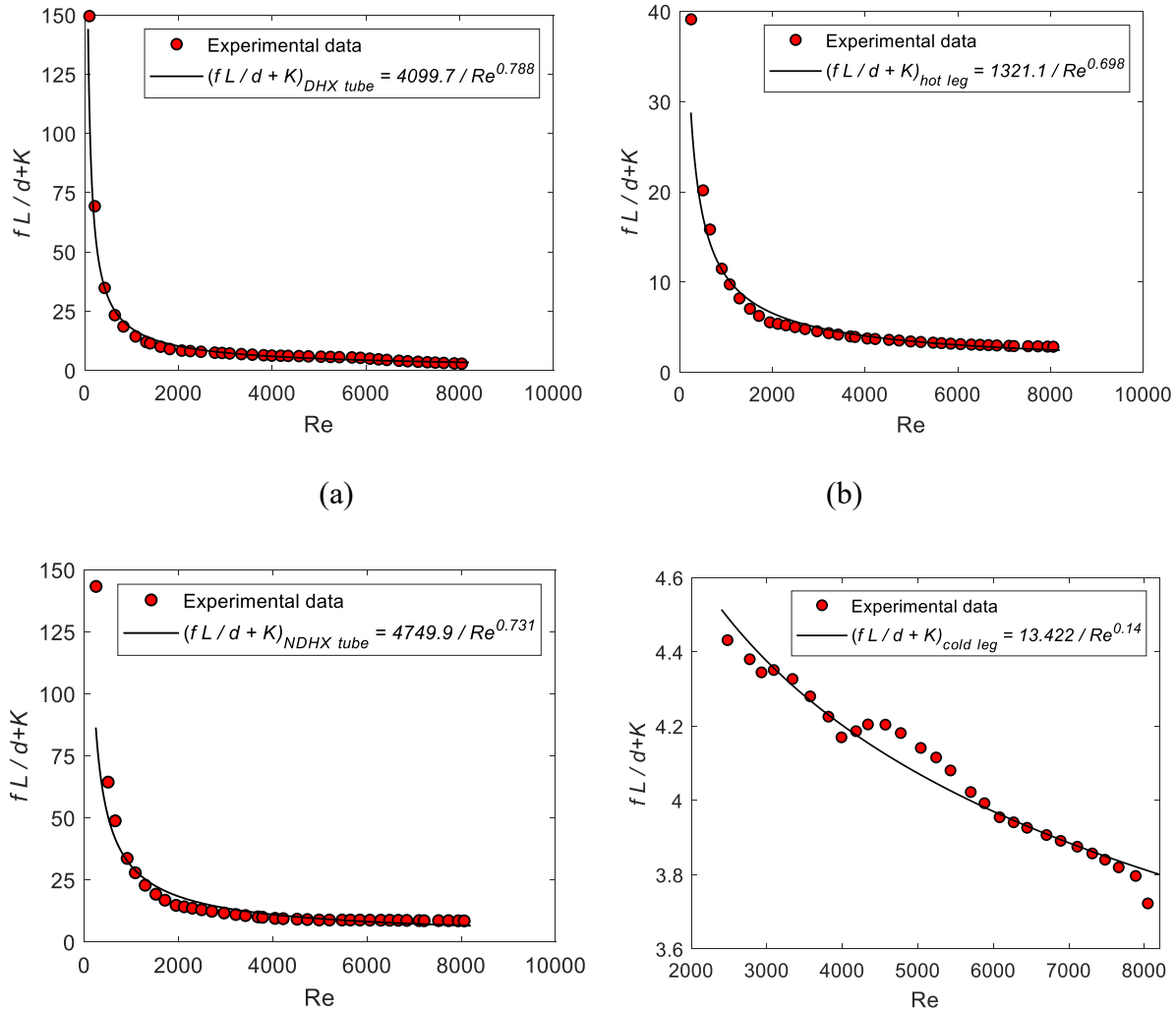

Figure 4-23 Pressure loss coefficient for the secondary natural circulation loop, including (a) DHX tube side; (b) hot leg from the DHX tube-side outlet to the NDHX tube-side inlet; (c) NDHX tube side; and (d) cold leg from the NDHX tube-side outlet to the DHX tube-side inlet

4.6 1D Code NACCO for the IET Facility FLUSTFA

The 1D code NACCO is applied for the IET facility FLUSTFA as shown in Figure 4-24, which resembles salt natural circulation in the reactor vessel and DRACS loop in the AHTR.

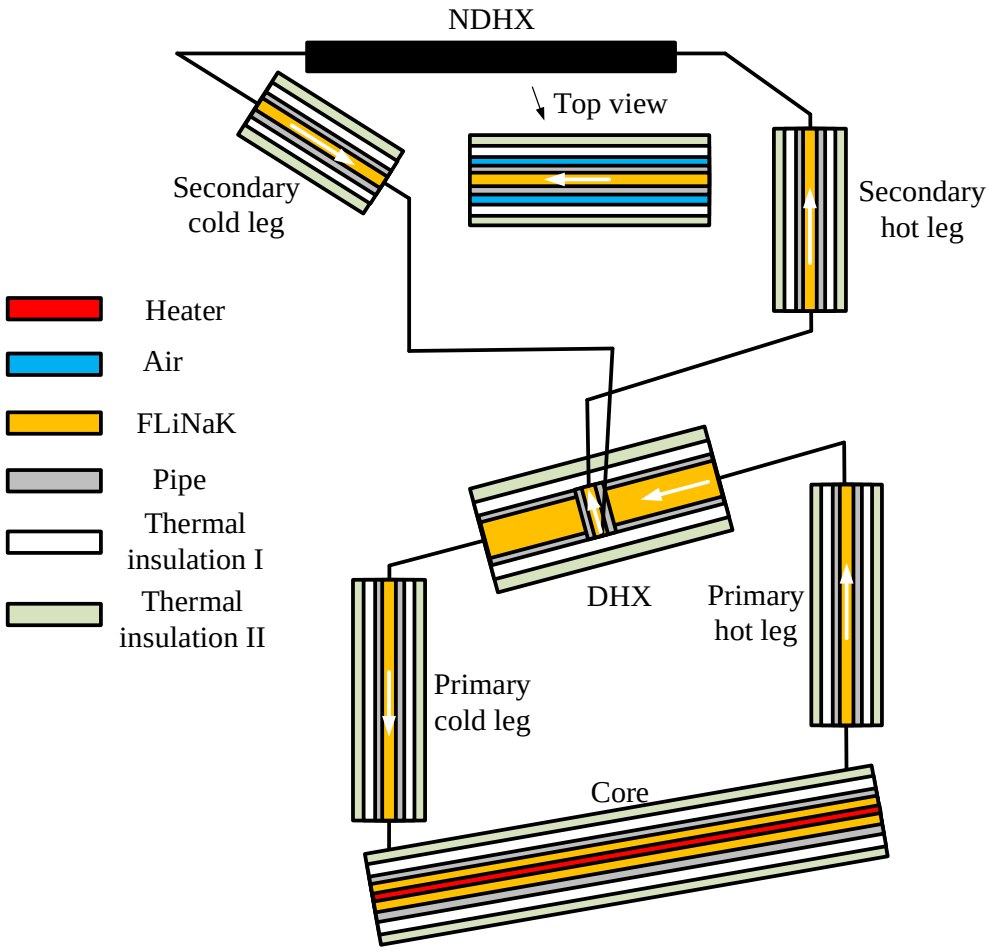

Figure 4-24 Schematic of modules used in the 1D code NACCO for modeling of the IET facility FLUSTFA

The following processes are evaluated by the 1D code NACCO for the IET facility FLUSTFA using the FLiNaK salt as the working fluid:

(1) Core: Conductive heat transfer across the heater sheath, convective heat transfer from the heater sheath to the FLiNaK salt, convective heat transfer from the FLiNaK salt to the core vessel, conductive heat transfer across the core vessel and thermal insulation, and finally convective and radiative heat transfer from the thermal insulation to the ambient air;

(2) DHX: One way is the convective heat transfer from the FLiNaK salt on the DHX shell side to the spirally fluted tube wall, conductive heat transfer across the fluted tube, and finally convective heat transfer from the fluted tube to the FLiNaK salt on the DHX tube side. Another way is the convective heat transfer from the FLiNaK salt on the DHX shell side to the DHX shell, conductive heat transfer across the shell and thermal insulation, and finally convective and radiative heat transfer from the thermal insulation to the ambient air;

(3) Primary/Secondary hot and cold legs: Convective heat transfer from the FLiNaK salt to the piping, conductive heat transfer across the piping and thermal insulation, and finally convective and radiative heat transfer from the thermal insulation to the ambient air;

(4) NDHX: Convective heat transfer from the FLiNaK salt on the NDHX tube side to the spirally fluted tube wall, conductive heat transfer across the fluted tube. One way is the convective heat transfer from the NDHX tube and shell to the air on the NDHX shell side if the NDHX shell temperature is higher than the air temperature. Another way is the radiative heat transfer from the NDHX tube to the NDHX shell. Then conductive heat transfer across the NDHX shell and thermal insulation, and finally convective and radiative heat transfer from the thermal insulation to the ambient air.

4.7 Shakedown Test

Two preliminary shakedown tests will be predicted by the 1D code NACCO: (1) Test #1, identification of the inherent safety time due to thermal inertia to recycle the liquid FLiNaK salt back to the reservoir tank under an unanticipated power outage condition and (2) Test #2, identification of the parasitic heat loss rate at different salt temperatures.

4.7.1 Test #1: Identification of the Inherent Safety Time

The FLiNaK salt has a melting temperature of 454 °C. Therefore, it may potentially freeze in some locations where the heat addition cannot sufficiently compensate the heat loss rate. Although trace heating is provided for the loop to avoid such cases, the salt freezing issue exists under an unanticipated power outage condition. It is therefore necessary to identify the amount of time estimated for the FLiNaK salt to freeze in the loop. If it is longer than the time needed to recycle all the FLiNaK salt from the loop to the reservoir tank, then it is believed the loop is inherently safe. The time for the FLiNaK salt temperature decreasing from its initial temperature to its melting temperature under a power outage condition (no heating power) is called the inherent safety time in this study.

Obviously, the inherent safety time depends on the thermal inertia of the loop and the working temperature. Larger thermal inertia and higher working temperature lead to a longer inherent safety time. Since the FLiNaK salt is charged to the loop from the reservoir tank, the FLiNaK salt temperature in both the primary and secondary loops is initially the same. It is assumed that the loop is preheated to the same temperature of the FLiNaK salt for a convenient analysis to identify the inherent safety time. Five cases for the salt initial temperature, 500 °C, 550 °C, 600 °C, 650 °C, and 700 °C, will be investigated.

Taking an initial salt temperature of 600 °C as an example, it is assumed that the FLiNaK salt is heated to 600 °C in the reservoir tank and charged to the loop, which has already been preheated to 600 °C. Then a power outage accidentally happens. The FLiNaK salt temperature decreases due to the parasitic heat loss of the loop, which is predicted by the 1D code NACCO as shown in Figure 4-25. The FLiNaK salt temperature decreases at a faster rate initially then at a relatively lower rate afterwards. This is because the FLiNaK salt velocity increases initially, while

it decreases afterwards as shown in Figure 4-26. It is identified that the inherent safety time is about 3.6 hours before salt freezing in the loop for an initial salt temperature of 600 °C under conditions of zero heating power and zero cooling rate for the NDHX.

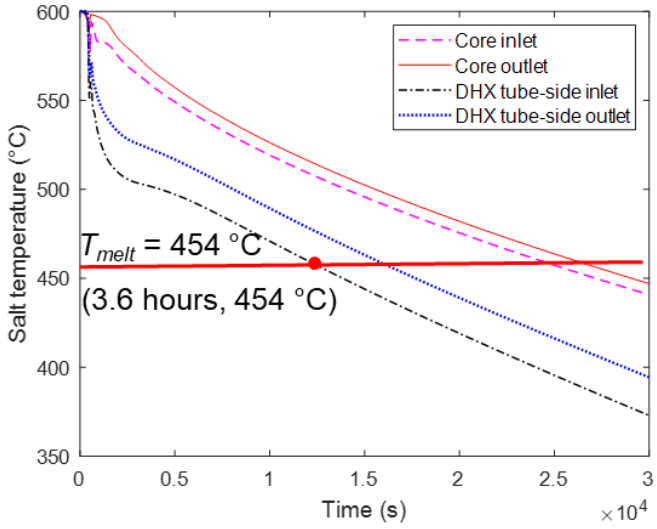

Figure 4-25 FLiNaK salt temperature for an initial temperature of 600 °C, zero heating power and air-cooling rate

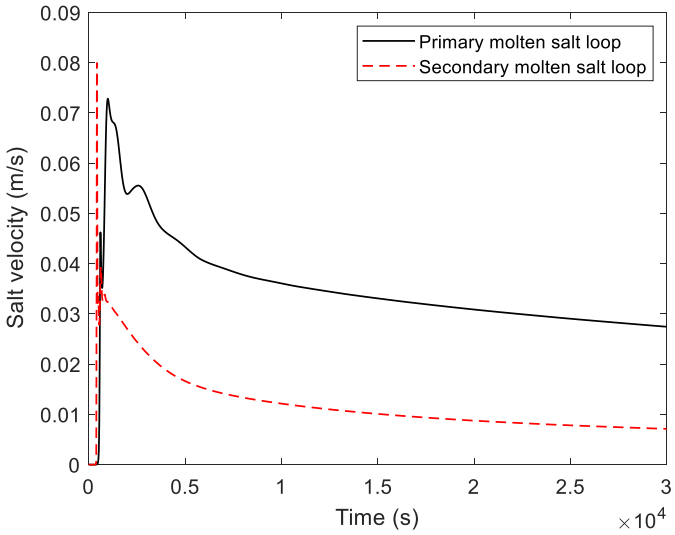

Figure 4-26 FLiNaK salt velocity for an initial temperature of 600 °C, zero heating power and air-cooling rate

Similarly, the inherent safety time for other cases could be identified as well. The FLiNaK salt temperature at the DHX tube-side entrance, where the lowest salt temperature occurs, is plotted for different salt temperatures as shown in Figure 4-27. The inherent safety times for an initial temperature of 500, 550, 600, 650, and 700 °C are 0.3, 0.7, 3.6, 6.1, and 8.3 hours, respectively. Since it takes about 0.5 hours to recycle all the FLiNaK salt to the reservoir tank, it is beneficial to operate the IET facility FLUSTFA at a temperature higher than 550 °C.

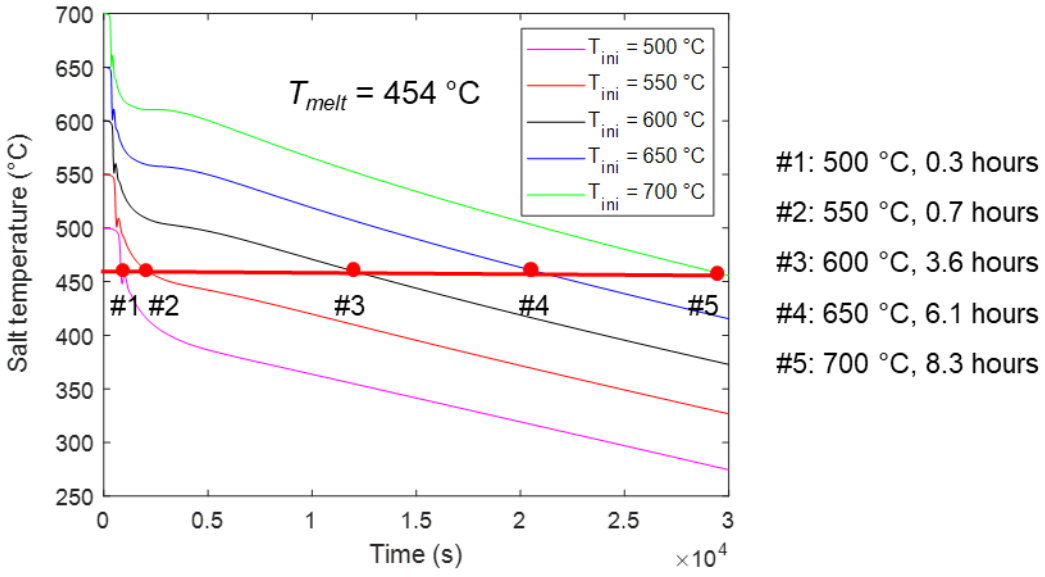

Figure 4-27 FLiNaK salt temperature at the DHX tube-side inlet for an initial temperature of 500 to 700 °C, zero heating power and air-cooling rate

4.7.2 Test #2: Identification of the Parasitic Heat Loss Rate

The parasitic heat loss rate could be significant for high-temperature test facilities. It is therefore necessary to evaluate the parasitic heat loss rate for the IET facility FLUSTFA under different salt temperatures.

Four different heating power levels, namely, 2.2, 2.5, 2.8, and 3.1 kW, are used to identify the achievable steady-state temperature for an initial salt temperature of 600 °C and an air forced cooling rate of 0 kg/s. Taking 2.5 kW and 2.8 kW as examples, the maximum salt temperature at the core outlet under steady-state conditions is 600.6 °C for a 2.5 kW heating power as shown in Figure 4-28(a), while it is 654.0 °C for a 2.8 kW heating power as shown in Figure 4-28(b). In other words, the parasitic heat loss rates for the core outlet temperature of 600.6 °C and 654.0 °C are 2.5 kW and 2.8 kW, respectively. It is also observed that the FLiNaK salt is not stagnant as shown in Figure 4-29, although the air forced cooling rate is 0 kg/s. This is because the salt temperature difference exists in the loop due to the parasitic heat loss.

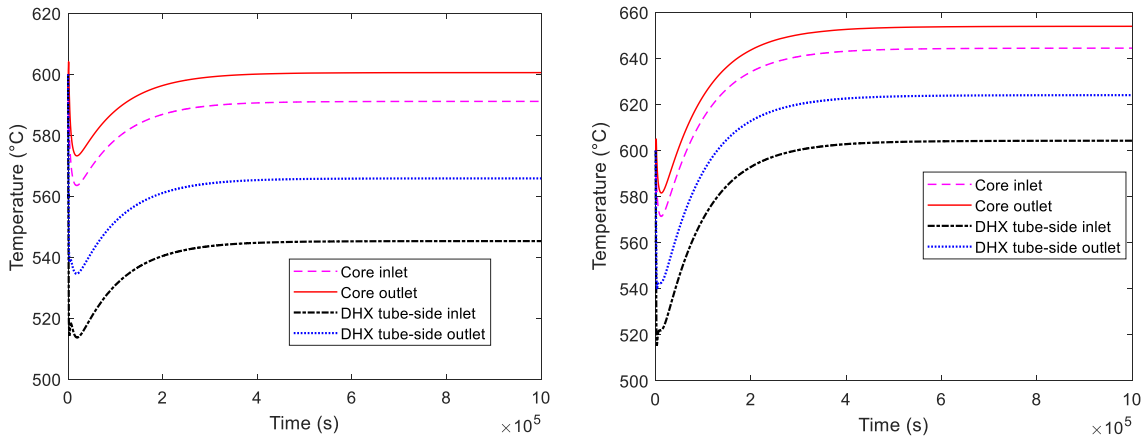

(a) (b)

Figure 4-28 FLiNaK salt temperature for an initial temperature of 600 °C, zero air-cooling rate, and heating power of (a) 2.5 kW and (b) 2.8 kW

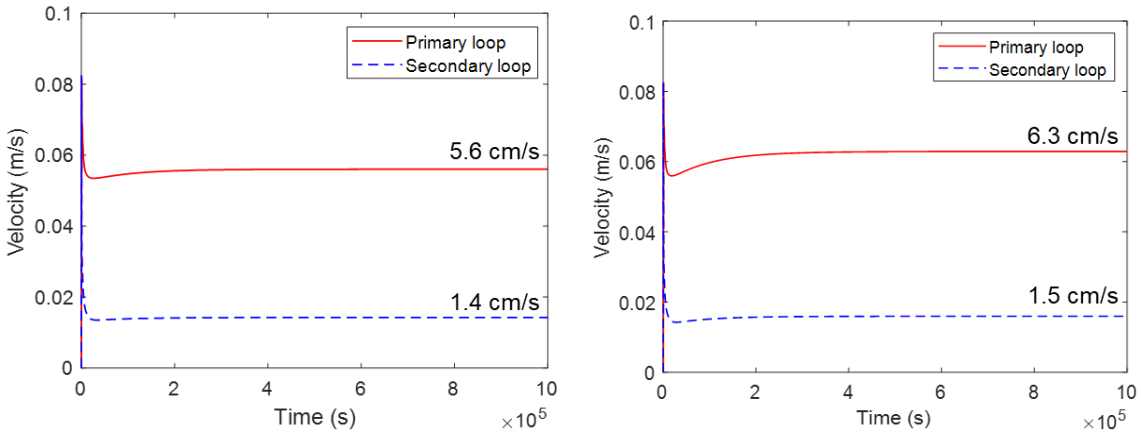

(a) (b)

Figure 4-29 FLiNaK salt velocity for an initial temperature of 600 °C, zero air-cooling rate, and heating power of (a) 2.5 kW and (b) 2.8 kW

Similarly, the parasitic heat loss rate could be determined for other salt temperatures as well. The parasitic heat loss rate is estimated to be 2.2 kW to 3.1 kW for the core outlet salt temperature of 547 to 707 °C. In addition, the heating power should be at least 2.1 kW to keep the DHX tube-side inlet salt temperature higher than the FLiNaK salt melting temperature 454 °C.

4.8 Overcooling Transient

Salt may freeze in the DRACS loop due to overcooling for the salt-to-air HX NDHX. Therefore, it is necessary to investigate the overcooling transient in the IET facility FLUSTFA. The overcooling transient will be predicted first by the 1D code NACCO.

Four different air-cooling rates for the NDHX will be investigated, namely, 0.01, 0.02, 0.03, and 0.04 kg/s. An air-cooling rate of 0.01 kg/s is used as an example. Initially, the loop is under a steady-state condition of the heating power 2.8 kW and air-cooling rate 0 kg/s. Then the air circulator starts to operate and provide an air-cooling rate of 0.01 kg/s. Therefore, the FLiNaK

salt has an axial temperature profile along the loop initially as shown in Figure 4-30. Due to the forced air cooling, the FLiNaK salt temperatures at different locations start to decrease from their respective initial value as shown in Figure 4-30. It takes about 3.0 hours for the FLiNaK salt temperature at the DHX tube-side inlet to reach its melting temperature.

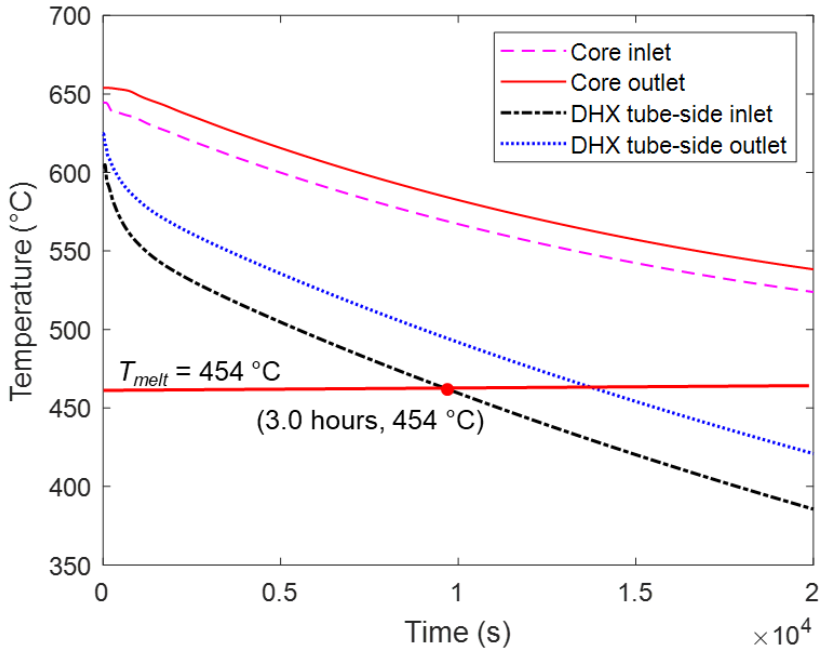

Figure 4-30 FLiNaK salt temperature for the overcooling transient at an air-cooling rate of 0.01 kg/s

Similarly, the time for the FLiNaK salt solidification could be estimated for other cooling rates as shown in Figure 4-31. It increases from 0.6 to 3.0 hours as the decrease of the air-cooling rate from 0.04 to 0.01 kg/s.

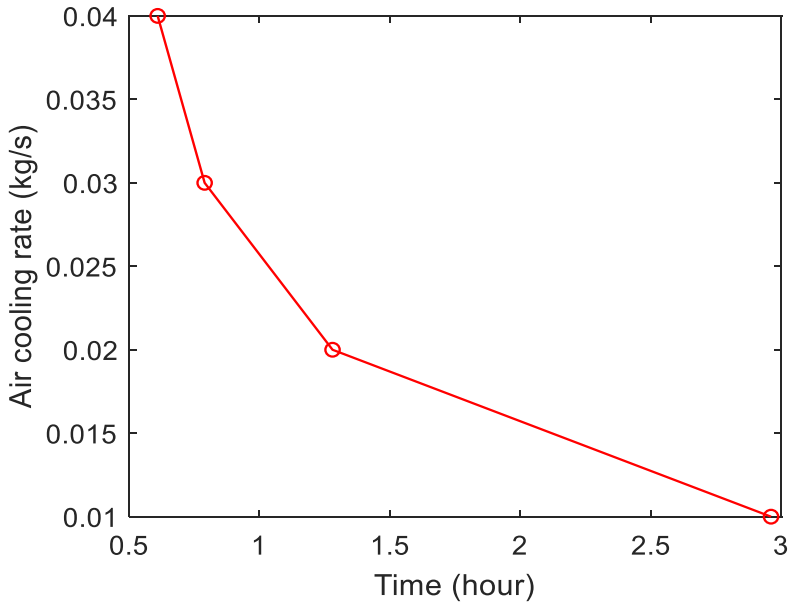

Figure 4-31 Time estimated for the FLiNaK salt solidification for the overcooling transient

4.9 Overheating Transient

The air chimney for the DRACS loop is closed under reactor normal operation conditions to reduce the parasitic heat loss. However, it should be open to enable air cooling under reactor accident scenarios, such as the SBO. If the air chimney fails to open, the reactor core temperature will increase and the coolant will be overheated due to the decay heat generation and loss of multiple DRACS loops. It is therefore necessary to investigate the overheating phenomenon in the IET facility FLUSTFA. This overheating transient will be predicted first by the 1D code NACCO.

The decay power for a typical LWR was proposed by EI-Wakil (1974) as

$$P/P_o \approx 0.1[(t+10)^{-0.2} - (t+t_s+10)^{-0.2} + 0.87(t+t_s+2\times10^7)^{-0.2} - 0.87(t+2\times10^7)^{-0.2}] \quad (4\text{-}60)$$

and it is plotted in Figure 4-32, where P, P_0, t, and t_s are the reactor current power, initial operation power, time after reactor shutdown, and reactor operating time before reactor shutdown, respectively. One-year operation time and the maximum heating power of 38 kW provided by the cartridge heaters in the IET facility FLUSTFA are used for the overheating transient.

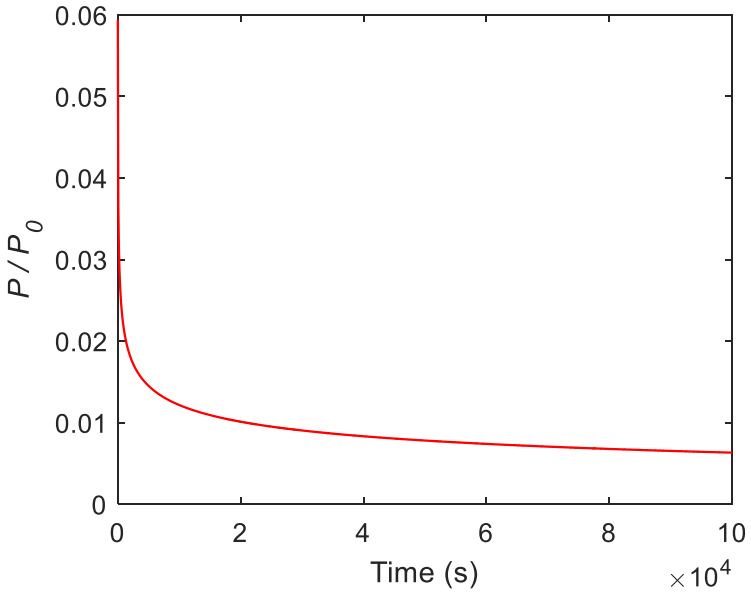

Figure 4-32 Decay power for a typical LWR (EI-Wakil, 1974)

Initially, the loop is under a steady-state condition. At time t = 0, the heating power starts to follow the decay curve as shown in Figure 4-32. The FLiNaK salt temperature decreases initially, then it starts to increase as shown in Figure 4-33. This is because the FLiNaK salt velocity increases initially and decreases afterwards as shown in Figure 4-34. After about 1.9 hours, the FLiNaK salt temperature at the core outlet exceeds 700 °C, the design temperature for the primary molten salt loop in the IET facility FLUSTFA.

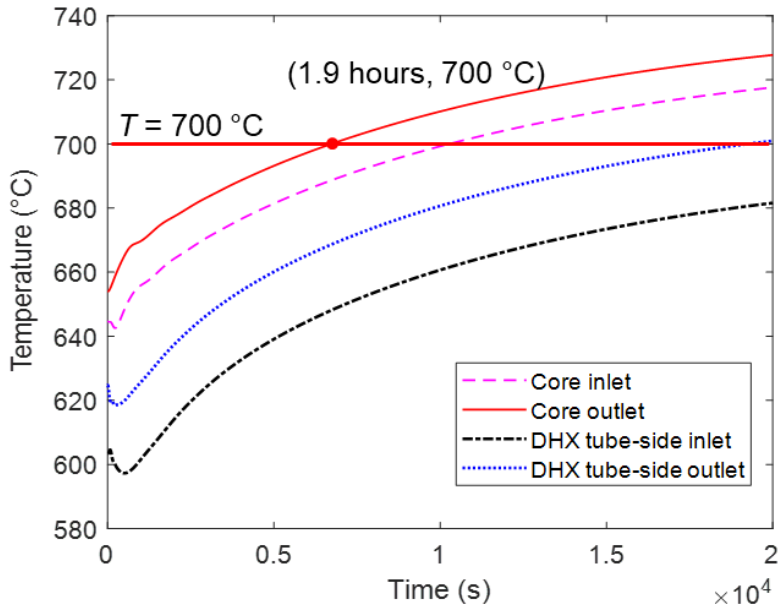

Figure 4-33 FLiNaK salt temperature for the overheating transient

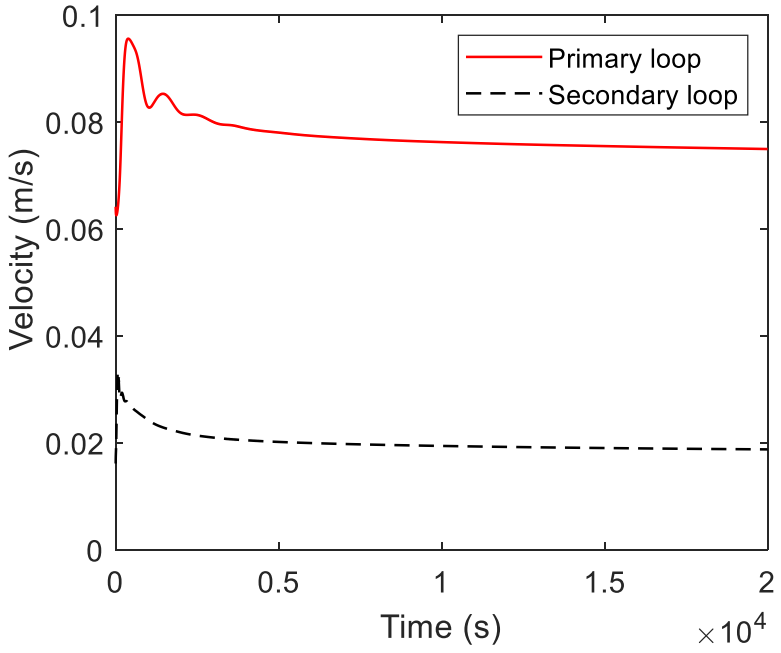

Figure 4-34 FLiNaK salt velocity for the overheating transient

4.10 Summary

A high-temperature IET facility, FLUSTFA, was designed based on a scaling analysis for the DRACS in a large-scale FHR, AHTR. The 1D code NACCO was then applied to predict the thermal-hydraulic performance of the working fluid FLiNaK in the IET facility FLUSTFA, including predictions for a number of shakedown tests, overcooling, and overheating transients.

Several concluding remarks are summarized as follows:

(1) The inherent safety times for different initial temperatures of 500, 550, 600, 650, and 700 °C are estimated to be 0.3, 0.7, 3.6, 6.1, and 8.3 hours, respectively. Since it takes about 0.5 hours to recycle all the FLiNaK salt to the reservoir tank, it is then necessary to operate the IET facility FLUSTFA at a temperature higher than 550 °C.

(2) The parasitic heat loss rate for the IET facility FLUSTFA is estimated to be 2.2 kW to 3.1 kW for the core outlet salt temperature of 547 to 707 °C. In addition, the heating power should be at least 2.1 kW to keep the DHX tube-side inlet salt temperature, the lowest salt temperature in the loop, higher than the FLiNaK salt melting temperature.

(3) The time for the FLiNaK salt freezing in the loop increases from 0.6 to 3.0 hours as the air-cooling rate decreases from 0.04 to 0.01 kg/s for the overcooling transient under conditions investigated.

(4) The FLiNaK salt temperature at the core outlet may exceed 700 °C, the design value for the primary molten salt loop in the IET facility FLUSTFA, after about 1.9 hours for the overheating transient under conditions investigated.

Chapter 5 Tritium Mitigation for FHRs

5.1 Introduction

The AHTR including the containment as shown in Figure 5-1 is a conceptual design of FHRs, which consists of three primary loops, three intermediate loops, three DRACS loops, and one power conversion loop. Argon acting as a cover gas in the reactor vessel, guard vessel, and containment, provides inert environment for the salts.

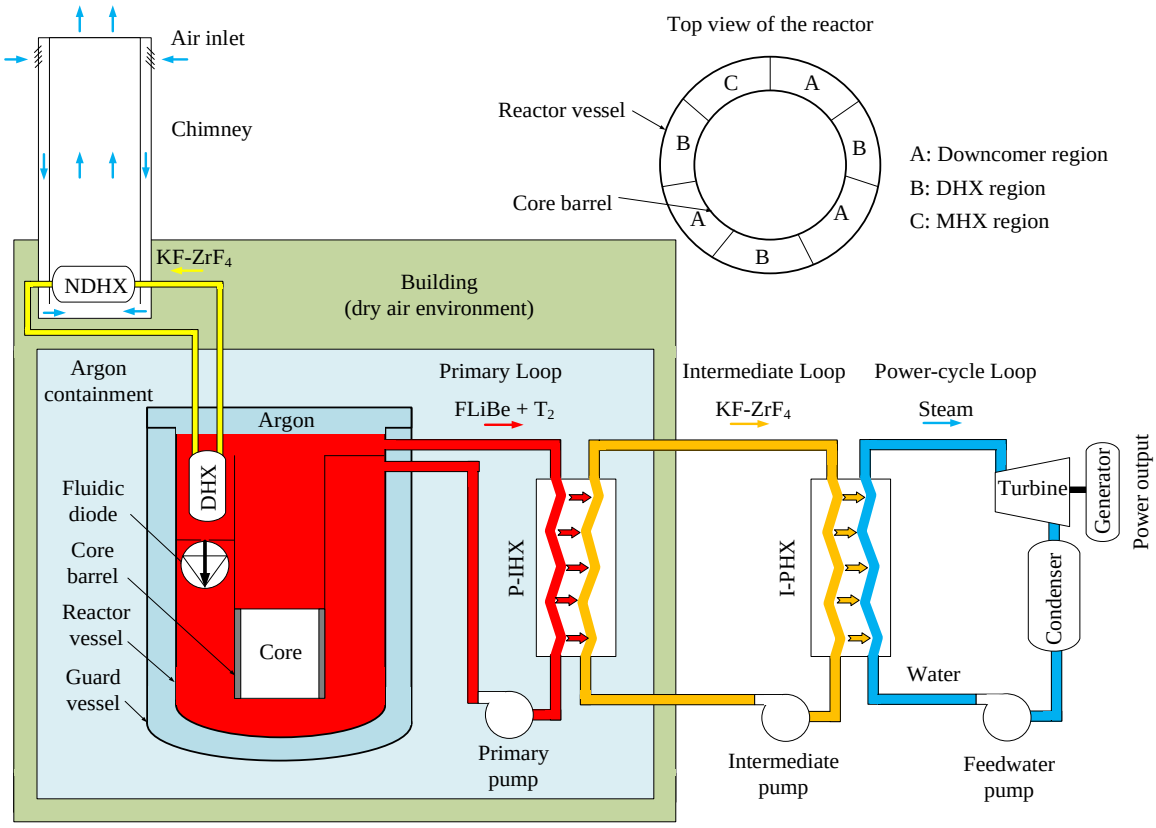

Figure 5-1 Schematic of the AHTR including containment

Due to the atmospheric working pressure and large electric power conversion efficiency, the AHTR becomes one of the promising Generation IV reactor designs. Tritium control is however a significant issue in the AHTR due to the large tritium production rate by the following reactions (Schmutz et al., 2012):

$$^{6}\mathrm{Li} + n \rightarrow {}^{4}\mathrm{He} + {}^{3}\mathrm{H} \tag{5-1}$$

$$^{7}\mathrm{Li} + n \rightarrow {}^{4}\mathrm{He} + {}^{3}\mathrm{H} + n' \tag{5-2}$$

$$^{19}\mathrm{F} + n \rightarrow {}^{17}\mathrm{O} + {}^{3}\mathrm{H} \tag{5-3}$$

$$^{9}\mathrm{Be} + \mathrm{n} \rightarrow {}^{4}\mathrm{He} + {}^{6}\mathrm{Li} \tag{5-4}$$

Reactions (5-1) to (5-3) represent the tritium (^{3}H) production due to the neutron reaction with ^{6}Li, which is continuously produced by Reaction (5-4), ^{7}Li, and ^{19}F, respectively. Since tritium produced is in the form of ^{3}HF (TF), which is corrosive to the structural materials, redox control should be adopted for the AHTR. It is assumed that all TF produced is finally converted to T_2 in this research. This is a conservative assumption since T_2 is more permeable than TF.

The tritium production rate in the AHTR was estimated to be 3400 Ci/day, which was several orders of magnitude faster than that in LWRs (Briggs, 1971). If no tritium-control method is adopted, the tritium leakage rate in the AHTR will be significantly larger than 1.9 Ci/day, an average tritium leakage rate in LWRs (U.S. NRC, 2003). It is therefore necessary to reduce the tritium leakage rate in the AHTR design and other FHR designs in general.

There are several paths for tritium leakage in the AHTR as shown in Figure 5-2: (a) Permeation from the reactor vessel downcomer region to the argon gas space between the reactor vessel and guard vessel; (b) Trapped by carbonaceous materials in the reactor core; (c) Permeation

from the reactor core region to the argon cover gas space on the top of the reactor vessel; (d) Permeation from the core-bypass region between the reactor vessel and core barrel, such as the regions reserved for three DHXs and one Maintenance HX (MHX), to the argon gas space between the reactor vessel and guard vessel; (e) Permeation through the MHX tube walls, then circulation by the MHX tube-side salt to a salt-to-air heat exchanger, and finally to the ambient air; (f) Permeation through the DHX tube walls, then circulation by the DRACS salt to the NDHXs, and finally to the ambient air; (g) Permeation from the hot legs to the argon containment; (h) Permeation from the P-IHX tube walls, then circulation by the intermediate salt to the I-PHXs, where tritium further permeates through the I-PHX tube walls to water/steam for Rankine cycle or helium/sCO_2 for Brayton cycle; (i) Permeation through the cold legs between the primary pumps and P-IHXs to the argon containment; (j) Permeation through the primary pumps to the argon containment; and (k) Permeation through the cold legs between the primary pumps and the reactor vessel to the argon containment.

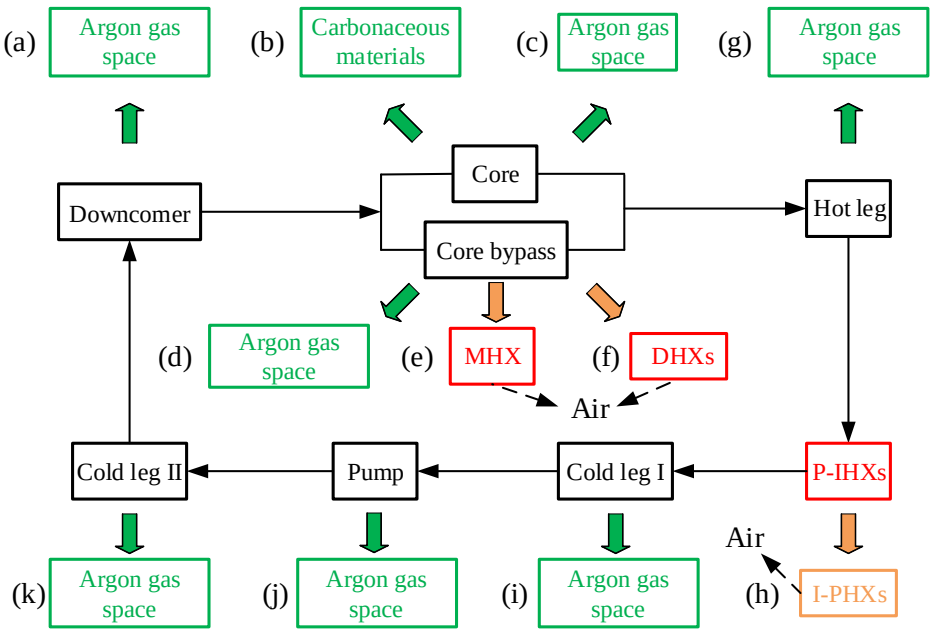

Figure 5-2 Pathways for tritium leakage in the AHTR

To simplify the analysis, several assumptions are made: (1) Tritium in the argon gas space is completely removed by the cleanup system designed for the cover gas argon; (2) Carbonaceous materials in the reactor core are saturated to capture tritium after a long-term operation; and (3) The tritium that permeates through the HX tube walls is finally released to the ambient air. Therefore, the three P-IHXs, three DHXs, and one MHX provide pathways for tritium leakage to the ambient air while other components provide pathways for tritium leakage to the argon gas space as shown in Figure 5-2.

A number of options have been investigated in the literature for tritium mitigation in FHRs. Forsberg et al. (2017) investigated a carbon bed option that used porous carbon to capture tritium in fluoride salts. Rubio et al. (2017) investigated a gas sparging option that disintegrated large tritium gas bubbles into smaller bubbles utilizing an ultrasonic technology and then used an inert gas to remove tritium. In addition, Wu et al. (2018) investigated a permeator window option in which metallic tubes were used to separate and remove tritium from fluoride salts using a carrier gas, such as helium. For these tritium management options, the pumping power for the primary loop may be significantly increased and/or a number of dedicated devices/systems are needed, such as an ultrasonic device, a gas sparging system, and a liquid/gas separation system. Other options that do not significantly increase the cost due to the additional pumping power or devices/systems needed for tritium removal, are therefore desirable. In this study, two options, namely, using Double-Wall HXs (DWHXs) with a tritium carrier or Single-Wall HXs (SWHXs) with a tritium barrier, are investigated for tritium mitigation in FHRs.

The DWHX with a tritium carrier design option adopts a tube-in-tube HX concept as shown in Figure 5-3(a). Each of the DWHX units forms three passages, i.e., an inner flow channel, an annular channel formed between the inner and outer tubes, and an outer channel. The outer fluid,

such as KF-ZrF_4, flows outside the outer tube (on the shell side) while the inner fluid, such as FLiBe carrying tritium, flows in the inner tube. The annular fluid acting as the tritium carrier could be either a gas or a liquid. Tritium in the inner fluid permeates through the inner tube and enters the annular/carrier fluid. A large fraction of the tritium in the carrier fluid then flows to a Tritium Getter Bed (TGB), where the tritium is removed and recovered from the carrier fluid. The remaining tritium in the carrier fluid further permeates through the outer tube and joins the outer fluid.

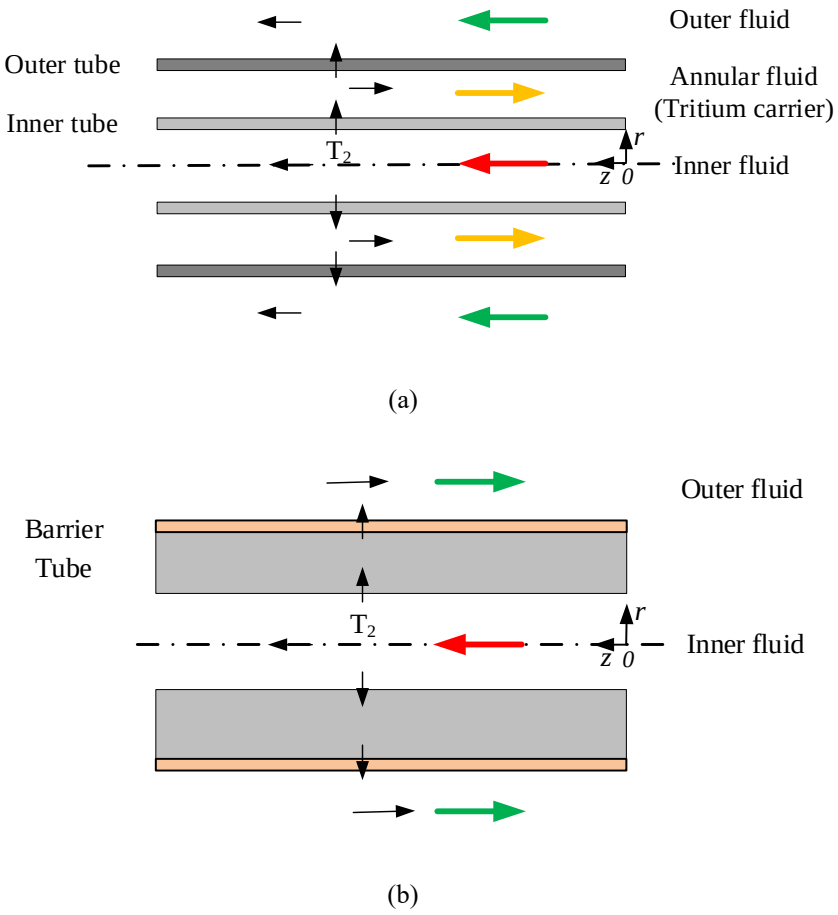

Figure 5-3 Schematic of: (a) A DWHX tube unit with a tritium carrier and (b) A SWHX tube unit with a tritium barrier

The other design option using SWHX with a tritium barrier adopts a barrier coated on the HX tube walls to reduce the tritium leakage rate to the outer fluid as shown in Figure 5-3(b). The tritium leakage rate from the SWHX with tube walls plated with a tritium barrier can be significantly reduced, however, most of the tritium in the inner fluid (the primary salt in FHRs) also permeates through other components in the primary loop. Since the entire primary loop is in the containment filled with argon, most of the generated tritium is trapped and can later be removed by the cleanup system designed for the containment.

The total thermal resistance of a DWHX is relatively large due to the additional thermal resistance of the annular fluid and tube wall. Therefore, the DWHX normally has a larger volume compared with a SWHX. The spirally fluted tubes which have larger surface area and heat transfer coefficient compared with plain tubes (Zhang et al., 2018) are therefore considered for the double-wall P-IHX design. A coupled heat and mass transfer model for the DWHX with a tritium carrier design option and a SWHX with a tritium barrier design option will be developed and used for the HX design.

For the DWHX with a tritium carrier design option, four potential double-wall configurations are investigated, i.e., Inner Plain tube with Outer Plain tube (IPOP), Inner Plain tube with Outer Fluted tube (IPOF), Inner Fluted tube with Outer Plain tube (IFOP), and Inner Fluted tube with Outer Fluted tube (IFOF). In addition, four potential tritium carriers, i.e., helium, FLiBe, FLiNaK, and KF-ZrF_4, are quantitatively analyzed for the Double-Wall Fluted-Tube (DWFT) P-IHX design. For the SWHX with a tritium barrier design option, various tritium barriers, such as the metallic barrier tungsten and ceramic barrier SiC, are investigated for the SWFT P-IHX design. Both these two P-IHX designs are optimized by the NSGA optimization approach.

5.2 A Coupled Heat and Mass Transfer Model for the DWHX

Both the heat and mass transfer in a DWHX tube unit can be described by a one-dimensional model under the following assumptions: (1) The heat transfer between each DWHX tube unit is neglected; (2) The axial conductive heat transfer in the inner and outer tubes, inner, annular, and outer fluids is neglected; and (3) Tritium concentrations in the solids (inner and outer tubes) and fluids (inner, annular, and outer fluids) are too small to affect their thermophysical and mass-transport properties. Both heat and tritium are transferred from the inner fluid, inner tube, annular fluid, outer tube, and finally to the outer fluid. The axial fluid and solid temperature profiles estimated by the heat transfer model will be applied as input parameters for the mass transfer model.

5.2.1. Heat Transfer Model

The steady-state energy balance equations for the inner fluid, annular fluid, outer fluid, inner tube, and outer tube are written as:

$$\frac{\mathrm{d}T_{if}}{\mathrm{d}z} = -\frac{h_{iiw}\left(T_{if} - T_{iiw}\right)}{c_{p,if}\dot{m}_{if}} \cdot \frac{\mathrm{d}A_{iiw}}{\mathrm{d}z} \tag{5-5}$$

$$\frac{\mathrm{d}T_{af}}{\mathrm{d}z} = -\frac{1}{c_{p,af}\dot{m}_{af}}\left[h_{oiw}\left(T_{oiw} - T_{af}\right) \cdot \frac{\mathrm{d}A_{oiw}}{\mathrm{d}z} - h_{iow}\left(T_{af} - T_{iow}\right) \cdot \frac{\mathrm{d}A_{iow}}{\mathrm{d}z}\right] \tag{5-6}$$

$$\frac{\mathrm{d}T_{of}}{\mathrm{d}z} = \frac{h_{oow}\left(T_{oow} - T_{of}\right)}{c_{p,of}\dot{m}_{of}} \cdot \frac{\mathrm{dA}_{\mathrm{oow}}}{\mathrm{d}z} \tag{5-7}$$

$$\frac{\mathrm{d}}{\mathrm{d}r}\left(k_{it} r \frac{\mathrm{d}T_{it}}{\mathrm{d}r}\right) = 0 \tag{5-8}$$

$$\frac{\mathrm{d}}{\mathrm{d}r}\left(k_{ot} r \frac{\mathrm{d}T_{ot}}{\mathrm{d}r}\right) = 0 \tag{5-9}$$

where T_{if}, T_{af}, T_{of}, T_{it}, and T_{ot} are temperatures of the inner fluid, annular fluid, outer fluid, inner tube, and outer tube, respectively. The heat transfer model is discussed in detail in the literature (Zhang et al., 2017b).

If the annular fluid is non-participating media, i.e., mono-atomic and diatomic gases, the boundary conditions for the tube walls considering the radiative heat transfer can be written as:

$$-k_{it}\left(\frac{\mathrm{d}T_{it}}{\mathrm{d}r}\right)_{r=r_2} = h_{oiw}\left(T_{oiw} - T_{af}\right) + \varepsilon_{it-ot}\sigma\left(T_{oiw}^4 - T_{iow}^4\right) \tag{5-10}$$

$$-k_{ot}\left(\frac{\mathrm{d}T_{ot}}{\mathrm{d}r}\right)_{r=r_3} = h_{iow}\left(T_{af} - T_{iow}\right) + \frac{A_{oiw}}{A_{iow}}\varepsilon_{it-ot}\sigma\left(T_{oiw}^4 - T_{iow}^4\right) \tag{5-11}$$

The axial temperature profiles in the inner fluid, inner tube, annular fluid, outer tube, and outer fluid are estimated by the heat transfer model. These temperature profiles will be applied as input parameters for the tritium mass transfer model to be discussed next.

5.2.2. Mass Transfer Model

Tritium produced in FHR reactor cores exists in the form of tritium ion T^+ in TF and molecular tritium T_2, depending on the redox environment of the primary salt (Wu et al., 2016). Redox control is widely used in recent studies for tritium management since tritium control becomes extremely important for tritium permeation and material corrosion in FHRs (Fukada et al., 2005). Tritium is mainly in the form of T_2 when the redox control method is adopted. In this study, it is assumed that all the tritium in the molten salts is in the form of T_2. This is a conservative

assumption to estimate the tritium permeation rates since tritium ion T^+ has a much lower permeation rate through HX structural materials (Suzuki et al., 2000).

The transport process for tritium permeation through a tube consists of several steps: (1) mass transfer of molecular tritium T_2 from the bulk fluid (salt) to the fluid-solid interface; (2) dissociative chemisorption of molecular tritium T_2 to two tritium atoms 2T on the fluid-solid interface; (3) bulk diffusion of tritium atoms through the bulk solid (tube wall); (4) re-combinative desorption from 2T to T_2 on the solid surface.

The tritium permeation rate depends on the tritium mass transfer rate in the bulk fluid containing tritium, dissociative chemisorption rate on the fluid-solid interface, bulk diffusion rate in the solid, and re-combinative desorption rate on the solid surface. In general, the dominating parameter affecting the tritium permeation rate is the one with the smallest rate. If none of them dominate, it will become a multi-rate-determining process. It is assumed that the tritium mass transfer in the bulk salt and diffusion in the bulk solid processes are the rate-determining processes (Fukada and Morisaki, 2006). A coupled model considering heat transfer, tritium mass transfer in the fluid, and diffusion in the solid is developed and discussed next.

The steady-state tritium concentration balance equations in the bulk inner fluid, bulk annular fluid, and bulk outer fluid are given by

$$\frac{\mathrm{d}}{\mathrm{dz}}\left(\frac{C_{T,bif}\dot{m}_{if}}{\rho_{if}}\right)\cdot \mathrm{dz} = -J_i \tag{5-12}$$

$$\frac{\mathrm{d}}{\mathrm{dz}}\left(\frac{C_{T,baf}\dot{m}_{af}}{\rho_{af}}\right)\cdot \mathrm{dz} = -\left(J_i - J_o\right) \tag{5-13}$$

$$\frac{\mathrm{d}}{\mathrm{dz}}\left(\frac{C_{T,bof}\dot{m}_{of}}{\rho_{of}}\right)\cdot \mathrm{dz} = J_o \tag{5-14}$$

where C and J are the tritium concentration and permeation rate, respectively.

Under steady-state conditions, the gas permeation rates J_i in the following three processes related to the inner tube are identical: tritium mass transfer from the bulk inner fluid to the inner-fluid-inner-tube interface; tritium diffusion through the bulk inner tube; and tritium mass transfer from the inner-tube-annular-fluid interface to the bulk annular fluid, which are denoted as

$$J_i = k_{m,iiw} \cdot \mathrm{d}A_{iiw} \cdot \left(C_{T,bif} - C_{T,if-it} \right) \tag{5-15}$$

$$J_i = \frac{k_{Pi} \left(p_{T,it-if}^{1/2} - p_{T,it-af}^{1/2} \right) \cdot 2\pi \cdot \mathrm{d}z}{\ln\left(r_2 / r_1 \right)} \tag{5-16}$$

$$J_i = k_{m,oiw} \cdot \mathrm{d}A_{oiw} \cdot \left(C_{T,af-it} - C_{T,baf} \right) \tag{5-17}$$

Similarly, the permeation rates J_o related to the outer tube are denoted as

$$J_o = k_{m,iow} \cdot \mathrm{d}A_{iow} \cdot \left(C_{T,baf} - C_{T,af-ot} \right) \tag{5-18}$$

$$J_o = \frac{k_{Po} \left(p_{T,ot-af}^{1/2} - p_{T,ot-of}^{1/2} \right) \cdot 2\pi \cdot \mathrm{d}z}{\ln\left(r_4 / r_3 \right)} \tag{5-19}$$

$$J_o = k_{m,oow} \cdot \mathrm{d}A_{oow} \cdot \left(C_{T,of-ot} - C_{T,bof} \right) \tag{5-20}$$

The permeation rates J_i and J_o calculated by Eqs. (5-16) and (5-19) are theoretically derived by Fick's First Law and Sieverts' Law for a diatomic gas. The half-order partial pressure dependence of the permeation rate has been validated for clean surfaces by experiments (Strehlow and Sawage, 1974; Bell et al., 1980) and is adopted in this research. The average wall temperature is used to estimate the permeability of the HX tubes at each axial location.

Stempien et al. (2016) assumed that the tritium partial pressure rather than tritium concentration was continuous on the fluid-solid interface. Under this assumption, the modeling results agreed well with the experimental data (Stempien et al., 2016). The same assumption of continuous tritium partial pressure at a fluid-solid interface is adopted in the development of the tritium mass transport model in this research. The tritium partial pressures on the inner-fluid-inner-tube interface, inner-tube-annular-fluid interface, annular-fluid-outer-tube interface, and outer-tube-outer-fluid interface have the following relationships:

$$p_{T,if-it} = p_{T,it-if} \tag{5-21}$$

$$p_{T,it-af} = p_{T,af-it} \tag{5-22}$$

$$p_{T,af-ot} = p_{T,ot-af} \tag{5-23}$$

$$p_{T,ot-of} = p_{T,of-ot} \tag{5-24}$$

Henry's law, expressed in Eq. (5-25), is used to relate the tritium concentration to its corresponding partial pressure. The Henry's law constant k_H is defined as the ratio of the concentration of a gas in a liquid to the partial pressure of the gas over the liquid.

$$C_T = k_H \cdot p_T \tag{5-25}$$

Per Henry's law, the tritium concentrations in various regions are expressed as Eqs. (5-26) to (5-29). If a gas is used as the annular fluid, ideal gas law will be applied to relate the concentration to the partial pressure.

$$C_{T,if-it} = k_{H,T,if} \cdot p_{T,if-it} \tag{5-26}$$

$$C_{T,af-it} = k_{H,T,af} \cdot p_{T,af-it} \tag{5-27}$$

$$C_{T,af-ot} = k_{H,T,af} \cdot p_{T,af-ot} \tag{5-28}$$

$$C_{T,of-ot} = k_{H,T,of} \cdot p_{T,of-ot} \tag{5-29}$$

Boundary conditions for the tritium mass transport model are denoted by

$$C_{T,bif}\left(z=0\right) = C_{bif,0} \tag{5-30}$$

$$C_{T,baf}\left(z=L\right) = \left(1-\eta_{TGB}\right) \cdot C_{T,baf}\left(z=0\right) \tag{5-31}$$

$$C_{T,bof}\left(z=0\right) = 0 \tag{5-32}$$

If an open loop is used for the annular fluid, $C_{T,baf}(z=L)=0$ (or $\eta_{TGB}=100\%$) will be applied. However, if a closed loop is adopted, $C_{T,baf}(z=L)>0$ (or $\eta_{TGB}<100\%$) will be used. The experiment (Wang et al., 2017) used to validate the mass transfer model adopted an open loop (sweep gas directly came from the gas cylinder and eventually was ventilated to the ambient air). Therefore, $\eta_{TGB}=100\%$ is applied to the model benchmark. However, in the actual applications, a closed loop will be most likely to be used for the annular fluid if the DWHX design is adopted for FHRs due to the economic consideration. In this research, it is assumed that $\eta_{TGB}=99\%$, which is achievable for an independent TGB (Kherani et al., 1988).

Utilizing Eqs. (5-12) to (5-32) and fluid temperature profiles obtained from the heat transfer model, the tritium concentration profiles in the inner fluid, annular fluid, and outer fluid can be calculated to evaluate the tritium mass transfer performance in the DWHX. An example will be given to help understand the function of the coupled heat and mass transfer model.

Figure 5-4 and Figure 5-5 show the axial (z) and radial (r) temperature profiles and tritium partial pressure profiles for a double-wall P-IHX with a length of L, respectively. The inner, annular, and outer fluids are FLiBe, helium, and KF-ZrF_4, respectively. The boundary conditions include: $T_{if}(z/L = 0) = 700$ °C, $T_{af}(z/L = 1) = 650$ °C, $T_{of}(z/L = 0) = 600$ °C, $C_{T,if}(z/L = 0) = 10^{-3}$ mol/m^3, $C_{T,af}(z/L = 1) = 0.01\, C_{T,af}(z/L = 0)$ and $C_{T,of}(z/L = 0) = 0.01\, C_{T,of}(z/L = 1)$. The flow directions of the inner and outer fluids are the same (from z/L = 0 to z/L = 1), but opposite to the flow direction of the annular fluid.

As shown in Figure 5-4(a), the inner fluid FLiBe temperature decreases from z/L = 0 to z/L = 1, while the temperatures of the annular fluid helium (from z/L = 1 to z/L = 0) and outer fluid KF-ZrF_4 (from z/L = 0 to z/L = 1) increase along their respective flow direction. The inner and outer surface temperature differences at each axial location of the inner tube (or outer tube) are within several degree Celsius. Therefore, it is appropriate to use an average wall temperature for the estimation of the tube permeability in the mass transfer model.

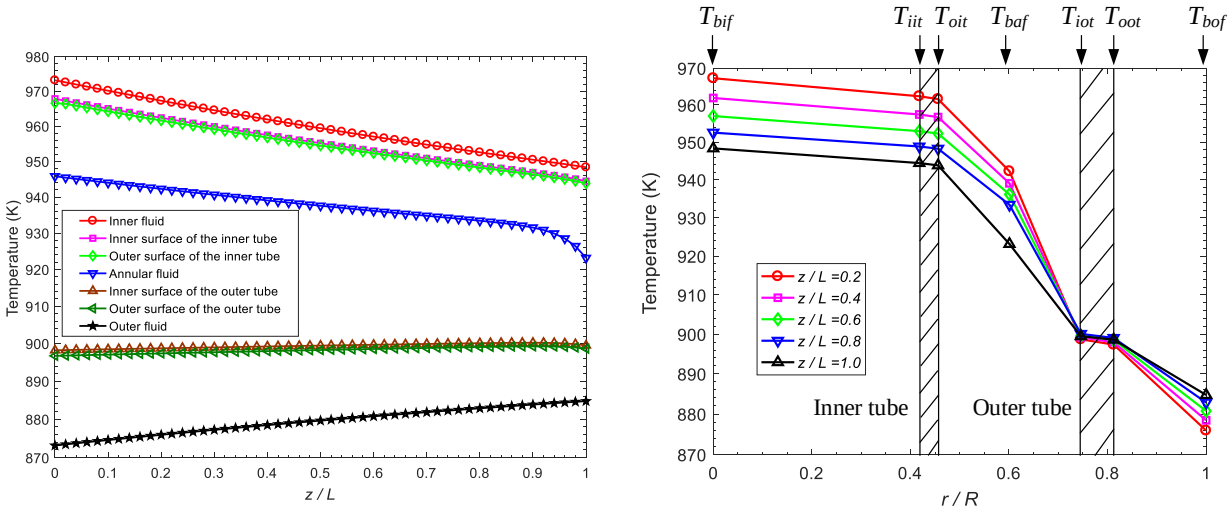

(a) (b)

Figure 5-4 (a) Axial and (b) radial temperature profiles of the three fluids and two tubes for a double-wall configuration

Figure 5-4(b) shows the radial temperature profiles at a number of axial locations, including the temperatures of the inner fluid, inner tube, annular fluid, inner and outer surfaces of the outer tube, and outer fluid. The temperature drop across the annular fluid is much higher than that across the inner and outer fluids due to the much larger thermal resistance of the annular fluid (smaller heat transfer coefficient). In addition, the temperature drops across the inner and outer tubes are much lower than those across fluids due to the much smaller thermal resistances of the tubes (much larger thermal conductivities).

Figure 5-5(a) shows the tritium partial pressure profiles along the axial direction. The tritium partial pressure in the inner fluid FLiBe decreases from $z/L = 0$ to $z/L = 1$, while the tritium partial pressures in the annular fluid helium (from $z/L = 1$ to $z/L = 0$) and outer fluid KF-ZrF_4 (from $z/L = 0$ to $z/L = 1$) increase along their respective flow direction. This is because tritium in the inner fluid permeates through the inner tube into the annular fluid, while a portion of tritium further permeates through the outer tube into the outer fluid. Figure 5-5(b) shows the tritium radial partial pressure profiles at a number of axial locations. The tritium partial pressure difference across the annular fluid is much lower than that across the inner and outer fluids due to the much smaller mass transfer resistance of the annular fluid.

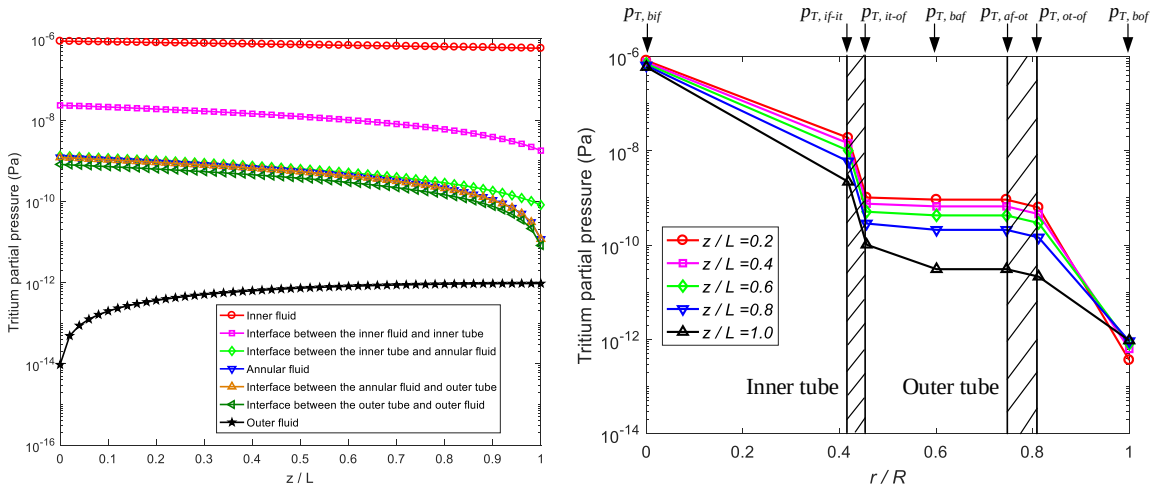

(a) (b)

Figure 5-5 (a) Axial and (b) radial partial pressure profiles of tritium for a double-wall configuration

5.2.3. Model Benchmark

The heat transfer and mass transfer are coupled processes. The heat transfer determines the axial temperature profile, which affects the mass transfer parameters, i.e., the diffusivity. In addition, the mass transfer changes the thermophysical properties of each fluid, which affects the heat transfer process. However, the change of thermophysical properties of fluids due to tritium permeation is small. It is therefore appropriate to benchmark the heat transfer and mass transfer models separately.

Benchmark of the heat transfer model

The predicted results by the heat transfer model are compared with the experimental data from a triple-tube HX experiment using water as the working fluid as well as ANSYS Fluent simulation results (Gomaa et al., 2016). As shown in Figure 5-6, the low-temperature cold water

acting as the inner fluid and intermediate-temperature normal water acting as the outer fluid flowed co-currently. Both the co-current and counter-current flow patterns were investigated by changing the flow direction of the annular fluid high-temperature hot water.

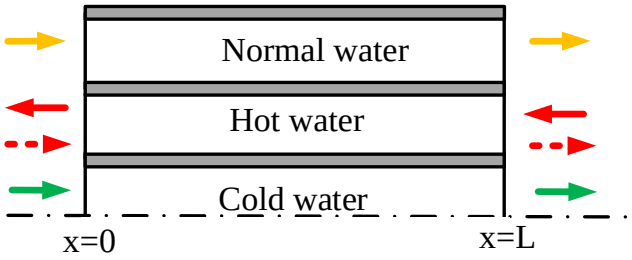

Figure 5-6 Flow directions for the inner, annular, and outer fluids (Gomaa et al., 2016)

The comparison of the predicted fluid temperature profiles by the heat transfer model with the experimental data are presented in Figure 5-7. The fluid axial temperature profiles for the counter-current and co-current flow patterns are plotted in a dimensionless coordinate system with its origin located at the tube entrance. As predicted by the heat transfer model for the counter-current flow pattern as shown in Figure 5-7(a), the hot-water temperature decreases from 70.0 to 52.3 $^{\circ}$C as the normal- and cold-water temperatures increase from 18.0 to 27.6 $^{\circ}$C, and 10.0 to 18.1 $^{\circ}$C, respectively. Similarly, for the co-current flow pattern as shown in Figure 5-7(b), the hot-water temperature decreases from 70.0 to 52.5 $^{\circ}$C as the normal- and cold-water temperatures increase from 18.0 to 27.3 $^{\circ}$C, and 10.0 to 18.2 $^{\circ}$C, respectively.

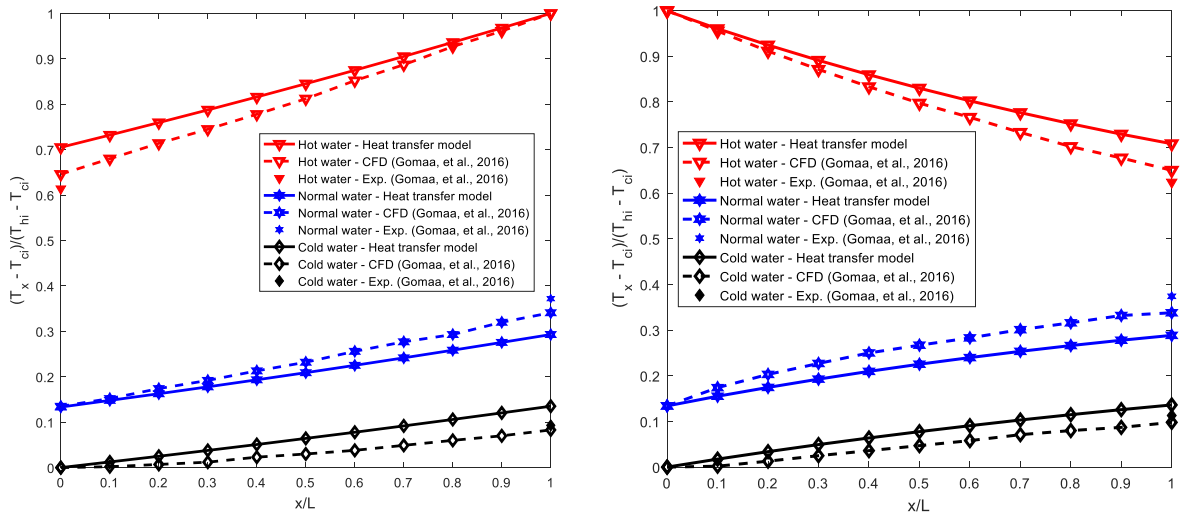

(a) (b)

Figure 5-7 Comparison of the fluid temperatures among the model predictions, experimental data, and ANSYS Fluent simulation results for (a) a counter-current flow pattern and (b) a co-current flow pattern

The relative discrepancies for the average heat transfer coefficients predicted for the hot water, normal water, and cold water compared with their respective experimental data are within 17%, 24%, 23%, respectively. In addition, the maximum relative differences between the predicted hot-water temperatures and the experimental data, the predicted normal-water temperatures and the experimental data, the predicted cold-water temperatures and the experimental data are 12%, 15%, and 16%, respectively. These discrepancies are acceptable considering the measurement uncertainty for the cold-water temperature in the experiment and the ±20% uncertainties for the heat transfer correlation (Ahn, 2003), Eq. (5-33), used for the annular fluid.

$$\mathrm{Nu} = 0.022\,\mathrm{Pr}^{0.5}\,\mathrm{Re}^{0.8}, \quad \mathrm{Re} < 5\times10^{3} \tag{5-33}$$

Benchmark of the mass transfer model

There appears no available experimental data related to tritium mass transfer in a DWHX. Predictions by the tritium mass transfer model were compared with the experimental data from a hydrogen separation experiment performed by Wang et al. (2017). A mixture of hydrogen and helium gases acting as a feeding gas flowed on the shell side of a nickel hollow fiber tube and nitrogen gas acting as a sweep gas co-currently flowed on the tube side as shown in Figure 5-8. The nickel hollow fiber tube was housed by a quartz tube, which itself was housed and heated by a tubular furnace. Since the furnace temperature varied significantly along its axial direction, the measured temperature profiles under different furnace temperature settings were used for the tritium mass transport model benchmark. Hydrogen permeated from the shell-side feeding gas to the tube-side sweep gas and the corresponding permeation rate was measured by a gas chromatograph.

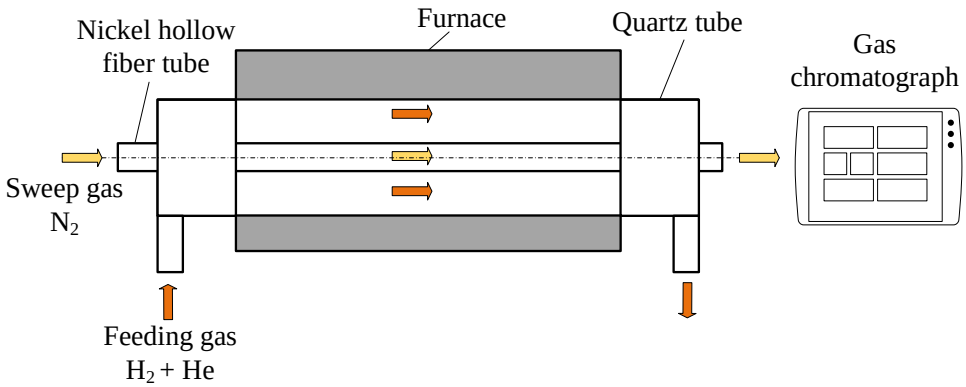

Figure 5-8 Schematic of the experimental setup by Wang et al. (2017)

The mass transfer correlation (Welty et al., 2007) used to benchmark the mass transfer model is given by

$$\mathrm{Sh} = 1.86\left(\frac{D}{L}\mathrm{Re}\,\mathrm{Sc}\right)^{1/3}, \quad 10 \le \mathrm{Re} \le 2\times10^{3} \tag{5-34}$$

where Sh, D, L, Re, and Sc are the Sherwood number, tube inner diameter, tube length, Reynolds number, and Schmidt number, respectively. The Schmidt number is defined as

$$\mathrm{Sc} = \frac{\mu}{\rho D_{AB}} \tag{5-35}$$

where μ, ρ, and D_{AB} are the dynamic viscosity, density, and diffusivity of species A in species B. Since the tritium diffusivities in some fluids are not available, the classical rate theory, which states that the diffusivities of hydrogen isotopes in the same material are inversely proportional to the square root of their molecular masses, is used to determine the tritium diffusivities in these fluids. The hydrogen diffusivity and solubility in various fluids are summarized in Table 5-1.

Table 5-1 Diffusivity and solubility of hydrogen in gases

	Diffusivity (m^2/s)	Solubility (mol/m^3 Pa)	References
He	$D_{H_2,He} = \dfrac{2.7\times10^{-6}T^{1.51}}{\left(\ln\dfrac{T}{5.34\times10^{-6}}\right)^2}$	$\left(\dfrac{C}{p}\right)_{T_2,He} = \dfrac{1}{R_g T}$	Marrero and Mason, 1972
N_2	$D_{H_2,N_2} = \dfrac{1.539\times10^{-6}T^{1.548}}{\left(\ln\dfrac{T}{3.16\times10^{-7}}\right)^2 e^{-2.8/T}e^{1.67/T^2}}$	$\left(\dfrac{C}{p}\right)_{T_2,N_2} = \dfrac{1}{R_g T}$	Marrero and Mason, 1972

Note: Temperature unit is Kelvin.

Figure 5-9 shows the comparison of the predicted hydrogen permeation rates with the experimental data for various nitrogen flow rates and testing temperatures. Under a given temperature, such as 1000 ˚C, the hydrogen permeation rate increases with the increase of the sweep gas flow rate. This is because as the sweep gas flow rate increases, tritium is more quickly taken out of the hollow fiber tube and consequently the hydrogen partial pressure difference across the tube wall acting as a driven force between the feeding gas and sweep gas increases, leading to larger hydrogen permeation rates.

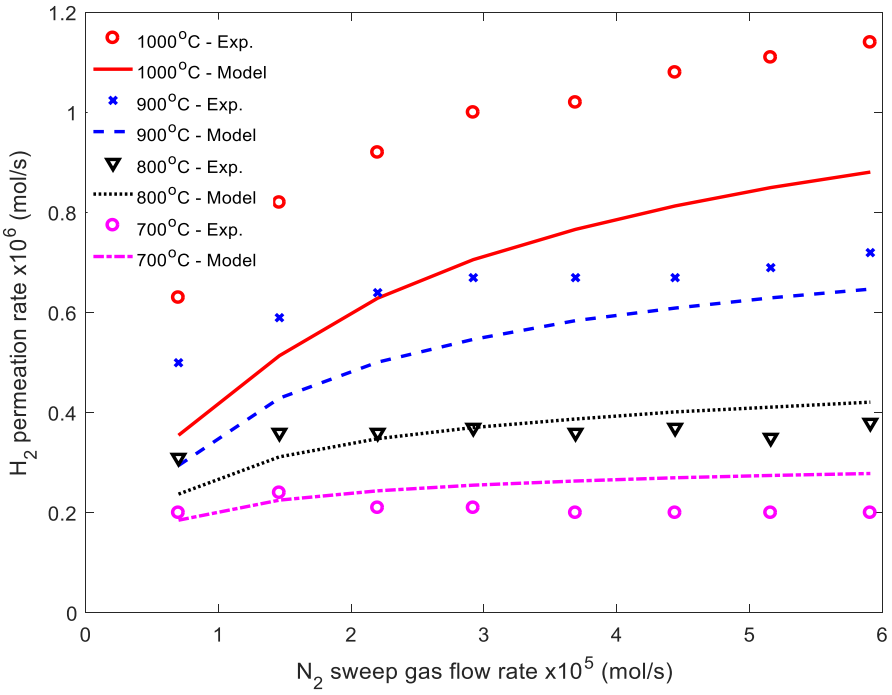

Figure 5-9 Comparison of the hydrogen permeation rates for different temperatures and sweep gas flow rates

In addition, the hydrogen permeation rate is less sensitive to the sweep gas flow rate at relatively lower temperatures, i.e., 700 ˚C as shown in Figure 5-9. At low temperatures, the major mass transfer resistance is the HX tube wall due to its low permeability. At high temperatures,

however, the mass transfer resistance from the HX tube wall is significantly reduced. Therefore, the hydrogen permeation rate increases faster as the increase of the sweep gas flow rate at higher temperatures, i.e., 1000 °C. That is the reason why the hydrogen permeation curve is steeper at high temperatures than that at lower temperatures.

For a given sweep gas flow rate, such as 5×10^{-5} mol/s as shown in Figure 5-9, much larger hydrogen permeation rates are observed at higher temperatures due to larger permeability through the tube wall at higher temperatures. Furthermore, as shown in Figure 5-9, the trend of the hydrogen permeation curve is predicted generally well by the model, especially at 700 and 800 °C, which is very encouraging as the maximum salt temperature in FHRs is expected to be at such temperatures.

A quantitative analysis shows that the maximum relative difference between the hydrogen permeation rates predicted by the tritium mass transport model and experimental results at 700, 800, 900, and 1000 °C are 35, 23, 41, and 44%, respectively. The much larger permeation rates in the experiments at higher temperatures, for example 1000 °C, most likely result from the additional mass transfer area (quartz tubes on the two ends of the test section), which is not considered in the current model. If the additional area were considered in the model, the discrepancies would be much smaller. To verify this hypothesis, we need to know the temperature profile and the permeability of the quartz tubes. However, none of these were provided in the experiment (therefore not considered in the current model). For a simple justification, it is assumed that the permeation rate is merely proportional to the mass transfer length/area. The actual mass transfer length should be the entire length between the inlet and outlet of the feeding gas, which is about 33 cm. Since only the nickel tube length, 23 cm, is considered as the mass transfer length in the

model, the experimental data should be about 43% higher than the predicted results, which accounts for the much larger experimental data points at elevated temperatures, i.e., 1000 ºC.

Figure 5-10 shows the comparison of the hydrogen permeation rates for various testing temperatures, hydrogen molar fractions, and tube sizes. For a given tube size and hydrogen molar fraction, such as a hydrogen molar fraction 50% in Figure 5-10(a), the hydrogen permeation rate increases with the temperature increase due to the larger permeability through tube wall at higher temperatures. For a given tube size and testing temperature, such as 1000 °C in Figure 5-10(a), larger hydrogen molar fractions result in larger hydrogen permeation rates, which is mainly due to the larger hydrogen partial pressure difference between the feeding gas and sweep gas. The predicted permeation rates by the model are smaller than the experimental data for these three tube sizes. The maximum relative discrepancies between the model results and experimental data for the three investigated hollow fiber tubes as shown in Figure 5-10 are 25, 30, and 38%, respectively. However at temperatures of 700 and 800 °C, between which the primary salt maximum temperature is expected to be located, the model results and experimental data have reasonably good agreement.

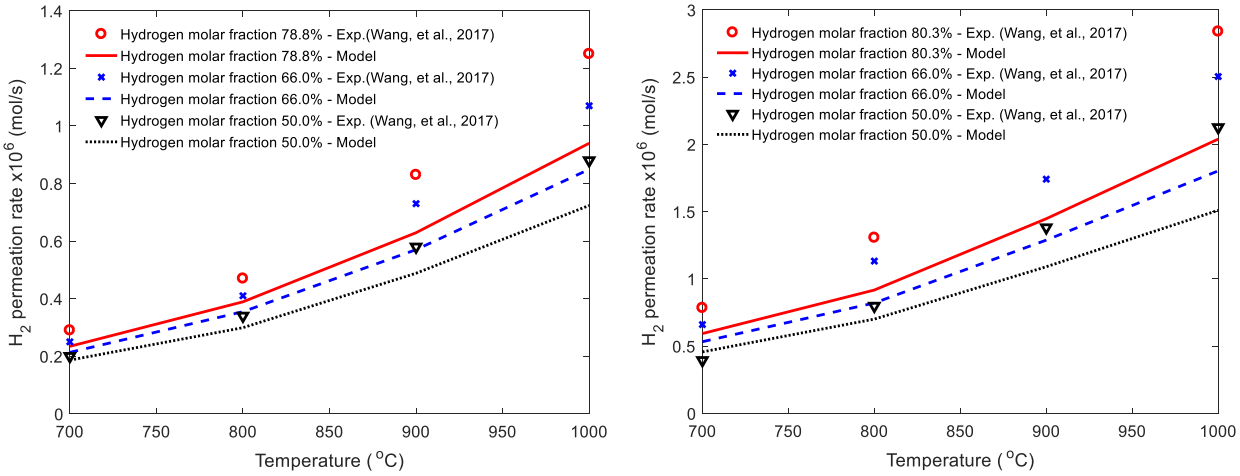

(a) (b)

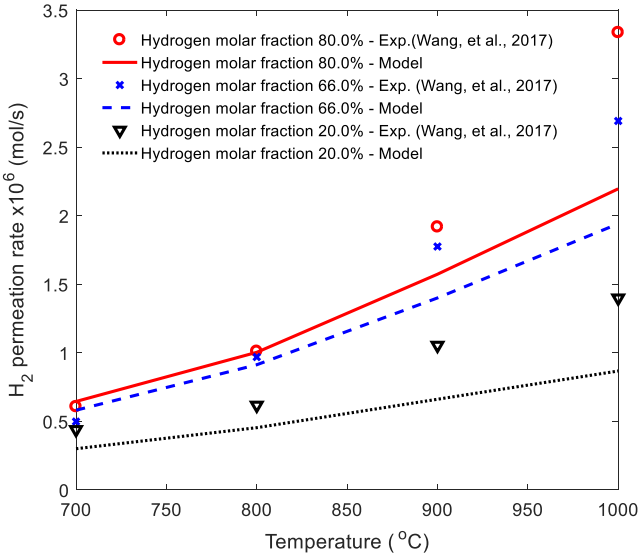

(c)

Figure 5-10 Comparison of the hydrogen permeation rates through: (a) HF-01 tube (ID 1.33 mm), (b) HF-03 tube (ID 1.75 mm), and (c) HF-06 tube (ID 1.40 mm) for different temperatures and hydrogen molar fractions

5.2.4. Selection of the Tube Surface Configuration and Tritium Carrier

For the DWHX with a tritium carrier design option, the inner and outer tubes of a DWHX tube unit may have different tube surface configurations, such as fluted and plain surfaces. In addition, the tritium carrier (annular fluid) could be a gas or a liquid. It is a cost-effective way to identify a best tube surface configuration and a best annular fluid prior to carrying out a DWFT P-IHX design optimization.

Tube surface configuration

There are four tube configurations initially considered for a DWHX unit, namely, IPOP, IPOF, IFOP, and IFOF. Both the heat and mass transfer performance should be considered to identify the best double-wall configuration for the P-IHX. For the heat transfer performance, it is expected to achieve a large heat transfer rate. In addition, most of the heat removal from the inner fluid is expected to be taken by the outer fluid rather than the annular fluid. If most of the heat removal is taken by the annular fluid, the annular fluid outlet temperature will increase significantly, which requires an additional cooler to cool down the annular fluid. For the mass transfer performance, it is expected to achieve a large mass transfer rate from the inner fluid. In addition, most of the tritium is expected to be removed by the annular fluid. Otherwise, an additional tritium removal device should be installed to prevent tritium leakage from the outer fluid.

As an example, the heat and mass transfer performance for these four double-wall configurations for the P-IHX are investigated. As a starting point, the inner, annular, and outer fluids in the P-IHX are FLiBe, helium, and KF-ZrF_4, respectively. The heat and mass transfer rates are normalized to their respective maximum value.

Figure 5-11 shows the effect of the annular-fluid Reynolds number on the heat transfer rate. Both the IFOF and IFOP designs have at least 48% larger heat transfer rates than the IPOF design and at least 127% larger heat transfer rates than the IPOP design. This is because both the IFOF and IFOP designs use fluted tubes as the inner tubes, which significantly increases the heat transfer area and heat transfer coefficients on the tube and annular sides. The IFOF configuration has a larger heat transfer rate than the IFOP configuration due to the larger heat transfer coefficient and area of the outer fluted tube in the IFOF configuration compared with plain tube in the IFOP configuration. In addition, larger than 85% of the heat removal is taken by the outer fluid and the remaining heat is taken by the annular fluid. The heat transfer rates for these four double-wall configurations are IFOF > IFOP >> IPOF >> IPOP, which is the priority sequence for selection as well if only the heat transfer performance is considered.

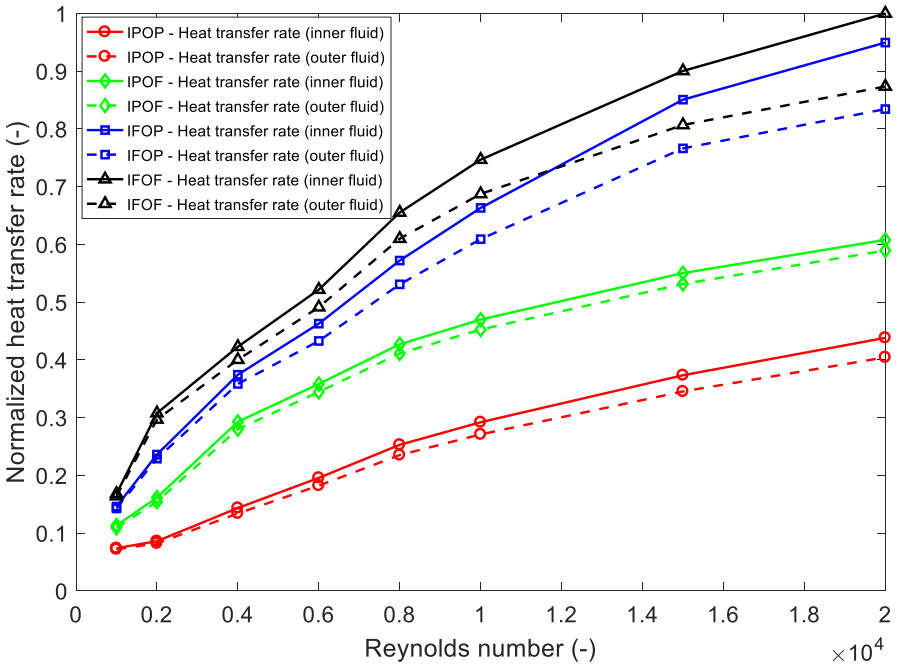

Figure 5-11 Effect of the annular-fluid Reynolds number on the heat transfer rate

Figure 5-12 shows the effect of the annular-fluid Reynolds number on the mass transfer rate. Both the IFOF and IFOP designs have at least 375% larger mass transfer rates than those of the IPOP and IPOF designs, which results from the increased mass transfer area and enhanced mass transfer coefficients on the tube and annular sides. The IFOF configuration has a larger mass transfer rate than the IFOP configuration due to the outer fluted tube which has a larger mass transfer coefficient and area in the IFOF configuration. In addition, at least 95% of tritium is taken by the annular fluid and the remaining tritium is taken by the outer fluid for all these four double-wall configurations. The tritium mass transfer rates for these four double-wall configurations are IFOF> IFOP >> IPOF ≈ IPOP, which is the priority sequence for selection as well if only the mass transfer performance is considered.

Considering both the heat and mass transfer performance, the IFOF configuration is superior to the IFOP, IPOF, and IPOP configurations and it is therefore adopted for the double-wall P-IHX design optimization.

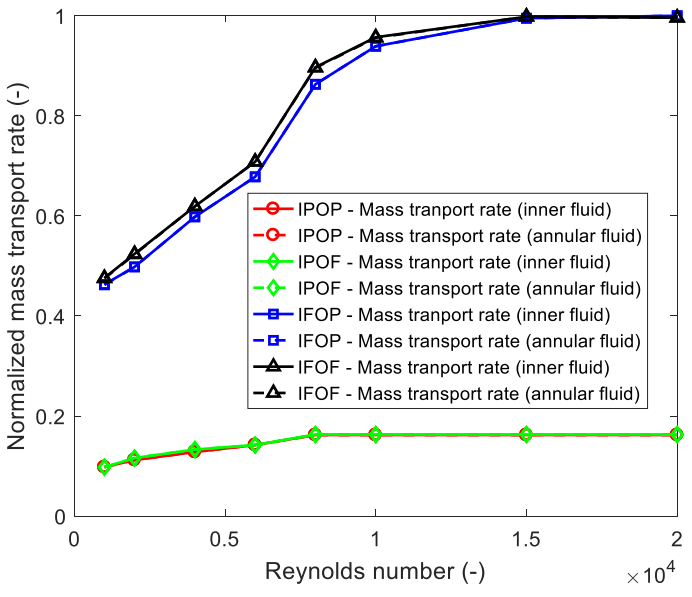

Figure 5-12 Effect of the annular-fluid Reynolds number on the mass transfer rate

Tritium carrier

In this study, FLiBe, FLiNaK, KF-ZrF4, and helium are initially considered as candidates for the tritium carrier fluid in the DWFT P-IHX. Both the heat and mass transfer performance need to be considered to identity the best tritium carrier for the DWFT P-IHX.

Figure 5-13 and Figure 5-14 show respectively the heat and mass transfer performance of the DWFT P-IHX for different tritium carriers (annular fluids). The heat and mass transfer rates are normalized to their respective maximum value. As shown in Figure 5-13, for a certain annular-fluid Reynolds number, the total heat transfer rate using FLiBe as the carrier fluid is 4 to 69%, 9 to 120%, and 115 to 633% larger than those using FLiNaK, KF-ZrF4, and helium as the annular fluid, respectively. Therefore, the order of heat transfer performance for the four potential carrier fluids is FLiBe > FLiNaK > KF-ZrF4 >> helium. In other words, a DWHX with a tritium carrier FLiBe would have the smallest size compared to the DWHXs with other tritium carriers investigated for the same thermal duty. However, the tritium carrier FLiBe would take away a significant fraction of heat, 30 to 52% under the conditions investigated, which should be recycled by an additional HX.

As shown in Figure 5-14, for a certain annular-fluid Reynolds number, the total mass transfer rate using helium as the carrier fluid is about 60 to 400%, 200 to 1600%, and 413 to 2000% larger than those using the FLiBe, FLiNaK, and KF-ZrF4 as the carrier fluid, respectively. Therefore, the order of the mass (tritium) transfer performance for the four potential carrier fluids under different annular-fluid Reynolds numbers is helium >> FLiBe >> FLiNaK > KF-ZrF4. In other words, a DWHX with helium as the tritium carrier effectively removes the tritium and reduces the tritium leakage rate to the outer fluid. For other tritium carriers, such as FLiBe, an additional tritium removal facility will be needed for the outer fluid.

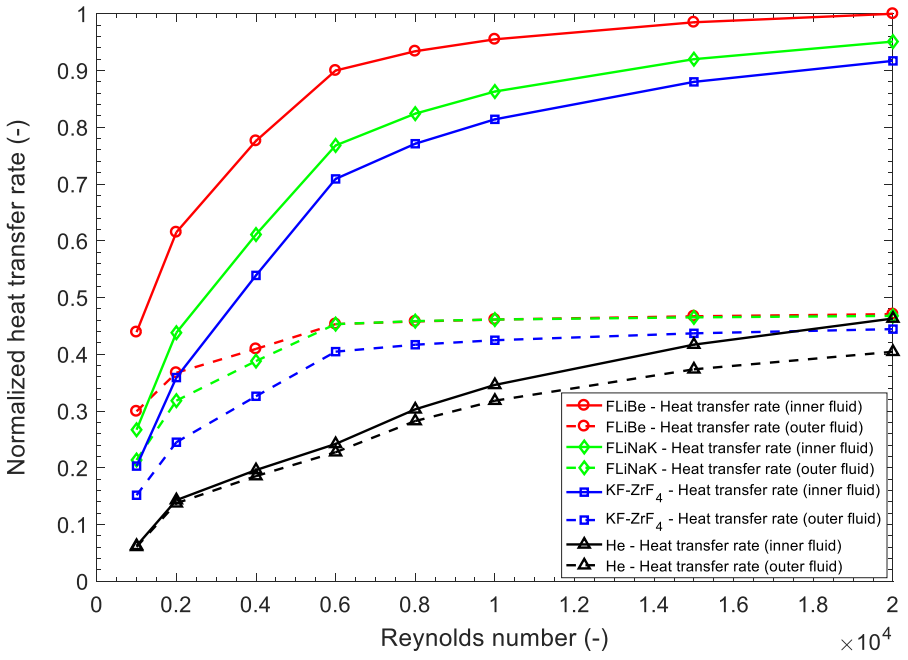

Figure 5-13 Comparison of heat transfer rates using different carrier fluids

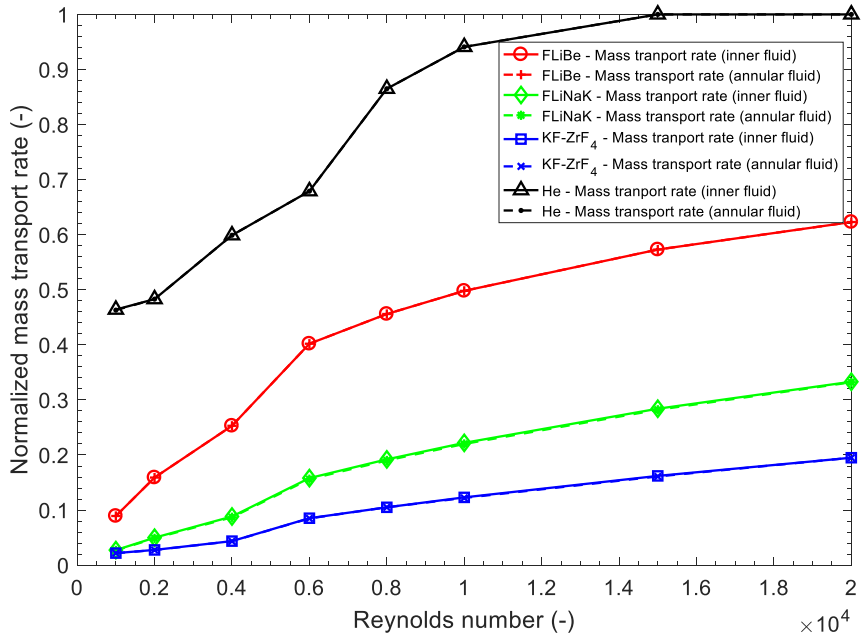

Figure 5-14 Comparison of mass transfer rates using different carrier fluids

Since FLiBe could effectively transfer heat and helium could effectively remove the tritium, both of them are better choices as a tritium carrier than the two other salts investigated for the DWFT P-IHX in terms of the heat and mass transfer performance. However, further considering (1) the additional HX needed to recuperate the heat taken by the carrier fluid; (2) the increased pumping power needed for the additional HX; and (3) the additional tritium removal facility needed to remove the tritium from the outer fluid for the option using FLiBe as the tritium carrier, helium appears to be superior. Helium is therefore proposed as the tritium carrier for the DWFT P-IHX design.

5.3 A Coupled Heat and Mass Transfer Model for the SWHX

5.3.1. Heat Transfer Model

Figure 5-15 shows a SWHX tube configuration. A triangular arrangement of the SWHX tube units and counter-current flow design are adopted to achieve a large heat transfer coefficient. The hexagonal flow sub-channel for the outer fluid is simplified and treated as a circular channel with an equivalent radius to keep the flow areas of these two cases the same.

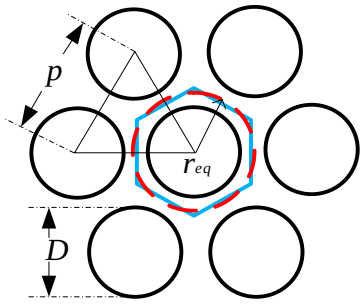

Figure 5-15 Triangular arrangement of SWHX tube units

Figure 5-16 shows a schematic of the 1D heat transfer process starting from the inner fluid, to the inner barrier, tube, outer barrier, and finally the outer fluid. The temperature is continuous on each interface. A counter-current flow is adopted for the inner and outer fluids to enhance the heat transfer coefficient.

The steady-state energy balance equation for the inner or outer fluids can be written as

$$\frac{\mathrm{d}T_f}{\mathrm{d}z} = -\frac{h_{f-b}\left(T_f - T_{f-b}\right)}{c_{p,f}\dot{m}_f} \cdot \frac{\mathrm{d}A_{f-b}}{\mathrm{d}z} \tag{5-36}$$

where the subscripts *f* and *f-b* are the fluid and interface between the fluid and barrier, respectively.

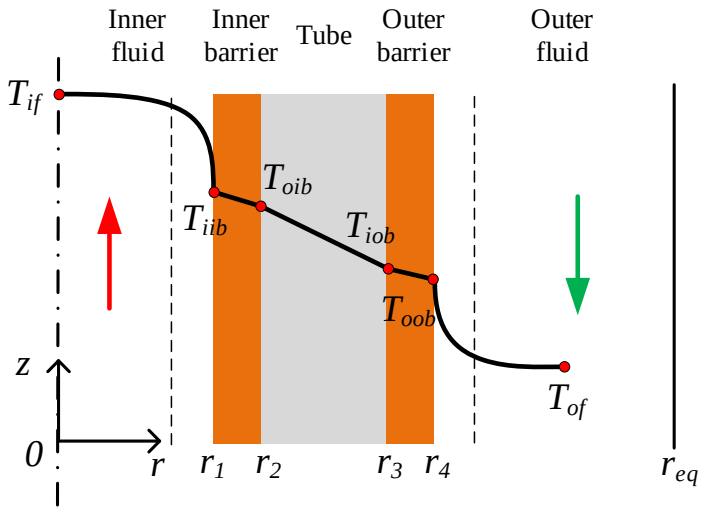

Figure 5-16 Schematic of the 1D heat transfer process through the SWHX

The steady-state energy balance equation for the solid, such as the inner barrier, tube, and outer barrier, can be written as

$$\frac{\mathrm{d}}{\mathrm{d}r}\left(k_s r \frac{\mathrm{d}T_s}{\mathrm{d}r}\right) = 0 \tag{5-37}$$

where the subscript *s* is the solid.

The boundary conditions for the 1D heat transfer model are written as

$$r = r_i,\ T_s = T_i \tag{5-38}$$

$$-k_b \left(\frac{\mathrm{d}T_b}{\mathrm{d}r} \right)_{r=r_1 \text{ or } r_4} = h_{f-b} \left(T_f - T_{f-b} \right) \tag{5-39}$$

$$-k_b \left(\frac{\mathrm{d}T_b}{\mathrm{d}r} \right)_{r=r_2 \text{ or } r_3} = -k_t \left(\frac{\mathrm{d}T_t}{\mathrm{d}r} \right)_{r=r_2 \text{ or } r_3} \tag{5-40}$$

$$T_{if} \left(z = 0 \right) = T_{if,0} \tag{5-41}$$

$$T_{if} \left(z = L \right) = T_{of,0} \tag{5-42}$$

where the subscript *i*, *b*, *t*, *if*, and *of* are the interface, barrier, tube, inner and outer fluids, respectively.

The temperature profiles for the inner fluid, inner barrier, tube, outer barrier, and outer fluid estimated by the heat transfer model will be applied as inputs for the tritium mass transfer model to be discussed next.

5.3.2. Mass Transfer Model

Figure 5-17 shows a schematic of the 1D mass transfer process from the inner fluid to the outer fluid. There is a concentration jump on each interface, while the partial pressure is continuously distributed across these interfaces.

The steady-state tritium concentration balance equation for tritium in the bulk inner or outer fluids can be written as

$$\frac{\mathrm{d}}{\mathrm{dz}}\left(\frac{C_{T,f}\dot{m}_f}{\rho_f}\right)\cdot \mathrm{dz} = -J_{\text{P-IHX}} \tag{5-43}$$

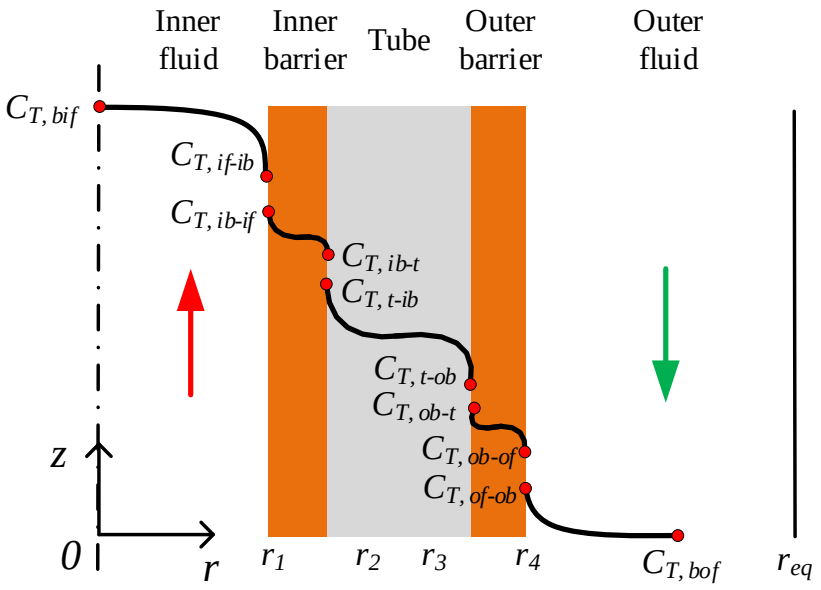

Figure 5-17 Schematic of the 1D mass transfer process through the SWHX

Under steady-state conditions, the permeation rate $J_{\text{P-IHX}}$ in the following processes are identical: tritium convective transfer from the bulk inner fluid to the inner-fluid-inner-barrier interface; tritium diffusion through the bulk inner barrier; tritium diffusion through the bulk tube; tritium diffusion through the bulk outer barrier; and tritium convective transfer from the outer-barrier-outer-fluid interface to the bulk outer fluid.

$$J_{\text{P-IHX}} = k_{m,iib}\cdot \mathrm{d}A_{iib}\cdot\left(C_{T,bif} - C_{T,if-ib}\right) \tag{5-44}$$

$$J_{\text{P-IHX}} = \frac{k_{P,ib}\left(p_{T,ib-if}^{1/2} - p_{T,ib-t}^{1/2}\right)\cdot 2\pi\cdot \mathrm{d}z}{\ln\left(r_2/r_1\right)} \tag{5-45}$$

$$J_{\text{P-IHX}} = \frac{k_{P,t}\left(p_{T,t-ib}^{1/2} - p_{T,t-ob}^{1/2}\right)\cdot 2\pi\cdot \mathrm{d}z}{\ln\left(r_3/r_2\right)} \tag{5-46}$$

$$J_{\text{P-IHX}} = \frac{k_{P,ob}\left(p_{T,ob-t}^{1/2} - p_{T,ob-of}^{1/2}\right)\cdot 2\pi\cdot \mathrm{d}z}{\ln\left(r_4/r_3\right)} \tag{5-47}$$

$$J_{\text{P-IHX}} = k_{m,oob}\cdot \mathrm{d}A_{oob}\cdot\left(C_{T,of-ob} - C_{T,bof}\right) \tag{5-48}$$

where k_m, k_p, and p are the mass transfer coefficient, permeability, and partial pressure, respectively. The subscripts *iib*, *oob*, *ib*, *ob*, *if-ib*, *ib-if*, *ib-t*, *t-ib*, *t-ob*, *ob-t*, *ob-of*, *of-ob*, *bif*, and *bof* are the inner surface of the inner barrier, outer surface of the outer barrier, inner and outer barriers, interfaces between the inner fluid and inner barrier close to the inner fluid and inner barrier sides, interfaces between the inner barrier and tube close to the inner barrier and tube sides, interfaces between the tube and outer barrier close to the tube and outer barrier sides, interfaces between the outer barrier and outer fluid close to the outer barrier and outer fluid sides, bulk inner and outer fluids, respectively.

The tritium concentration profile in the P-IHXs could be estimated utilizing the continuous profile of the partial pressure across the interfaces and boundary conditions:

$$C_{T,bif}\left(z=0\right) = C_{T,bif,0} \tag{5-49}$$

$$C_{T,bof}\left(z=L\right) = C_{T,bof,0} \tag{5-50}$$

Since tritium transports in a closed loop, the inlet tritium concentration in the inner fluid FLiBe is not zero. A systematic model for the tritium transport in the primary loop is therefore necessary. In addition, it is assumed that the inlet tritium concentration in the outer fluid KF-ZrF_4 is zero, which is conservative for the P-IHX design.

5.4 1D Code HEMAT

To estimate the tritium leakage rate in the primary loop, it is necessary to investigate tritium transfer in all key components, including the HX, downcomer, core, core bypass, pump, hot and cold legs. In addition to the models developed for HXs discussed earlier, similar models are developed as well for other components as shown in Figure 5-18, which have been discussed in detail in the literature (Zhang et al., 2020c).

An iterative approach as shown in Figure 5-19 is adopted in the 1D code HEMAT to estimate the tritium mass flow rate in each key component of a closed loop. A tritium concentration at the inlet of the downcomer is initially assumed. The tritium concentrations in the downcomer, core, DHX, MHX, hot leg, P-IHX, cold leg I between the P-IHX and the pump, pump, and cold leg II between the pump and the reactor vessel are then calculated using the models developed. If the tritium concentration at the outlet of the cold leg II is the same as that at the inlet of the downcomer, iteration will terminate. Otherwise, the tritium concentration at the outlet of the cold leg II is used as the initial tritium concentration at the inlet of the downcomer.

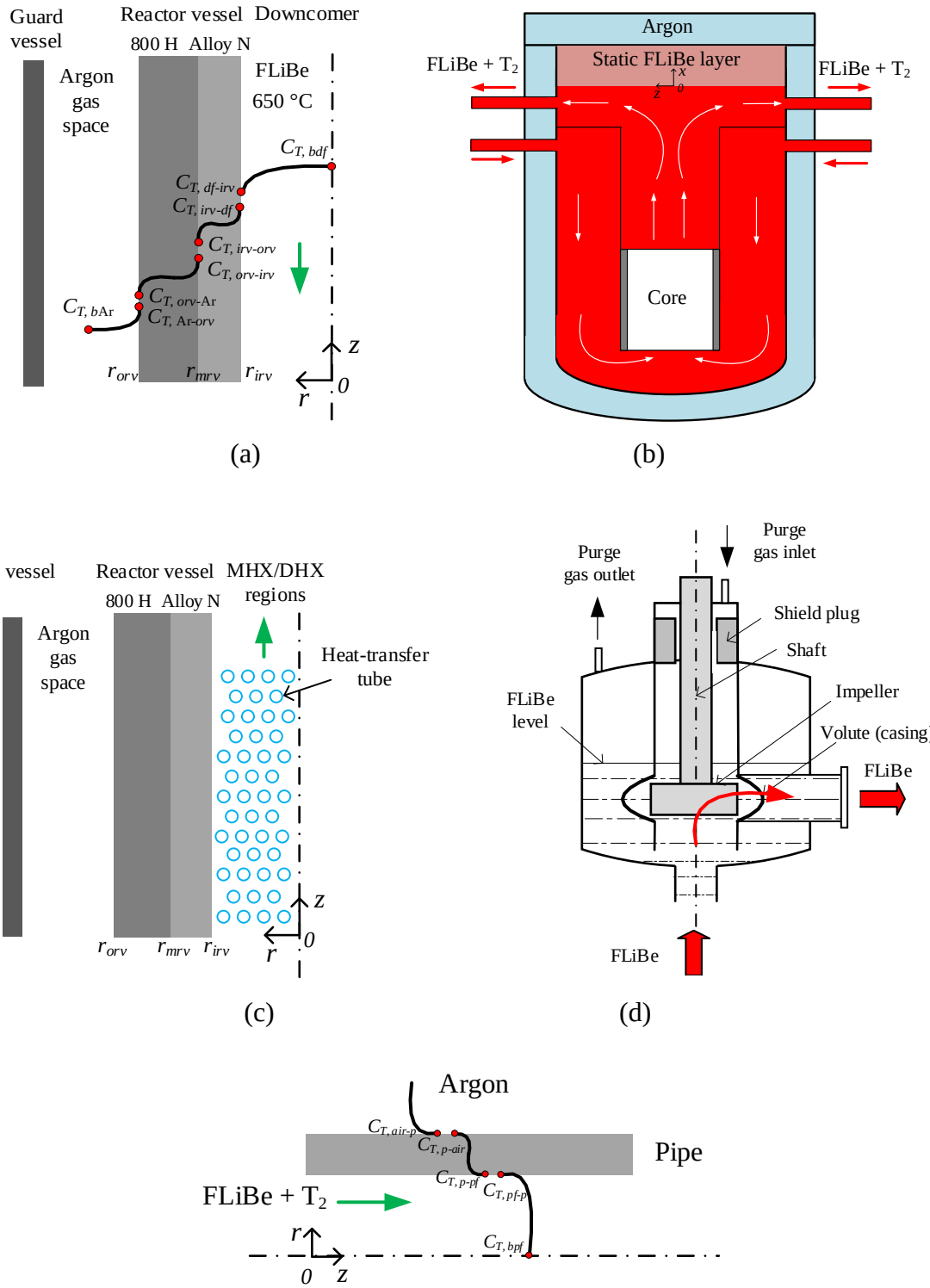

Figure 5-18 Tritium permeation in the (a) downcomer; (b) core; (c) core bypass; (d) pump; and (e) cold/hot legs

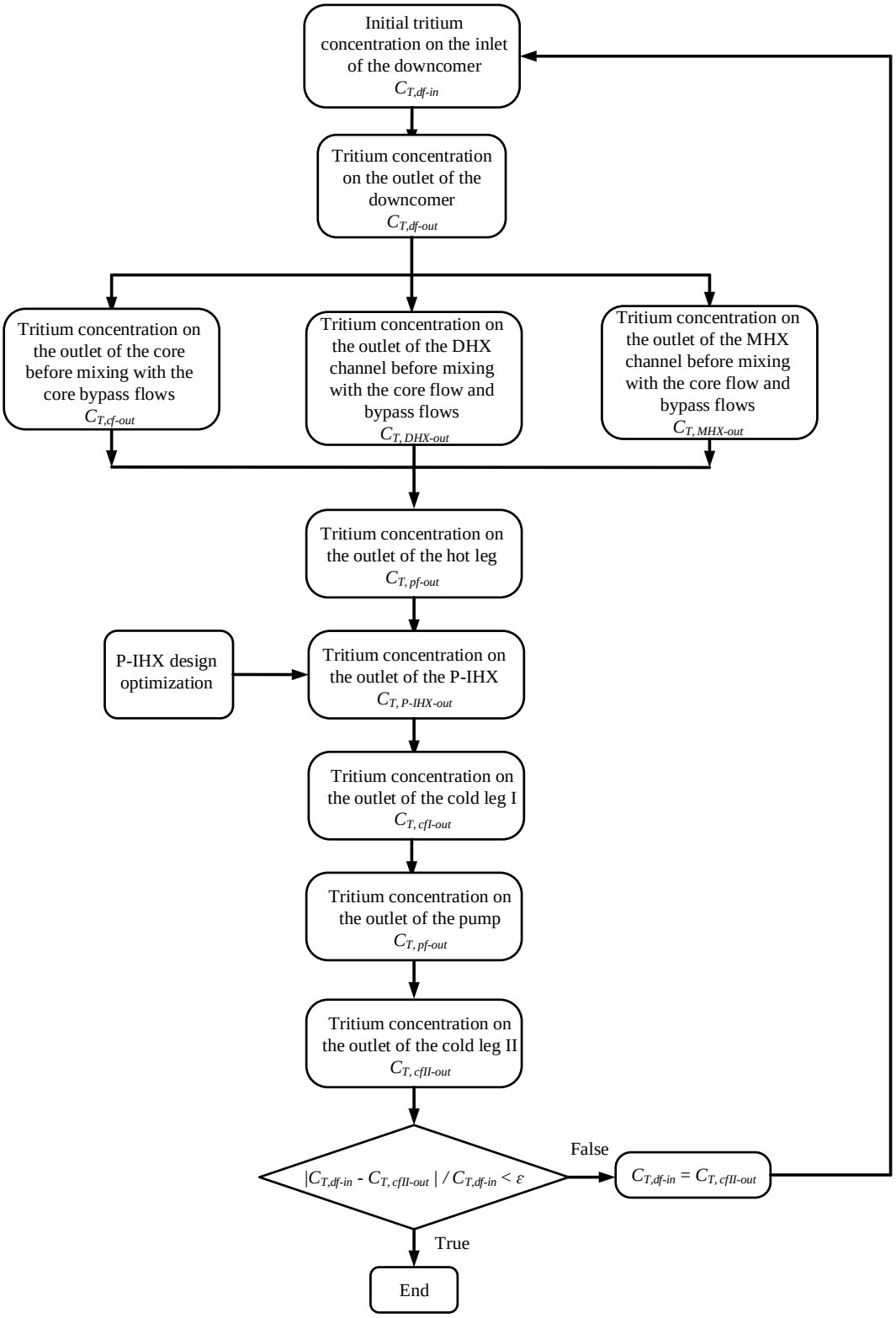

Figure 5-19 Iterative process in the 1D code HEMAT to predict the tritium leakage rate in a closed loop

5.5 DWHX with a Tritium Carrier

5.5.1 Introduction

There are four potential flow directions as shown in Figure 5-20 for a DWHX. However, not all of them are applicable for the DWFT P-IHX. Based on the pre-conceptual AHTR design (Varma et al., 2012), the tube-side FLiBe temperature should decrease from 700 to 650 °C, while the shell-side KF-ZrF_4 temperature should increase from 600 to 675 °C. Therefore, the inner and outer fluids should be in a counter-current flow configuration. Considering the annular fluid will eventually flow through a separate TGB for tritium capture which normally operates at elevated temperatures, a high outlet temperature for the annular fluid is desirable. A parallel flow configuration between the annular and outer fluids is therefore adopted for the DWFT P-IHX design optimization.

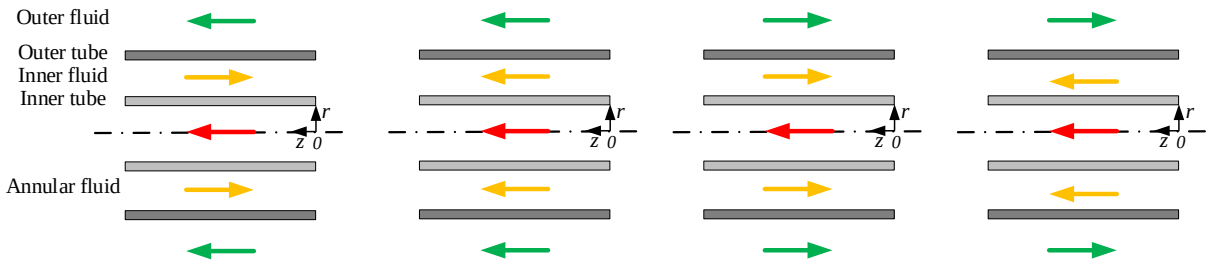

Figure 5-20 Potential flow directions for the inner, annular, and outer fluids

Figure 5-21 shows a layout of the DWFT P-IHX unit (totally three P-IHX units for the AHTR). The DWFT P-IHX can be one tube-side pass as shown in Figure 5-21(a) or two tube-side passes as shown in Figure 5-21(b) if necessary. As an example, the one tube-side pass configuration is adopted in this research.

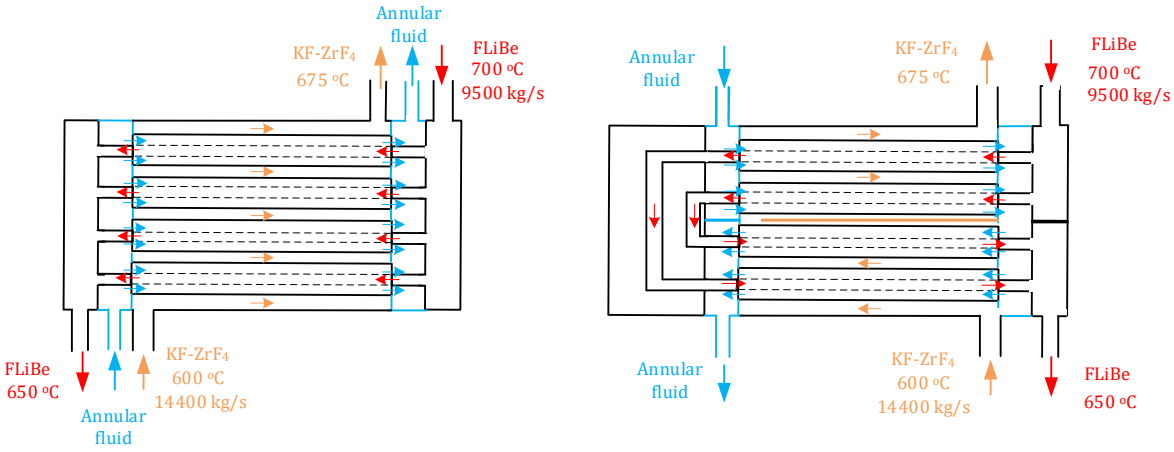

(a) (b)

Figure 5-21 Layout of a DWHX for (a) one tube-side pass and (b) two tube-side passes

5.5.2 Design Optimization for the DWFT P-IHX

Two objectives are proposed for the DWFT P-IHX design optimization, such as the HX surface area per unit power output as defined as

$$AP = \frac{A_t}{\dot{Q}_t} \tag{5-51}$$

and the total cost, including the HX cost and the operation cost as defined as

$$C_t = C_{HX} + C_{op\_i} + C_{op\_a} + C_{op\_o} \tag{5-52}$$

where $A_t, \dot{Q}_t, C_{HX}, C_{op\_i}, C_{op\_a},$ and C_{op_o} are the total surface area of the DWFT P-IHX, thermal power of one DWFT P-IHX unit, HX cost, operation cost of the inner fluid, annular fluid, and outer fluid, respectively.

The operation cost is evaluated by

$$C_{op} = \dot{Q}_{pump} \tau_t C_e \tag{5-53}$$

and the pumping power is defined as

$$\dot{Q}_{pump} = \frac{\dot{m}\Delta p}{\eta_p \rho} \tag{5-54}$$

where $\tau_t, C_e, \dot{m}, \Delta p, \eta_p, and\ \rho$ are the total hours of operation during the HX life time, price of the electricity, mass flow rate, pressure drop, pump efficiency, and fluid density, respectively. In this research, 20 years operation time, 0.12 $/kWh electricity cost, and 90% pump efficiency are adopted for illustration.

Several parameters, such as the inlet and outlet salt temperatures and mass flow rates of the primary salt FLiBe and intermediate salt KF-ZrF_4, have been determined for the P-IHX in the pre-conceptual AHTR design (Varma et al., 2012), while others are design parameters for the design optimization of the DWFT P-IHX with helium as the tritium carrier. The NSGA usually used for a multi-objective optimization issue is adopted for the DWFT P-IHX design optimization.

5.5.3 Optimum Design

Figure 5-22 shows the NSGA results for the DWFT P-IHX design optimization with helium as the tritium carrier. After ten generations, the design points originally scattered fall on the pareto front. This result proves that the two objectives, the total cost and HX surface area per unit power output are conflict objectives. The least squares in regression analysis is therefore applied to identify one optimum design for the DWFT P-IHX, whose key geometry are summarized in Table 5-2.

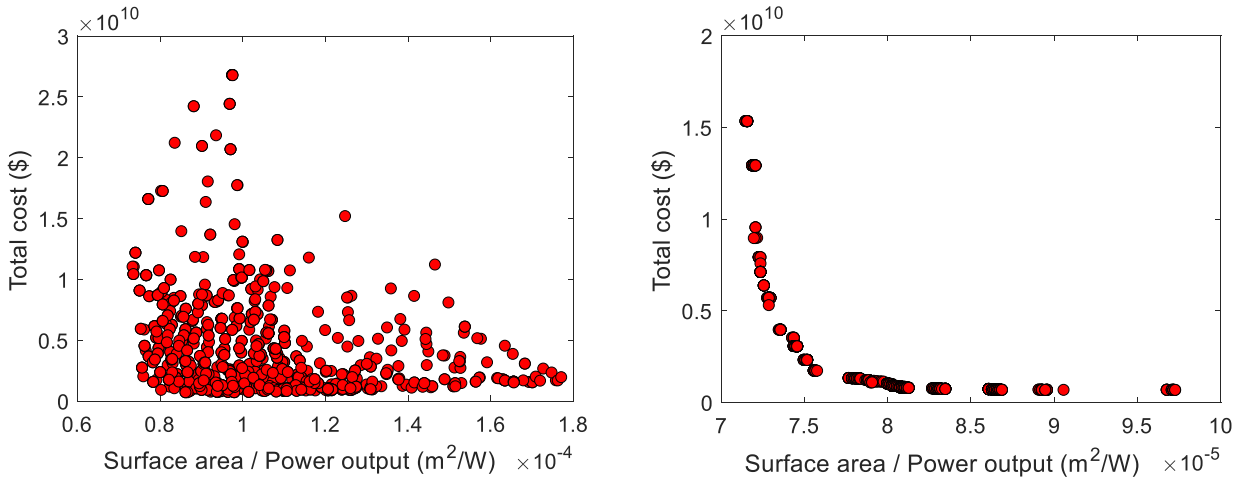

(a) (b)

Figure 5-22 NSGA results for the DWFT P-IHX design optimization (helium as the tritium carrier) after (a) one generation and (b) ten generations

Table 5-2 Optimum designs for the DWFT and SWFT P-IHXs

Items	DWFT P-IHX	SWFT P-IHX
Tube arrangement	Triangular and horizontal	
Tube type	Fluted tube	
Tube material	Hastelloy N	
Inner tube size (mm)	D_{bi} = 8.08, D_{eo} = 12.83, T_w = 0.406, p = 6.1, N_s = 4	N/A
Outer tube size (mm)	D_{bi} = 14.96, D_{eo} = 19.94, T_w = 0.711, p = 15.24, N_s = 4	
Tube length (m)	26.3	15.6
Quantity of the tube unit	50,802	11,920
Pitch to diameter ratio (Pitch/D_{eo})	1.0	
Inner/Annular (if applicable)/Outer fluids	FLiBe/Helium/KF-ZrF_4	FLiBe/KF-ZrF_4
Mass flow rate for the inner/annular (if applicable)/outer fluids (kg/s)	9,500/50.5/14,400	9,500/14,400
Inner-fluid inlet/outlet temperature (°C)	700/651	700/650
Annular-fluid inlet/outlet temperature (°C)	602/683	N/A
Outer-fluid inlet/outlet temperature (°C)	600/675	
Heat load (MW/one unit)	1133.3	
Heat loss rate to the outer fluid (%)	98.1	100
Heat loss rate to the annular fluid (%)	1.9	0

5.5.4 Tritium Leakage Rate in the AHTR Primary Loop

The 1D code HEMAT developed is used to evaluate the tritium leakage rate in the primary loop of the AHTR. The tritium leakage rate through different components in the AHTR primary loop is summarized in Table 5-3 and the geometric information used is summarized in Table 5-4 .

For the option of the DWFT P-IHX with a tritium carrier helium design, most of the tritium generated in the reactor core (about 99.85%) permeates through the P-IHXs, while the remaining tritium enters the argon environment through other components, which is to be removed later by the cleanup system designed for the containment. If the tritium production rate in the AHTR is 3,400 Ci/day, the tritium leakage rates to the atmosphere for the tritium carrier helium design through three P-IHXs, three DHXs, and one MHX will be 3.91, 0.03, and 0.06 Ci/day, respectively. Since the total tritium leakage rate to the atmosphere, a combination of the three tritium leakage rates through the HXs (4.0 Ci/day), is on the same order of magnitude as the tritium leakage rate in LWRs (1.9 Ci/day), no additional tritium mitigation measures need to be adopted for design option of the DWFT P-IHX with helium as the tritium carrier.

Table 5-3 Tritium leakage rate in the loop for the DWFT P-IHX with the tritium carrier helium design option

Tritium production rate (%)	100
Leakage rate from downcomers to the argon gas space between the reactor vessel and guard vessel (%)	0.012
Leakage rate to the top argon gas space in the reactor vessel	0.000
Leakage rate from DHXs (%)	0.001
Leakage rate from the MHX (%)	0.002
Leakage rate from hot legs to the argon containment (%)	0.137
Leakage rate from P-IHXs (%)	99.731 (To the annular fluid)
	0.115 (To the outer fluid)
Leakage rate from the cold leg I to the argon gas space (%)	0.001
Leakage rate from pumps to the argon gas space (%)	0.000
Leakage rate from the cold leg II to the argon gas space (%)	0.001

Table 5-4 Information used to evaluate the tritium leakage rate in the loop

Item	Value
Primary coolant	FLiBe
Downcomer	
Reactor vessel outer diameter (m)	10.5
Reactor vessel height (m)	19.1
Thickness of the inner layer - Hastelloy N (m)	0.01
Thickness of the outer layer – Alloy 800 (m)	0.1
core	
Thickness of the top static FLiBe layer (m)	0.5
Core bypass flow rate through one DHX (%)	0.6
Core bypass flow rate through one MHX (%)	0.6
Tritium generation rate (mol T/s)	1.36×10^{-6}
Core bypass through one DHX	
DHX shell-side salt	FLiBe
DHX tube-side salt	KF-ZrF_4
Fluted tube size (mm)	D_{bi} = 10.67, D_{eo} = 16.64, T_w = 0.508, p = 8.23, N_s = 4, L=3000
Tube quantity	2100
Mass flow rate in one tube (kg/s)	0.01
Core bypass through one MHX	
MHX shell-side salt	FLiBe
MHX tube-side salt	KF-ZrF_4
Fluted tube size (mm)	D_{bi} = 10.67, D_{eo} = 16.64, T_w = 0.508, p = 8.23, N_s = 4, L=3000
Tube quantity	10000
Mass flow rate in one tube (kg/s)	0.01
Hot leg	
Pipe inner diameter (m)	1.24
Pipe thickness (m)	0.009525
Pipe length (m)	10
Cold leg I (P-IHX to the primary pump)	
Pipe inner diameter (m)	1.24
Pipe thickness (m)	0.009525
Pipe length (m)	5
Pump	
Thickness of the top static FLiBe layer (m)	0.3
Casing diameter (m)	0.5
Cold leg II (Primary pump to the reactor vessel)	
Pipe inner diameter (m)	1.24
Pipe thickness (m)	0.009525
Pipe length (m)	5

5.6 SWHX with a Tritium Barrier

Both tungsten and Chemical Vapor Deposition Silicon Carbide (CVD-SiC) could be tritium barriers and they are adopted for the SWFT P-IHX design optimization. The tritium barrier thickness has a negligible effect on the heat transfer performance of the SWFT P-IHX due to its negligible thermal resistance compared with the tube material under the conditions investigated. Therefore, zero tritium barrier thickness is initially applied to the SWFT P-IHX design optimization to identify an optimum design. The two objectives, HX surface area per unit power output and the total cost as defined earlier are adopted for the SWFT P-IHX design optimization.

Figure 5-23 shows the NGSA results for the SWFT P-IHX design optimization. The design points originally scattered fall on the pareto front after ten generations. Since the two objectives, are competitive, the least squares in regression analysis is therefore applied to identify one optimum design with optimum parameters summarized in Table 5-2 for the SWFT P-IHX.

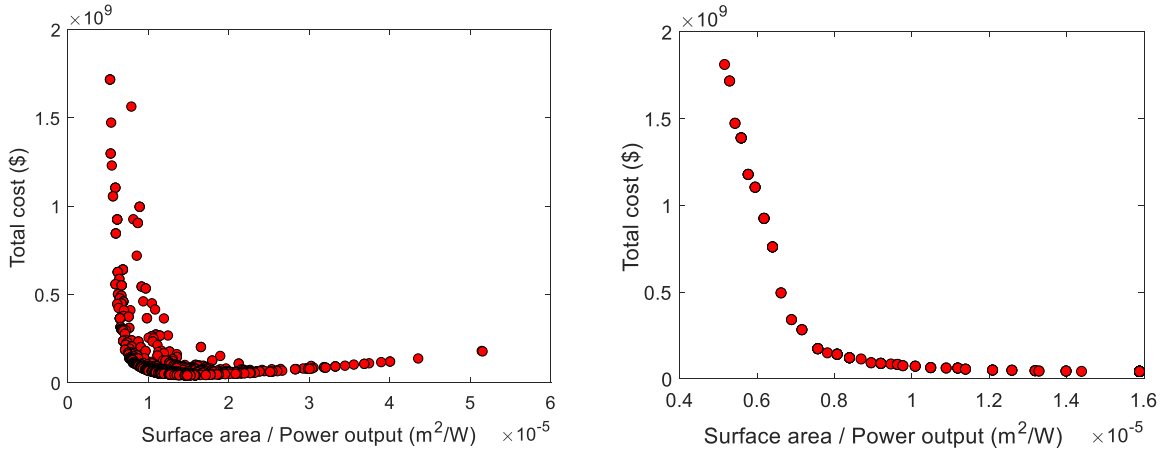

(a) (b)

Figure 5-23 NSGA results for the SWFT P-IHX design optimization after (a) one generation and (b) ten generations

Figure 5-24 and Figure 5-25 show the effect of the tritium barrier thickness on the tritium leakage rate through HXs for tungsten and CVD-SiC design options, respectively. If the tritium barrier tungsten is plated on the three P-IHXs, the tritium leakage rate through the P-IHXs decreases, while the tritium leakage rate through other HXs, such as DHXs and MHX increases as shown in Figure 5-24(a). This is because the mass transfer resistance of the P-IHX tube including the tritium barrier tungsten increases as the thickness of the tritium barrier increases. However, the total tritium leakage rate remains as high as 390.5 Ci/day even for a 10^4 μm thick tungsten plated on the three P-IHXs as shown in Figure 5-24(a). Another option is to apply the tungsten coating on the three P-IHXs, three DHXs, and one MHX. The tritium leakage rate through these HXs decreases as the increase of the barrier thickness as shown in Figure 5-24(b). However, the total tritium leakage rate remains to be a relatively large value, 189.0 Ci/day.

If a 30-μm thick tritium barrier CVD-SiC is plated on the three P-IHXs, the tritium leakage rate through the three P-IHXs will drop to ~1.9 Ci/day as shown in Figure 5-25(a), the average tritium leakage rate in LWRs. However, the total tritium leakage rate through the three P-IHXs, three DHXs, and one MHX is as high as 141.6 Ci/day. If a 30-μm thick CVD-SiC barrier is plated on the three P-IHXs, three DHXs, and one MHX, the total tritium leakage rate will be reduced to 1.7 Ci/day as shown in Figure 5-25(b).

In addition, the tritium leakage rate through each component in the AHTR primary loop for the SWFT P-IHX with the tritium barrier CVD-SiC design option is summarized in Table 5-5. A large fraction of tritium permeates through the downcomers and is then removed by the cleanup system designed for the containment, while a much smaller fraction of the generated tritium permeates through the HXs to the ambient.

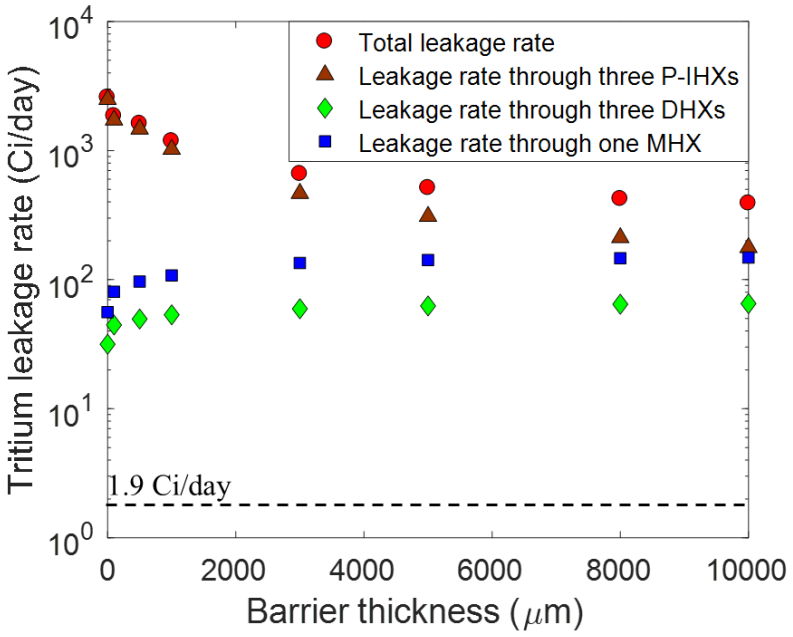

(a)

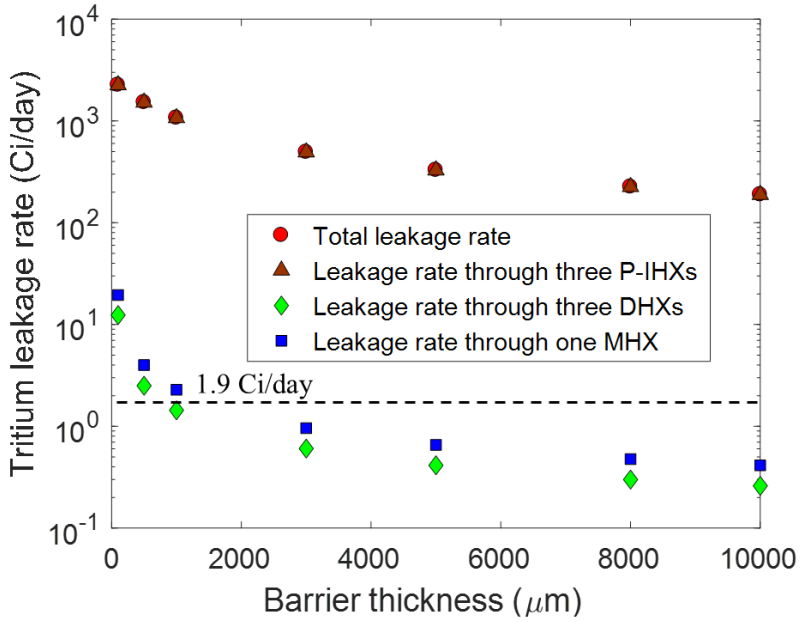

(b)

Figure 5-24 Effect of the tritium barrier thickness on the leakage rate for tungsten plated on (a) three P-IHXs and (b) three P-IHXs, three DHXs, and one MHX

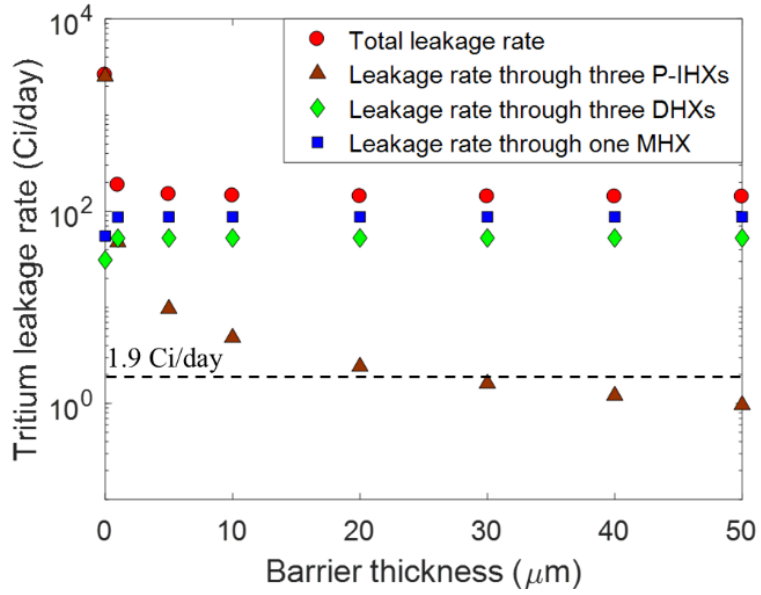

(a)

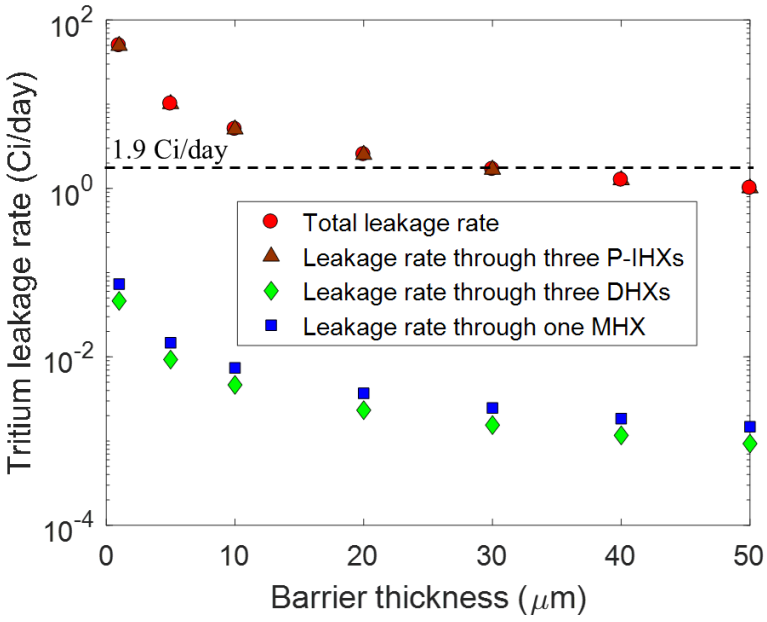

(b)

Figure 5-25 Effect of the tritium barrier thickness on the leakage rate for CVD-SiC plated on (a) three P-IHXs and (b) three P-IHXs, three DHXs, and one MHX

Table 5-5 Tritium leakage rate in the loop for the SWFT P-IHX with the tritium barrier CVD-SiC design option

Items	CVD-SiC	
Production rate (%)	100	
Coating thickness (μm)	30 (on the three P-IHXs)	30 (on the three P-IHXs, three DHXs, and one MHX)
Tritium leakage rate from the three downcomers to the argon gas space between the reactor vessel and guard vessel (%)	68.169	71.110
Tritium leakage rate to the top argon gas space in the reactor vessel (%)	0.000	0.001
Tritium leakage rate from three DHXs (%)	1.549	0.000
Tritium leakage rate from one MHX (%)	2.570	0.000
Tritium leakage rate from the three hot legs to the argon containment (%)	15.963	16.648
Tritium leakage rate from three P-IHXs (%)	0.047	0.037
Tritium leakage rate from the three cold legs I to the argon gas space (%)	5.851	6.102
Tritium leakage rate from the three pumps to the argon gas space (%)	0.000	0.000
Tritium leakage rate from the three cold legs II to the argon gas space (%)	5.851	6.102

It should be noted that the analysis on tritium removal for the SWHX with a tritium barrier option was perfomed based on a number of assumptions: (1) Uinform coating thickness; (2) No cracks or any defects in the coating; and (3) Negligible corrosion effect. However, the actual case, especially after long-period operation of the SWHX with a tritium barrier in high-temperature salt environment, may make these assumptions less applicable. In other words, the actual tritium leakage rate for the SWHX with a tritium barrier option would be larger than the ideal results obtained earlier. Future investigation of the quality (uniformity and durability) on the SiC coating on different HX tube materials for FHRs in high-temperature salt environments is suggested.

5.7 Preliminary Economic Analysis

A preliminary economic analysis has been performed to identify a superior choice between the two strategies proposed for tritium mitigation/control. The material cost and operation cost are considered in the economic analysis for the DWHX and SWHX design options, while the labor cost of the SiC coating on the FTHXs is not considered since such information is not available in the literature.

For the DWHX design option, the tritium carrier (annular fluid) helium in an auxiliary system as shown in Figure 5-26(a) "carries" tritium in the DWHX to a TGB for tritium capture. The "fresh" helium with negligible tritium residual is then circulated back to the DWHX to complete one cycle for tritium removal. For the SWHX design option, the clean-up system existed in the AHTR could be used to removal tritium and other fission gases in the argon containment as shown in Figure 5-26(b). Since the SWHX design option utilizes the clean-up system that already exists in the AHTR, the cost of the clean-up system is not explicitly considered in the ecomonic analysis. In addition, the cost of the common components in these two tritium-mitigation strategies is not considered.

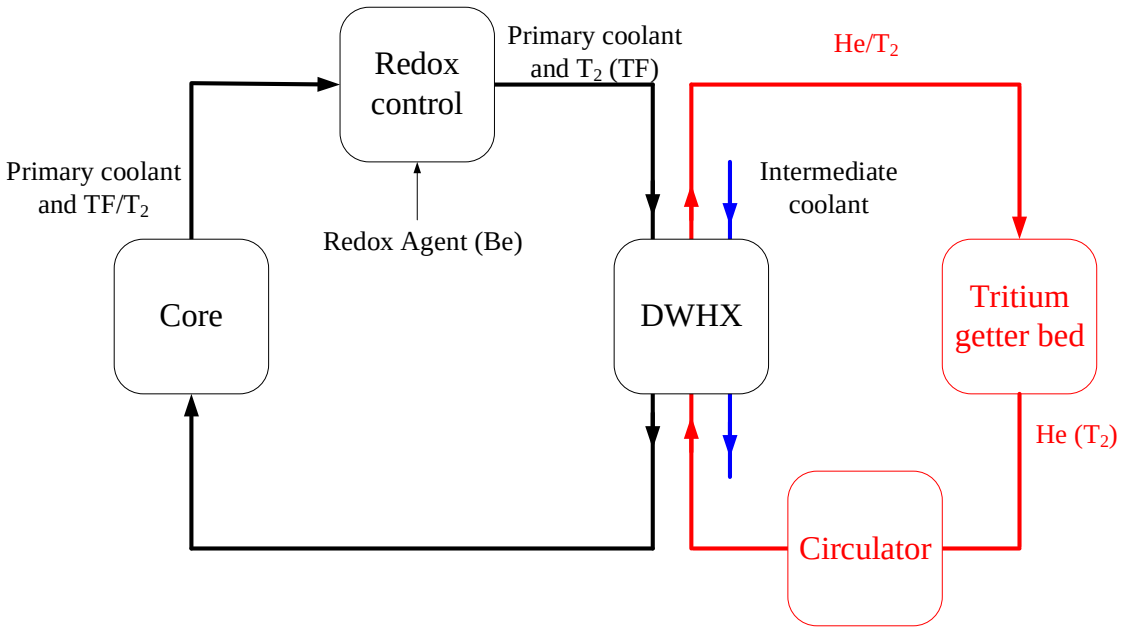

(a)

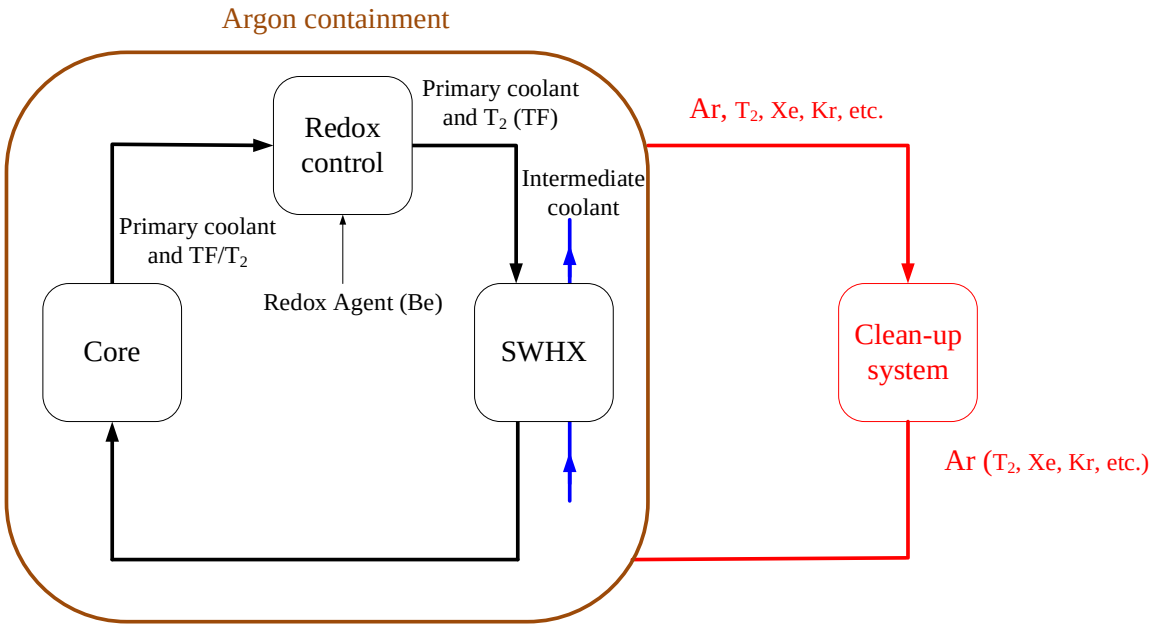

(b)

Figure 5-26 Auxiliary system for tritium mitigation: (a) DWHX and (b) SWHX design options

Since it is difficult to estimate the cost of an FTHX, i.e., DWFT P-IHX and SWFT P-IHX, the cost evaluation for a shell and plain tube HX (Corripio et al., 1982), estimated by

$$C_{HX} = C_b F_d F_p F_m F_i \tag{5-55}$$

is therefore adopted as a reference, where $C_b, F_d, F_p, F_m,$ and F_i are respectively the base cost estimated by Eq. (5-56), HX type cost factor estimated by Eq. (5-57), design pressure cost factor, which should be unity for the atmospheric pressure, material construction cost factor estimated by Eq. (5-58) for SS 316, and inflation cost factor, which was 2.54 in 2017 compared with the cost in 1982. Based on the unit price of Hastelloy N and SS 316 (MetalPrices Inc., 2016), the unit price ratio is estimated to be 2.6, which is then adopted to convert the SS 316 material construction cost factor to the Hastelloy N material construction cost factor.

$$C_b = e^{8.202+0.01506\ln A+0.06811(\ln A_t)^2} \tag{5-56}$$

$$F_d = e^{-0.9003+0.0906\ln A_t} \tag{5-57}$$

$$F_m = 1.4144 + 0.23296\ln A_t \tag{5-58}$$

In addition to the HX cost, the cost of the working fluids, such as the primary coolant FLiBe, intermediate coolant KF-ZrF_4, and tritium carrier helium (if applicable) is evaluated as summarized in Table 5-6. However, other material cost, such as the cost of a TGB and circulator for the DWHX design option is not considered since it depends on the specific design of the auxiliary tritium-mitigation system. The operation cost estimated by Eq. (5-53) is applied for the FLiBe salt, KF-ZrF_4 salt, and helium (if applicable) as summarized in Table 5-6.

Table 5-6 Preliminary economic analysis of two different tritium control methods

Item		DWHX design option (M$)	SWHX design option (M$)
Material cost	P-IHX	456.39	9.76
	FLiBe salt in the P-IHX	19.67	8.75
	KF-ZrF_4 salt in the P-IHX	64.38	9.04
	Helium in the P-IHX	< 0.01	N/A
	TGB	Unknown	N/A
	Circulator	Unknown	N/A
Operation cost	FLiBe salt in the P-IHX	76.76	22.42
	KF-ZrF_4 salt in the P-IHX	125.69	457.17
	Helium in the P-IHX	195.20	N/A
Total		938.10	507.14

Notes:

1. ^{7}LiF: 150 $/kg for 99.995% Li-7 enrichment, BeF_2: 96 $/kg (Zhu et al., 2019), KF: 21 $/kg, ZrF_4: 157 $/kg (quotation provided by Synquest Inc.);
2. Helium: 4.29 $/m^3 (https://pubs.usgs.gov/periodicals/mcs2020/mcs2020-helium.pdf)
3. Operation cost: 20 years operation time, 0.12 $/kWh electricity cost, and 90% pump efficiency.

Our study shows that the SWHX design option is superior to the DWHX design option in terms of the cost. However, it should be noted that the labor cost of the SiC coating on the FTHXs is not included in the current economic analysis, which may be nonnegligible. A more in-depth economic analysis is therefore suggested. In addition, future investigation on the quality (uniformity and durability) of the SiC coating on different HX tube materials for FHRs in high-temperature salt environments is also suggested.

5.8 Summary

The AHTR is attractive due to its improved safety designs, low working pressure and high working temperature. However, tritium management is a critical issue in the AHTR and similar FHRs due to the significantly higher tritium production rate compared to that in LWRs. Two approaches have been proposed and investigated for tritium mitigation: (1) A DWFT P-IHX design with a tritium carrier, including helium, FLiBe, FLiNaK, and KF-ZrF_4 and (2) A SWFT P-IHX design with a tritium barrier, including silicon carbide (SiC) and tungsten (W) plated on the tube surface. In addition, a 1D model, HEMAT, was developed for the AHTR to quantitively analyze the tritium leakage rate in the primary loop, including the downcomer, core channel, core bypass channel, P-IHX, pump, hot and cold legs.

It has been identified that the spirally fluted tube used as both the inner and outer tubes (IFOF) for a DWHX has superior heat and mass transfer performance compared with other configurations, such as IPOP, IPOF, and IFOP. Therefore, the IFOF configuration is adopted for the DWFT and SWFT P-IHX design optimizations. A preliminary analysis screens helium as the tritium carrier for the DWFT P-IHX and CVD-SiC as the tritium barrier for the SWFT P-IHX.

For the DW-FTHX design option, our study shows that: (1) Helium is a superior choice as the tritium carrier since it can take away as high as 99.7% of the tritium in FLiBe but a much smaller fraction (1.9%) of the heat in FLiBe compared with other tritium carriers investigated; (2) The DWFT P-IHXs provide a major pathway for tritium permeation, where 99.8% of the tritium generated in the reactor core escapes from the primary salt in the DWFT P-IHXs and 99.7% of the tritium can be removed by the tritium carrier helium; and (3) The total tritium leakage rate into the ambient from the AHTR for the DWFT P-IHX design with helium as the tritium carrier is estimated to be 4.0 Ci/day, the same order of magnitude of the average tritium leakage rate in a typical LWR.

For the SW-FTHX design option, our study concludes that: (a) The downcomer provides a major pathway for tritium permeation, where 68.2% of the tritium generated in the reactor core escapes from the primary salt to the cover gas space for a 30-μm thick SiC coating plated on the tubes of the three P-IHXs or 71.1% of the generated tritium escapes to the cover gas space for the same thick SiC coating plated on the tubes of three P-IHXs, three DHXs, and one MHX and (2) A 30-μm thick SiC coating plated on the P-IHX tubes help reduce the tritium total leakage rate to 141.6 Ci/day while a SiC coating of the same thickness on the tubes of three P-IHXs, three DHXs, and one MHX reduces the total tritium leakage rate to 1.7 Ci/day.

Both the DW-FTHX with helium as the tritium carrier and SW-FTHX with a SiC coating as the tritium barrier designs can effectively reduce the total tritium leakage in the AHTR or other similar FHRs to the same order of magnitude as that in LWRs. Based on a preliminary economic analysis, the SW-FTHX with a SiC coating as the tritium barrier seems to be a superior choice due to its much lower cost as compared with the DW-FTHX design. Investigation of the quality (uniformity and durability) of the SiC coating on different HX tube materials for FHRs in high-temperature salt environments is suggested, whih help determine the practicality of the second proposed tritium mitigation strategy

Chapter 6 Summary, Conclusions, and Future Work

6.1 Summary and Conclusions

The advanced non-LWRs, FHRs, feature high thermal efficiencies for electricity generation and are capable of providing high-temperature heat for process heat applications. Although FHRs promise these benefits, there are a number of key technology gaps/issues that need to be addressed for FHR development and future deployment. This research is therefore intended to address two key technology gaps/issues: (1) molten salt natural circulation in the passive decay heat removal system and (2) tritium control/management for FHRs.

A CFD tool, STAR-CCM+, was first used to investigate heat transfer and friction characteristics of molten salts in simple geometry, such as straight circular pipes. The numerical results were validated by comparing with (1) experimental data that were re-reduced and analyzed by using more accurate and consistent thermophysical properties of molten salts identified in this research through a literature review and (2) widely used forced convective heat transfer and friction factor correlations. It has been identified that the effects of buoyancy and radiative heat transfer are generally non-negligible for laminar flows of molten salts to have accurate predictions.

The buoyancy effect could be evaluated by comparing the forced and mixed convective heat transfer correlations. To quantitatively evaluate the effect of radiative heat transfer in participating or semi-transparent fluids, such as molten salts, a radiative heat transfer model was then developed and benchmarked in this research. In addition, a sensitivity study was performed for a number of parameters, including the pipe size (ID from 5 to 50 mm), salt temperature (500

to 1000 °C), salt and wall temperature difference (5 to 100 °C), and salt absorption coefficient (1 to 100 m^{-1}).

Both the non-negligible buoyancy effect and radiative heat transfer effect identified earlier were included in the development of a 1D code NACCO to predict the thermal-hydraulic performance of molten salts in natural circulation loops. The 1D code NACCO was then benchmarked with three natural circulation experiments using water, a nitrate salt $NaNO_3$-KNO_3 (60-40 wt%), and a fluoride salt FLiBe (LiF-BeF_2 66-34 mol%) as the working fluids, respectively. The 1D code NACCO validated was then applied to a high-temperature IET facility, FLUSTFA, which was designed based on a scaling analysis to experimentally investigate the DRACS performance in a 3400-MWth solid-fuel MSR, AHTR.

Several concluding remarks related to the first objective in this research are summarized as follows:

(1) Both the hydrodynamic and thermal entrance lengths for laminar and turbulent flows of molten salts could be preliminarily estimated by conventional correlations, Eqs. (2-23) to (2-27). The discrepancies between the correlation results and CFD predictions ranged from 9.6% to 35%;

(2) The friction factor of molten salts in the fully-developed laminar flow regime could be appropriately estimated through a CFD analysis and conventional correlation, Eq. (2-28). The maximum discrepancies by comparing the CFD and correlation results with the majority of the experimental data were ±6.3% and ±18.8%, respectively. However, the friction factor values for fully-developed turbulent flows of molten salts estimated by STAR-CCM+ and correlations, Eqs. (2-29) and (2-30), were in general much lower (< 38%) than the experimental data. Since the initial value of the relative roughness was

negligibly small, the large discrepancy most likely resulted from the increased roughness of the pipe inner surface, which could likely be due to corrosion of the pipe material in the salt environment at elevated temperatures;

(3) The Nusselt number of molten salts in transitional and turbulent flow regimes could be estimated by both the CFD tool STAR-CCM+ and conventional forced convective heat transfer correlations, including the Dittus-Boelter, Gnielinski, Sieder-Tate (turbulent), and Hausen correlations. It was identified that these four correlations predicted the molten salt Nusselt number with ±20% uncertainties for $10{,}000 \leq Re \leq 50{,}000$ and $4 \leq Pr \leq 12$; $2{,}300 \leq Re \leq 50{,}000$ and $4 \leq Pr \leq 19$; $10{,}000 \leq Re \leq 120{,}000$ and $4 \leq Pr \leq 27$; and $5{,}000 \leq Re \leq 50{,}000$ and $4 \leq Pr \leq 27$, respectively;

(4) The Nusselt number of fuel/molten salts in laminar flow regime was underestimated by the Sieder-Tate (laminar) correlation, which was 27% and 40% lower than the experimental data in the fuel salt and nitrate salt experiments, respectively. Two potential reasons were proposed: the entrance effect underestimated by the Sieder-Tate (laminar) correlation and incapability of the Sieder-Tate (laminar) correlation to consider the effects of buoyancy and radiative heat transfer in the salts. These two reasons were subsequently justified by CFD analyses considering the entrance effect, buoyancy effect, and radiative heat transfer effect. Our analysis showed that these effects were non-negligible for the fuel salt and nitrate salt experiments, where the flows were in the laminar flow regime;

(5) A radiative heat transfer model was developed to quantitatively analyze the radiative heat transfer effect in molten salts and benchmarked by comparing with the CFD results. It was then incorporated in the 1D code NACCO developed and benchmarked in this research to predict the thermal-hydraulic performance of molten salts in natural circulation loops. This

1D code NACCO generally captured the overall trend of the salt axial temperature profile in the experiments. The relative salt temperature difference between the 1D code predictions and experimental data (the salt centerline temperature in the pipe) was less than 3.8% for the nitrate salt experiment (Kudariyawar et al., 2016) and 5.3% for the fluoride salt experiment (Britsch et al., 2019). However, the absolute salt temperature difference using the salt centerline temperature in the experiments as a reference could be as high as 18 °C and 35 °C for these two salt experiments, respectively. The overestimation for the salt temperature predicted by the 1D code was mainly due to the heat removal rate underestimated by the code compared with its actual value in the experiments;

(6) The salt bulk temperature in the experiments is a more meaningful choice than the salt centerline temperature for the code benchmark study. However, it is usually unavailable since both the radial temperature and velocity profiles are not necessarily be known in the high-temperature salt experiments. It is then necessary to know the maximum difference between the centerline temperature and bulk temperature. Through an analysis for the FLiBe salt natural circulation experiment (Britsch et al., 2019), the difference between the centerline temperature and bulk temperature ranged from 5 to 10 °C for the experiments where the FLiBe salt centerline temperature was up to 750 °C;

(7) The 1D code NACCO developed was applied to the IET facility FLUSTFA to model a number of shakedown tests, overcooling, and overheating transients. These predictions helped optimize the operation procedure of the IET facility and understand the transient scenarios.

In addition, a number of strategies for tritium mitigation and control were investigated and evaluated by a 1D code HEMAT developed in this research. To reduce tritium leakage rate in

FHRs, two design options, such as the DW-FTHX with a tritium carrier and SW-FTHX with a tritium barrier options were proposed for HXs, while the latter design appeared to be a superior choice through a preliminary economic analysis performed in this study.

Several concluding remarks related to the second objective in this research are summarized as follows:

(1) In the DW-FTHX design option, four tube/pipe surface configurations, such as IFOF, IFOP, IPOP, and IPOF, and four tritium carriers, such as helium, FLiBe, KF-ZrF_4, and FLiNaK, were investigated. The IFOF configuration with a tritium carrier helium design was finally selected for P-IHXs considering its superior heat and mass transfer performance. The total tritium leakage rate to the ambient can be reduced to 4.0 Ci/day in the AHTR, the same order of magnitude of the average tritium leakage rate in a typical LWR (1.9 Ci/day).

(2) The SW-FTHX adopted spirally fluted tubes with a tritium barrier plated on the tube surface to prevent tritium permeation. Both tungsten and SiC acting as the tritium barrier were investigated, and SiC was finally selected due to its much lower permeability for tritium. Our study showed that a 30-μm thick SiC coating plated on the pipes of three P-IHXs, three DHXs, and one MHX helped reduce the total tritium leakage rate to 1.7 Ci/day in the AHTR, slightly lower than the average leakage rate of tritium in LWRs.

6.2 Main Contributions

This research provides a comprehensive study of thermal-hydraulic characteristics of molten salts. The key findings identified in this research can help improve design and modeling of passive decay heat removal systems for FHRs/MSRs and accuracy of code predictions of

FHR/MSR performance. In addition, the two strategies identified as effective ways for tritium mitigation can support advancing the development of FHRs, fusion reactors, and other reactors/fields where tritium control/management is needed.

6.3 Future Work

Additional effort summarized as follows will be required to close the two technology gaps/issues discussed earlier for FHR development and future deployment.

(1) Accurate thermophysical properties of fluoride salts of interest have been identified through a literature review. However, the uncertainties of the thermal conductivity and dynamic viscosity of those fluoride salts could be as high as ±10% to ±20%. It is suggested to develop advanced techniques for more accurate measurements of these properties;

(2) The friction factor for fully-developed turbulent flows of molten salts derived from the experiments were much higher than the CFD predictions and correlation results for circular tubes/pipes. It is suggested to investigate the effect of salt corrosion on the tube surface characteristics, including the roughness;

(3) Additional thermal-hydraulic experimental data using molten salts as the working fluids for different transient scenarios, such as SBO, are needed for code benchmark and validation to support MSR licensing;

(4) Experiments for DW-FTHX with a tritium carrier helium and SW-FTHX with a tritium barrier SiC are suggested for code benchmark. In addition, investigation of the quality (uniformity and durability) of the SiC coating on different HX tube materials for FHRs in high-temperature salt environments will help determine the practicality of the second proposed tritium mitigation strategy.

Appendix: Derivation of the Net Radiative Heat Flux

A. Zero reflectivity condition

The net radiative heat flux from Medium 1 to Media 2 and 3 in a three-medium system as shown in Figure 2-26 under zero reflectivity condition will be illustrated here.

The energy absorbed by Medium 1 per unit area due to photons with a radiative heat flux of E_1 emitted from Media 1 to 2 is given by

$$E_{1a,1-2}(\rho_1 = 0) = \alpha_1\rho_2E_1 + \alpha_1\rho_2E_1(\tau_1\rho_3) + \alpha_1\rho_2E_1(\tau_1\rho_3)(\tau_1\rho_2) + \alpha_1\rho_2E_1(\tau_1\rho_3)^2(\tau_1\rho_2) + \alpha_1\rho_2E_1(\tau_1\rho_3)^2(\tau_1\rho_2)^2 + \cdots \quad \text{(A1)}$$

The photons emitted from Media 1 to 3 with a radiative heat flux of E_1 undergo the similar steps in Figure 2-28(a). The energy absorbed by Medium 1 per unit area due to the photons emitted from Media 1 to 3 is given by

$$E_{1a,1-3}(\rho_1 = 0) = \alpha_1\rho_3E_1 + \alpha_1\rho_3E_1(\tau_1\rho_2) + \alpha_1\rho_3E_1(\tau_1\rho_2)(\tau_1\rho_3) + \alpha_1\rho_3E_1(\tau_1\rho_2)^2(\tau_1\rho_3) + \alpha_1\rho_3E_1(\tau_1\rho_2)^2(\tau_1\rho_3)^2 + \cdots \quad \text{(A2)}$$

Considering the photons emitted from Media 1 to 2 and 3 simultaneously, the total energy absorbed by Medium 1per unit area due to the photons emitted from Medium 1 is given by

$$E_{1a}(\rho_1 = 0) = E_{1a,1-2}(\rho_1 = 0) + E_{1a,1-3}(\rho_1 = 0) = \alpha_1\rho_2E_1 + \alpha_1\rho_2E_1(\tau_1\rho_3) + \alpha_1\rho_2E_1(\tau_1\rho_3)(\tau_1\rho_2) + \cdots + \alpha_1\rho_3E_1 + \alpha_1\rho_3E_1(\tau_1\rho_2) + \alpha_1\rho_3E_1(\tau_1\rho_2)(\tau_1\rho_3) + \cdots \quad \text{(A3)}$$

By introducing Eqs. (A4) to (A6b), Eq. (A3) can be re-written as Eq. (A7):

$$\beta_1 = \tau_1\rho_2 \tag{A4}$$

$$\beta_2 = \tau_1\rho_3 \tag{A5}$$

$$\frac{1}{1-\beta_2} = 1 + \beta_2 + \beta_2^2 + \cdots \tag{A6a}$$

$$\frac{1}{1-\beta_1\beta_2} = 1 + \beta_1\beta_2 + (\beta_1\beta_2)^2 + \cdots \tag{A6b}$$

$$E_{1a}(\rho_1 = 0) = \alpha_1 E_1 \frac{\rho_2+\rho_3+\rho_2\beta_2+\rho_3\beta_1}{1-\beta_1\beta_2} = \alpha_1 E_1 \frac{\rho_2+\rho_3+2\tau_1\rho_2\rho_3}{1-\tau_1^2\rho_2\rho_3} \tag{A7}$$

Similar to the derivation of Eq. (A7), the total energy absorbed by Medium 1 per unit area due to the photons emitted from Medium 2 with a radiative heat flux of E_2 and the photons emitted from Medium 3 with a radiative heat flux of E_3 is given by

$$E'_{1a}(\rho_1 = 0) = E'_{1a,2-1}(\rho_1 = 0) + E'_{1a,3-1}(\rho_1 = 0) = \alpha_1 E_2 \frac{1+\beta_2}{1-\beta_1\beta_2} + \alpha_1 E_3 \frac{1+\beta_1}{1-\beta_1\beta_2} =$$

$$\alpha_1 E_2 \frac{1+\tau_1\rho_3}{1-\tau_1^2\rho_2\rho_3} + \alpha_1 E_3 \frac{1+\tau_1\rho_2}{1-\tau_1^2\rho_2\rho_3} \tag{A8}$$

Therefore, the net radiative heat flux from Media 1 to 2 and 3 is given by

$$E_{1-2\&3}(\rho_1 = 0) = \left[E_1 - E_{1a,1-2}(\rho_1 = 0)\right] + \left[E_1 - E_{1a,1-3}(\rho_1 = 0)\right] - E'_{1a,2-1}(\rho_1 = 0) -$$

$$E'_{1a,3-1}(\rho_1 = 0) = 2E_1 - \alpha_1 \frac{(1+\tau_1\rho_3)(\rho_2E_1+E_2)+(1+\tau_1\rho_2)(\rho_3E_1+E_3)}{1-\tau_1^2\rho_2\rho_3} \tag{A9}$$

Similarly, the net radiation heat fluxes from Medium 2 to Media 1 and 3 is expressed by

$$E_{2-1\&3}(\rho_1 = 0) = E_2 - \alpha_2 \frac{E_1+\tau_1E_3+\tau_1\rho_3(E_1+\tau_1E_2)}{1-\tau_1^2\rho_2\rho_3} \tag{A10}$$

Eq. (A10) is used to estimate the net radiation heat flux between two planar surfaces with semi-transparent medium. The net radiation heat flux between two gray, infinite, planar surfaces without semi-transparent medium can be developed as

$$E_{2-3} = \frac{\sigma\left(T_2^4 - T_3^4\right)}{\frac{1}{\varepsilon_2} + \frac{1}{\varepsilon_3} - 1} \tag{A11}$$

using Eq. (A10) and additional equations, i.e., $\alpha_1 = \rho_1 = 0, \tau_1 = 1, E_1 = 0$.

B. Zero transmissivity condition

The net radiative heat flux from Medium 1 to Media 2 and 3 in a three-medium system as shown in Figure 2-29 under zero transmissivity condition will be illustrated here.

The energy absorbed by Medium 1 per unit area due to the photons emitted from Media 1 to 2 and from Media 1 to 3 can be respectively calculated by

$$E_{1a,1-2}(\tau_1 = 0) = \alpha_1\rho_2 E_1 + \alpha_1\rho_2 E_1(\rho_1\rho_2) + \alpha_1\rho_2 E_1(\rho_1\rho_2)^2 + \cdots \quad \text{(B1)}$$

$$E_{1a,1-3}(\tau_1 = 0) = \alpha_1\rho_3 E_1 + \alpha_1\rho_3 E_1(\rho_1\rho_3) + \alpha_1\rho_3 E_1(\rho_1\rho_3)^2 + \cdots \quad \text{(B2)}$$

The energy absorbed by Medium 1 per unit area due to the photons emitted from Media 2 to 1 and from Media 3 to 1 can be respectively estimated by

$$E'_{1a,2-1}(\tau_1 = 0) = \alpha_1 E_2 + \alpha_1 E_2(\rho_1\rho_2) + \alpha_1 E_2(\rho_1\rho_2)^2 + \cdots \quad \text{(B3)}$$

$$E'_{1a,3-1}(\tau_1 = 0) = \alpha_1 E_3 + \alpha_1 E_3(\rho_1\rho_3) + \alpha_1 E_3(\rho_1\rho_3)^2 + \cdots \quad \text{(B4)}$$

Therefore, the net radiative heat flux from Media 1 to 2 and 3 is given by

$$E_{1-2\&3}(\tau_1 = 0) = \left[E_1 - E_{1a,1-2}(\tau_1 = 0)\right] + \left[E_1 - E_{1a,1-3}(\tau_1 = 0)\right] - E'_{1a,2-1}(\tau_1 = 0) - E'_{1a,3-1}(\tau_1 = 0) = 2E_1 - \alpha_1\left[\frac{\rho_2 E_1 + E_2}{1-\rho_1\rho_2} + \frac{\rho_3 E_1 + E_3}{1-\rho_1\rho_3}\right] \quad \text{(B5)}$$

Bibliography

Abe, Y., Kosugiyama, O., and Nagashima, A., "Viscosity of LiF-BeF_2 Eutectic Mixture (X_{BeF2}=0.328) and LiF Single Salt at Elevated Temperatures," *Journal of Nuclear Materials*, **99**, pp. 173-183 (1981).

Adamson, G.M., Crouse, R.S., and Manly, W.D., "Interim Report on Corrosion by Alkali-Metal Fluorides, Oak Ridge National Laboratory, ORNL-2337 (1953).

Ahn, S., "Experimental Studies on Heat Transfer in the Annuli with Corrugated Inner Tubes," *KSME International Journal*, **17**, pp. 1226-1233 (2003).

Aicher, T. and Kim, W.K., "Experimental Investigation of the Influence of the Cross Flow in the Nozzle Region on the Shell-Side Heat Transfer in Double-Pipe Heat Exchangers," *International Communications in Heat and Mass Transfer*, **25**, pp. 43-58 (1998).

Ambrosek, J., Anderson, M., Sridharan, K., and Allen, T., "Current Status of Knowledge of the Fluoride Salt (FLiNaK) Heat Transfer," *Nuclear Technology*, **165**, pp. 166-173 (2009).

An, X., Cheng, J.H., Yin, H.W., Xie, L.D., and Zhang, P., "Thermal Conductivity of High Temperature Fluoride Molten Salt Determined by Laser Flash Technique," *International Journal of Heat and Mass Transfer*, **90**, pp. 872-877 (2015).

Andreades, C.H., Cisneros, A.T., and Choi, J.K., "Technical Description of the "Mark 1" Pebble-Bed Fluoride-Salt-Cooled High-Temperature Reactor (PB-FHR) Power Plant," UCBTH-14-002, University of California, Berkeley (2014).

Baes, C.F., "The Chemistry and Thermodynamics of Molten Salt Reactor Fuels," *Journal of Nuclear Materials*, **51**, pp. 149-162 (1974).

Baldwin, C.M. and Mackenzie, J.D., "Preparation and Properties of Water-free Vitreous Beryllium Fluoride," *Journal of Non-Crystalline Solids*, **31**, pp. 441-445 (1979).

Bell, J., Redman, J., and Bittner, H., "Tritium Permeation through Clean Incoloy 800 and Sanicro 31 Alloys and through Steam Oxidized Incoloy 800," *Metallurgical Transactions A*, **11A**, pp. 775-782 (1980).

Bergman, A.G. and Dergunov, E.P., "Fusion Diagram of LiF-KF-NaF," *Comptes Rendus Chimie*, U.R.S.S. **31**, pp. 753-754 (1941).

Bergman, T., Lavine, A., Incropera, F., and Dewitt, D., "Fundamentals of Heat and Mass Transfer, seventh edition," John Wiley & Sons (2011).

Briggs, R., "Tritium in Molten-Salt Reactors," *Reactor Technology,* **14.** pp. 335-343 (1971).

Britsch, K., Anderson, M., Brooks, P., and Sridharan, K., "Natural Circulation FLiBe Loop Overview," *International Journal of Heat and Mass Transfer*, **134**, pp. 970-983 (2019).

Cantor, S., Cooke, J.W., Dworkin, A.S., Robbins, G.D., Thoma, R.E., and Watson, G.M., "Physical Properties of Molten-Salt Reactor Fuel, Coolant, and Flush Salts," ORNL/TM-2316, Oak Ridge National Laboratory (1968).

Cantor, S., "Density and Viscosity of Several Molten Fluoride Mixtures," ORNL/TM-4308, Oak Ridge National Laboratory (1973).

Chaleff, E.S., Blue, T., and Sabharwall, P., "Radiation Heat Transfer in Molten Salt FLiNaK," *Nuclear Technology*, **196**, pp. 53-60 (2016).

Chaleff, E.S., Antolin, N., Windl, W., and Blue, T., "Ab-Initio Calculation of Spectral Absorption Coefficients in Molten Fluoride Salts with Metal Impurities," *Nuclear Technology*, **204**, pp. 59-65 (2018).

Chen, X., Xu, X., Nguang, S., and Bergles, A., "Characterization of the Effect of Corrugation Angles on Hydrodynamic and Heat Transfer Performance of Four-Start Spiral Tubes," *Journal of Heat Transfer*, **123**, pp. 1149-1158 (2001).

Chen, M., Sun, X., and Christensen, R., "Thermal-hydraulic Performance of Printed Circuit Heat Exchangers with Zigzag Flow Channels," *International Journal of Heat and Mass Transfer*, **130**, pp. 356-367 (2019).

Chen, Y., Wang, Y., Zhang, J., Yuan, X., Tian, J., Tang, Z., Zhu, H., Fu, Y., and Wang, N., "Convective Heat Transfer Characteristics in the Turbulent Region of Molten Salt in Concentric Tube," *Applied Thermal Engineering*, **98**, pp. 213-219 (2016).

Chen, Y., Tian, J., Sun, S., Sun, Q., Fu, Y., Tang, Z., Zhu, H., and Wang, N., "Characteristics of the Laminar Convective Heat Transfer of Molten Salt in Concentric Tube," *Applied Thermal Engineering*, **125**, pp. 995-1001 (2017).

Cheng, J., Zhang, P., An, X., Wang, K., Zuo, Y., Yan, H., and Li, Z., "A Device for Measuring the Density and Liquidus Temperature of Molten Fluorides for Heat Transfer and Storage," *Chinese Physics Letters,* **30**, 126501, pp. 1- 4 (2013).

Chrenkova, M., Danek, V., Silny, A., and Polyakov, E., "Density and Viscosity of the (LiF-NaF-KF) eut-KBF_4-B_2O_3 Melts," *Journal of Molecular Liquids,* **102**, pp. 213-226 (2003).

Cibulkova, J., Chrenkova, M., Vasiljev, R., Kremenetsky, V., and Boca, M., "Density and Viscosity of the $(LiF + NaF + KF)_{eut}$ (1) + K_2TaF_2(2) + Ta_2O_5(3) Melts," *Journal of Chemical & Engineering Data*, **51**, pp. 984-987 (2006).

Cimbala, Y.A. and Cengel, J.M., "Fluid Mechanics: Fundamentals and Applications, 1st edition," Boston: McGraw-Hill Higher Education (2005).

Cohen, A.B. and Rohsenow, W.M., "Thermally Optimum Spacing of Vertical, Natural Convection Cooled, Parallel Plates," *Journal of Heat Transfer*, **106**, pp.116-123 (1984).

Cooke, J. and Cox, B., "Forced Convection Heat Transfer Measurements with A Molten Fluoride Salt Mixture Flowing in a Smooth Tube," ORNL-TM-4079, Oak Ridge National Laboratory (1973).

Cooper, L. and Claiborne, S.J., "Measurement of the Thermal Conductivity of FLiNaK," ORNL 52.8-163, Oak Ridge National Laboratory (1952).

Corripio, A., Chrien, K., Evans, L., "Estimate Costs of Heat Exchangers and Storage Tanks via Correlations," *Chemical Engineering*, **89**, pp. 125-127 (1982).

Coyle, C., Baglietto, E., and Forsberg, C., "Advanced Radiative Heat Transfer Modeling in High-Temperature Liquid-Salts," *18th International Topical Meeting on Nuclear Reactor Thermal Hydraulics*, NURETH-18, Portland, OR, August 18-22 (2019).

Dai, Z. and Liu, W., "Thorium-based Molten Salt Reactor (TMSR) Project in China," *Proceedings of the Conference on Molten Salts in Nuclear Technology*, **44**, Bhabha Atomic Research Centre, India (2013).

Darienko, S. E., Desyatnik, V. I., Katyshev, S.F., and Chervinskii, Y.F., "Density and surface Tension of Melts of the KF-KCl-ZrF4 System," *Atomnaya Energiya*, **65**, pp. 223-224 (1988). (Soviet Atomic Energy)

Depew, C.A. and August, S.E., "Heat Transfer due to Combined Free and Forced Convection in a Horizontal and Isothermal Tube," *Journal of Heat Transfer*, **93**, pp. 380-384 (1971).

Derdeyn, W., Dbai, M., Scarlat, R., and Trujillo, M., "FLiBe Radiative Heat Transfer," *Transactions of the American Nuclear Society*, **118**, Philadelphia, Pennsylvania, June 17-21 (2018).

EI-Wakil, M.M., "Nuclear Heat transport," International Textbook Co., Scranton, PA (1971).

Feron, D., "Nuclear Corrosion Science and Engineering," WP Woodhead Publishing (2012).

Forsberg, C., Lam, S., Carpenter, D., Whyte, D., Scarlat, R., Contescu, C., Wei, L., Stempien, J., and landford, E., "Tritium Control and Capture in Salt-Cooled Fission and Fusion Reactors: Status, Challenges, and Path Forward," *Nuclear Technology*, **197**, pp.119-139 (2017).

Fukada, S., Anderl, R., Sagara, A., and Nishikawa, M., "Diffusion Coefficient of Tritium through Molten Salt FLiBe and Rate of Tritium Leak from Fusion Reactor System," *Fusion Science and Technology*, **48**, pp. 666-669 (2005).

Fukada, S. and Morisaki, A., "Hydrogen Permeability through A Mixed Molten Salt of LiF, NaF, and KF (FLiNaK) as A Heat-Transfer Fluid," *Journal of Nuclear Materials*, **358**, pp. 235-242 (2006).

Garimella, S., Christensen, R.N., Garrabrant, M.A., and Boos, M.E., "An Experimental Investigation of Heat Transfer Characteristics of Spirally Fluted Tubes in Confined Cross-Flow," *ASHRAE Transactions*, **96** (1990).

Gomaa, A., Halim, M., and Elsaid, A., "Experimental and Numerical Investigations of A Triple Concentric-Tube Heat Exchanger," *Applied Thermal Engineering*, **99**, pp. 1303-1315 (2016).

Greene, S.R., Gehin, J.C., Holcomb, D.E., et al., "Pre-Conceptual Design of a Fluoride-Salt-Cooled Small Modular Advanced High-Temperature Reactor (SmAHTR)," ORNL/TM-2010/199, Oak Ridge National Laboratory (2010).

Grele, M. and Gedeon, L., "Forced Convection Heat Transfer Characteristics of Molten FLiNaK Flowing in an Inconel X System," NACA RM E53L18, National Advisory Committee for Aeronautics (1954).

Grimes, W. R., "Reactor Chemistry Division Annual Progress Report for Period Ending December 31, 1965," ORNL-3913, Oak Ridge National Laboratory (1966).

Gruszcynski, M.J. and Viskanta, R., "Heat Transfer to Water from a Vertical Tube Bundle under Natural-Circulation Conditions," ANL-83-7, Argonne National Laboratory (1983).

Hallinan, K.P. and Viskanta, R., "Heat Transfer from a Vertical Tube Bundle under Natural Circulation Conditions," *International Journal of Heat and Fluid Flow*, **6**, pp.256-264 (1985).

Hallinan, K.P. and Viskanta, R., "Dynamics of a Natural Circulation Loop: Analysis and Experiments," *Heat Transfer Engineering*, **7**, pp.43-52 (1986).

Hausen, H,."Neue Gleichungen fur die Wameiibertragung bei Freier oder Erzwungerner Stromung," Allg. Warmetchn., **9**, pp. 75–79 (1959).

Hoffman, H. and Lones, J., "Fused Salt Heat Transfer, Part II: Forced Convection Heat Transfer in Circular Tubes Containing NaF-KF-LiF Eutectic," ORNL-1777, Oak Ridge National Laboratory (1955).

Hoffman, H. and Cohen, S., "Fused Salt Heat Transfer, Part III: Forced Convection Heat Transfer in Circular Tubes Containing the Salt Mixture $NaNO_2$-$NaNO_3$-KNO_3," ORNL-2433, Oak Ridge National Laboratory (1960).

Holcomb, D., Peretz, F., and Qualls, A., "Advanced High Temperature Reactor Systems and Economic Analysis," ORNL/TM-2011/364, Oak Ridge National Laboratory (2011).

Ishii, M., "Scaling Laws for Thermal-Hydraulic System Under Single-Phase and Two-Phase Natural Circulation," *Nuclear Engineering and Design*, **81**, pp. 411-425 (1984).

Janz, G. and Tomkins, R., "Physical Properties Data Compilations Relevant to Energy Storage, IV. Molten Salts: Data on Additional Single and Multi-Component Salt Systems," NSRDS-NBS 61, National Standard Reference Data System (1981).

Jeong, H.S. and Bang, K.H., "A Design of He-Molten Salt Intermediate Heat Exchanger for VHTR," *Transactions of the Korean Nuclear Society Autumn Meeting*, Jeju, Korea, October 21-22 (2010).

Kairos Power, "Design Overview for the Kairos Power Fluoride Salt-cooled High-temperature Reactor," KP-NRC-1811-002, Kairos Power, LLC. (2018).

Kakac, S., Yener, Y., and Pramuanjaroenkij, A., "Convective Heat Transfer," Third Edition, CRC Press (2014).

Kherani, N., Jalbert, R., and Shmayda, W., "Tritium Removal from Inert Gases Using ST 198 Alloy," CFFTP-G-88039, Canadian Fusion Fuels Technology Project (1988).

Khokhlov, V., Ignatiev, V., and Afonichkin, V., "Evaluating Physical Properties of Molten Salt Reactor Fluoride Mixtures," *Journal of Fluorine Chemistry*, **130**, pp. 30–37 (2009).

Kubikova, B., Pavlik, V., and Mackova, I., "Surface Tension and Viscosity of the Molten $(LiF-NaF-KF)_{eut} - K_2ZrF_6$ System," *Monatshefte Fur Chemie*, **143**, pp. 1459-1462 (2012).

Kubikova, B., Mackova, I., and Boca, M., "Phase Analysis and Volume Properties of the $(LiF-NaF-KF)_{eut}$ $-K_2ZeF_6$ System," *Monatshefte Fur Chemie,* **144**, pp. 295-300 (2013).

Kudariyawar, J.Y., Srivastava, A.K., Vaidya, A.M., Maheshwari, N.K., and Satyamurthy, P., "Computational and Experimental Investigation of Steady State and transient Characteristics of Molten Salt Natural Circulation Loop," *Applied Thermal Engineering*, **99**, pp. 560-571 (2016).

Li, H.H., "Absorption Coefficient of Alkali Halides (Part II)," CINDAS Report 55 (1979).

Lin, H.C., Zhang, S., Diamond, D., Bajorek, S., Christensen, R., Guo, Y., Yoder, G., Shi, S. Lv, Q., and Sun, X., "Phenomena Identification and Ranking Table Study for Thermal Hydraulics for Advanced High Temperature Reactor," *Annals of Nuclear Energy*, **124**, pp. 257-269 (2019).

Lin, H.C., "Thermal Hydraulics System-Level Code Validation and Transient Analyses for Fluoride Salt-Cooled High-Temperature Reactors," PhD dissertation, University of Michigan (2020).

Liu, B., Wu, Y., Ma, C., Ye, M., and Guo, H., "Turbulent Convective Heat Transfer with Molten Salt in a Circular Pipe," *International Communications in Heat and Mass Transfer*, **36**, pp. 912-916 (2009).

Liu, L., Zhang, D., Lu, Q., Wang, K., and Qiu, S., "Preliminary Neutronic and Thermal-Hydraulic Analysis of a 2 MW Thorium-based Molten Salt Reactor with Solid Fuel," *Progress in Nuclear Energy*, **86**, pp. 1-10 (2016).

Lv, Q., Lin, H.C., Kim, I.H., Sun, X., Christensen, R.N., Blue, T.E., Yoder, G.L., Wilson, D.F., and Sabharwall, P., "DRACS Thermal Performance Evaluation for FHR," *Annals of Nuclear Energy*, **77**, pp. 115-128 (2015a).

Lv, Q., Wang, X., Kim, I.H., Sun, X., Christensen, R.N., Blue, T.E., Yoder, G., Wilson, D., and Sabharwall, P., "Scaling Analysis for the Direct Reactor Auxiliary Cooling System for FHRs," *Nuclear Engineering and Design*, **285**, pp. 197-206 (2015b).

Marrero T. and Mason, E., "Gaseous Diffusion Coefficient," *Journal of Physics Chemistry Reference Data* 1," 3 (1972).

Martinelli, R.C. and Boelter, L.M.K., "The Analytical Prediction of Superposed Free and Forced Viscous Convection in a Vertical Pipe," University of California, Publications in Engineering, **5**, pp. 23-58 (1942).

Massey, B.S., "Mechanics of Fluids, eighth edition," Taylor & Francis (2006).

Mehos, M., Turchi, C., Vidal, J., Wagner, M., and Ma, Z., "Concentrating Solar Power Gen3 Demonstration Roadmap," NREL/TP-5500-67464, National Renewable Energy Laboratory (2017).

Merzlyakov, A., Ignatiev, V., and Abalin, S., "Viscosity of LiF-NaF-KF Eutectic and Effect of Cerium Trifluoride and Uranium Tetrafluoride Additions," *Nuclear Engineering and Design*, **278**, pp. 268-273 (2014).

MetalPrices Inc., www.metalprices.com, accessed on 2/24/2016

Moody, L.F., "Friction Factors for Pipe Flow," *Transactions of the ASME,* **66**, pp. 671-684 (1944).

Mohanty, A.K. and Sahoo, K.M., "Laminar Convection in Wall Sub-Channels and Transport Rates for Finite Rod-Bundle Assemblies by Superposition," *Nuclear Engineering and Design,* **92**, pp. 169-180 (1986).

Morris, F. and Whitman, W., "Heat Transfer for Oils and Water in Pipes," *Industrial and Engineering Chemistry*, **20**, pp. 234-240 (1928).

Mouchart, J., Lagier, G., and Pointu, B., "Determination Des Constantes Optiques n et K de Materiaux Faiblement Absorbants," *Applied Optics*, **24**, pp. 1808-1814 (1985).

Olson, L., "Materials Corrosion in Molten LiF-NaF-KF Eutectic Salt," PhD dissertation, University of Wisconsin-Madison (2009).

Olson, L., Sridharan, K., Anderson, M., and Allen, T., "Nickel-plating for Active Metal Dissolution Resistance in Molten Fluoride Salts," *Journal of Nuclear Materials,* **411**, pp. 51-59 (2011).

Parker, W.J., Jenkins, R.J., Butler, C.P., and Abbott, G.L., "Method of Determining Thermal Diffusivity, Heat Capacity and Thermal Conductivity," *Journal of Applied Physics*, **32**, pp. 1679-1684 (1961).

Powers, W.D., Cohen, S.L., and Greene, N.D., "Physical Properties of Molten Reactor Fuels and Coolant," *Nuclear Science and Engineering*, **71**, pp. 200-211 (1963).

Qian, J., Kong, Q., Zhang, H., Zhu, Z., Huang, W., and Li, W., "Performance of a Gas Cooled Molten Salt Heat Exchanger," *Applied Thermal Engineering*, **108**, pp. 1429-1435 (2016).

Qian, J., Kong, Q., Zhang, H., Zhu, Z., Huang, W., and Li, W., "Experimental Study for Shell-and-tube Molten Salt Heat Exchangers," *Applied Thermal Engineering*, **124**, pp. 616-623 (2017).

Rahnema, F., "Integrated Approach to Fluoride High Temperature Reactor Technology and Licensing Challenges," 2nd Molten Salt Reactor Workshop, Oak Ridge, TN, October 4-5 (2016).

Rahnema, F., Diamond, D., Serghiuta, D., and Burke, P., "Phenomena, Gaps, and Issues for Neutronics Modeling and Simulation of FHRs," *Annals of Nuclear Energy*, **123**, pp. 172-179 (2019).

Rao, M.R., "Thermal Conductivity of Liquids," *Indian Journal of Physics*, **16**, pp. 347-367 (1942).

Rogers, D., Yoko, T., and Janz, G., "Fusion Properties and Heat Capacities of the Eutectic LiF-NaF-KF Melt," *Journal of Chemistry Engineering Data*, **27**, pp. 366-367 (1982).

Romatoski, R.R. and Hu, L.W., "Fluoride Salt Coolant Properties for Nuclear Reactor Applications: A Review," *Annals of Nuclear Energy*, **109**, pp. 635-647 (2017).

Rosenthal, M.W., Briggs, R.B., and Kasten, P.R., "Molten Salt Reactor Program Semiannual Progress Report," ORNL-4344, Oak Ridge National Laboratory (1969).

Rubio, F., Bond, L., and Blandford, E., "Scaled Experiment Investigating Sonomechanically Enhanced Inert Gas Sparging Mass Transfer," *Nuclear Engineering and Design*, **324**, pp.171-180 (2017).

Sabharwall, P., Ebner, M., Sohal, M., Sharpe, P., Anderson, M., Sridharan, K., Ambrosek, J., Olson, L., and Brooks, P., "Molten Salts for High Temperature Reactors: University of Wisconsin Molten Salt Corrosion and Flow Loop Experiments – Issues Identified and Path Forward," INL/EXT-10-18090, Idaho National Laboratory (2010).

Sahoo, K.M. and Mohanty, A.K., "Finite Element Analysis for Laminar Flow and Heat Transfer in Finite Rod Bundles," *Chemical Engineering Communications*, **51**, pp. 129-140 (1987).

Schmutz, H., Sabharwall, P., and Stoots, C., "Tritium Formation and Mitigation in High Temperature Reactors," INL/EXT-12-26758, Idaho National Laboratory (2012).

Schwer, L., "Is Your Mesh Refined Enough? Estimating Discretization Error using GCI," LS-DYNA Anwenderforum, Bamberg (2008).

Sieder, E. and Tate, G., "Heat Transfer and Pressure Drop of Liquids in Tubes," *Industrial and Engineering Chemistry*, **28**, pp. 1429-1435 (1936).

Silverman, M., Huntley, W., and Robertson, H., "Heat Transfer Measurements in a Forced Convection Loop with `Two Molten-Fluoride Salts: LiF-BeF_2-ThF_4-UF_4 and Eutectic $NaBF_4$-NaF," ORNL/TM-5335, Oak Ridge National Laboratory (1976).

Singh, P.M., Chan, K., Deo, C., Deodeshmukh, V., Keiser, J., Ren, W., Sham, T.L., Wilson, D., Yoder, G., and Zhang, J., "Phenomena Identification and Ranking Table (PIRT) Study for Metallic Structural Materials for Advanced High-Temperature Reactor," *Annals of Nuclear Energy*, **123**, pp. 222-229 (2019).

Smirnov, M.V., Khokhlov, V.A., and Filatov, E.S., "Thermal Conductivity of Molten AlKali Halides and Their Mixtures," *Electrochemica Acta*, **32**, pp. 1019-1026 (1987).

Special Metals, www.specialmetals.com, accessed on 4/20/2018.

Speirs, J.L., "The Binary and Ternary Systems Formed by Calcium Fluoride, Lithium Fluoride, and Beryllium Fluoride: Phase Diagrams and Electrolytic Studies," Ph.D. Thesis, University of Michigan (1952).

Srinivas, N. and Deb, K., "Multi-objective Optimization Using Non-Dominated Sorting in Genetic Algorithms," *Evolutionary Computation*, **2**, pp. 221-248 (1994).

Srinivasan, V., "Experimental and Numerical Investigation of Heat Transfer and Pressure Drop in Flow through Spirally Fluted Tubes," PhD thesis, Ohio State University (1993).

Srivastava, A.K., Kudariyawar, J.Y., Borgohain, A., Jana, S.S., Maheshwari, N.K., and Vijayan, P.K., "Experimental and Theoretical Studies on the Natural Circulation Behavior of Molten Salt Loop," *Applied Thermal Engineering*, **98**, pp. 513-521 (2016).

Stempien, J., Ballinger, R., and Forsberg, C., "An Integrated Model of Tritium Transport and Corrosion in Fluoride Salt-Cooled High-Temperature Reactors (FHRs) – Part I: Theory and Benchmarking," *Nuclear and Engineering Design*, **310**, pp. 258-272 (2016).

Strehlow, R. and Savage, H., "The Permeation of Hydrogen Isotopes through Structural Metals at Low Pressures and through Metals with Oxide Film Barriers," *Nuclear Technology*, **22**, pp. 127-137 (1974).

Suzuki, A., Terai, T., and Tanaka, S., "Tritium Release Behavior from Li_2BeF_4 Molten Salt by Permeation through Structural Materials," *Fusion Engineering and Design*, **51-52**, pp. 863-868 (2000).

Thoma, R.E., "Phase Diagrams of Nuclear Reactor Materials," ORNL-2548, Oak Ridge National Laboratory (1959).

Toth, L. and Gilpatrick, L., "The Equilibrium of Dilute UF_3 Solutions Contained in Graphite," ORNL-TM-4056, Oak Ridge National Laboratory (1972).

U.S. NRC, https://www.nrc.gov/reactors/operating/ops-experience/tritium/faqs.html#normal

Varma, W., Holcomb, D., Peretz, F., Bradley, E., IIas, D., Qualls, A., and Zaharia, N., "AHTR Mechanical, Structural, and Neutronic Preconceptual Design," ORNL/TM-2012/320, Oak Ridge National Laboratory (2012).

Vijayan, P.K. and Austregesilo, H., "Scaling Laws for Single-Phase Natural Circulation Loops," *Nuclear Engineering and Design*, **152**, pp. 331-347 (1994).

Vriesema, I., "Aspects of Molten Fluorides as Heat Transfer Agents for Power Generation," Delft University of Technology, Doctor Dissertation, Netherlands (1979).

Wang, D., Yoder, G., Pointer, D., and Holcomb, D., "Thermal Hydraulics Analysis of the Advanced High Temperature Reactor," *Nuclear Engineering and Design*, **294**, pp. 73-85 (2015).

Wang, M., Song, J., and Li, Y., "Hydrogen Separation at Elevated Temperatures using Metallic Nickle Hollow Fiber Membranes," *American Institute of Chemical Engineers*, **63**, pp. 3026-3034 (2017).

Welty, J., Wicks, C., Wilson, R., and Rorrer, G., "Fundamentals of Momentum, Heat, and Mass Transfer. 5th Edition," John Wiley & Sons, Inc. (2007).

Williams, D. F., Toth, L. M., and Clarno, K. T., "Assessment of Candidate Molten Salt Coolants for the Advanced High-Temperature Reactor (AHTR)," ORNL/TM-2006/12, Oak Ridge National Laboratory (2006).

Wu, X., Zhang, S., Shi, S., Sun, X., Holcomb, D., Christensen, R., and Sabharwall, P., "Tritium Release Limit for Fluoride Salt-cooled High-temperature Reactors," *Transactions of the American Nuclear Society*, **115**, Las Vegas, NV, USA, November 6-10 (2016).

Wu, X., Shi, S., Zhang, S., Arcilesi, D., Christensen, R., Sabharwall, P., and Sun, X., "Mass Transport Analysis for Tritium Removal in FHRs," *Annals of Nuclear Energy*, **121**, pp. 250-259 (2018).

Wu, Y., Liu, B., Ma, C., and Guo, H., "Convective Heat Transfer in the Laminar-turbulent Transition Region with Molten Salt in a Circular Tube," *Experimental Thermal and Fluid Science*, **33**, pp. 1128-1132 (2009).

Yoder, G., "Examination of Liquid Fluoride Salt Heat Transfer," Proceedings of ICAPP 2014, Charlotte, NC, USA, pp. 1765-1774 (2014a).

Yoder, G., Bopp, A., Holcomb, D., Pointer, W., and Wang, D., "Advanced High Temperature Reactor Thermal Hydraulics Analysis and Salt Clean-up System Description," ORNL/TM-2014/499, Oak Ridge National Laboratory (2014b).

Zhang, S., Chen, M., Shi, S., Sun, X., and Christensen, R., "Corrosion Behavior of Stainless Steel SS 316H in LiF-NaF-KF (FLiNaK) at High temperatures," *Transactions of the American Nuclear Society*, **117**, Washington, D.C., October 29 – November 2 (2017a).

Zhang, S., Shi, S., Wu, X., Sun, X., and Christensen, R., "Double-wall Natural Draft Heat Exchanger Design for Tritium Control in FHRs," *Proceedings of the 2017 25th International Conference on Nuclear Engineering*, ICONE25, Shanghai, China, July 2-6 (2017b).

Zhang, S., Wu, X., Shi, S., Sun, X., Christensen, R., and Yoder, G., "A Coupled Heat Transfer and Tritium Mass Transport Model for A Double-wall Heat Exchanger Design for FHRs," *Annals of Nuclear Energy*, **122**, pp.328-339 (2018).

Zhang, S., Lin, H.C., Cheng, K., and Sun, X., "Design of a Direct Reactor Auxiliary Cooling System (DRACS) Considering Tritium Management for Advanced High-Temperature Reactor (AHTR)," *18th International Topical Meeting on Nuclear Reactor Thermal Hydraulics*, Portland, Oregon, USA, August 18-23 (2019a).

Zhang, S., Lin, H.C., Cheng, K. and Sun, X., "Design of a High-Temperature Fluoride Salt Test Facility (HT-FSTF)," *Transactions of the American Nuclear Society*, **121**, pp.1649-1652 (2019b).

Zhang, S., Sun, X., and Dominguez-Ontiveros, E., "Numerical Study on Convective Heat Transfer and Friction Characteristics of Molten Salts in Circular Tubes," *Annals of Nuclear Energy*, **142**, pp. 107375-107389 (2020a).

Zhang, S. and Sun, X., "Convective and Radiative Heat Transfer in Molten Salts," *Nuclear Technology*, DOI: 10.1080/00295450.2020.1749481 (2020b).

Zhang, S., Wu, X., and Sun, X., "Numerical Study of Tritium Mitigation Strategies for Fluoride Salt-cooled High-Temperature Reactors," *ASME's Nuclear Engineering Conference powered by ICONE*, Virtual Conference, August 4-5 (2020c)

Zhu, G., Zou, Y., Yan, R., Tan, M., Zou, C., Kang, X., Chen, J., Guo, W., and Dai, Y., “Low Enriched Uranium and Thorium Fuel Utilization under Once-Through and Offline Reprocessing Scenarios in Small Modular Molten Salt Reactor,” *International Journal of Energy Research*, **43**, pp. 5775:5787 (2019).